TECHNISCHE UNIVERSITÄT WIEN
VIENNA UNIVERSITY OF TECHNOLOGY

Dissertation

Development of Large Area Silicon Sensors for the High Granularity Calorimeter at CMS

ausgeführt zum Zwecke der Erlangung des akademischen Grades eines Doktors der technischen Wissenschaften unter der Leitung von

Univ.-Doz. Dipl.-Ing. Dr.techn. Manfred Krammer
Univ.-Lektor Dipl.-Ing. Dr.techn. Thomas Bergauer
Institut für Hochenergiephysik
der Österreichischen Akademie der Wissenschaften
und
Atominstitut der Technischen Universität Wien

eingereicht an der Technischen Universität Wien
Fakultät für Physik

von

Elias Pree, M.Sc.

Matrikelnummer: 01527933
Kölblgasse 29/10
1030 Wien

Wien, am 9. September 2018

Kurzfassung

Der Large Hadron Collider (LHC) befindet sich am CERN, der europäischen Organisation für Kernforschung. Der LHC ist der größte Kreisbeschleuniger der Welt. Er beschleunigt Protonen zu einer Schwerpunktsenergie von 13 TeV und lässt diese kollidieren. Aus diesem Prozess werden grundlegende Informationen über die Wechselwirkung von Teilchen und die fundamentalen Naturgesetze gewonnen. Das Compact Muon Solenoid (CMS) Experiment befindet sich an einem der vier Interaktionspunkte des LHC.

Mitte der 2020er Jahre wird die Kollisionsrate am LHC und damit die Menge an gesammelten Daten signifikant erhöht. Durch diese Erhöhung können statistisch seltenere Zerfälle von Teilchen beobachtet und vom Hintergrund besser unterschieden werden. Diese neue Betriebsphase wird High-Luminosity-LHC (HL-LHC) genannt. Um die Detektoren des CMS Experiments in dieser neuen Phase betreiben zu können, müssen einige Systeme erneuert und verbessert werden. Diese Erneuerung wird *CMS Phase II upgrade* genannt. Ein Teil dieses Projekts ist der vollständige Ersatz der gegenwärtigen elektromagnetischen und hadronischen Kalorimeterendkappe durch ein komplett erneuertes, innovatives und komplexes System, das *High Granularity Calorimeter* (HGCal). Das Kalorimeter ist als ein Sampling-Kalorimeter mit einer Gesamtfläche von ungefähr 600 m^2 aus planaren, großflächigen Siliziumsensoren als aktivem Detektormaterial konzipiert.

Das Hauptziel dieser Doktorarbeit ist die Entwicklung großflächiger hexagonaler Siliziumdetektoren für das Kalorimeter. Auf Grund der Ergebnisse in dieser Doktorarbeit und der Arbeit des Instituts für Hochenergiephysik (HEPHY), konnte die Standardgröße von Siliziumdetektoren für das HGCal von 6-Zoll auf 8-Zoll erhöht werden. Um die Machbarkeit von 8-Zoll Detektoren für das Kalorimeter zu zeigen, entwickelte der Autor 8-Zoll Demonstrationssensoren für das HGCal. Das Layout der Detektoren wurde durch das Programmieren von Skripten erstellt, welche jedes Polygon jeder einzelnen Detektormaske genau definieren. Die Masken werden für die einzelnen Lithographieschritte in der Produktion der Siliziumdetektoren benötigt. Dieses Design wurde von Infineon Technologies Austria AG verwendet, um 8-Zoll HGCal Demonstrationsdetektoren zu produzieren. Die Dissertation präsentiert die Layoutdetails und vergleicht ausgewählte Detektoren mit Hilfe mehrerer verschiedener Strom- und Kapazitätsmesstechniken.

Basierend auf dem Erfolg der Demonstrationssensoren wird das Design mit Hilfe von TCAD Simulationen optimiert. Dabei werden Geometrieparameter variiert, um die Hochspannungsfestigkeit der Sensoren zu erhöhen. Diese Information ist ein wertvoller Teil des neuen Prototypdesigns, das vom Author erschaffen wurde. Das optimierte Design wird von allen Herstellern benutzt werden, die HGCal Detektoren mit 192 Pads produzieren. Die Detektoren mit diesem Design sollen letztendlich in das *High Granularity Calorimeter* eingebaut werden.

Detektoren in einem Kalorimeter sind einer hohen Strahlungsbelastung ausgesetzt. Das Verständnis der Auswirkungen von Strahlungsschäden in Silizium und die Beschreibung dieser mit Hilfe von TCAD Simulationen, sind wichtig für die Entscheidung welche Art von Siliziumdetektoren letztendlich für das Kalorimeter benutzt werden. Der Autor untersucht

die Auswirkung von Strahlungsschäden in Siliziumdetektoren mit unterschiedlicher Dicke, Resistivität und Polarität des Grundmaterials. Um die Qualität der Simulationsergebnisse zu verbessern, werden Messungen an Teststrukturen durchgeführt, damit für die Simulation relevante Parameter extrahiert werden können. Vier verschiedene Bestrahlungsmodelle werden in Hinblick auf Strom, Kapazität und Ladungssammlungseffizienz nach Bestrahlung verglichen.

Abstract

The Large Hadron Collider (LHC) is located at CERN, the European Organization for Nuclear Research. The LHC is the world's largest circular particle collider and collides protons at a centre of mass energy of 13 TeV. This process gives information about the interaction of particles and provides insights into the fundamental laws of nature. The Compact Muon Solenoid (CMS) experiment is located at one of the four interaction points of the LHC.

The LHC will increase its proton-proton collision rate in the mid 2020s. With the resulting increase of collision data, rare decays of particles can be distinguished from the background more easily. This new phase of operation is called High Luminosity-LHC (HL-LHC). To be able to operate the detectors of the CMS experiment in this new phase, several systems have to be upgraded. This upgrade is called *CMS Phase II upgrade*. As part of this upgrade, the current electromagnetic and hadronic endcap calorimeter will be replaced with the *High Granularity Calorimeter* (HGCal). The device is designed as a sampling calorimeter with planar, large-area silicon sensors as active detector material, covering a total area of $600\,\mathrm{m}^2$.

The main goal of this thesis is the development of large hexagonal silicon sensors for the calorimeter upgrade. Because of the work presented in this thesis and the work of the Institut of High Energy Physics (HEPHY), the size of the silicon sensors for the HGCal shifted from 6-inch to 8-inch. To show the feasibility of an 8-inch sensor production, the author designed an 8-inch HGCal demonstrator sensor by the programming of scripts that define the geometry of each polygon of all lithography masks needed for the various production steps of a silicon device. Using this design, Infineon Technologies Austria AG manufactured a batch of 8-inch HGCal demonstrator sensors. The thesis presents the design details and shows a comparison of selected sensors. These sensors are compared using several different measurement techniques, comprising various current and capacitance measurements.

Based on the success of the demonstrator, the design is optimised using TCAD simulations. Parameters defining the geometry are varied to optimise the high-voltage stability of the device. This information is a crucial part of a new prototype design created by the author. The design will be used by all vendors producing HGCal sensors segmented into 192 pads. The sensors with the optimised design will be implemented in the *High Granularity Calorimeter*.

Sensors in the calorimeter will be exposed to high irradiation. Understanding and describing the effects of irradiation damage in silicon using TCAD simulations is important for the desicion what kind of silicon sensors to use. The effect of irradiation damage in silicon devices with different thickness, resistivity, and bulk polarity is investigated by the author. To improve the predictive quality of the simulations, test structure measurements are conducted to extract parameters relevant for simulation. Furthermore, several different irradiation models are compared with regard to their ability to reproduce the current, capacitance, and charge collection efficiency after irradiation.

Contents

1

Particle Physics at CERN

1.1 LHC at CERN

The Large Hadron Collider (LHC) is the world's largest particle collider ring with a circumference of 26.7 km. It is located at the European Organization for Nuclear Research (CERN). The beam tunnel is located about 100 m below the surface of the earth and is situated between the Jura mountains and Lake Geneva. Figure 1.1 shows an aerial view of the CERN area. The LHC tunnel is indicated with a yellow circle and the positions of the main experiments are highlighted.

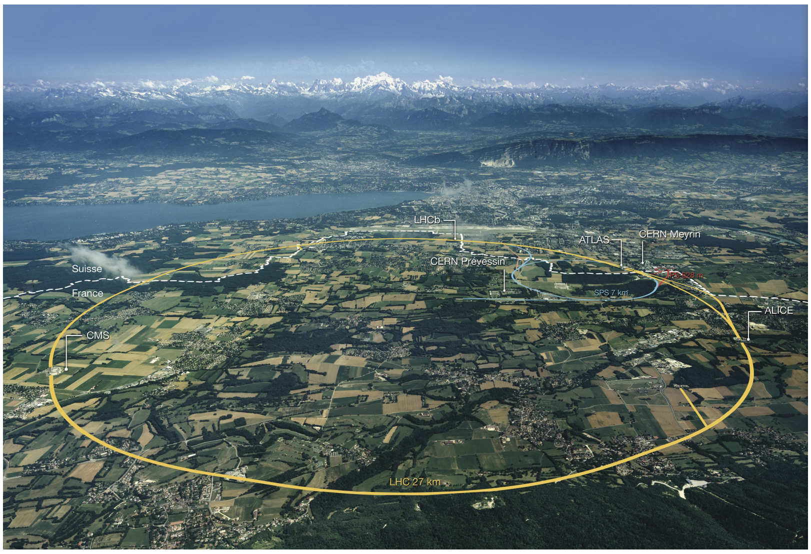

Figure 1.1: An aerial view of the CERN area. The large yellow circle highlights the course of the LHC tunnel. The picture is taken from [1].

The LHC can collide bunches of protons at each of the interaction points (IP) where an experiment is located. The four major experiments are the Compact Muon Solenoid (CMS) experiment, A Toroidal LHC ApparatuS (ATLAS), A Large Ion Collider Experiment (ALICE), and Large Hadron Collider beauty (LHCb). At the start in 2009, the centre of mass energy of the proton collisions was $\sqrt{s} = 900\,\mathrm{GeV}$. Currently it is operated at $\sqrt{s} = 13\,\mathrm{TeV}$. In the near future it will reach its design value of a centre of mass energy of $\sqrt{s} = 14\,\mathrm{TeV}$. The energy available for the production of new particles or effects is the most important parameter for particle physics experiments. The high values of the LHC can only be reached with powerful bending magnets to keep the accelerated particles on track. Therefore, 1232 superconducting dipole magnets, which generate a magnetic field strength of 8.33 T, are used. To focus the particles, 392 quadrupole magnets are used. This is necessary to reach high luminosities [2]. The concept of luminosity is explained in Section 1.2.1.

1.2 High Luminosity LHC

1.2.1 Concept of Luminosity

The luminosity $\mathcal{L}$ is the quantity that measures the ability of a particle accelerator to produce a certain number of interactions for events with a production cross section σ_p. The luminosity is the proportionality factor between the number of events per second dR/dt and the production cross section [3]:

$$\frac{dR}{dt} = \mathcal{L} \cdot \sigma_p. \tag{1.1}$$

The unit of the luminosity $\mathcal{L}$ is $\mathrm{cm}^{-2}\mathrm{s}^{-1}$. To calculate the luminosity of two gaussian beams colliding head-on, Equation 1.2 can be used:

$$\mathcal{L} = \frac{N_1 N_2 f N_b}{4\pi\sigma_x\sigma_y}. \tag{1.2}$$

N_1 and N_2 are the numbers of particles per bunch, f is the revolution frequency, and N_b is the number of colliding bunches. The spatial spread of the bunches is described by σ_x and σ_y. The LHC design value for the instantaneous luminosity, which is described in Equation 1.2, is $1 \times 10^{34}\,\mathrm{cm}^{-2}\,\mathrm{s}^{-1}$.

To calculate the actual number of obtained events, one can integrate the spontaneous luminosity $\mathcal{L}$ over time. The integrated luminosity is defined in Equation 1.3 [3].

$$\mathcal{L}_{int} = \int \mathcal{L}(t')dt' \tag{1.3}$$

The unit of the integrated luminosity is fb^{-1}. For example, the LHC delivered to CMS an integrated luminosity of $49.8\,\mathrm{fb}^{-1}$ for 13 TeV proton collisions in the year 2017 [4].

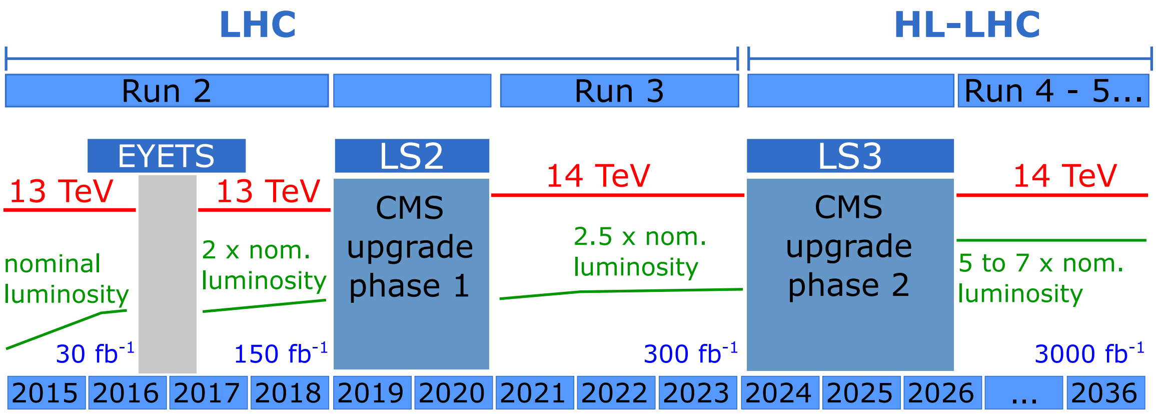

Figure 1.2: Schedule for the HL-LHC upgrade plan. The periods of data taking are called "run". "LS3" is a long shut down period where the detector and the LHC beam are offline to implement the phase 2 upgrade. The figure presents the information from [5].

1.2.2 High Luminosity LHC Upgrade

At the start of the LHC in 2009, it provided proton-proton collisions at a centre of mass energy $\sqrt{s} = 900\,\text{GeV}$. During Run 1, between 2010 and 2011, the energy could be increased to $\sqrt{s} = 7\,\text{TeV}$ and in 2012 even further up to $\sqrt{s} = 8\,\text{TeV}$. After a two year long shutdown (LS1), during which the accelerator and the experiments were upgraded, Run 2 was started in 2015 at $\sqrt{s} = 13\,\text{TeV}$ (1.2). After 2018, Run 2 is followed by another shutdown called LS2 for two years. This period is referred to as the CMS upgrade phase 1, where various detector or LHC accelerator upgrades in CMS are conducted to cope with the steadily increasing radiation damage und luminosity increases. The last run of the LHC phase will be Run 3 between 2021 and 2023 at the design energy of $\sqrt{s} = 14\,\text{TeV}$.

The instantaneous luminosity was increased from up to $2.1 \times 10^{32}\,\text{cm}^{-1}\,\text{s}^{-1}$ in 2010 to $1.5 \times 10^{34}\,\text{cm}^{-1}\,\text{s}^{-1}$ in 2016, which already exceeded the LHC design value by $50\,\%$. It is forseen to collect an integrated luminosity of about $300\,\text{fb}^{-1}$ until the end of Run 3. After Run 3, in 2024 the period called *High Luminosity LHC* (HL-LHC) begins. During LS3, the *CMS Phase II upgrade* takes place. The upgrade enables the detector and accelerator to cope with the increased instantaneous luminosity of $5 \times 10^{34}\,\text{cm}^{-1}\,\text{s}^{-1}$ to $7 \times 10^{34}\,\text{cm}^{-1}\,\text{s}^{-1}$. It is intended to collect $3000\,\text{fb}^{-1}$ during the first 10 years of HL-LHC running with about 140 pileup events. Pileup refers to the number of collisions taking place during a single bunch crossing. The protons in the LHC are clustered in colliding bunches. One bunch contains about 1×10^{11} protons. In an ultimate instantaneus luminosity scenario with 200 pileup events up to $4000\,\text{fb}^{-1}$ could be achieved. For high luminosity operation, it is also foreseen to increase the L1 trigger rate to $750\,\text{kHz}$ and the latency to $12.5\,\mu\text{s}$. During the *CMS Phase II upgrade*, the calorimeter in the forward region is upgraded. CMS plans to replace the existing electromagnetic and hadronic endcap calorimeters with the *High Granularity Calorimeter (HGCal)*, which will be the topic in Chapter 3.

1.2.3 Physics Motivation

The standard model (SM) of particle physics describes the fundamental particles and their interactions. It is based on discoveries and theoretical breakthroughs of the last century. But it is known that the SM is incomplete. The LHC and HL-LHC want to address the following open topics.

Cosmological observations show that the visible matter in the universe makes up only about 15 % of the total matter. The remaining 85 % are called dark matter, because they cannot be observed directly with telescopes, but only by the effects of gravitation. These values should not be confused with the total energy density content of the universe, where about 68 % is dark energy, 27 % is dark matter, and 5 % is visible matter. The SM cannot provide a suitable candidate for dark matter. Hence, the LHC is looking for dark matter candidates.

The SM predicts that at the beginning of the universe matter and antimatter should have been created in equal quantity. Today's universe mostly consists of matter. The abundance of normal matter cannot yet be explained with the SM.

The particle masses in the SM arise through spontaneous symmetry breaking caused by the Higgs field. In the SM the Higgs boson mass is much smaller than the quantum corrections because of the presence of virtual particles. Consequently, the mass parameter of the Higgs boson has to be fine-tuned to cancel these quantum corrections. The need for fine-tuning is indicating that some parts are most likely missing in the theory.

Many extensions of the SM expect particles at the TeV scale that have not been found so far [6]. This means that the particle masses are above the current level of sensitivity, the production cross sections are lower than expected, or the experimental signatures are difficult to observe. To solve these issues, the LHC is upgraded to the HL-LHC with higher energy and luminosity to increase the chance of discovery of a new particle.

Since the Higgs boson may be the connection to dark matter particles, it is expected that the Higgs boson properties are sensitive to new physics. It is therefore necessary to perform precision measurements of the Higgs boson, like the coupling to other particles, detailed CP analysis of the Higgs boson, measurements of rare decay channels, and measurement of the Higgs mass. The HL-LHC is the only machine in the near future capable of studying the Higgs particle.

1.3 CMS Experiment

The CMS detector is a general purpose collider experiment. In proton-proton collisions the partons collide and the centre of mass energy $\sqrt{s}$ is converted from kinetic energy to new particles. The such generated mass may be larger than that of the initial u- and d-quarks. CMS wants to achieve its goals with this method. The goals are similar to the LHC goals mentioned previously and comprise the continuous study of the Standard Model (SM) and the search for new physics like supersymmetry, extra dimensions, dark matter and the Higgs boson. In 2012 CMS and ATLAS discovered the Higgs boson [7] and are continuing detailed studies of it since then. The Higgs studies focus for example on the precision measurement of the Higgs mass, the decay width and branching ratios. Furthermore, the search for new physics include reactions initiated by vector boson fusion (VBF) [8]. VBF is the second most dominant production mechanism of the Higgs boson at the LHC. In this mechanism two quarks radiate W or Z bosons, which fuse to a Higgs boson, while the quarks continue to move forward (parallel to the beam axis). These quarks produce characteristic narrow jets in the region close to the beam line. A sketch of the Feynman diagramme of the Higgs production via VBF is shown in 1.3.

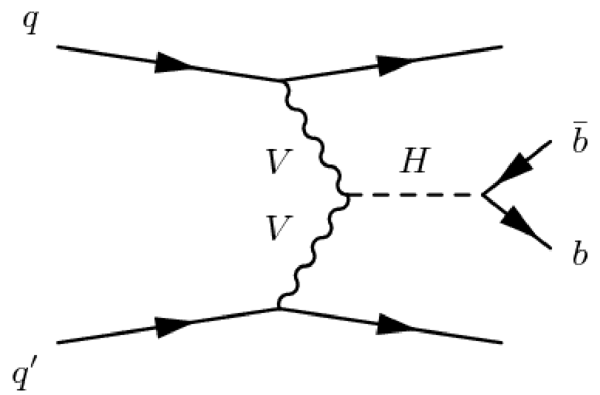

Figure 1.3: Higgs production via vector boson fusion (VBF). Figure taken from [9].

Another measurement at CMS and improved with the HL-LHC upgrade, is vector boson scattering (VBS). With this study precision measurements in the electroweak sector and studies of processes that have sensitivity to the electroweak symmetry breaking can be performed [6]. It is accomplished by the interaction of two vector bosons, which are emitted from two quarks of the colliding protons. The typical identification signature are the two quarks, which get deflected and produce jets of hadrons, called tag jets. New resonances in the VBS invariant mass spectrum or a deviation of measurement data from the SM expectations indicate new physics. Since the cross section of this electroweak process is small and the background due to hadronic jets is large, the study is challenging. For example, it is only possible in HL-LHC in CMS with the upgrade of the tracker and calorimeter system. The current tracker and calorimeter system of CMS are described in the next sections in 1.3. With the overlap of 140 pileup events, background from misidentification of hadronic jets as leptons, arises. Additionally, overlap of jets from different events can mimic features of a tag jet. The new detectors reduce the misidentification rate and background of jets from pileup events and allow the triggering on these events with higher efficiency [6].

In the following the structure of the CMS experiment will be explained. With an overall diameter of 15 m and overall length of 28.7 m it weighs 14 000 t. Part of the CMS detector is

the 3.8 T superconducting solenoid and the iron return yoke. The resulting magnetic field of the solenoid is parallel to the beam axis. The magnet provides large bending power for momentum measurements in the tracker and the muon system. Excellent muon momentum reconstruction is for example important in processes like the Higgs boson decay through two Z bosons to two or four muons.
The CMS experiment consists of a cylindrical shaped detector with an onion-like layer structure. This means, that the interaction point is surrounded by several layers of different detector systems. Each subsystem measures different particle attributes. To reconstruct a collision event, the information from all systems is combined. A 3D image of the CMS detector with the current subsystems is displayed in Figure 1.4.

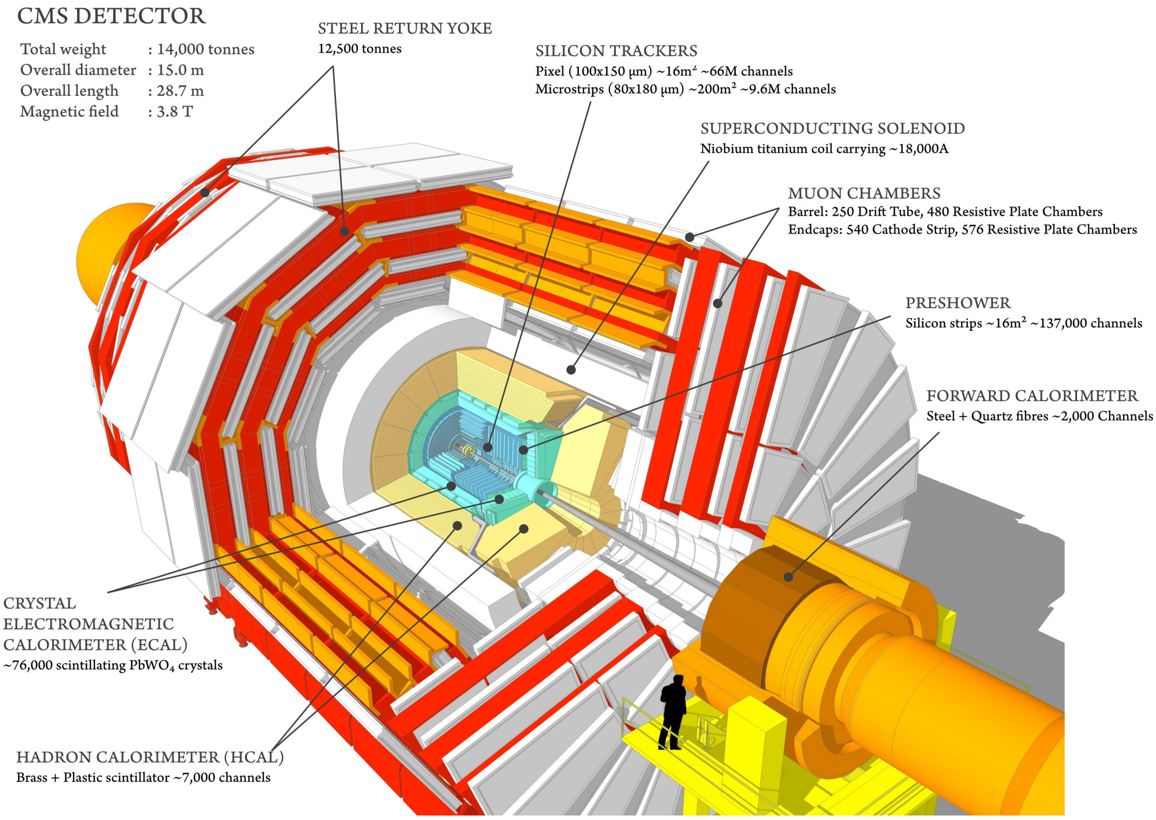

Figure 1.4: 3D image of the CMS detector with the subsystem used in run 1.

A cut through the detector highlighting the paths of different particle types through the individual subcomponents is shown in Figure 1.5. The subcomponents are explained in more detail in the following sections.

For the explanation of the sub systems it is helpful to introduce the term of pseudorapidity η, which is defined in the following way:

$$\eta = -\ln[\tan(\theta/2)], \tag{1.4}$$

where θ is the angle between the particle momentum vector and the beam axis. Hence

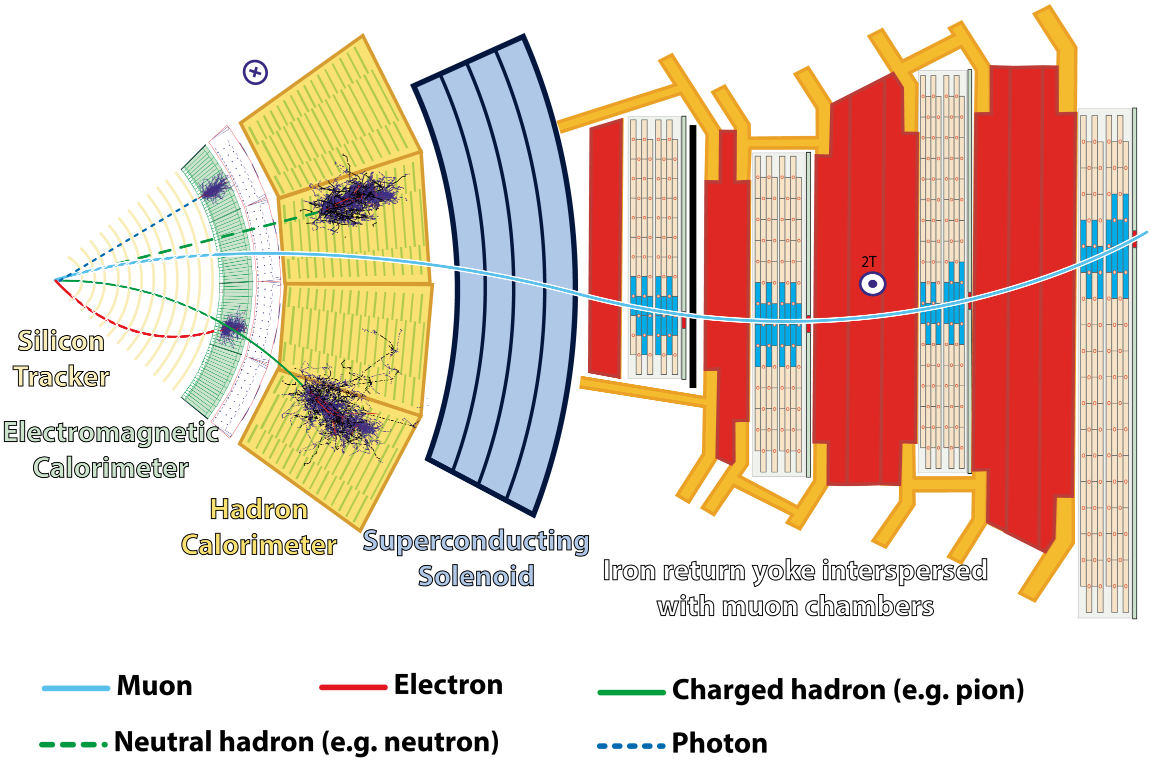

Figure 1.5: Cross section view of the CMS detector components. Example tracks of various particle types are highlighted. Figure from [10].

$\eta = 0$ means the particle path is perpendicular to the beam axis and $\eta = \infty$ means the particle path is parallel to the beam axis.

1.3.1 Tracker

The CMS tracking system is located in the innermost section. The primary goal of a tracker is to measure the path of the charged particles emerging from the proton-proton collisions at the interaction point and reconstruct secondary vertices from decays of particles containing b and c quarks. It is made entirely of silicon, and, with an area of about $200\,\mathrm{m}^2$, it is the largest tracker ever built. The CMS Tracker has an inner and outer part. The inner Tracker uses pixel sensors with a combined area of about $1\,\mathrm{m}^2$ and about 66 million channels. During the extended end-of-year technical stop (EYETS) between 2016 and 2017 the CMS inner Tracker was completely replaced. For example, some of the changes incorporated an increase of the number of barrel layers from three to four and the increase of the number of the end cap disks from two to three. Additionally, the number of pixels almost doubled to 124 million in total. This is referred to as the CMS pixel Phase-1 upgrade. One reason for the replacement was due to the steadily increasing instantaneous luminosity of the LHC beyond the design luminosity of $1 \times 10^{34}\,\mathrm{cm}^{-1}\,\mathrm{s}^{-1}$. At a higher luminosity the original pixel detector would have suffered from increasing hit inefficiencies due to buffer overflows in the readout chips [11]. Another stringent reason is the immense radiation damage for the innermost pixel layer. An integrated luminosity of $500\,\mathrm{fb}^{-1}$, the designed limit of the CMS phase 1 pixel detector, corresponds to a hadron fluence of about $3 \times 10^{15}\,\mathrm{n_{eq}cm^{-2}}$. Due to radiation damage the performance of the silicon sensors degrade and have to be replaced eventually. Effects of radiation damage in silicon sensors are for example an increased leakage current, increase of the full depletion voltage and a drop in the charge collection efficiency. Due to the known effects of radiation damage in silicon, the inner Tracker is designed in such a way that modules with sensors can be replaced relatively easily.

With increasing radial distance from the interaction point, the particle track density decreases and hence less granularity is required to resolve the tracks. To avoid unnecessary costs, strip sensors are used for the outer Tracker. Ten layers of microstrip sensors are employed. Since the whole tracker is within the solenoidal magnetic field, it allows excellent momentum discrimination. This is realised by making use of the Lorentz Force. This effect leads to the exertion of force on a charged particle perpendicular to its path of motion in a magnetic field. The path of the particle, the magnetic field and the resulting Lorentz Force are all perpendicular to each other. Therefore, with the measurement of the curvature of the particle in the Tracker the momentum of the particle can be calculated. Higher curvature means a higher momentum of the particle.

1.3.2 Calorimeter

The electromagnetic calorimeter (ECAL) is surrounding the tracker and is within the superconducting solenoid as well. It is a homogenous calorimeter made out of 75848 lead tungstate ($PbWO_4$) scintillating crystals. Its main purpose is to measure the energy of particles, which interact via the electromagnetic force like electrons and photons. Due to interaction with the calorimeter material the particles lose energy and are eventually stopped. During this process particle showers are created by the incident particle. The lead tungstate crystals produce scintillation light proportional to the energy deposited by the particles. This light is detected by silicon avalanche photodiodes (APDs) in the barrel (EB) and vacuum phototriodes (VPTs) in the endcaps (EE). The barrel covers a pseudorapidity region of $|\eta| < 1.48$ and the two endcaps extend the coverage up to $|\eta| < 3.0$. In front of the ECAL endcaps is a preshower system, consisting out of silicon strip sensors, installed for π^0 rejection. π^0 particles decay with a probability of about 98.8 % [12] into two photons. The ECAL cannot distinguish a single photon shower from the two closely spaced photons of a π^0 decay. The preshower system measures the start of the electromagentic shower with much higher granularity than the scintillating crystals of the ECAL and such allows discrimination of single photon showers and π^0 decays. The energy resolution of the current ECAL is between $\frac{\sigma(E)}{E} = \frac{2.2\,\%\sqrt{\mathrm{GeV}}}{\sqrt{E}} \bigoplus 1.0\,\%$ and $\frac{\sigma(E)}{E} = \frac{5.0\,\%\sqrt{\mathrm{GeV}}}{\sqrt{E}} \bigoplus 1.5\,\%$ [13]. The first term of the energy resolution describes the statistic fluctuations and the second term the constant contribution.

The next part of the calorimetry system is a hadron calorimeter (HCAL). The barrel (HB) and endcap (HE) section are sampling calorimeters, which means that brass absorber plates and scintillator tiles alternate. In the absorber plates the incident particle loses energy and produces particle showers, which produce light signals in the scintillators. This light is converted by wavelength shifting fibres and is guided to hybrid photodiodes (HPDs) for readout. Initially, HPD technology was chosen due to its high gain and magnetic field tolerance. But in Run 1 (between 2010-2012), electrical discharges were observed, varying with the orientation and strength of the magnetic field with respect to the HPD [14]. Additionally, gain variations with unknown origin were observed. Therefore, the HPDs got replaced by silicon photomultipliers (SiPMs) during the phase 1 upgrade of CMS. The HCAL Outer calorimeter (HO) is outside of the solenoid magnet and uses plastic scintillator tiles as active material and the CMS magnet material as absorber. Initially in the HO, HPDs are used for readout as well. They got replaced by SiPMs for the same reason as it was the case for the HB and HE during the phase 1 upgrade. The HO is needed, since the hadronic showers cannot be fully stopped in the barrel region due to insufficient space inside of the solenoid. The energy loss of particles in matter will be discussed in Section 2.2 and the calorimeter basics with the explanation of the hadronic showers in Section 3.1.

For increased coverage up to $|\eta| = 5$, outside the solenoid, a forward calorimeter (HF) consisting of steel with embedded quartz fibres is used. The Cherenkov light produced by showers in the steel absorber is collected in the quartz fibres and the signal is detected by photomultiplier tubes (PMTs).

Anomalous signals were seen in the PMTs of the HF during Run 1. They originated from muon and particle shower hits on the PMT windows and manifest in supposedly very high energy deposits. These signals arrive earlier in comparison to the Cherenkov light signals. During Run 1 these signals were rejected by adjusting the HF readout phase such that these early hits occurred in an empty bunch crossing immediately prior to the bunch crossing containing the collision. In Run 2 this method is no longer possible, since every bunch crossing will lead to collisions. The time between bunch crossings is reduced from 50 ns to 25 ns from Run 1 to Run 2. Hence the PMTs are replaced by other PMTs and new front-end electronics is used which is capable of precise timing measurements. This new electronics is shared in parts with those needed in HB and HE to read out the new SiPMs. The new PMTs are thinner, since the signal in a PMT window hit is proportional to the path length through the window. Additionally, the new PMTs have a multi-anode readout. This way, single PMTs that are hit can be identified and their energy contribution is substracted. In comparison, a real shower would produce a signal in several anodes and not only one. During LS1 the HF PMT and back-end electronics replacement was performed. The new front-end electronics were installed in the year-end technical stop from late 2015 to early 2016. For the HB and HE, the back-end was installed in 2014 and the front-end is replaced during the LS2. The energy resolution of the HE is about $\frac{\sigma(E)}{E} = \frac{84.7\,\%\sqrt{\mathrm{GeV}}}{\sqrt{E}} \bigoplus 7.4\,\%$ [15].

1.3.3 Muon System

The muon system of CMS is located outside of the superconducting solenoid. Only neutrinos and muons are able to pass through the tracker, calorimeter and even the muon system. Since neutrinos only interact weakly, they can solely be detected indirectly in CMS. This can be accomplished by reconstruction of the missing transverse energy of an event in the calorimeter system. Hence the need for a hermetic design of the CMS detector. Due to the iron return yoke, the magnetic return field of the solenoid is confined and shaped and hence can be used to provide large enough bending power for momentum measurements of muons. Between the iron yoke are four muon tracking layers, which consist of several layers of aluminum drift tubes (DT) in the barrel region and cathode strip chambers (CSCs) in the endcap region. Additionally, resistive plate chambers (RPCs) are used to help each system in their triggering capability. Most of the detectors were installed in 2007, but large detector chambers in the fourth endcap disk were missing until 2014 [16]. They were implemented to ensure enough redundancy for future higher luminosity conditions.

1.3.4 Trigger

The designed bunch crossing frequency at LHC is 40 MHz. At each bunch crossing about 20 proton-proton collisions happen at the design luminosity ($1 \times 10^{34}\,\mathrm{cm}^{-1}\,\mathrm{s}^{-1}$). Each crossing produces about 1 MB of zero-suppressed data [17]. These enormous data rates are beyond the capability of any storage system. Therefore, CMS requires a dedicated system to reduce the number of events that need to be saved. This is accomplished by the CMS trigger. It consists of two parts. The first part (Level-1 Trigger or L1) reduces the number of accepted events to 100 kHz. It is realised using field programmable gate arrays (FPGAs). The L1 trigger must be able to provide a decision for every bunch crossing event every 25 ns. This is done by using only coarsely segmented data from the calorimeter and muon detectors, while still saving all data in pipeline memories in the front-end electronics. The data can be saved for 3.2 µs, which is called L1 trigger latency. This latency includes signal propagation delays and the actual calculation time for the L1 trigger accept. The whole detector system is read out when a L1 trigger accept is given. In a second step the final output rate is reduced to 100 Hz by the High-Level Trigger (HLT). Due to the rate reduction after the L1 accept, it is possible to apply complex event reconstruction algorithms on the remaining full event data from all detectors. During the processing of the data, the data is stored in random-access memories (RAM). After the event reconstruction, the HLT decides whether to send it to mass storage or discard the event.

1.4 CMS Phase II Upgrade

In the environment of the HL-LHC several systems of CMS have to be upgraded. The short summary of the CMS Phase 2 upgrade of each component follows [6].

Tracker Due to radiation damage the silicon sensors of the complete tracker have to be replaced for the HL-LHC phase. To be able to cope with the higher pileup levels the granularity of the strip sensors and the pixel systems are increased. Improved design leads to a lower material budget, which improves the momentum measurement of the tracker and the energy measurement in the calorimeter. A new module design allows track-stub information to the L1 trigger at 40 MHz for tracks with transverse momentum $p_{\mathrm{T}} \geq 2\,\mathrm{GeV}$ [6]. This improves the background rejection. Additional pixel disks in the forward direction extend the coverage almost up to $|\eta| = 4$.

Calorimeter endcaps Due to radiation damage the electromagnetic and hadronic endcap calorimeters will have to be replaced for Run 3. The new system is called the *High Granularity Calorimeter* (HGCal). It has an electromagnetic and hadronic section with high transversal and longitudinal segmentation. The design is based on the ILC/CALICE [18][19] concept for 3D measurements of shower topologies. It is a sampling calorimeter, which uses silicon sensors as active material. The term sampling calorimeter and the details of the HGCal are discussed in Chapter 3.

Muon endcaps The current installed muon system in the region $1.5 \leq |\eta| \leq 2.4$ consists of four stations of cathode strip chambers (CSC) and lacks redundant coverage. In the upgrade the first two stations get additional gas electron multiplier (GEM) chambers with good position resolution to improve momentum resolution. The last two stations will use resistive plate chambers (RPC) with lower granularity but good timing resolution. Additional GEM chambers behind the new endcap calorimeter will be implemented to increase the coverage to $|\eta| \approx 3$.

Trigger The current L1 trigger latency will be upgraded from 3.4 µs to 12.5 µs. This is needed for the hardware to be able to reconstruct tracks and match them with information from the muon system and the calorimeter. Therefore, some of the readout electronics of the existing sub-detectors will require an upgrade. Additionally, an upgraded data acquisition system will be needed for the increased demand for bandwidth and computing power due to the increased event size and L1-trigger rate.

2

Particle Detection with Silicon Sensors

2.1 Semiconductor Physics

The sensors in development in this work for the new HGCal use silicon as bulk material. The working principle and the underlying physics is explained in this chapter. The explanations of the next topics follow the ideas of [20].

2.1.1 Energy Bands

Silicon is a semiconductor and part of the fourth main group of the periodic table of elements. The silicon atoms in the crystal are arranged in a diamond lattice structure, which means that each atom has four neighbours in a tetrahedron configuration. With each neighbour atom one of the four electrons in the outer orbit is shared and forms a covalent bond. At temperatures $T > 0$, thermal vibration can break covalent bonds and the resulting free electrons can participate in current conduction. If an electron is missing in a covalent bond it may get replaced by a neighbouring electron. This vacancy can shift position in the crystal and is therefore considered as a virtual particle, which is similar to the electron. It is called a hole.

Isolated atoms or atoms with large distance to each other have discrete energy niveaus. If two atoms are brought together the two times degenerate energy level splits into two levels due to the interaction between the atoms. When N atoms, which form a crystal, are brought together the N-fold degenerate energy levels split into N closely spaced energy levels. The result is basically a continuous band of energy. At a lattice constant of $5.43\,\text{Å}$ for silicon, two energy bands called conduction and valence band are formed. They are separated by a region of energy levels called bandgap with energy E_g, which marks the energy levels electrons in the solid cannot have. The bandgap for silicon at room temperature and under normal atmospheric pressure is $1.12\,\mathrm{eV}$. The valence electrons in the highest energy level can easily interact with the ones of the neighbour atoms and can easily be removed from a single atom. For a large number of atoms a single electron cannot be allocated to a single atom anymore and hence the energy bands of the single atoms merge to the continuous valence band. If electrons can overcome the bandgap energy, which can happen at room temperature for semiconductors by thermal excitation, they enter the conduction band. This means they can participate in current conduction. In isolators the bandgap E_g is so high that there are no free electrons, at room temperature, which can contribute to current conduction. On the other hand in conductors, the bands overlap. The electrons at the top of the valence band easily reach the next higher energy levels by gaining kinetic energy. The difference in the energy band modell between semiconductors, isolators and conductors is schematically shown in Figure 2.1.

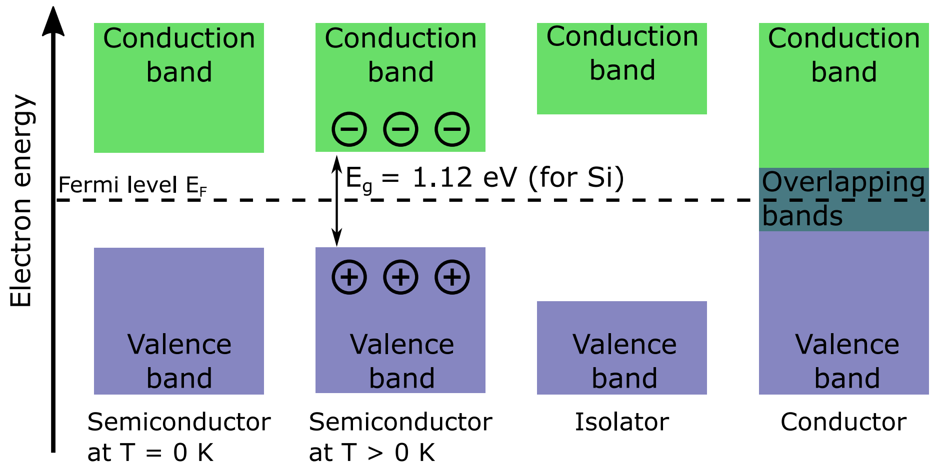

Figure 2.1: The schematic energy band representation is shown for semiconductors, isolators and conductors. The figure is an adapted version from [20].

2.1.2 Doping of semiconductors

As mentioned in 2.1.1, at temperatures T > 0 electrons can be thermally excited from the valence band to the conduction band. This results in an equal number of holes in the valence band. The number of electrons n and the number of holes p are equal to the intrinsic charge carrier density, n_i = n = p. If a semiconductor contains only relatively small amounts of impurities compared to the thermally generated electrons and holes, it is called an *intrinsic semiconductor* [20]. The intrinsic charge carrier density n_i can be calculated by Equation 2.1:

$$n_i = \sqrt{N_C N_V} \exp\left(-\frac{E_g}{2k_B T}\right) \tag{2.1}$$

N_C and N_V is the effective density of states in the conduction and valence band. k_B is the boltzmann constant. For silicon at room temperature the number of states are in the order of $\mathcal{O}(10^{19})$ per cubic centimetre. For silicon at room temperature n_i is in the order of $\mathcal{O}(10^{10})$ per cubic centimetre.

As described by the Fermi-Dirac distribution function, the Fermi level is the energy E_F at which the probability that a state is occupied by an electron is 0.5. For an intrinsic semiconductor at room temperature the Fermi level is very close to the middle of the band gap (2.1). It can be calculated by:

$$E_F = \frac{E_C + E_V}{2} + \frac{k_B T}{2} \ln \frac{N_V}{N_C} \tag{2.2}$$

E_C and E_V are the energy levels of the conduction and valence band.

To achieve a similar conductivity in an intrinsic semiconductor as in metals, a temperature of several hundred degrees Celsius is required. To change the conductivity of semiconductors, atoms from the third or fifth main group can be deposited in them. This process is called doping and the implanted atoms are the dopants. The semiconductor becomes extrinsic with this process. When doping with an atom from the fifth main group (e.g. phosphorus), a silicon atom in the crystal lattice gets replaced by a new atom, which could make five covalent bonds but only has four neighbours. Consequently one electron is not bound and becomes a conduction electron. It is "donated" to the conduction band. Therefore elements from the fifth main group are called *donators*. The silicon becomes *n-type* due to the addition of the negative charge carrier. For elements of the third main group the process is reversed. An electron is missing to make four covalent bonds with the neighbouring silicon atoms. Hence, an extra electron is "accepted" to form the covalent bonds and a new hole comes into existence in the valence band. The third main group elements (e.g. boron) are therefore called *acceptors* and make the semiconductor *p-type*. In n-type semiconductors the electrons are the majority charge carriers and the holes are the minority charge carriers. The charge carrier type which is present in a larger amount is the majority charge carrier. For p-type, holes are the majority charge carriers. The hole and electron concentration p_p and n_p for p-type is given by [21]:

$$p_p \approx N_A = n_i \exp\left(\frac{E_i - E_F}{k_B T}\right) \tag{2.3}$$

$$n_p = \frac{{n_i}^2}{p_p} \approx \frac{{n_i}^2}{N_A} \tag{2.4}$$

Depending on the amount of acceptor and donor concentration (N_A and N_D) and the mobility of electrons μ_n and holes μ_p, the resistivity ρ of the extrinsic semiconductor can be defined:

$$\rho = \frac{1}{q(N_D \mu_n + N_A \mu_p)} \tag{2.5}$$

For p-type or n-type semiconductors there is a difference in the eletron and hole concentration by many orders of magnitude. For p-type, $N_\mathrm{A} >> N_\mathrm{D}$ and the N_D term can be dropped and vice versa for n-type.

The dopants are impurities, which create additional energy states in the band gap. Acceptors create states, which are close to the valence band and donators create states, which are close to the conduction band. Doping with acceptors (p-type silicon) shifts the fermi energy level towards the valence band, whereas donators shift it towards the conduction band.

2.1.3 Charge Carrier-Transport in Semiconductors

The drift of charge carriers in silicon arises when applying an electric field. The drift velocity v_d is proportional to the electric field $\vec{E}$:

$$\vec{v_d} = \mu \vec{E} \tag{2.6}$$

μ is the proportionality constant called mobility. It is mostly influenced by interactions with acoustic phonons of the crystal lattice μ_l and carrier scattering on impurities μ_i. The mobilities of both mechanisms decrease with increased conductivity effective mass but have different temperature dependence. $\mu_\mathrm{l} \propto T^{-3/2}$ and $\mu_\mathrm{i} \propto T^{3/2}$. Both mobilities can be combined by making use of the Matthiessen rule:

$$\mu = \left(\frac{1}{\mu_l} + \frac{1}{\mu_i} \right)^{-1} \tag{2.7}$$

The mobility can also be related qualitatively to the mean free time τ_m or mean free path λ_m:

$$\mu = \frac{q\tau_m}{m_c} = \frac{q\lambda_m}{\sqrt{3k_BTm_c}} \tag{2.8}$$

k_B is the boltzmann constant and m_c is the effective mass of the charge carrier. Different scattering mechanisms mean different mean free times, which can be combined to a single effective one with the Mathiessen rule.

The drift current density $\vec{J}$, when an electric field $\vec{E}$ is applied, is given by:

$$\vec{J} = q \left(\mu_n n + \mu_p p \right) \vec{E} \tag{2.9}$$

Another important carrier transport mechanism is the diffusion. Within regions of different doping concentrations (carrier concentration) the carriers move from high concentration regions to low concentration ones. The reason is to effectively level the concentration inhomogeneity. The flow of carriers, described by Fick's law is proportional to the concentration gradient with a proportionality constant called diffusivity D. For n-type the diffusivity D_n can be written as in Equation 2.10, whereas for p-type the electrons have to be replaced with holes. This relation is known as the Einstein relation.

$$D_n = \left(\frac{k_B T}{q}\right) \mu_n \tag{2.10}$$

The diffusion current density J_n is given by Equation 2.11:

$$\vec{J} = k_B T \mu_n \vec{\nabla} n \tag{2.11}$$

In the case of a carrier concentration gradient and an electric field both currents will flow and can simply be added up to the total conduction density. Both contributions for electrons and holes have to be summed.

When the equilibrium condition of a semiconductor system is disturbed, a recombination process happens when $pn > n_\mathrm{i}^2$ or a thermal generation happens when $pn < n_\mathrm{i}^2$. There are direct and indirect recombination and generation mechanisms. In direct bandgap semiconductors direct transitions can happen, which mean that an electron from the valence band can be excited directly to the conduction band and create an electron-hole pair (generation) or vice versa (recombination). In indirect bandgap semiconductors the recombination and generation will most likely take place via bulk traps, of density N_t and energy E_t within the bandgap. In indirect semiconductors, like Silicon, direct transitions would require a simultaneous lattice interaction to conserve energy and momentum in the crystal lattice. The recombination at a single-level trap in the forbidden region can be described by electron capture and hole capture. The Shockley-Read-Hall statistics in Equation 2.12 describes the net transition rate U.

$$U = \frac{\sigma_n \sigma_p v_{th} N_t (pn - n_i{}^2)}{\sigma_n \left[n + n_i \exp\left(\frac{E_t - E_i}{k_B T}\right)\right] + \sigma_p \left[p + n_i \exp\left(\frac{E_i - E_t}{k_B T}\right)\right]} \tag{2.12}$$

σ_n and σ_p are the electron and hole capture cross sections. $v_\mathrm{th} = \sqrt{\frac{3k_\mathrm{B}T}{m_\mathrm{c}}}$ is the thermal velocity of the charge carrier. Depending on the sign of the term $pn - n_\mathrm{i}^2$ net recombination or generation takes place. Additionally, U is largest when $E_\mathrm{t} = E_\mathrm{i}$. This means, that a trap near the mid-gap is the most efficient recombination or generation centre. Assuming such a trap in combination with low-level injection in a n-type semiconductor, U can be simplified to Equation 2.13.

$$U \approx \sigma_p v_{th} N_t \Delta p \equiv \frac{\Delta p}{\tau_p} \tag{2.13}$$

Low-level injection is the introduction of additional charge carriers $\Delta p = \Delta n$, for example, by means of optical excitation or forward biasing a p-n junction (see 2.1.4). The introduced carriers must have a concentration smaller than the majority carrier concentration. τ_p in Equation 2.13 is the hole lifetime, which is the minority charge carrier in n-type. So in this case the recombination rate is limited by the minority carriers, which are much less abundant than the majority ones. For low-level injection in p-type the role of holes and electrons are reversed.

When the product of the carrier concentrations is smaller than the square of the intrinsic charge carrier concentration ($np < {n_\mathrm{i}}^2$), carrier generation in opposition to the previously mentioned recombination of excess carriers will occur. For example, due to reverse biasing of a p-n junction. In this case Equation 2.12 can be reduced to Equation 2.14:

$$U = -\frac{\sigma_p \sigma_n v_{th} N_t n_i}{\sigma_p \left[1 + (p/n_i)\right] + \sigma_n \left[1 + (n/n_i)\right]} \equiv -\frac{n_i}{\tau_g} \tag{2.14}$$

The generation carrier lifetime τ_g is given by Equation 2.15.

$$\tau_g = \frac{1 + (n/n_i)}{\sigma_p v_{th} N_t} + \frac{1 + (p/n_i)}{\sigma_n v_t h N_t} = \left(1 + \frac{n}{n_i}\right) \tau_p + \left(1 + \frac{p}{n_i}\right) \tau_n \tag{2.15}$$

$\tau_\mathrm{p} = \frac{1}{\sigma_\mathrm{p} v_\mathrm{th} N_\mathrm{t}}$ is the lifetime of the holes in n-type silicon and τ_n the lifetime of the electrons in p-type silicon.

The combination of the effects of drift, diffusion, recombination and generation can be described by the *Continuity Equations* 2.16 and 2.17:

$$\frac{\partial n}{\partial t} = \frac{1}{q} \frac{\partial J_n}{\partial x} + (G_n - R_n) \tag{2.16}$$

$$\frac{\partial p}{\partial t} = -\frac{1}{q} \frac{\partial J_p}{\partial x} + (G_p - R_p) \tag{2.17}$$

$G_\mathrm{n,p}$ and $R_\mathrm{n,p}$ are the generation and recombination rates for electrons and holes respectively. In addition to Equation 2.16 and Equation 2.17, *Poisson's Equation* has to be satisfied aswell:

$$\nabla \cdot (\epsilon \nabla \phi) = \rho_s - \rho_{trap} \tag{2.18}$$

ϵ is the electrical permittivity and $\rho_\mathrm{s} = q(p - n + N_\mathrm{D} - N_\mathrm{A})$ is the space charge density in silicon and ρ_trap is the charge density due to traps and fixed charges [22].

2.1.4 The p-n Junction

When a p-type and n-type semiconductor are put together they form a p-n junction. This configuration is also referred to as diode, which is a very important building block of electronic devices. This junction can, for example, be realized by implanting acceptor impurities N_A (making silicon p-type) in a part of a silicon region, which was previously doped with donor impurities N_D (making silicon n-type). N_A and N_D are, of course, interchangeable.

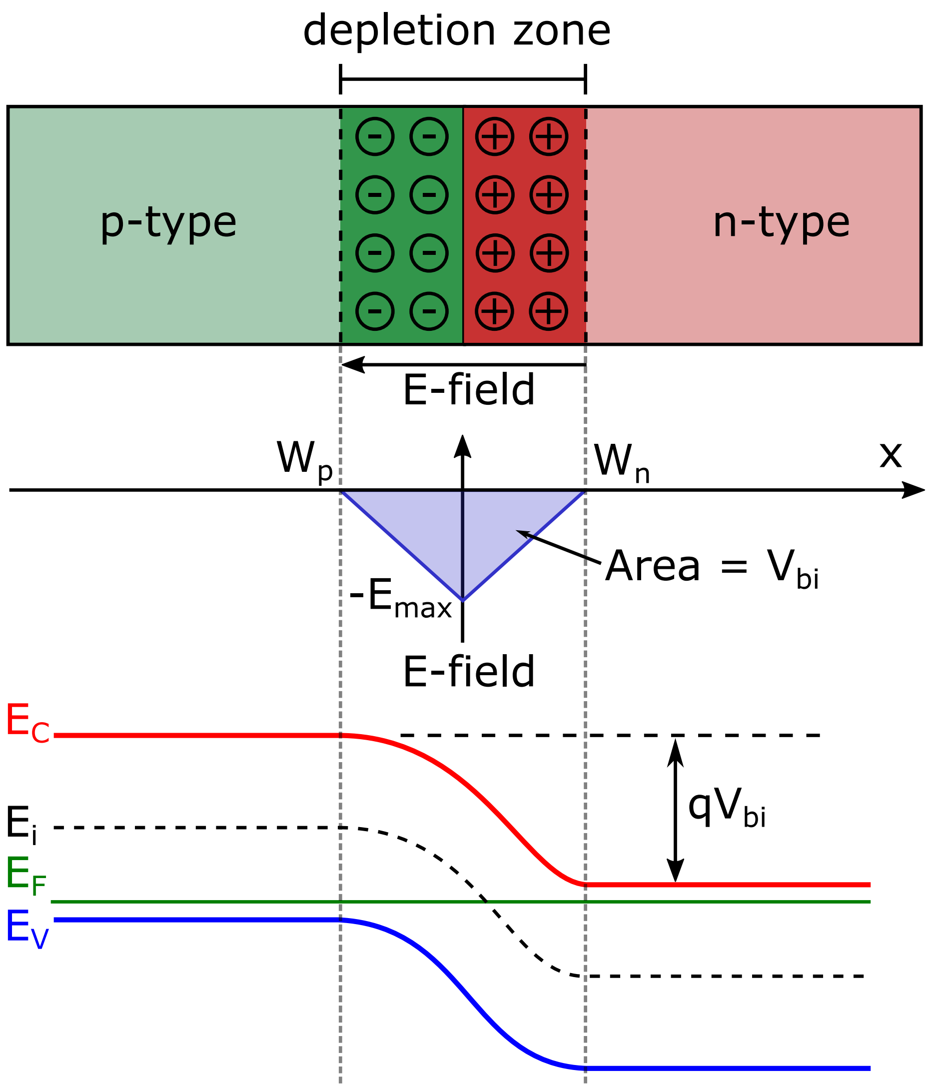

Figure 2.2: A p-n junction in thermal equilibrium is shown. The electric field and the energy band diagramme are displayed.

Figure 2.2 shows a p-n junction where N_A and N_D are present in an equal number. Due to the large charge carrier gradient of the electrons and holes at the junction, diffusion of the carriers arises. Holes move from the p-type region towards the n-type region and electrons vice versa to level out the inhomogenous carrier distribution. Some of the negative acceptor impurity ions N_A^- near the junction are not compensated due to the fixed position of the acceptors in the crystal lattice and the mobility of the holes. In the n-type region, N_D^+ ions also cannot be fully compensated due to the electrons diffusing to the p-type region. On the p-side of the junction a negative space charge forms, while a positive one forms at the n-side. Both regions with space charge are also called *depletion region* (or space charge region), because the mobile carrier densities are zero, or in other words depleted of mobile charge carriers. These space charges lead to an electric fiel E, whose orientation is from the positive charges towards the negative charges. Due to the electric field being in opposite direction of the diffusion current, a drift current arises which is opposite to the diffusion current. At thermal equilibrium both currents are equal and the net current is zero. Thermal equilibrium means, that the junction is at a fixed temperature and no external voltage or current is applied to the junction. It can be deduced that due to the zero net current the Fermi energy level has to remain constant [20]. But the space charges between p-type and n-type region lead to a potential difference, the so called built-in voltage V_{bi}, which is described in Equation 2.19. Therefore, in a p-n junction the energy bands are bent. This is shown in the bottom of Figure 2.2. The shift of energy due to the built-in voltage is qV_{bi}.

$$V_{bi} = \frac{k_B T}{q} \ln \frac{N_A N_D}{n_i^2} \tag{2.19}$$

The spread of the depletion region is determined by the doping concentration. If there is a large difference between the n-type and p-type doping concentration, the depletion region spreads more into the region with lower doping concentration. This is due to the fact that the total negative space charge per unit area in the p-type region has to equal the total positive space charge per unit area in the n-side. The depletion widths W_{p} and W_{n} in p-type and n-type are calculated by Equation 2.20 [21].

$$W_p = \sqrt{\frac{2\epsilon_0\epsilon_r V_{bi}}{q}\frac{N_D}{N_A(N_A+N_D)}} \tag{2.20a}$$

$$W_n = \sqrt{\frac{2\epsilon_0\epsilon_r V_{bi}}{q}\frac{N_A}{N_D(N_A+N_D)}} \tag{2.20b}$$

In the case of a junction, where, for example, N_{A} is much larger than N_{D} , Equation 2.20 can be reduced to Equation 2.21. It calculates the whole depletion depth. Additionally, N_{D} can be exchanged with N_{A}, when N_{D} is much larger than N_{A}.

$$W = \sqrt{\frac{2\epsilon_0\epsilon_r(V_{bi}-V)}{qN_D}} \tag{2.21}$$

When no external bias voltage is applied, V is zero. In case positive voltage is applied to the p side with respect to the n side, the p-n junction becomes forward biased. This means that the electrostatic potential difference decreases from qV_{bi} to $qV_{\mathrm{bi}} - V$. Consequently the depletion width becomes smaller. In case negative voltage is applied to the p side with respect to the n side, the p-n junction becomes reverse biased. The opposite effect takes place, where the potential difference is increased and hence the depletion width is increased as well.

The application of forward biasing reduces the electrostatic potential difference and hence the drift current in comparison to the diffusion current. More holes diffuse from the p side to the n side and more electrons diffuse from the n side to the p side, which is called minority carrier injection. With reverse bias the electrostatic potential increases, which reduces the diffusion currents greatly and hence a reduced reverse current arises. The current voltage characteristics of the ideal p-n junction in forward and reverse direction are described by the Shockley equation 2.22, where V is the bias voltage and I_0 is the saturation current.

$$I = I_0 \left[exp\left(\frac{qV}{k_B T}\right) - 1 \right] \tag{2.22}$$

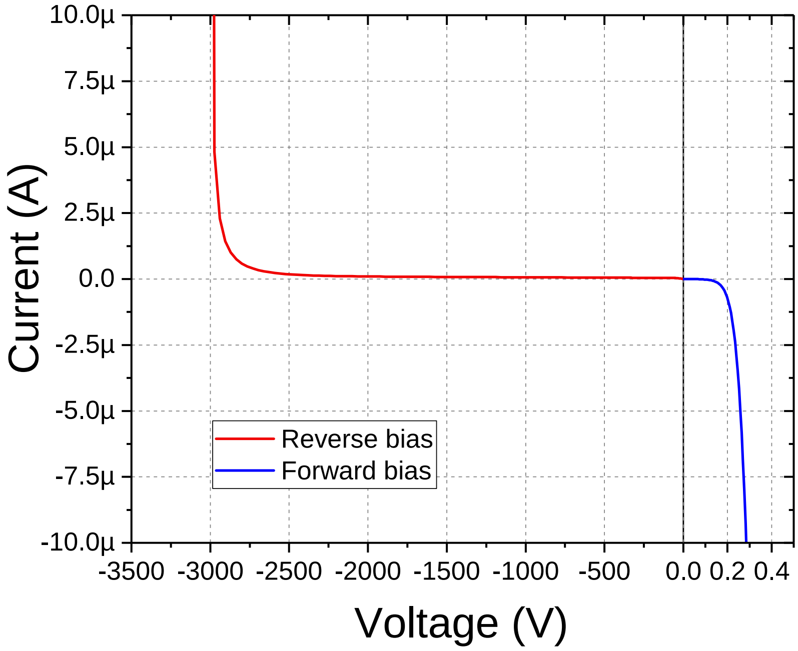

Figure 2.3: Current-voltage characteristis of a silicon p-n junction. In reverse bias low current occurs until the junction breaks down. In forward bias direction, already at small voltages ($< 1V$) high current arises. The current-voltage characteristics is simulated in Synopsys TCAD.

At infinitly high reverse bias voltage ($V \rightarrow -\infty$) the current of the diode saturates at I_0. Biasing in forward direction leads to an exponential increase of the current. This behavior is shown in Figure 2.3, where the current voltage characteristics of a diode is simulated in TCAD. It should be noted that the Shockley equation only describes an ideal p-n junction. This means junction breakdown effects like avalanche multiplication or the tunneling effect are not taken into account. The simulation shown in Figure 2.3 includes these effects, hence the observed breakdown in reverse biasing direction.

The capacitance of a reverse biased junction can be described by combining the parallel plate capacitor formula with Equation 2.21. The depletion region can be seen as the dielectric between the n side and p side electrodes. A denotes the area of the junction and N_B is the doping concentration, which is much smaller in comparison to the one on the other side of the junction. In typical diodes this concentration N_B corresponds to the bulk doping concentration.

$$C = \epsilon_0 \epsilon_r \frac{A}{W} = A\sqrt{\frac{q\epsilon_0\epsilon_r N_B}{2(V_{bi} - V)}} \tag{2.23}$$

It can be seen in Equation 2.23 that the capacitance declines with increasing reverse bias voltage. The capacitance decreases until the space charge region spreads throughout the end of the much lower doped side of the junction. At this point the so-called full depletion voltage V_depl is reached. Increasing the reverse bias voltage further will not lead to more decrease of the capacitance. The full depletion voltage V_depl is determined by $1/C^2$ vs. V measurements of the diode. V_depl is the intersection point of two linear fits from the regions $V < V_\mathrm{depl}$ and $V > V_\mathrm{depl}$.

With the combination of Equation 2.5 and 2.21 it is possible to calculate the resistivity of the bulk when knowing the thickness d of the diode and the full depletion voltage V_depl. The combination results in Equation 2.24.

$$\rho = \frac{d^2}{2\epsilon_0\epsilon_r\mu V_{depl}} \tag{2.24}$$

2.2 Charge Generation

Charged particles passing through matter can lose energy by ionization of atoms, excitation of atoms, Bremsstrahlung, Cherenkov radiation and transition radiation. The amount of contribution of these effects to the total energy loss depends, for example, on the kinetic energy of the particle or the composition of the traversed material. Low energetic electrons and positrons lose most energy due to ionization. At the critical energy E_c the energy of the electron is equal to the ionization loss per radiation length. In an alternate definition of the critical energy, the energy loss of ionization is equal to the energy loss of the Bremsstrahlung. Both definitions are very similar, but the former can describe transverse shower development better [23]. At higher energies the energy loss by Bremsstrahlung is the dominating contribution and is proportional to E/m^2. Bremsstrahlung arises if particles are accelerated in the coulomb field of a nucleus.

The radiation length X_0 is the mean distance over which the high-energy electron loses all but 1/e ≈ 37 % of its energy. Additionally, the radiation length is $\frac{7}{9}$ of the mean free path for pair production by high energy photons. Electrons, positrons and photons are the main particles that are detected in an electromagnetic calorimeter. Hence, the thickness of an electromagnetic calorimeter is typically described in multiples of X_0. Furthermore, the radiation length can also be used to define the transverse size of electromagnetic showers given by the Molière radius $\mathrm{R_M}$, as defined in Equation 2.25.

$$R_M = \frac{21\,\mathrm{MeV}}{E_c} X_0 \tag{2.25}$$

For the description of the mean rate of energy loss by charged moderately relativistic heavy particles, the “Bethe equation” 2.26 can be used [23]. Heavy particles are particles heavier than electrons and positrons. The “Bethe equation” does not work for electrons or positrons because of their low masses and the fact that the collision of electrons with the electrons of the target is between quantum mechanical indistinguishable particles.

$$\left\langle \frac{dE}{dx} \right\rangle = Kz^2 \frac{Z}{A} \frac{1}{\beta^2} \left[\frac{1}{2} \ln \frac{2m_e c^2 \beta^2 \gamma^2 W_{max}}{I^2} - \beta^2 - \frac{\delta(\beta\gamma)}{2} \right] \tag{2.26}$$

Table 2.1: Variables used in Equation 2.26.

Symbol	Definition	Value or units
K	$4\pi N_A r_e^2 m_e c^2$	$0.307\,\mathrm{MeV\,mol^{-1}\,cm^2}$
r_e	classical eletron radius: $\frac{e^2}{4\pi\epsilon_0 m_e c^2}$	2.818 fm
N_A	Avogadro’s number	$6.022 \times 10^{23}\,\mathrm{mol^{-1}}$
z	charge number of incident particle	-
Z	atomic number of absorber	-
A	atomic mass of absorber	-
β	v/c	-
$m_e c^2$	eletron mass × c^2	0.511 MeV
γ^2	$1/(1-\beta^2)$	-
$W_{\max}$	max. energy transfer to an electron in a single collision	MeV
I	mean excitation energy	eV
$\delta(\beta\gamma)$	density effect correction to ionization energy loss	-

The parameters used in Equation 2.26 are explained in Table 2.1. The “Bethe equation” is accurate within a few percentages in the region of $0.1 \lesssim \beta\gamma \lesssim 1000$ for intermediate Z-materials. This mass stopping power is similar for most material, but it decreases slowly with Z. Figure 2.4 displays the mass stopping power for positive muons in copper as a function of $\beta\gamma = p/Mc$. It can be seen that a minimum is reached at about $\beta\gamma = 3.0 - 3.5$. This characteristic point of minimum ionization is similar for different absorber materials. Particles in this energy range are called minimum ionizing particles (MIP). For silicon the minimum ionization or minimum mean mass stopping power is

$1.664\,\mathrm{MeV\,g^{-1}\,cm^2}$ [23]. Cosmic muons, for example, have an energy deposition comparable to MIPs.

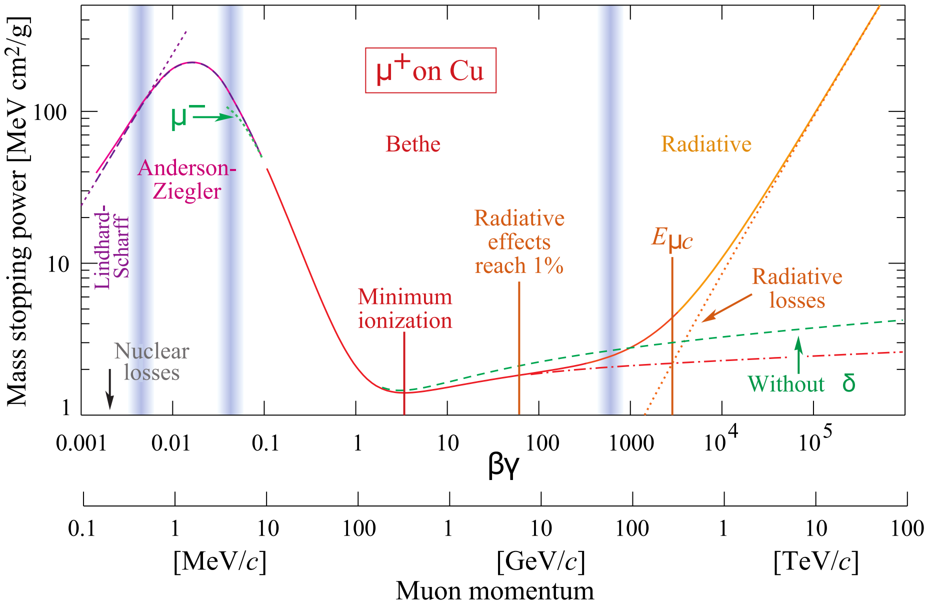

Figure 2.4: Mass stoping power for positively charged muons in copper as function of $\beta\gamma = p/Mc$ over several orders of magnitude in momentum. Figure taken from [23].

With the mean energy loss of a MIP in silicon it is possible to calculate the energy deposition and consequently the number of electron-hole pairs created in silicon when a MIP traverses it. Multiplying the mean energy loss with the density of silicon results in a mean energy deposition of $387.5\,\mathrm{eV\,\mu m^{-1}}$ silicon. This value is multiplied with the thickness of the silicon and divided by the ionization energy $E_{pair} = 3.63\,\mathrm{eV}$ [24], which is the minimum energy to create electron-hole pairs. For $300\,\mathrm{\mu m}$ thick silicon this calculation results in 32029 electron-hole pairs.

It should be noted, that the energy loss described by Equation 2.26 is a statistical process and hence the number of collisions and energy loss varies from particle to particle. Collisions with a small energy transfer are more likely than those with a large energy transfer. Therefore, the energy loss distribution cannot be described with a Gaussian function but is rather described by a Landau-Vavilov distribution [23]. The high energy tail of the energy loss spectrum originates due to rare high energy transfer collisions (δ-electrons). This moves the mean of the distribution towards the tail, even though the most probable collisions deposit less energy than the mean. The most probable energy loss in comparison to the mean energy loss is shown in Figure 2.5. For typical silicon thicknesses used in detectors the most probable energy loss is only 60 % to 70 % of the mean energy loss [23]. Using this information on the previously calculated ≈ 32000 electron-hole pairs, it can be concluded that the most probable number of generated electron-hole pairs by a MIP in $300\,\mathrm{\mu m}$ thick silicon is ≈ 21500.

Another mechanism to produce charge in a detector is due to elastic and inelastic collisions

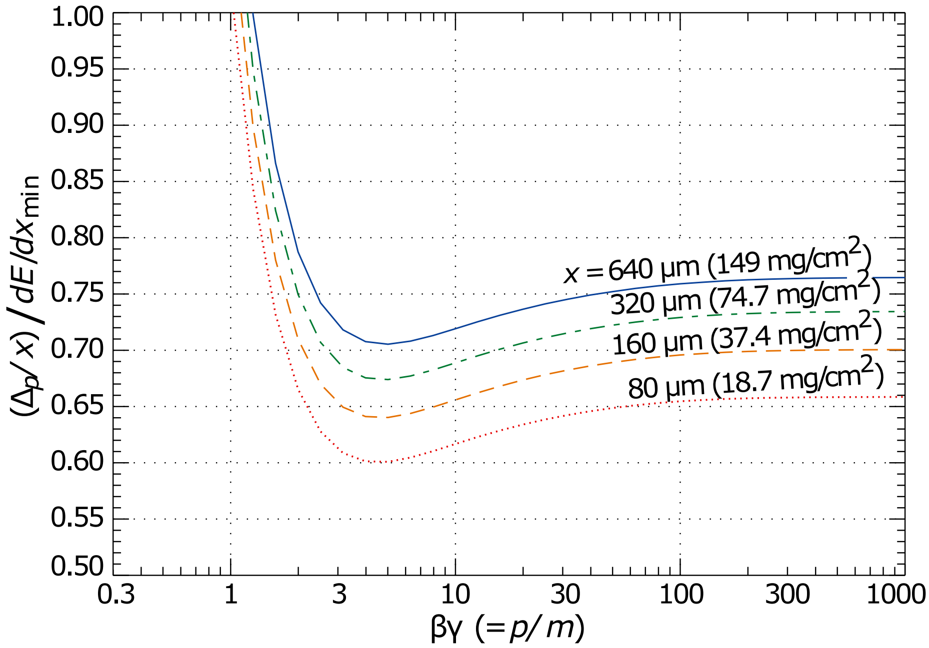

Figure 2.5: The figure shows the most probable energy loss Δ_p/x in silicon, which is scaled to the mean energy loss of a MIP. Depending on the thickness of silicon, the most probable energy loss is only 60 % to 70 % of the mean energy loss. Figure taken from [23].

of hadrons with the nuclei of the absorber material. Since the strong interaction has a short range and the probability for the reaction is small, neutrons are very penetrating. The total cross section for hadronic interactions is $\sigma_{tot} = \sigma_{el} + \sigma_{inel}$, where $\mathcal{O}(\sigma_{el}) = 10\,\text{mb}$ is the elastic cross section and $\sigma_{inel} \propto A^{\frac{2}{3}}$ is the inelastic or absorption cross section. The collision λ_c and absoption length λ_I ($\equiv$ interaction length) are defined by Equation 2.27 and 2.28.

$$\lambda_c = \frac{A}{N_A \rho} \frac{1}{\sigma_{tot}} \tag{2.27}$$

$$\lambda_I = \frac{A}{N_A \rho} \frac{1}{\sigma_{inel}} \tag{2.28}$$

Table 2.2 summarizes the most important parameters for various materials used in the *High Granularity Calorimeter.*

Table 2.2: Radiation length, critical energy, Molière radius, interaction length and density for silicon and other materials present in HGCal. Values are taken from [23]

Material	$X_0(\mathrm{g}^2\,\mathrm{cm}^{-1})$	E_c (MeV)	$R_M(\mathrm{g}^2\,\mathrm{cm}^{-1})$	$\lambda_I(\mathrm{g}^2\,\mathrm{cm}^{-1})$	$\rho(\mathrm{g}\,\mathrm{cm}^{-3})$
Silicon	21.82	40.19	11.51	108.4	2.33
Lead	6.37	7.43	18.18	199.6	11.4
Iron	13.84	21.68	13.53	132.1	7.874
Copper	12.86	19.42	14.05	137.3	8.96

2.3 Using Silicon Diodes for Particle Detection

The working principle of silicon diodes is used in the sensors of the HGCal project. Figure 2.6 shows the cross section of a schematic n-in-p diode with a particle passing through the detector. The p-type silicon bulk is heavily doped on top with n-type dopants to create a p-n junction and heavily p-type doped at the bottom to create an ohmic contact. The top and bottom implant are coated with aluminum to allow better contacting of the device with needles or wire bonds. The aluminum on top and bottom form two electrodes, which are biased depending on the polarity of the bulk. The electrons and holes created by the traversing particle are drifting towards the electrodes depending on the polarity. These charges form a signal.

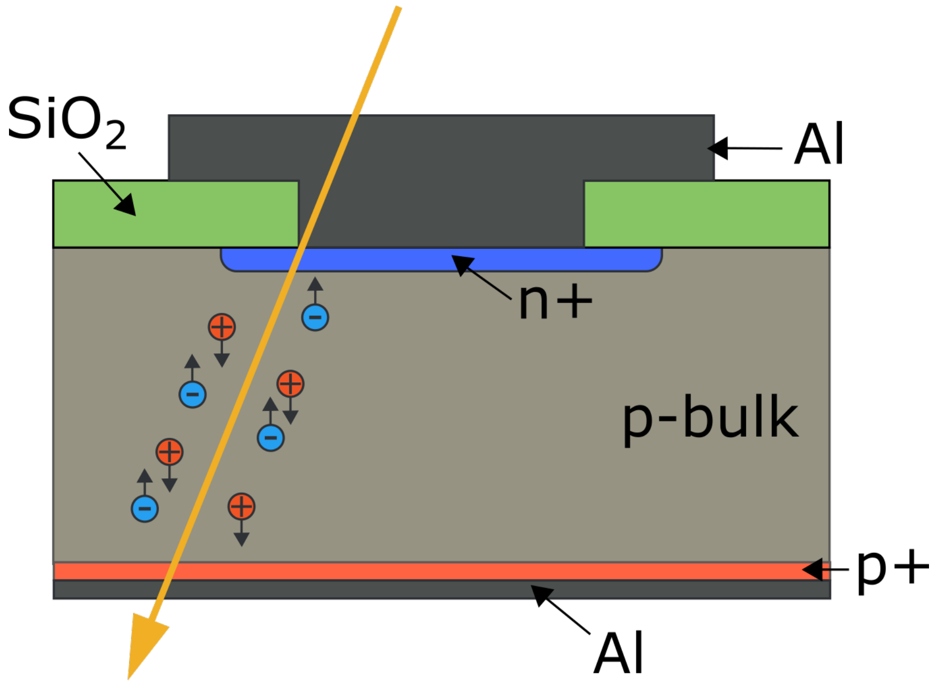

Figure 2.6: Cross section of a schematic p-type diode with a particle passing through the detector. The particle deposits energy and creates electron and hole pairs which produce the signal at the aluminum electrodes.

In Section 2.2 the number of electron-hole pairs created by a MIP in a $d = 300\,\mu\text{m}$ thick silicon is calculated to be $\approx 3.2 \times 10^4$. The number of intrinsic charge carriers (electron-hole pairs) at $T = 300\,\text{K}$ in a silicon detector with the same thickness d and an area $A = 1\,\text{cm}^2$ is:

$$n_i d A = 1.45 \times 10^{10}\,\text{cm}^{-3} \cdot 0.03\,\text{cm} \cdot 1\,\text{cm}^2 \approx 4.35 \times 10^8.$$

Comparing these numbers it can be seen that the thermally created electron-hole pairs are four orders of magnitude larger than a MIP signal. With this ratio a detector signal can not be distinguished from the background. Therefore, the free charge carriers are removed by reverse biasing the p-n junction. For the p-type detector shown in Figure 2.6 it means that the bottom side has to be biased with a more negative voltage than the top side. Typically the bottom of a real p-type detector is biased up to $-1000\,\text{V}$ while the top remains on ground potential.

The signal formation does not start when the charges reach the electrodes but starts when the charges start moving. This effect is due to the induction of electric current when charges move in an electric field and is fully described by the laws of electrostatics. This has been first established by Shockley (1938)[25] and Ramo (Ramo 1939)[26]. Ramo's theorem is given by Equation 2.29.

$$i = -qvE_w \tag{2.29}$$

In Equation 2.29 i is the induced current in the electrodes, q is the charge, v is the drift velocity of the charge due to the electric field, and E_w is the weighting field. In the original paper by Ramo in 1939 E_w is defined as: "... the component in the direction [...] of that electric field which would exist at the electron's instantaneous position under the following circumstances: electron removed, given electrode raised to unit potential, all other conductors grounded." The concept of using the weighting field is used to define how the charges couple to the electrodes. The weighting field only depends on the geometry of the electrodes. As stated by Ramo it is calculated by applying unit potential (U= 1 V) to the measurement electrode and zero to the rest. In a parallel plate capacitor, for example, the weighting field $E_\text{w} \propto \frac{1}{d}$, where d is the distance between the plates. Only in this simplest case the electric field and the weighting field are of the same form. The current induced by all charges in the parallel plate configuration is described by Equation 2.30.

$$i = \frac{q}{d}\left(\sum_i v_{i,e} + \sum_i v_{i,h}\right) \tag{2.30}$$

Figure 2.7 shows the signal of a MIP in a $300\,\mu\text{m}$ thick silicon diode, with a geometry similar to the diode shown in Figure 2.6. The curves are simulated in the programme called "Weightfield2" [27]. The programme discretizes the geometry with a mesh and calculates the (drift) potential on each grid point by solving Poisson's equation. The solving considers space charges according to the bulk doping concentration and the boundary conditions of the top and bottom electrodes. For the calculation of the weighting potential ϕ_{w} ($E_{\mathrm{w}} = \nabla\phi_{\mathrm{w}}$) it is similar, but the space charges are zero and therefore Poisson's equation reduces to the Laplace's equation. In this case the previously mentioned boundary conditions for the weighting field, as stated by Ramo, are taken into account as well. In the simulation the full depletion voltage of the sensors is $V_{\mathrm{FD}} = 120\,\mathrm{V}$. In Figure 2.7a the bias voltage is the same as the full depletion voltage. It can be seen that the electron contribution to the total current decays faster over time in comparison to the hole contribution. This is due to the different mobilities of electrons and holes. In the case, where the bias voltage is the full depletion voltage, the maximum electric field is located at the readout electrode at the top and decreases to zero at the bottom electrode. Near the bottom electrode the charges see only a low electric field and hence the lower drift velocity and consequently the asymptotic tail in the current-time diagramme. The current decays exponentially. In the case of over depletion (2.7b) the electric field is higher and at the back not zero anymore. The current components lead to a triangular shape. Integrating the current over time results in the deposited charge.

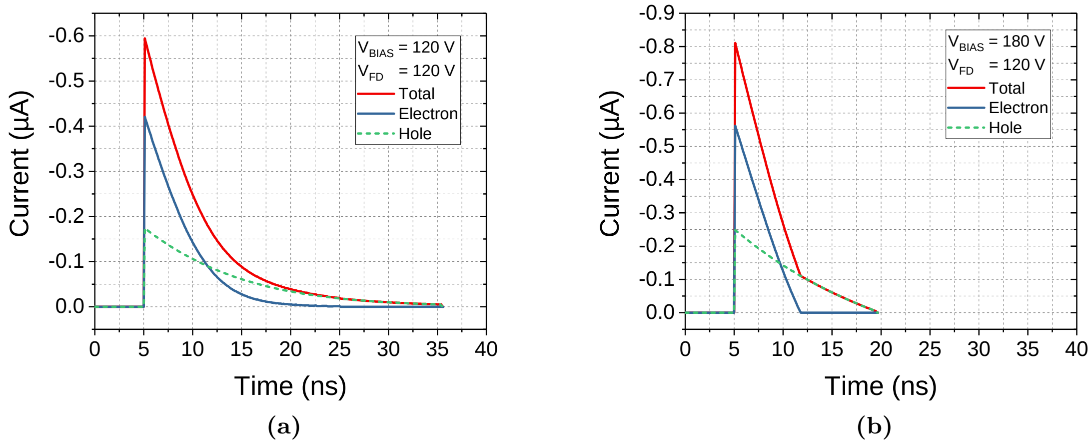

Figure 2.7: Signal of a 300 µm thick diode with a full depletion voltage $V_{\mathrm{FD}} = 120\,\mathrm{V}$ simulated with Weightfield2 [27]. The electron and hole contribution to the total current is shown at a bias voltage $V_{\mathrm{BIAS}} = 120\,\mathrm{V}$ (a) and at $V_{\mathrm{BIAS}} = 180\,\mathrm{V}$ (b).

2.4 Irradiation Damage in Silicon

Radiation damage occurs in silicon sensors, for example, in the environment of high energetic hadron collisions. The particles resulting form the collision, which pass the silicon sensor, deposit energy and create crystal defects. In general the irradiation damage can be split in two types. Surface damage and bulk damage. Surface damage, meaning damage in the Si-SiO_2 interface and the SiO_2, is due to ionizing radiation. It leads to an increase of the positive oxide charge at the SiO_2 interface and interface traps. The following effects of surface damage are summarized from [28]. The first macroscopic effect on the sensor is an increase of the inter-pad capacitance, which leads to an increasing electronic noise. The second one is the decrease of inter-pad resistance, which increases the cross-talk. And finally, it leads to an increase of the flat band voltage, which is due to increased oxide charges. The flat band voltage is the voltage, which can compensate the electric field generated by the fixed oxide charges. The relation between the oxide charges and the full depletion voltage is given by Equation 4.1. Surface damage is especially important to consider for AC-coupled sensors, where the signal is capacitatively coupled from the bulk to the strip (or pad) and the oxide is used as dielectric. For the sensors used in the HGCal project the main part of radiation damage is bulk damage and is therefore described in more detail in the following.

Particles traversing the silicon deposit energy. This energy is not only deposited exclusively by just ionizing the silicon atoms but also by electromagnetic and strong force interaction with the atoms of the lattice itself (≡ Non Ionizing Energy Loss NIEL). This means, that single atoms in the lattice can be displaced and create so-called interstitials (I), vacancies (V) and other more complex constructs. An interstitial is an additional atom in between the regular atoms in the crystal lattice. A vacancy is a missing atom in the lattice. The main defect types perturbing the crystal lattice structure are explained in Figure 2.8 and are basically combinations of vacancies and interstitials. Impurities can take the place of silicon atoms and are labelled by their atomic sign with an index defining whether it is an interstitial oder vacancy.

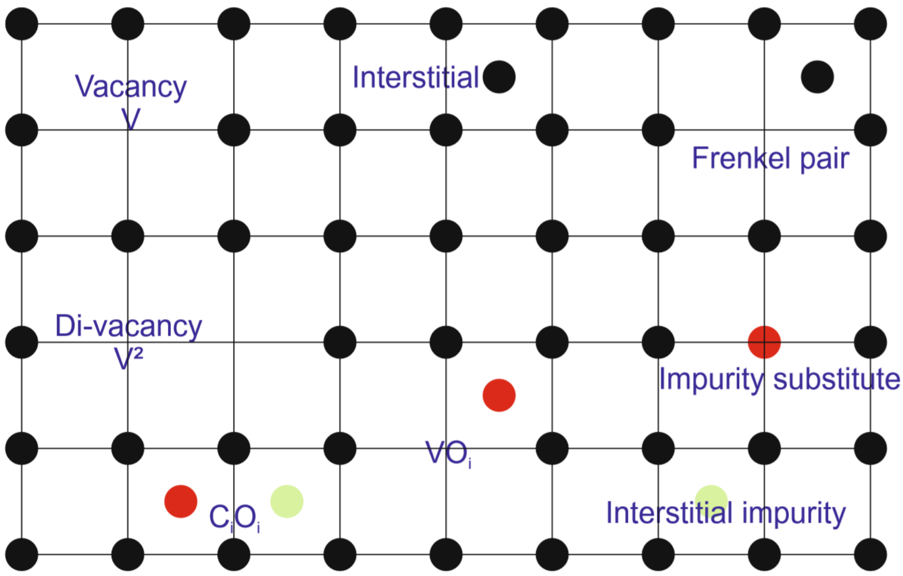

Figure 2.8: Irradiation damage in the silicon lattice leads to displacement of silicon atoms (black balls). New crystal lattic structure leads to new energy levels in the energy band scheme. Impurities are labeled with their atomic sign and the index defines if it is a substitute (vacancy) or interstitial. For example, C_i is a carbon atom interstital. The figure is taken from [28].

The changes in the lattice create extra energy levels in the band gap. Figure 2.9 shows the macroscopic effect of these changes. Defects in the upper half of the band gap (left part of the figure) result in extra donors and defects in the lower half result in extra acceptors. These changes in the donor and acceptor concentration change the effective space charge N_{eff}, which leads to a change of the full depletion voltage of the device. Deep level traps (middle of figure) lead to charge trapping which leads to charge loss and hence the charge collection efficiency is degraded. A charge is trapped when the detrapping time of the charge carriers is longer in comparison to the signal readout time of the system. From SRH recombination it became already known that energy levels near mid-gap are mainly responsible for leakage current generation. The same is true in the case here where irradiation damage produces new levels in the energy band scheme.

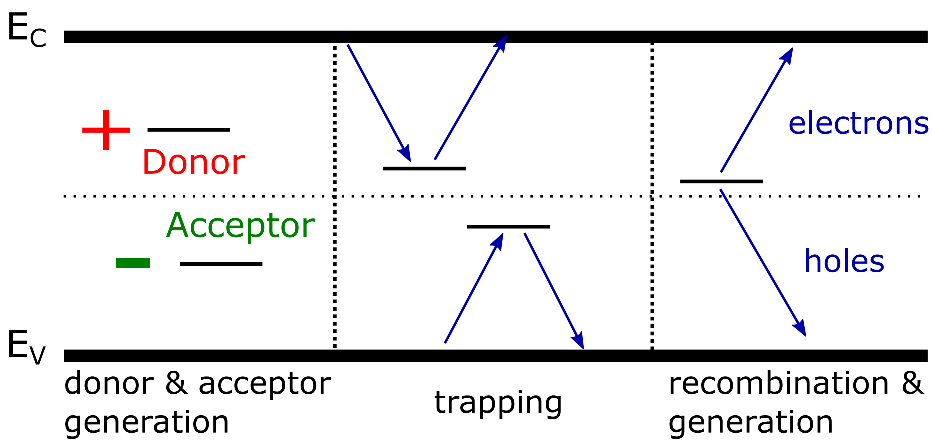

Figure 2.9: Irradiation damage creates extra energy levels in the silicon band gap. Different energy levels have different effects on the behaviour of the detector.

Different particle types traversing the silicon cause different damage. For example, protons can lose energy by ionization and elastic scattering on the nuclei, while neutrons only by the latter. Additionally, the kinetic energy of the particle determines the energy deposition dE/dx (2.2). Figure 2.10 shows the simulated vacancy distribution for protons with 10 MeV (left) and 23 GeV (middle), and neutrons with 1 MeV (right). Low energetic protons produce vacancies homogeneously scattered over a large volume. Neutrons on the other hand produce damage clustered in high density 2.10. For high energy protons the damage distribution is a mixture of both previously mentioned cases 2.10.

2.4.1 Non Ionizing Energy Loss

The NIEL hypothesis assumes that the damage done by different particles scales linear with the NIEL and the number of vacancies (as seen, for example, in 2.10) is a measure of the damage irrespective of the distribution [30]. The NIEL can be defined as displacement damage function D with the units MeV mb. The damage of 1 MeV neutrons is used as reference value. The 1 MeV neutron equivalent (n_{eq}) damage is fixed to 95 MeV mb in the displacement damage function. With the hardness factor κ (Equation 2.31) it is possible to scale the damage of different particles at different energies to the damage of 1 MeV neutrons [31].

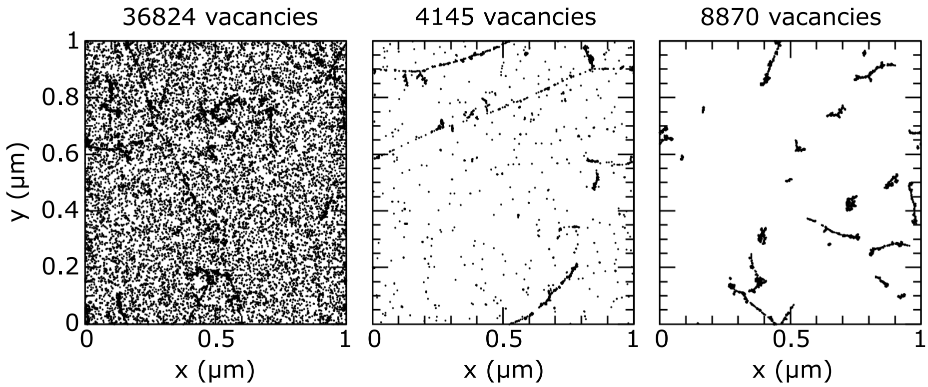

Figure 2.10: Different irradiation types produce a different distribution of vacancies. The plot on the left shows a simulation of the effect of 10 MeV protons, the plot in the middle the effect of 23 GeV protons, and the plot on the right the effect of 1 MeV neutrons. The particle fluence in all three cases is $10^{14}\,\mathrm{cm}^{-1}$. The plots are projected over 1 µm depth (on the z-axis). The Figure is taken from [29].

$$\kappa = \frac{\int D(E)\,\phi(E)\,dE}{95\,\mathrm{MeV\,mb}\cdot\int \phi(E)\,dE} \tag{2.31}$$

Using the hardness factor the fluence ϕ can be related to the equivalent fluence of 1 MeV neutrons ϕ_{eq}, which creates the same displacement damage according to the NIEL hypothesis.

$$\phi_{eq} = \kappa\,\phi = \kappa \int \phi(E)\,dE \tag{2.32}$$

2.4.2 Leakage Current

Increasing fluence ϕ_{eq} leads to a change of detector properties as mentioned previously. The leakage current of the silicon sensor changes in the following way. First, it is dependent on the fluence, but not on the silicon type, resistivity or impurity content [32, 33]. Figure 2.11a shows the linear increase in leakage current with increasing fluence ϕ_{eq}. The measurements are performed on samples which were annealed for 80 min at 60 °C and normalized to 20 °C. This increase of the volume current $\Delta I/V$ can be parameterized with the current related damage factor α.

$$\Delta I = \alpha\,V\,\phi_{eq} \tag{2.33}$$

The factor $\alpha(80\,\mathrm{min}, 60\,°\mathrm{C}) = (3.99 \pm 0.03) \times 10^{-17}\,\mathrm{A\,cm}^{-1}$ can be extracted, after temperature scaling, for the measurements at 20 °C. Part of the irradiation damage can be mitigated by thermal excitation. This process where some of the crystal lattice atoms move and reinstate the pre-irradiated lattice structure is called annealing. With annealing the current related damage factor and therefore the leakage current decreases for different temperatures and durations. This is shown in Figure 2.11b.

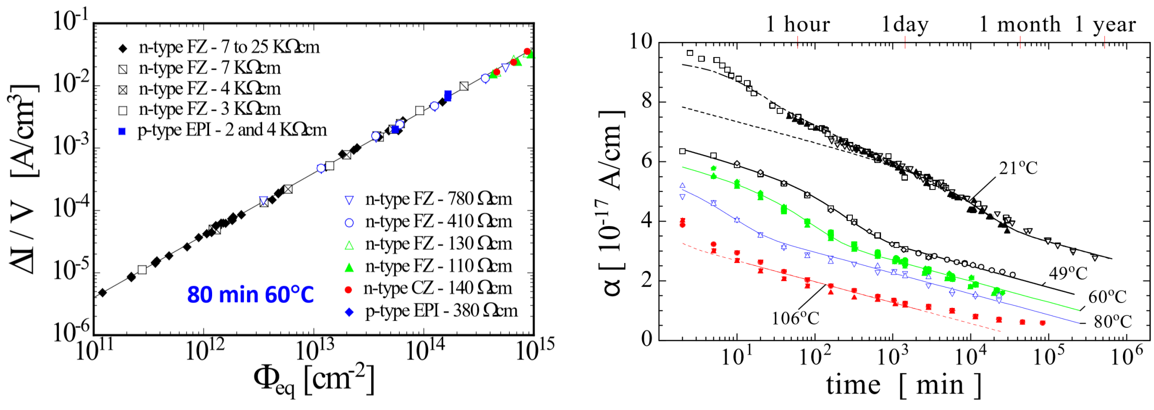

Figure 2.11: The leakage current increases with fluence. This behaviour is the same for various detector types (a). The current decreases with annealing. Different temperatures lead to different current related damage factors α.(b). Figures taken from [30].

The third influencing factor on the leakage current is temperature. The generation and recombination mechanism described by Shockley favours defect levels near the mid of the band gap (= at the intrinsic energy level). Therefore the leakage current temperature dependence is the same as for the intrinsic carrier concentration [30]. The temperature dependence of this generation and recombination current, which holds true for the non-irradiated and irradiated case, is described by Equation 2.34.

$$I(T) = A \cdot T^2 exp(-E_{eff}/2k_B T) \tag{2.34}$$

$E_{eff} = (1.214 \pm 0.014)\,\text{eV}$ is the effective energy and A is a proportionality constant. With this equation the current can be scaled from temperature T_1 to temperature T_2 by Equation 2.35.

$$\frac{I(T_1)}{I(T_2)} = \left(\frac{T_1}{T_2}\right)^2 exp\left(-\frac{E_{eff}}{2k_B}\left[\frac{1}{T_1} - \frac{1}{T_2}\right]\right) \tag{2.35}$$

Equation 2.35 means that increasing the temperature by 7 °C increases the leakage current roughly by a factor two.

2.4.3 Effective Doping Concentration

As seen in Figure 2.9, irradiation damage can induce acceptor and donor-like defects, which changes the effective doping concentration N_{eff} of the silicon bulk. In Figure 2.12a an example of the change of N_{eff} and hence the full depletion voltage can be seen. In this example the sensor is initially n-type with a high resistivity meaning it has a positive space charge. With irradiation, negative space charge forms, which eventually compensates the positive charges until it reaches the minimum at values corresponding with the ones of intrinsic silicon [30]. This minimum is the point of *type inversion* or *space charge sign inversion* (SCSI) as the space charge gets more and more negativ with increasing fluence from this point on. The space charge getting more and more negative is equivalent to the removal of donors together with an increase of acceptor-like levels. An initially p-type sensor does not undergo type inversion. The full depletion voltage increases directly with increasing fluence.

Figure 2.12b shows the effects of annealing at 60 °C. In contrast to the leakage current behaviour with annealing, the full depletion voltage is not decreasing continuously. The change of the effective doping concentration with irradiation ΔN_{eff} and annealing is given by Equation 2.36 [30].

$$\Delta N_{eff} = N_{eff,0} - N_{eff}(t) = N_A(t) + N_C + N_Y(t) \tag{2.36}$$

$$\begin{aligned} N_A(t) &= g_a \phi_{eq} exp(-t/\tau_a) \\ N_C &= N_{C,0}(1 - exp(-c\phi_{eq})) + g_c \phi_{eq} \\ N_Y(t) &= g_y \phi_{eq}(1 - exp(-t/\tau_y)) \end{aligned}$$

$\Delta N_{eff,0}$ is the value before irradiation and $N_{eff}(t)$ the value after irradiation. g_a, g_c and g_y are the introduction rate coefficients. τ_a and τ_y are temperature dependent time constants for beneficial and reverse annealing defined by Equation 2.37.

$$\frac{1}{\tau_{a,Y}} = k_{0a,0Y}\, exp\left(-\frac{E_{a,Y}}{k_B T_{anneal}}\right) \tag{2.37}$$

For beneficial annealing the activation energy is $E_a = (1.09 \pm 0.03)$ eV and the frequency factor is $k_{0a} = 2.4^{+1.2}_{-0.8} \times 10^{13}\text{s}^{-1}$. The reverse annealing parameters are $E_Y = (1.33 \pm 0.03)$ eV and $k_{0Y} = 1.5^{+3.4}_{-1.1} \times 10^{15}\text{s}^{-1}$ [31]. With Equation 2.37 it is possible to scale the annealing time from one temperature to another. This is done in a similar fashion as the scaling of the leakage current with temperature.

The annealing behaviour can be described by three components. $N_A(t)$ describes the short term or beneficial annealing. N_C is the so-called stable damage component, which does not change with annealing. The third component is N_Y, which specifies the long term or reverse annealing. Since ΔN_{eff} is positive in Figure 2.12b, it is clear that $N_{eff}(t)$ in Equation 2.36 is negative. Additionally, the short term annealing component is also called beneficial annealing because $|N_{eff}|$ and hence the full depletion voltage is decreasing during this period. The long term component is called reverse annealing because the full depletion voltage increases with increasing annealing time. To be able to operate a highly irradiated sensor efficiently, the full depletion voltage should be as low as possible. Therefore reverse annealing should be avoided as much as possible. This, for example, is one of the reasons the HGCal sensors in CMS will be cooled down to −30 °C.

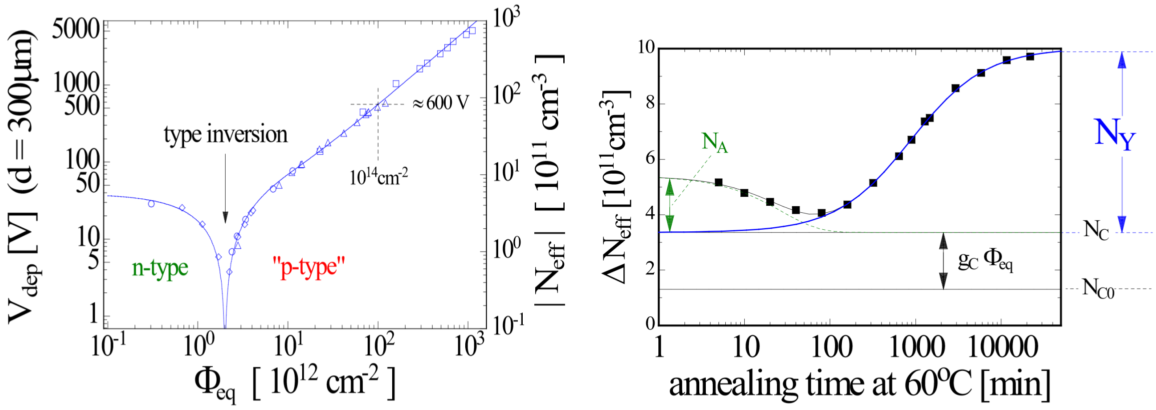

(a) **(b)**

Figure 2.12: The effective doping concentration is fluence dependent. A n-type silicon sensor will undergo type inversion and become effectively p-type after irradiation (a). The effective doping concentration changes with the annealing time (b). The three different components of the effective doping concentration are highlighted . Figures taken from [30].

2.4.4 Trapping

The third macroscopic effect increasing fluence has on a silicon sensor is the decreased charge collection efficiency (CCE). Figure 2.13a shows the inverse effective trapping time $1/\tau$ for different fluences ϕ_{eq}. Both electron and hole inverse trapping times increase linearly with fluence. The following explanation follows the work of [28]. The trapping probability can be described by Equation 2.38

$$\frac{1}{\tau_{eff}} = \sum_i N_i(1-P_i)\sigma_i v_{th} \tag{2.38}$$

N_{i} is the concentration of trapping centres resulting from irradiation damage, P_{i} is the occupation probability, σ_{i} is the charge carrier cross-section and v_{th} is the thermal velocity. The thermal velocity is proportional to the square root of the temperature. The number of trapping centres is assumed to be linear with fluence therefore Equation 2.39 can be used to relate the effective trapping time with fluence.

$$N_i = g_i \phi_{eq} f_i(t) \Rightarrow \frac{1}{\tau_{eff}} = \gamma \phi_{eq} \tag{2.39}$$

g_i is the introduction rate and $f_i(t)$ is used to describe the time dependent annealing behaviour. The decline of the CCE is then described by Equation 2.40.

$$Q_{e,h}(t) = Q_{0_{e,h}} exp\left(-\frac{t}{\tau_{eff_{e,h}}}\right) \tag{2.40}$$

To describe the annealing behaviour shown in Figure 2.13b, $\gamma(t)$ from Equation 2.39 is parameterized in Equation 2.41.

$$\gamma(t) = \gamma_0\, exp\left(-\frac{t}{\tau_a}\right) + \gamma_\infty \left[1 - \exp\left(\frac{t}{\tau_a}\right)\right] \tag{2.41}$$

γ_0 and γ_∞ denote the trapping rates at the beginning and end of the annealing proces. τ_a is the annealing time constant [30, 34].

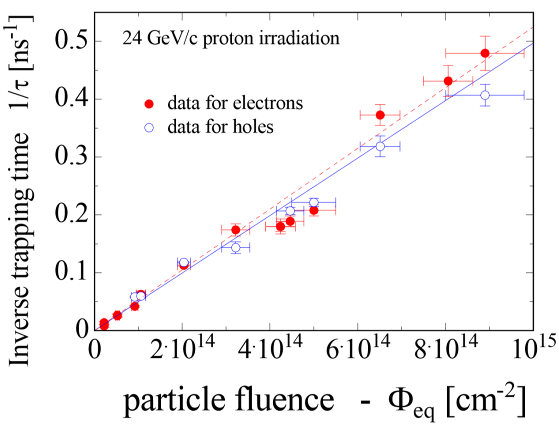

(a)

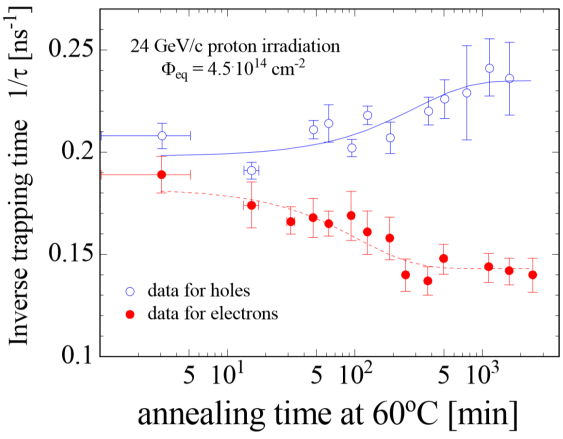

(b)

Figure 2.13: Inverse trapping time increases with increasing fluence. The data has been taken at 0 °C after an annealing of 30 to 60 min at 60 °C(a). The inverse trapping time of holes increases with annealing, while the inverse trapping time for electrons decreases with annealing time (b). Figures taken from [30].

The annealing effect shown in Figure 2.13b shows, that the trapping probability decreases for holes and increases for electrons.

3

High Granularity Calorimeter at the CMS Experiment

3.1 Calorimeter Basics

A calorimeter is a detector, which measures the energy of particles. Particles entering the calorimeter deposit energy and create secondary particles, which again deposit energy and create further secondary particles. This process, called particle shower, continues until the particle is absorbed. Due to the absorption of the particles the calorimeter measurement is destructive. The energy deposition of different particles in matter is described in Section 2.2. A calorimeter detector is designed in a way that the calorimeter signal is proportional to the energy.

Calorimeters are needed in a particle physics detector, because they can not only measure the energy but also the direction of neutral particles. Furthermore, depending on the shower shape different particle types can be distinguised. Calorimetry is based on the deposition of energy by collisions of particles with the atoms in the absorber material, which is a statistical process. On average N secondary particles are produced, where N is proportional to the energy. Therefore, the energy resolution is dominated by statistical fluctuations of N. With higher energy the relative energy resolution improves. An important feature for high energy colliders is the fact, that the necessary thickness of a calorimeter, to stop the shower in the detector volume, scales with the logarithm of the particles energy. Another information the calorimeter can provide at a hadron collider is information regarding timing, which is important for the trigger system.

Two types of calorimeters with different shower development exist. The first is the electromagnetic calorimeter, which describes showers by electrons, positrons and photons. The second is the hadronic calorimeter for single hadrons or a multitude of closely spaced hadrons in the form of so-called jets. Jets consist of a mixture of charged and neutral particles. The difficulty for hadronic calorimetry is that all different particles with the same energy should create the same signal in the detector.

3.1.1 Electromagnetic Shower

High energetic electrons, positrons and photons interact with matter and produce electromagnetic showers. For the description of the electromagnetic shower the model of Rossi [35] is used and follows the explanations of [36].

The most important process for shower formation by electrons and positrons is the energy loss by Bremsstrahlung and for photons the pair production. The cross section for both processes is proportional to the square of the atomic number Z^2. Therefore, the detector material for electromagnetic showers should have a Z as high as possible. The characteristic length for both processes is the radiation legth X_0, which is defined in Section 2.2. Penetrating electrons or positrons emit bremsstrahlung near the atomic field of nuclei of the absorber material. The high energy photon produces electron and positron pairs via pair production. These electrons and positrons including the primary electron or positron can again emit more photons. The process continues until the mean particle energy equals roughly the critical energy E_c. For particle energies lower than the critical energy ionization and excitation processes are more dominant. The electromagnetic shower can also be started with a photon, which produces an electron and positron pair via pair production. The shower continues in the same way.

It is assumed that after one radiation length X_0 either the bremsstrahlung or pair production process occurs and that one half of the energy is transferred from the primary to the secondary particle. After the path length $s = t\,X_0$ the number of particles is $N=2^t$, and the energy is $E = \frac{E_0}{2^t}$. Then the maximum number of shower particles N_{max} can be determined to be $N_{max} = \frac{E_0}{E_c}$ and the maximum shower range $t_{max} = \frac{\ln E_0/E_k}{\ln 2}$ [36].

The important message is that the number of particles in the electromagnetic shower is proportional to the energy and that the range of the shower is proportional to $\ln E$.

The lateral shower extension is described by the Molière radius R_M, defined in Equation 2.25. The transversal deviation originates from multiple scattering of the low energetically charged particles and compton scattering of the photons.

3.1.2 Hadronic Shower

Hadron shadows originate from inelastic hadronic interactions of the primary hadron with the nuclei of the absorber material. Resulting secondary particles produce more particles again. The hadronic shower is more complex than an electromagnetic shower as it consists of more different reactions. Due to the fluctuations of the contributions of the different reactions it is very difficult to reach good energy resolution in a hadronic calorimeter. The hadronic shower development scales with the nuclear absorption length λ_I, as defined in Equation 2.28. Since the nuclear absorption length is larger than the radiation length, a hadronic calorimeter has to be thicker than an electromagnetic calorimeter. Therefore, in an experiment the electromagnetic calorimeter is always in front of the hadronic calorimeter.

A highly energetic hadron interacts inelastically with a nucleon and produces highly energetic particles. This transformation process of the nucleus is called spallation, during which a large number of elementary particles or larger debris of the nucleus are emitted. These secondary particles can undergo inelastic interactions with the nucleons of another nuclei. This continues as long as the energy of the secondary particles is sufficient. After spallation the excited nucleus can undergo nuclear evaporation, meaning that all kinds of particles are emitted until the remaining excitation energy is below the binding energy of the components in the nucleus. In elements with a high atomic number, fission can occur after spallation as well. The created hadronic particles in the spallation process are, for example, π^0 mesons, which mostly decay into two photons. The photons created by the decay of neutral mesons initiate an electromagnetic shower within the hadronic shower. The fraction of energy converted to electromagnetic showers is higher for higher initial energy. Additionally, there is a large variation how much energy goes into the electromagnetic shower, which worsens the energy resolution. In a purely hadronic shower energy is lost in the absorber, which is not measured. They involve for example the production of neutrons and high energy muons, or the kinetic energy of debris of nuclei, or the nuclear binding energy. In a electromagnetic shower no such energy loss mechanisms exist. Therefore, the response of the calorimeter to the electromagnetic component is better than to the hadronic part. In an ideal calorimeter the response to both parts is equal.

3.1.3 Calorimeter types

Two different calorimeter types exist, homogenous calorimeters and sampling calorimeters. In a homogenous calorimeter the detector material is the absorbing material and the active signal producing material at the same time. An example for this type is the CMS ECAL, which consists of scintillation crystals. The energy of the electromagnetic shower gets converted to light, which is a measure of the energy. In a homogenous calorimeter the best possible energy resolution is achievable. One disadvantage is that it is expensive. Homogenous calorimeters are usually only used as electromagnetic calorimeters, since they are expensive and the hadronic calorimeter needs to be much bigger.

In a sampling calorimeter the absorber material and the active detector material alternate. Incoming particles deposit energy in the absorber and produce particle showers, which produce a signal in the active material. Typical absorber materials have high density like lead. Typical active detectors are plastic scintillators, noble liquid ionization chambers, gas detectors, and silicon sensors. The advantage of this calorimeter type is that the material for the absorber and active material can be chosen individually according to the application. With very dense absorbers the calorimeter can be made compact. Additionally, typical absorber materials are cheap. A drawback of this calorimeter type is that only part of the energy is actually measured in the detetors, since most of the energy is deposited in the absorbers. Due to the energy deposition processes being statistical processes, the energy resolution in this type of calorimeter is worse than in homogenous calorimeters. The current hadronic calorimeter of CMS is a sampling calorimeter.

3.2 Motivation for Upgrade

The following section will explain the motivation and reasons for the upgrade of the endcap calorimeter system during LS3. The current scintillator based ECAL and HCAL were designed for an integrated luminosity of $500\,\mathrm{fb}^{-1}$. In principle, radiation damage does not change the scintillation mechanism in the lead tungstate crystals of the ECAL. But the light transmission in the crystal is reduced through the formation of colour centres [6]. This leads to a reduction of the light output, which cannot be annealed out at room temperature. In the ECAL barrel ($|\eta| < 1.48$) the light output will only be halved after $3000\,\mathrm{fb}^{-1}$, while the light output in the endcap crystals will be reduced by more than a factor of 10 for $\eta > 2$ [6].

The HCAL endcap, which presently consists of plastic scintillator tiles, will receive radiation doses of up to 3×10^5 Gy in comparison to 2×10^3 Gy of the barrel region after $3000\,\mathrm{fb}^{-1}$. A dose of $\sim 10^3$ Gy leads to a light output reduction of 30 %.

Figure 3.1a shows the decrease of the light signal at layer 1 for increasing delivered integrated luminosity in the HCAL endcap. The measurement data is from $23.3\,\mathrm{fb}^{-1}$ data collected during 2012 and fitted with an exponential function. The parameter D is a parameter, which depends on the tile position, tile size, manufacturing process, handling of the tile, conditions of irradiation, temperature and dose rate [6]. The dose rate influences how much light output is lost per dose in the plastic scintillators [8], hence a different parameter D for different pseudorapidity η. With decreasing pseudorapidity the distance from the beam pipe increases and hence the lower dose rate. The figure shows, that with the current system the light output after $3000\,\mathrm{fb}^{-1}$ will practically be zero. Figure 3.1b shows the light output at $1000\,\mathrm{fb}^{-1}$ for different scintillator layers and pseudorapidities. The closer the position to the interaction point the higher the dose and hence a lower light signal. At this level of integrated luminosity most of the sctintillators in the endcap would already have a relative signal below 10 %.

Additionally at high pileup, for the clustering algorithm, the cluster size is extended due to low-energy deposits surrounding the shower core that imitate radiated energy. This increasing shower size with increasing pileup leads to energy fluctuations, which degrade the energy resolution.

In the ECAL endcaps, fixed sets of crystals are used to calculate trigger sums. Due to loss of light output, the noise of a single crystal rises up to a level where jet, electromagnetic and missing-$\mathrm{E_T}$ triggers are severely affected.

The previous points only allow the conclusion that the existing calorimeter endcaps have to be reworked entirely for the HL-LHC operation.

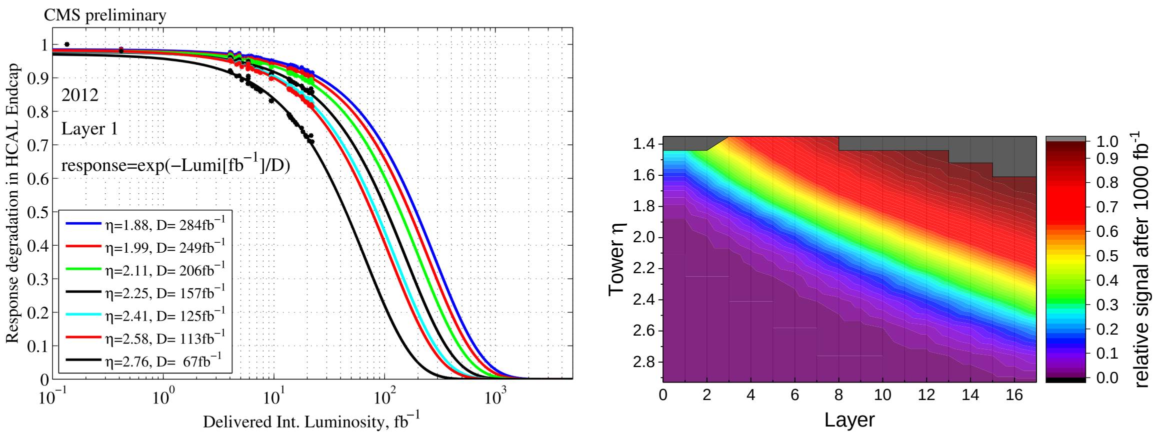

(a) (b)

Figure 3.1: Degradation of the response of the HCAL scintillator tiles used in run 1 with increasing luminosity (a). After an integrated luminosity of $1000\,\mathrm{fb}^{-1}$ the expected relative signal of the plastic scintillators of the hadron calorimeter endcap is decreasing drastically as the radial distance to the interaction point decreases (b).

3.3 Features and Requirements of the HGCal

First of all, the new calorimeter endcap should be able to cope with the immense radiation environment of the HL-LHC phase. Figure 3.2 [8] shows a FLUKA simulation of the expected fluence distribution in the endcap after $3000\,\mathrm{fb}^{-1}$. The highest 1 MeV neutron equivalent fluence of about $10^{16}\,\mathrm{n_{eq}/cm^2}$ corresponding to a dose of about 2 MGy can be found at the point closest to the interaction point. Scintillator technology will not work in this region, and another radiation hard detector technology is needed. It will be introduced in the next section.

The following requirements for the HGCal upgrade follow the ideas from [8]. The radiation tolerance is needed to ensure a good energy resolution even after the full HL-LHC duration. The energy resolution of photons for example is about $\frac{\sigma}{E} = \frac{24\,\%}{\sqrt{E}} \bigoplus 0.8\,\%$ [8]. This is sufficient to maintain the excellent invariant mass resolution for the benchmark channel of a Higgs boson decaying into two photons, which is achieved with the current ECAL. This requires a proper inter-cell calibration, which is best performed by the use of minimum-ionizing particles.

Additionally, a fine lateral granularity is required to get a high enough signal to noise ratio to allow MIP calibration. Finer lateral granularity means smaller cell sizes and hence smaller cell capacitances. This translates to smaller electronic noise. Smaller cell sizes are also beneficial for the separation of two showers and the observation of narrow jets. Furthermore, the energy resolution is improved when using smaller cell sizes due to the improved ability to exclude wrong inclusion of energy from particles in high pileup interactions. A fine lateral granularity is also needed for particle flow calorimetry. Particle flow analysis in CMS is for example used in the reconstruction of hadronic jets. Typically about 55 % of the jet energy is in charged particles, 30 % in photons and 15 % in neutral hadrons [6]. Conventional jet

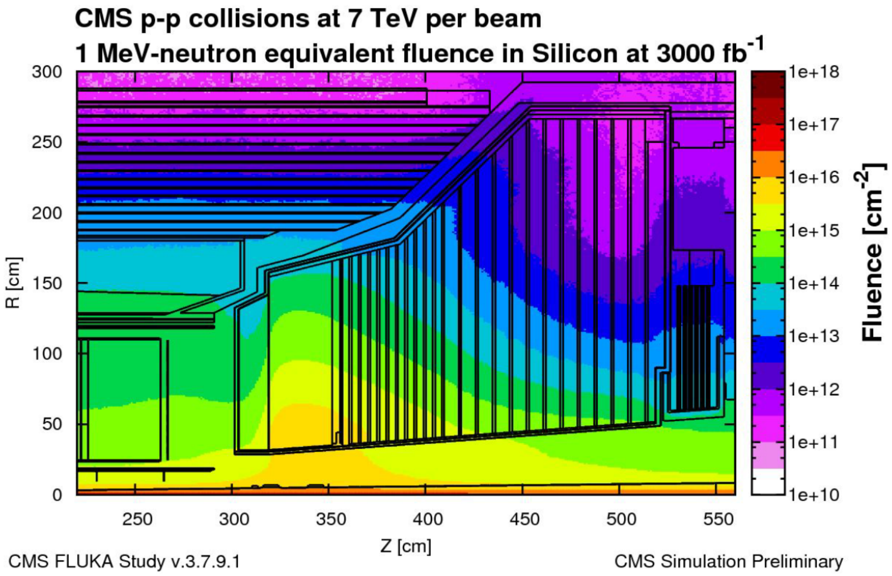

Figure 3.2: Cross section of the new calorimeter endcaps with the expected position dependent fluences at $3000\,\mathrm{fb}^{-1}$

reconstruction uses only information from the electromagnetic and hadronic calorimeter to identify and reconstruct jets. Since the momentum information and consequently the energy of charged hadrons can be better determined in the tracking system, particle flow analysis uses this information together with the information from the calorimeter to produce the best measurement of the jet momentum vectors. More information on particle flow in CMS can be found in [37]. On the other hand, arbitrarily small granularity is not feasible due to increasing dissipation of energy with an increasing cell number and hence increasing cooling requirements.

Another requirement is to have a fine longitudinal granularity. Since the new endcap calorimeter is a sampling calorimeter, a higher lateral granularity will lead to better sampling of the shower development in a longitudinal direction. Better longitudinal sampling helps in pileup discrimination and improves the energy resolution. With the pointing capability of the HGCal due to transverse and longitudinal granularity it is possible to implement a dedicated trigger at Level-1 for displaced objects.

The next requirement is to have good timing capability to measure the time of the high energy showers. This helps to reject energy from pileup, helps to identify the vertex of the triggered interaction and helps particle flow reconstruction. The needed resolution is $\mathcal{O}(25\,\mathrm{ps})$ [38], which has been proven to be possible, for example, in [38] and [39]. In comparison, the time intervall of a bunch crossing, where all collisions happen, is about a few hundred pico seconds.

3.3.1 Design of new High Granularity Endcap Calorimeter

In this section the design of the new HGCal, which meets the previously mentioned requirements, will be explained in detail. The general design idea to use tungsten and silicon in an electromagnetic calorimeter was previously studied by the CALICE collaboration in works like [18]. CMS (and CALICE) continues this work and realizes the concept in the HGCal project.

The whole calorimeter is thermally shielded and cooled by a CO_2 cooling system down to the operational temperature of $-30\,°C$. The new endcap replaces the old ECAL and HCAL and consists of two parts called CE-E and CE-H. The former denotes the electromagnetic compartment of the calorimeter endcap, while the latter denotes the hadronic compartment of the calorimeter endcap. Figure 3.3a shows the CMS detector with one HGCal endcap highlighted. The inner part is the CE-E and the outer one is the CE-H. Figure 3.3b shows a cross sectional view of one half of the CE (Calorimeter Endcap).

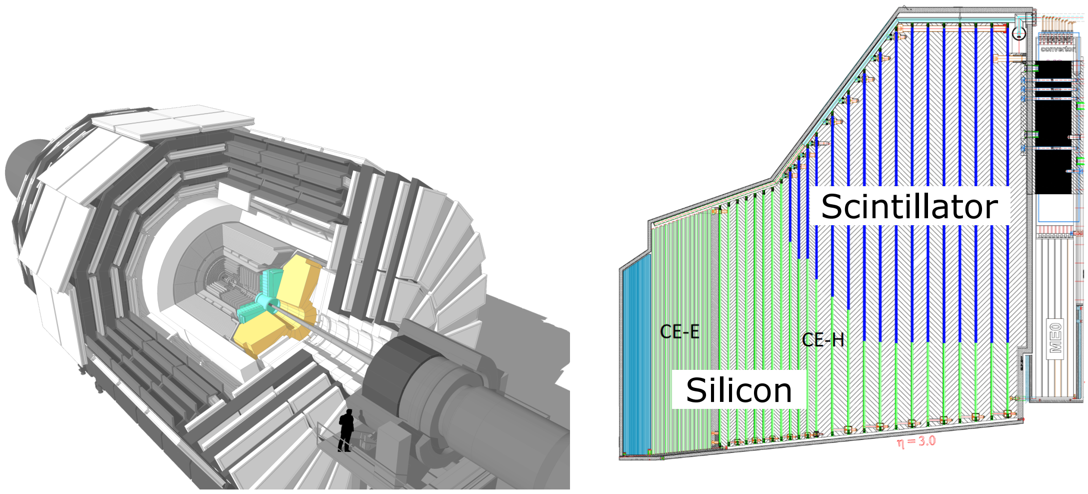

(a) (b)

Figure 3.3: The figure highlights the HGCal in the CMS detector (a). The cross section of the HGCal, which consists of the electric calorimeter endcap (CE-E) and the hadronic calorimeter endcap (CE-H) is shown in (b). Figures from [8].

The CE-E consists of 28 sampling layers, where silicon sensors as active material are used and WCu in addition to Cu plates are used as absorbers. The longitudinal segmentation is shown in Figure 3.8. The whole compartment has a longitudinal thickness of 34 cm and a radiation length of about 26 X_0 and an absorption length of 1.7 λ_I. A silicon module is composed of the silicon sensor, which is located between the 1.4 mm thick WCu baseplate and a printed ciruit board that carries the front-end electronics. The layers of a silicon module are shown in Figure 3.4a. Additionally, a photo of a hole in the printed circuit board, the hexa-board, of a 6-inch prototype is shown in Figure 3.4b. It is used to connect the readout chips with the sensor pads underneath by wirebonds. The WCu baseplates of two silicon modules are tiled on either side of the 6 mm Cu plate to form one absorber layer.

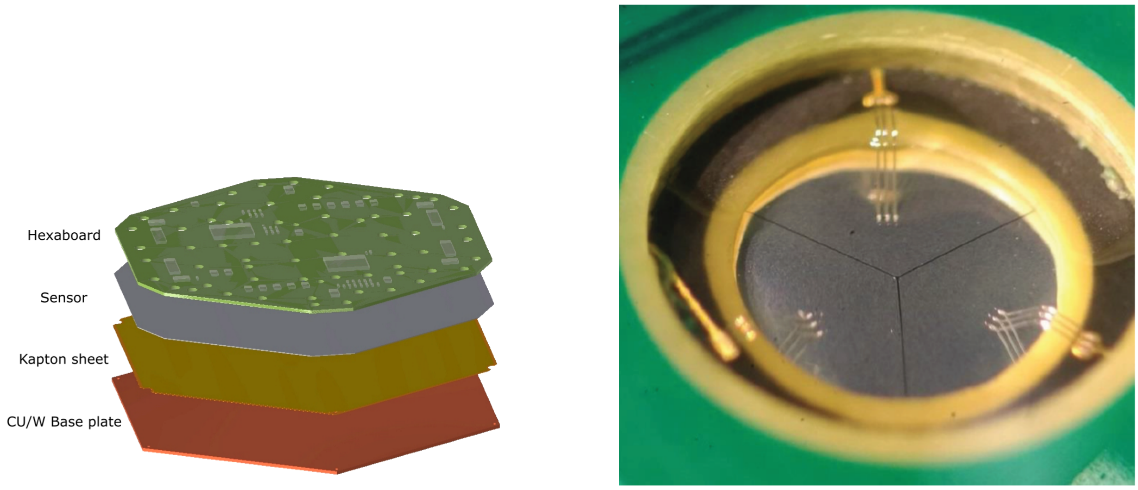

(a) (b)

Figure 3.4: Schematic drawing of the layers of a silicon module (a). A photo of a hole in the printed circuit board (so-called hexa-boad) to show the wirebond connection between the sensor pads and the readout chips. Figures from [8].

Additionally, there is an alternate absorber layer, which consists of two 2.1 mm thick lead plates clad with 0.3 mm stainless steel. Two lead plates surround the module-cooling plate-module sandwich on either side. Every layer of the before described structure is subdivided in 60° units and called *cassettes*. The 28 sampling layers are formed by 14 layers of these cassettes. A view of the plane of one sampling layer of the CE-E is shown in Figure 3.5. Six 60° cassettes are shown by alternating colours. The position of sensors with different sensor thicknesse are marked.

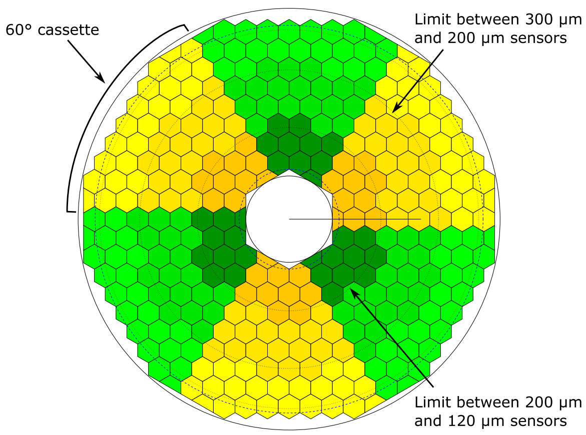

Figure 3.5: Front view of the schematics of a sampling layer of the CE-E showing only the silicon sensors. Figure from [8].

The CE-H features 12 planes of 35 mm thick steel absorber plates, where silicon modules on a cooling plate are in between the first 8 planes. The difference to the CE-E is, that there is a module only on one side of the cooling plate and not both. The remaining 4 planes are followed by another 12 steel planes of 68 mm thickness. Between these 16 layers silicon modules and plastic scintillator tileboards are mixed. Figure 3.3b shows the CE-H region and its division in a silicon and a scintillator region. These regions are defined by the radiation levels in the CE-H. In the scintillator region the maximum radiation levels correspond to a fluence of $8 \times 10^{13}\,\mathrm{n_{eq}/cm^2}$ and a dose of 3 kGy (= 300 krad). This is the chosen limit where the light loss in the scintillators is not more than 50 %.

The CE-E and the CE-H together have a total absorption length of 10.7 λ_I and a weight of 228 t.

3.3.2 Silicon Sensors

The silicon sensors have a thickness of 300 µm, 200 µm or 120 µm depending on the position in the CE. Close to the interaction point a higher fluence is expected in the CE, as shown in Figure 3.2, and therefore thinner sensors are used in comparison to the regions further away. Thinner silicon sensors have a higher charge collection efficiency at a certain radiation level in comparison to thicker ones. This behaviour is shown in Figure 3.6. The figure shows the amount of electrons, which are induced by minimum ionizing particles (MIPs), for different fluences and different sensor thicknesses and types. The amount of electrons is normalized to electrons per micro meter. In a not pre-irradiated sensor the MIP produces a signal proportional to the sensor thickness. But for heavily irradiated sensors charges get “trapped” and hence lost. This mechanism is further explained in 2.4.4. In thinner sensors the probability for the charges to get lost is smaller, which results in higher charge collection efficiency.

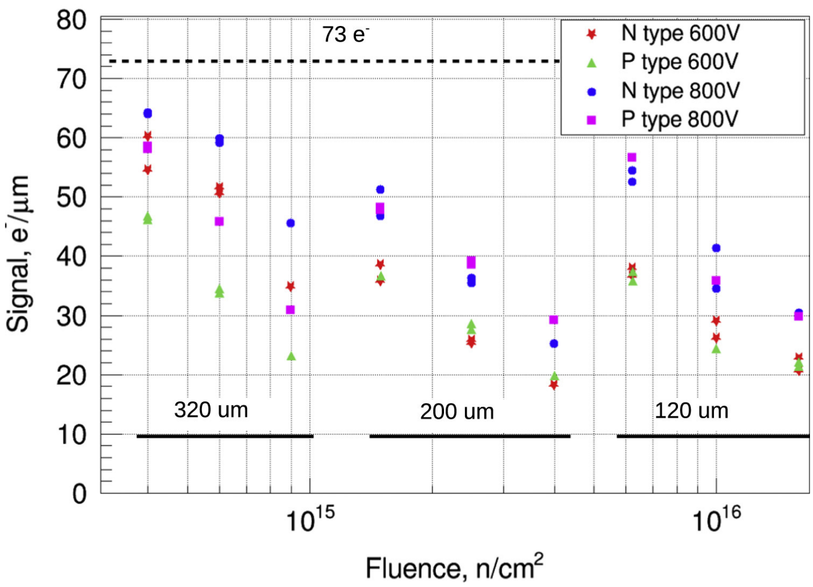

Figure 3.6: The signal for different neutron equivalent fluences is plotted for different sensor types and thicknesses. Thin sensors (e.g. 120 µm) deliver a higher signal in comparison to thick sensors at the expected HL-LHC fluences in the CE. Figure from [39]

The silicon sensors have a hexagonal shape with a width of 163 mm and are produced on 8-inch wafers. Each sensor is further segemented and has 192 or 432 smaller hexagonal pads (or cells) with a size of 0.5 cm^2 or 1 cm^2 depending on the sensor thickness. A representation of both sensor types is shown in Figure 3.7.

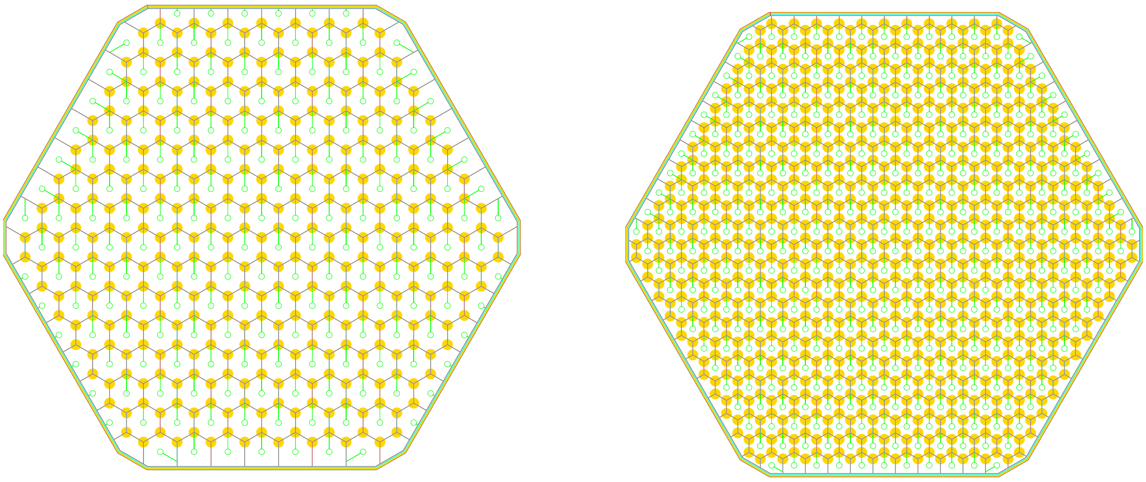

(a) (b)

Figure 3.7: Sketch of the 192 pad silicon sensor (a) and the 432 pad silicon sensor (b). Figure from [8].

Each of these pads is read out and forms a total channel number of almost 6 million. The total area covered by silicon sensors in both endcaps is about 600 m^2. The scintillator tiles are directly connected to and read out by silicon photomultipliers (SiPMs). They are located on a printed circuit board and together form so called *SiPM-on-tile* modules. Almost four thousand of such modules are implemented in the CE-H. The numbers of the active elements are summarized in Table 3.1.

Table 3.1: Quantity of the active elements of the High Granularity Calorimeter.

	CE-E	CE-H	
Material	Silicon	Silicon	Scintillator
Area (m^2)	368	215	487
Channels (k)	3916	1939	389
Si modules (tileboards)	16008	8868	3960
Partial modules	1008	1452	-
Weight (t)	23	205	
Si-only planes	28	8	
Mixed planes	-	16	

The detailed numbers for the properties and specifications of silicon sensors are listed in Table 3.2. They comprise information for example about cell size, the largest expected fluence after the full lifetime and the total number of silicon wafers required.

Table 3.2: Properties and specifications of the silicon sensors of the High Granularity Calorimeter.

Active thickness (μm)	300	200	120
Cell size (cm^2)	1.18	1.18	0.52
Number of cells	192	192	432
Cell capacitance (pF)	45	65	50
Bulk polarity	p or n	p	p
Initial S/N for MIP	11	6	4.5
Smallest S/N after 3000 fb^{-1}	4.7	2.3	2.2
Lifetime dose (Mrad)	3	20	100
Lifetime fluence (n$_{eq}$/cm^2)	0.5×10^{15}	2.5×10^{15}	7×10^{15}
Number of wafers	13164	8712	3000
Number of partial wafers	1284	144	324
Total number of wafers		26628	

With increasing irradiation during the HL-LHC phase, the silicon sensors need to be biased with higher and higher voltage. This is done to compensate the effects of irradiation damage in silicon, which will be explained at a later point in this work. It is foreseen to operate the silicon sensors up to a bias voltage of −800 V, which are applied on the back of the sensors. The cells on the front of the sensors are kept on ground potential by the on-module readout electronics. When the leakage current of a single cell is too high, for example due to electrical breakdown, then the cell cannot be read out anymore. Even in this case the readout chip will not be damaged. But the power supplies, which can deliver up to 10 mA [8], will have to be able to supply the increased current in case of cell break down. The maximum total leakage current of all sensor cells is 4 mA for sensors exposed to maximum fluence. A 120 µm thick sensor irradiated with a fluence of $7 \times 10^{15}\,\mathrm{n_{eq}/cm^2}$ at −30 °C has a leakage current of ≈ 3.6 mA, estimated with Equation 2.33 and 2.35. The sensors in the lower fluence regions draw much less current. Therefore it is possible to group several sensors together on the same power supply. A system is also foreseen to be able to disconnect faulty sensors from the power supply. To avoid sensor failure and early breakdowns it is important to have silicon sensors, which can operate up to 1000 V. The design, optimization and development of these silicon sensors for the HGCal was the core of the authors' doctoral thesis.

3.3.3 Front-End Electronics

The silicon module PCB, the hexa-board, has the readout chips mounted. The readout chips (HGCROC) are connected directly with the silicon sensor pads via wirebonds. In general, the front-end (FE) electronics measure and digitise the charge deposited in the silicon sensor pads, provide a high precision measurement of the time of arrival of the signal pulses, and transmit the digitized data to the back-end electronics located in the service cavern [8].

The on-module readout electronics, are capable of performing a leakage current reduction up to 20 µA per cell [8]. This reduction is needed, because the dynamic range of the analog to digital converter (ADC) on the readout chip is limited. The dynamic range from 0.2 fC to 10 pC is split into a linear range, read by a 10-bit ADC, and a time over treshold (ToT) range. The ToT range covers 100 fC to 10 pC on a 12-bit time-to-digital-converter (TDC), when the preamplifier saturates. For signals larger than 10 fC to 15 fC time of arrival (ToA) information is available as well [8]. This large dynamic range means, that it is able to measure MIP signals in the silicon sensor and that it is able to measure high-energy deposits from electromagnetic showers. To be able to detect MIPs, the electronic noise has to be lower than 2500 electrons for a 65 pF capacitance pad. The chip is also compatible with negative and positive input voltages, to be able to read out p-on-n and n-on-p sensors. Another requirement for the chip is that it is able to provide timing information with a precision better than 100 ps for signal pulses above 12 fC [8]. This value corresponds to the signal of about 3 MIPs in a 300 µm thick silicon sensor. Additionally, the HGCROC chip has to be able to withstand radiation levels up to 2 MGy and a fluence of $1 \times 10^{16}\,\mathrm{n_{eq}/cm^2}$. Therefore, the chip is manufactured in 130 nm CMOS technology.

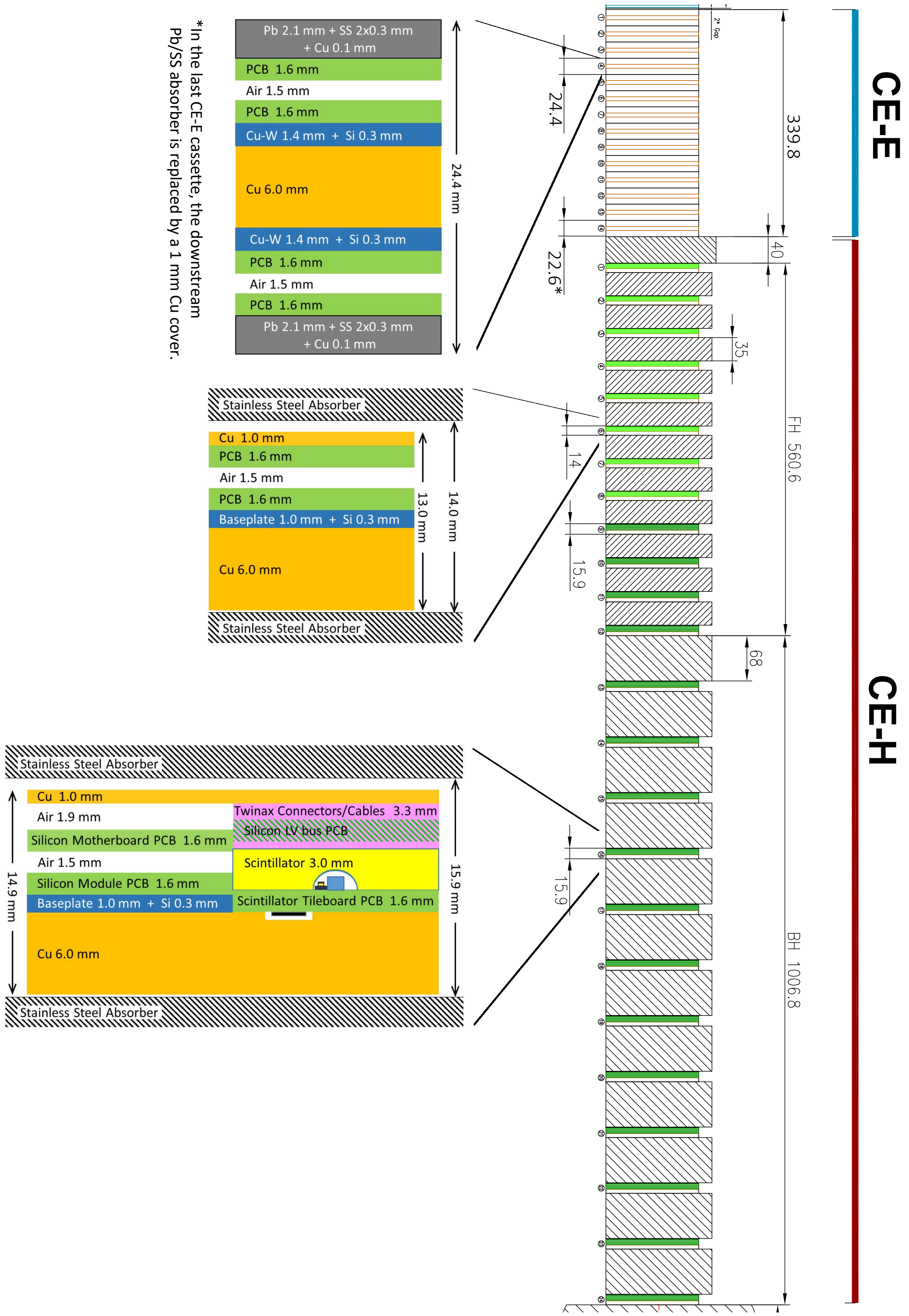

Figure 3.8: Longitudinal structure of the HGCal. The schematic cross sections of the CE-E, CE-H silicon sensor, and CE-H mixed silicon/scintillator cassettes are shown. Figure from [8].

4

Design and Layout of HGCal Sensors

4.1 Motivation and General Concepts

The HGCal project wants to use highly granular silicon sensors with a large area. Highly granular means that in the lateral direction the pad size is either $\approx 0.5\,\mathrm{cm}^2$ or $\approx 1.0\,\mathrm{cm}^2$. The high granularity in the transversal direction is achieved by using thin silicon sensors and stacking several layers of sensors successively. The reasons for the high granularity are described in 3.3. The number of channels of the new HGCal are about 6.1 million in comparison to about 76 k of the current ECAL in CMS.

The shape of the sensor is hexagonal and the pads in the sensor are hexagonal as well. A representation of the sensors is shown in 3.7. This is due to the fact that the sensors are produced on circular wafers and a hexagon is a tile-able polygon with the highest possible number of corners. This means that the area on the circular wafer is used most efficiently, which is an important aspect to reduce costs.

The hexagonal pads are individual diodes. The working principle of the diodes is explained in 2.3. The pads in the HGCal sensor need to be biased individually, as there is no common biasing scheme. High voltage is applied on the back of the whole HGCal sensor for all pads at the same time. Low voltage connections on each individual pad is realized by wirebonds as shown in Figure 3.4b. Each pad is DC coupled, meaning that the generated current from a signal is directly routed to the readout chip. The metal layer on each pad is directly connected to the silicon surface by holes in the silicon dioxide called metal vias. In contrast for example, in the CMS tracker silicon strip sensors are used, which have AC coupled strips [40]. In this case, the signal is capacitatively coupled from the silicon bulk to the metal pad, which is isolated from the bulk with a silicon dioxide layer.

Another determining factor of the design is the high voltage stability. Due to the nature of irradiation damage in silicon, the sensor operation voltage has to be increased over the years of operation. At the end of the HL-LHC lifetime the sensor is biased with 800 V, the limit of the currently foreseen power supplies. A decision about the exact bias system specification will be made in 2019 [8]. To have some margin, for example, in case of unexpected higher irradiation damage or too small signal to noise ratio, the sensors should be designed to withstand a bias voltage of 1000 V. To achieve this the periphery of the sensor consists of two guard rings and an edge ring. A single floating guard ring would be sufficient with regard of the breakdown stability. But to avoid a capacitative coupling of a signal in the outer pads to the floating guard ring and then to the other outer pads, so-called “square events” [41], the innermost guard ring is biased with the same potential as the pads. Typically they are grounded. The second guard ring is floating, meaning no voltage is applied. This is to achieve a high breakdown voltage by smoothing out the electrical field between the grounded guard ring and the high potential edge ring.

The sensors of the HGCal should be able to be calibrated by using MIPs. For this calibration purpose smaller cells, called calibration cells, are needed. Smaller cells have lower capacitance and hence a lower electronic noise. The calibration cell is realized by subdividing a normal hexagonal full cell in an outer and inner part. The inner part is the small circular or hexagonal cell with defined capacitance, which is used for MIP calibration. A figure of a calibration cell is shown in 4.6b

4.2 Sensor Design Framework

The programme used to develop the HGCal sensor design is Klayout [42]. It is a free open source software to view and edit GDS and the newer OASIS file formats. These are standard file formats for layouts of integrated circuits. The programme includes an development environment for ruby scripts, which the author used in the creation of the 8-inch HGCal layouts.
Klayout works on all operating systems and is still gradually enhanced and supported. New features can be requested aswell. But it already has some features other viewers don’t have. For example it allows the placement of two layouts over each other for comparison. Additionally, it is really precise meaning it shows the design as it is and the design is not changed when zooming in. At last, it is possible to make layers transparent or animate certain layers to blink, in order to highlight them. This is usefull when viewing a stack of layers. Layouts can be created by using the GUI of Klayout or using scripts. Klayout comes with an extensive documentation of the programme describing all methods and classes. Together with the user manual and example scripts it is possible to quickly learn how to create designs.

4.3 Main Sensor

For clarification of the nomenclature and the colouring scheme throughout this section, the region between two pads is highlighted in Figure 4.1. The layers throughout all different designs are coloured in the way indicated in the figure. It should be noted, that the passivation opening shown in Figure 4.1a is the area where no passivation layer is applied on the wafer. In Figure 4.1b the passivation layer is shown and the passivation opening is a blank space.

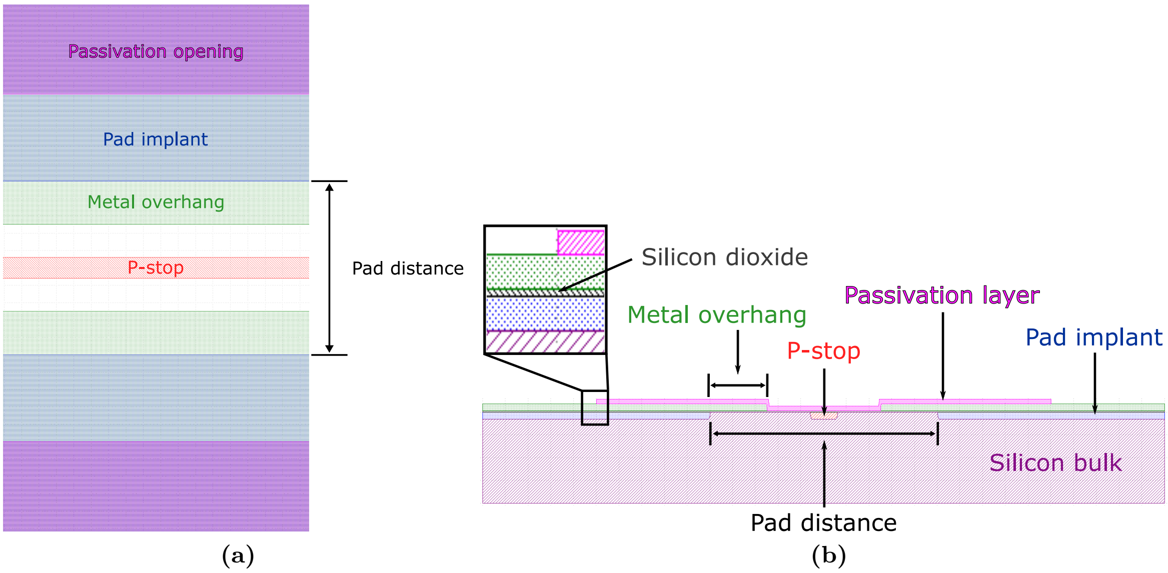

Figure 4.1: The region between two pads is shown. Top view of mask layers (a). Cross sectional view of the region, created with a Klayout script (b).

The structure of the periphery with its components is shown in Figure 4.2. The periphery consists of a biased guard ring, a floating guard ring, and an edge ring. A legend for the different colours can be found as well.

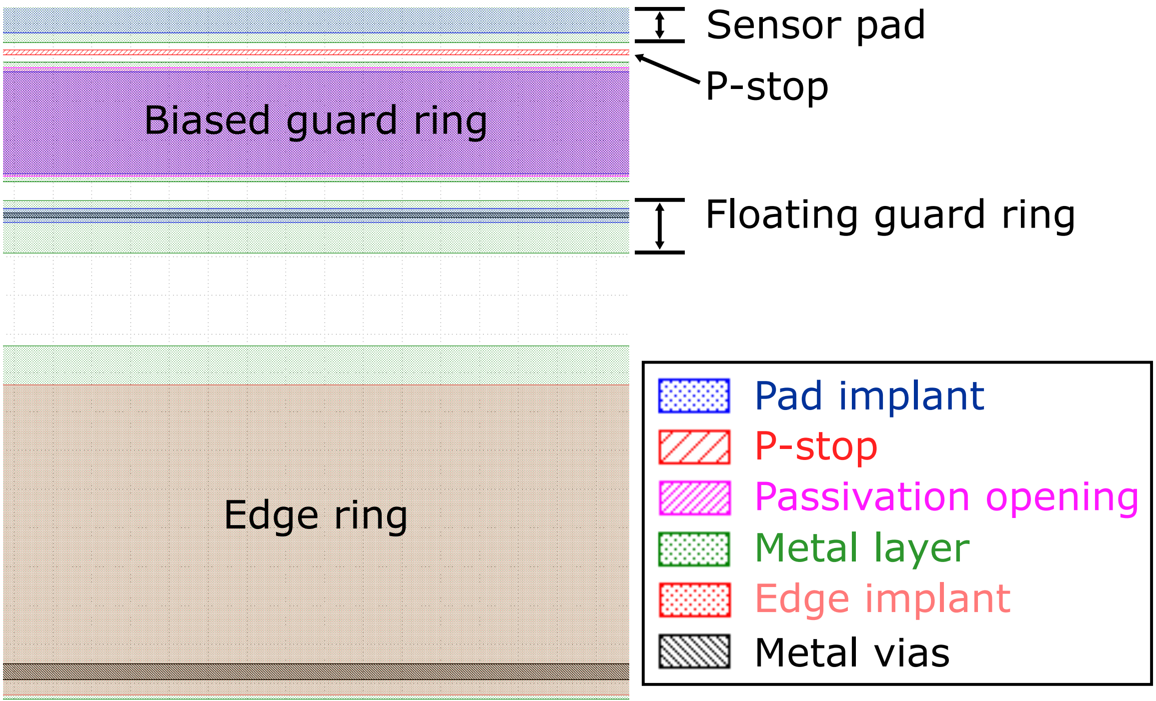

Figure 4.2: Top view of the periphery, as designed in Klayout. The pad area, two guard rings, and an edge ring is indicated.

4.3.1 6-Inch Prototypes

The first prototype of HGCal sensors were designed and produced by Hamamatsu Photonics K.K. (HPK) on 6-inch wafers as a proof of principle before the start of this thesis. Two variants with a different number of pads exist.

Figure 4.3a shows the design of the 134-pad version. The sensor has an incircle diameter of 12.49 cm, which is measured from the outer edge of the edge ring implant of one side to the other. Two of these cells are calibration cells, which are counted twice. The area of the full hexagonal pads is $\approx 1.08\,\text{cm}^2$. The outermost cells also consist of different cell types including half hexagons (four corner polygons) and pentagons at the mousebite area. The mousebite areas are the areas at each corner of the regular hexagonal sensor which are missing. The sensor is glued onto a hexagonal baseplate in module construction (see Figure 3.4a). The baseplate area, which is not covered by the sensor is needed for screws in the tiling of the sensor modules. Additionally, this design has four quadrants with four different pad distances (20 µm, 40 µm, 60 µm, 80 µm). Pad distance is referred to as the distance between the edge of the pad implant of one pad to the edge of the pad implant of its neighbouring pad.

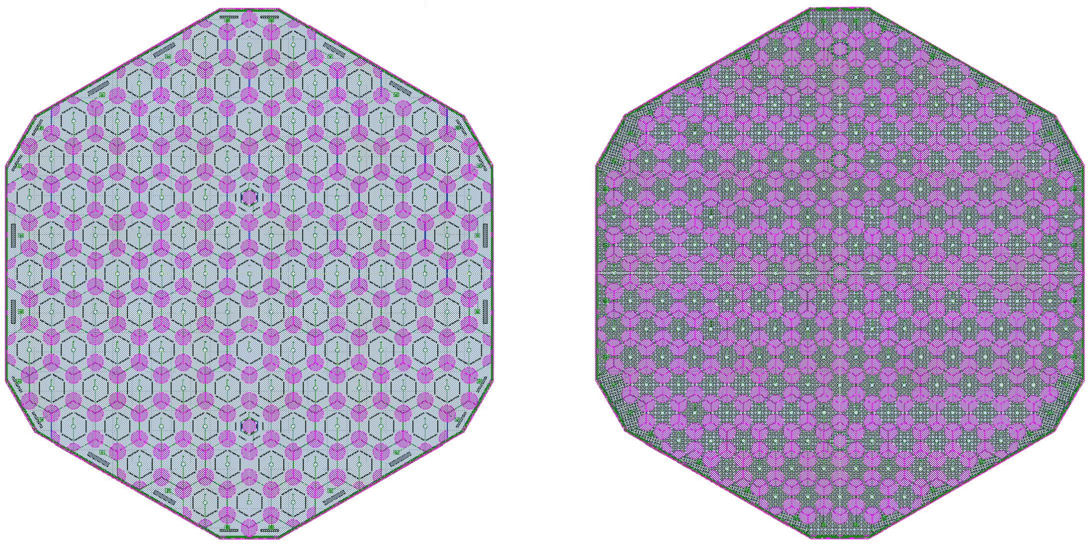

(a) (b)

Figure 4.3: 6-inch prototype designs from HPK. Figure a) shows the design with 134 pads, where 2 pads called calibration cells were counted twice. Each full hexagonal pad has an area of $\approx 1.08\,\text{cm}^2$. Figure b) displays a design with 239 pads, 4 of which are calibration cells. The full cells feature an area of $\approx 0.58\,\text{cm}^2$.

Figure 4.3b displays the design of the 239 pad 6-inch prototype. The outer dimensions of this sensor type are identical to the previous prototype version. This version contains four calibration cells, which are again counted twice. The pad area of the full cell is $\approx 0.58\,\text{cm}^2$. The deviation from the regular hexagonal form and reason for the mousebites is the same as for the previously described design. This design version has two halves with two different full cells with pad distances of 30 µm and 50 µm.

4.3.2 Demonstrator on 8-Inch Wafers

In the technical proposal initially only 6-inch wafers were available. Due to the development of 8-inch demonstrator sensors presented in this thesis together with the efforts from the CMS Tracker group with Infineon [43][44], the 8-inch sensors have become the new base line for the HGCal sensors. The advantage of the 8-inch sensor is that fewer sensors and modules are needed, which greatly reduces cost. The area of the 6-inch sensor is only $\approx$ 56 % of the area of an 8-inch sensor.

The first 8-inch demonstrator design, completely designed by the author, is shown in Figure 4.4. The design incorporates the main sensor in the middle and test structures on the outside of the turquoise lines. These lines are called dicing lines. Purple areas are the passivation openings, which are the areas where the sensor pads can be contacted. The blue area denoting the pad implantation is overlayed with a green layer representing the metal layer. The black (or darker) areas are the contact areas, which are the metallic connection between the silicon bulk and the metal layer. In contrast to the 6-inch designs the contact areas have an area as large as possible. Its area is restricted by holes in the metal layer or the passivation openings. Red areas represent the edge ring implantation. This design contains 237 pads, out of which two are calibration cells which are counted twice. The area of the full cells is $\approx 1.00\,\mathrm{cm}^2$. The incircle diameter of the sensor hexagon is 16.307 cm. Four quadrants with different pad distances are implemented by having cells of slightly different size. The centres off all cells are positioned on a uniform grid. The pad distances are 21 µm, 40 µm, 60 µm and 80 µm.

The design has been realized by Infineon. A photograph of the produced wafer, containing the main sensor in the middle and test structures on the outside is displayed in Figure 4.5.

Each pad is labelled with a number to make identification and distinction of the pads easier. In the sensor several different types of cells are implemented. The full pads are displayed in Figure 4.6a and the calibration cells in Figure 4.6b. Both cell types have a hole in the centre of the metal layer with a diameter of 1000 µm. This allows signal measurements with a laser. The purple circular sectors with 120° central angle and a radius of 1500 µm are located at every corner of the pad and represent the passivation openings. This configuration is chosen because it enables the wire bonding of three pads through a single hole in the readout board, which is placed directly on top of the sensor. The aforementioned numbering of the pads is visible at the bottom of both pads in Figure 4.6. The digits have a height of 500 µm and can even be read with the naked eye. Under the microscope it is, of course, more easily readable.

When looking at Figure 4.7, two additional different cell types can be identified at the sensor border. The number of pads, the area of pads, and the total sensor area are balanced in

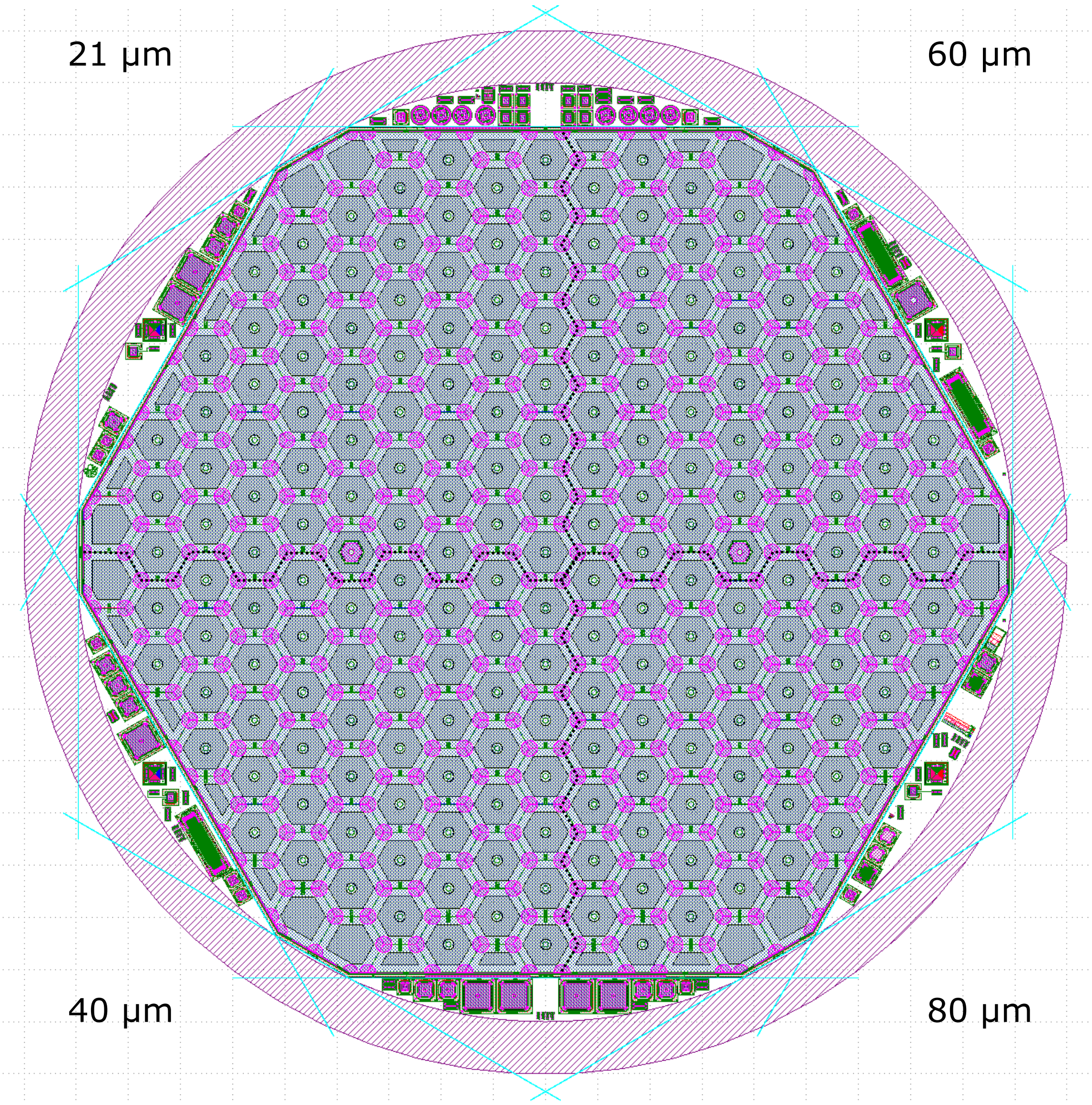

Figure 4.4: Layout of the first version of the 8-inch HGCal wafer as designed by the author. The main sensor forms a regular hexagon but with truncated tips. On the outside area several different test structures are placed. Four different quadrants with different pad distances exist and are separated in the figure by a black dotted line. The turquoise lines are dicing lines and the rest of the colour coding of the different layers is the same as for both 6-inch designs.

such a way in this design, that one cell type at the border is exactly one half of a regular (full) hexagon. The half hexagon is highlighted with blue lines. In the border region the half pads and full pads alternate. This order is interrupted in the mousebite region by introducing irregular hexagonal pads, where two of the six corners are shifted. The resulting new area is $\approx 0.99\,\mathrm{cm}^2$. This solution is chosen to avoid smaller ($\approx 0.025\,\mathrm{cm}^2$) triangular pads, one of which is indicated with red lines. Working with pads of that size causes unnecessary problems, because testing of such small pads becomes more difficult

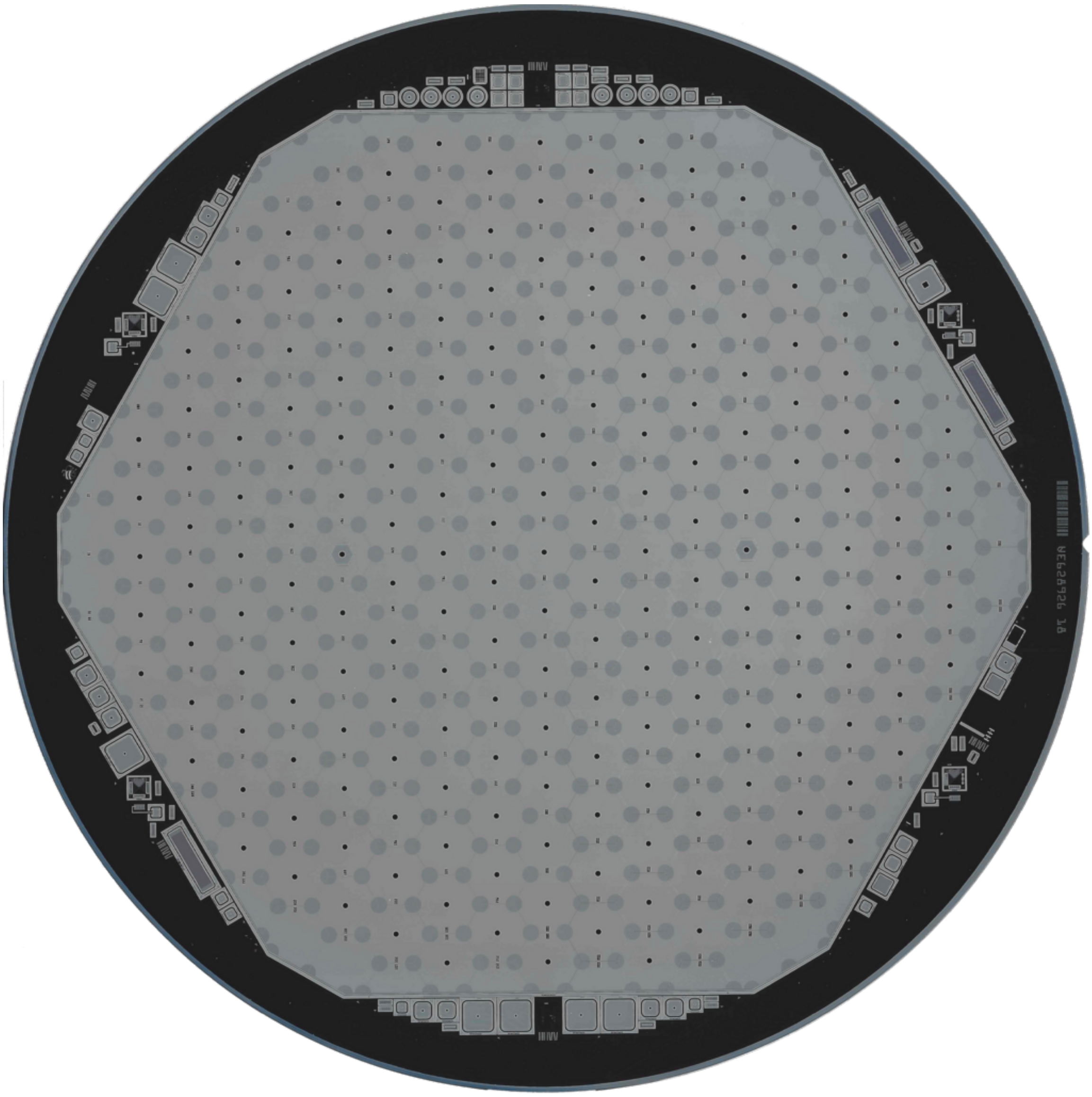

Figure 4.5: Photo of the demonstrator of the 8-inch HGCal wafer produced by Infineon.

and the increased channel number imposes more difficulties for the design of the read out electronics. In each mousebite corner such a irregular hexagonal pad and its mirrored version are implemented.

It has been mentioned that four quadrants of different pad spacings exist in this design. This leads to a slightly different area of the full pads. To achieve an equal distance of 62 µm between the implant of all of the outermost pads and the implant of the innermost guard ring, the geometry of all border cells is slightly adjusted. Consequently, a total number of 8 different versions of the mousebite pads are implemented. For the half hexagons and the full hexagons at the border 4 versions of each type are required.

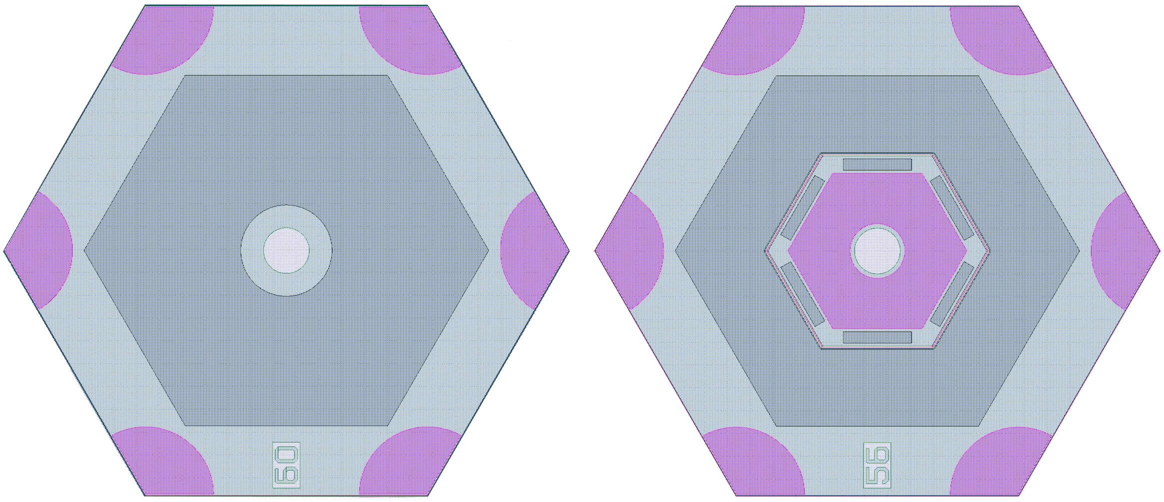

(a) (b)

Figure 4.6: A full cell in the first 8-inch demonstrator design is shown (a). The calibration cell with the small pad on the inside is displayed (b). In the middle of both pads is a 1000 µm diameter hole to enable signal measurements with a laser. The passivation openings in the shape of a circular sector with 120° central angle and a radius of 1500 µm are positioned at each corner of the hexagon.

Figure 4.8 shows an enlarged view of the periphery of the sensor. The blue area on top is the implantation of the outermost pad of the sensor. Next to the pad is the inner guard ring, which is mostly covered by a passivation opening at this part of the sensor. This area is needed to contact the inner guard ring and bias it to the same potential as the pads during measurements. Right next to it is the floating guard ring, which does not need to be contacted and can therefore be made thinner. At the bottom, the outermost ring called edge ring can be seen with an implantation layer in red. The green layer on top is the metal. With openings in the metal layer, texts and labels can be printed on the sensor.

One of the main principles of the sensor design is the high voltage stability. Therefore, one of the methods to implement this feature in the design is by having a so called metal overhang. With increasing metal overhang the electric field maxima near the pad implants are pushed into the silicon dioxide. This is useful, because the break down field in silicon dioxide ($\approx 9.5\,\mathrm{MV\,cm^{-1}}$ [45]) is one order of magnitude higher than in silicon ($\approx 0.3\,\mathrm{MV\,cm^{-1}}$ [28]). As it will be shown in Chapter 5, the metal overhang should be higher than 5 µm, but depending on the pad distance not much higher. These metal overhang values in the design are taken into consideration. More details are shown and explained by simulations in Chapter 5. Figure 4.8 shows the periphery, which has metal overhang implemented at each side of the sensor pad, guard rings, and edge ring.

For a separation of the pads, each pad is surrounded by a 6 µm thick ring of edge ring polarity implant (= p-type for p-type sensors). It is called p-stop and is only needed for p-type sensors and not for n-type sensors. The doping concentration is higher than the bulk doping concentration but lower than the pad and edge ring implantation. A concentration of

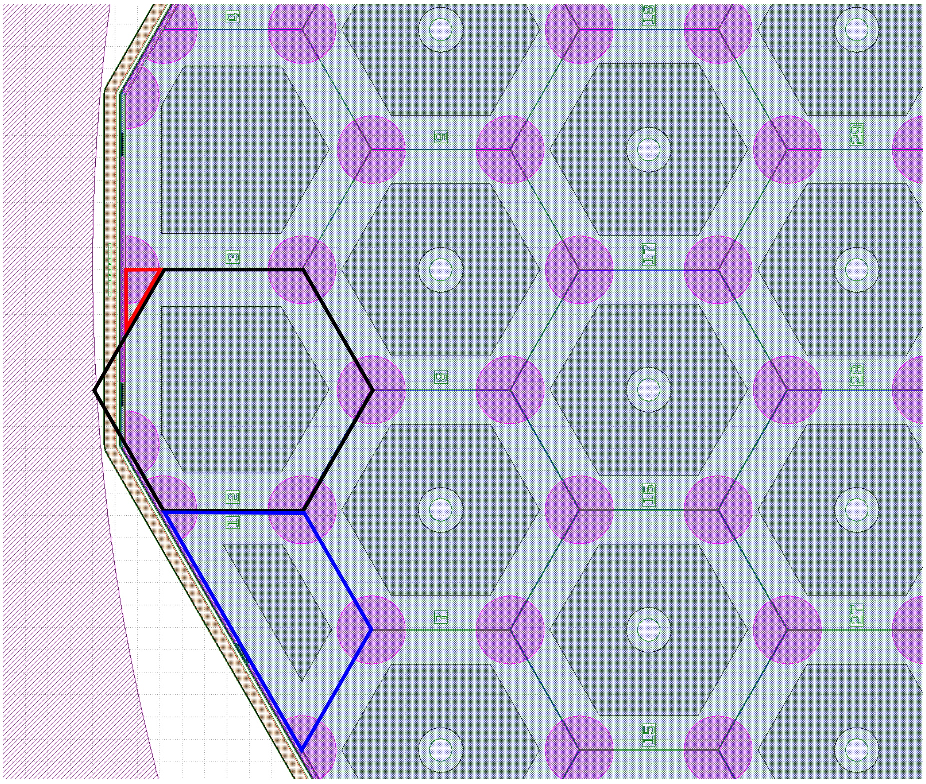

Figure 4.7: Enlargement of the mousebite area of the sensor. Cells closest to the mousebite have six corners but are not in the shape of a regular hexagon. Another cell type is highlighted with blue lines. It has four corners and corresponds to the half of a regular hexagon.

$\approx 1 \times 10^{16}\,\mathrm{cm}^{-3}$ has been shown to work best in [46]. In Figure 4.8 the p-stop is displayed as the bright red line between the pad and the inner guard ring.

In the areas where three full pads meet, the p-stop configuration is shown in Figure 4.9. In the design two different p-stop masks are implemented for different sensor splits. A sensor split is a predefined process variation of the ordered prototype sensors. For example, the doping concentration of various layers or the mask of the p-stop are varied. In process development this is a typical way to find the best solution. Figure 4.9a shows a single p-stop implantation between all pads. This is typically called p-stop common, as both pads have a common p-stop. The second configuration is called p-stop atoll, where each pad has its own p-stop ring.

4.3.3 Prototype Design for 8-Inch Wafers

After the design and production of the first 8-inch demonstrator wafer, many simulations have been performed to optimise the geometry. Additional changes in the test procedures and the tiling of the HGCal sensors lead to many changes, like the change in the pad number. The prototype design incorporates all changes and is shown in Figure 4.10. In

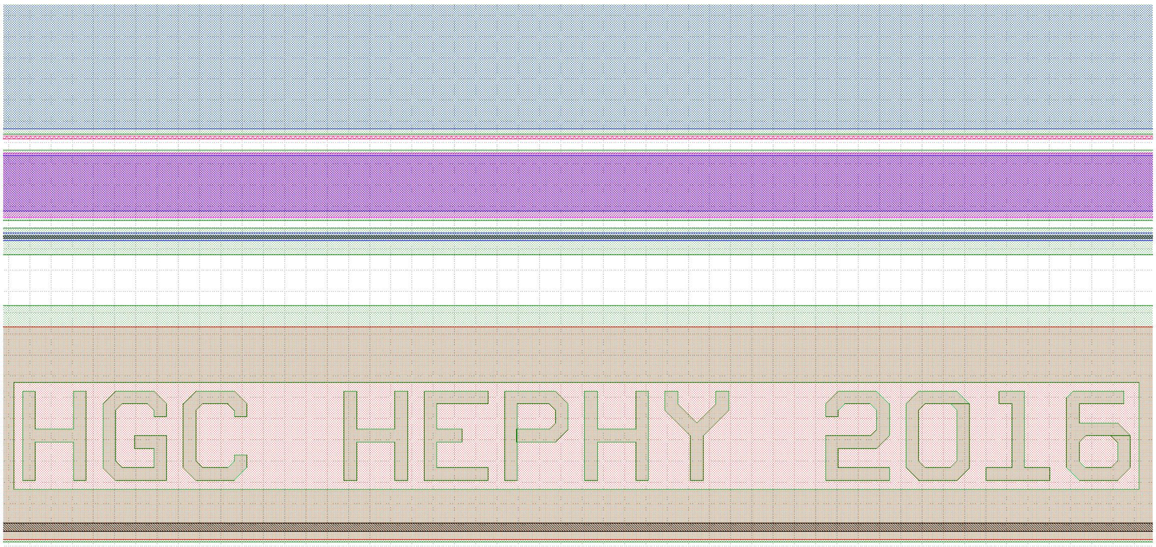

Figure 4.8: Enlarged view of the periphery of the first 8-inch demonstrator sensor. The label in the metal layer of the edge ring is visible as well. Location of the sensor pad, guard rings, and edge ring is indicated in 4.2.

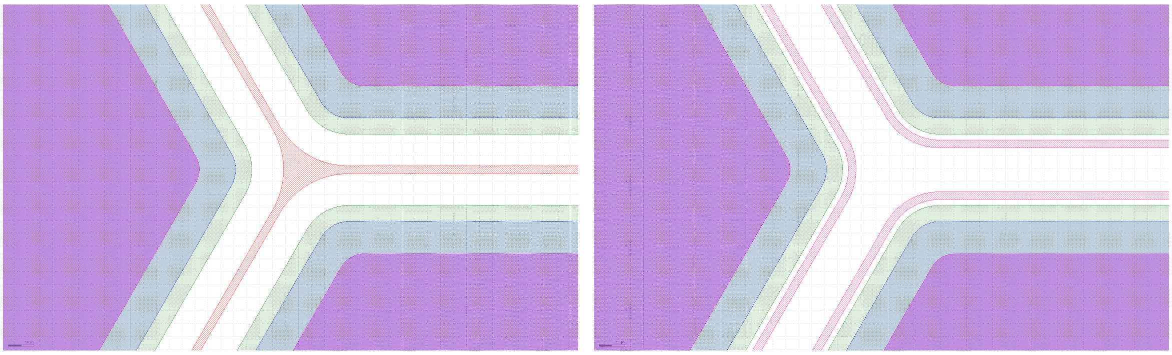

(a) (b)

Figure 4.9: Enlarged view of the area, where three pads meet. In the case when p-stop is in the middle of two pads it is called common p-stop (a). When both pads have a separate p-stop it is called p-stop atoll (b).

general it is similar to the previous 8-inch design, but many details differ. It features 198 pads, out of which 6 are calibration cells.

This design does not have quadrants with different pad distances but has only one fixed pad distance of 50 µm. Therefore all full hexagonal pads and the outer part of the calibration cells have the same size. The area of the implant of the full cell is $\approx 1.25\,\mathrm{cm}^2$. The distance between the outer pads and the periphery is the same distance as well. Taking a closer look at the full cell shown in Figure 4.11a, it can be seen that an additional contact pad is above the centre of the pad. The purpose of this pad is to facilitate the measurement of all pads with its neighbours on the same potential with the least amout of different probe

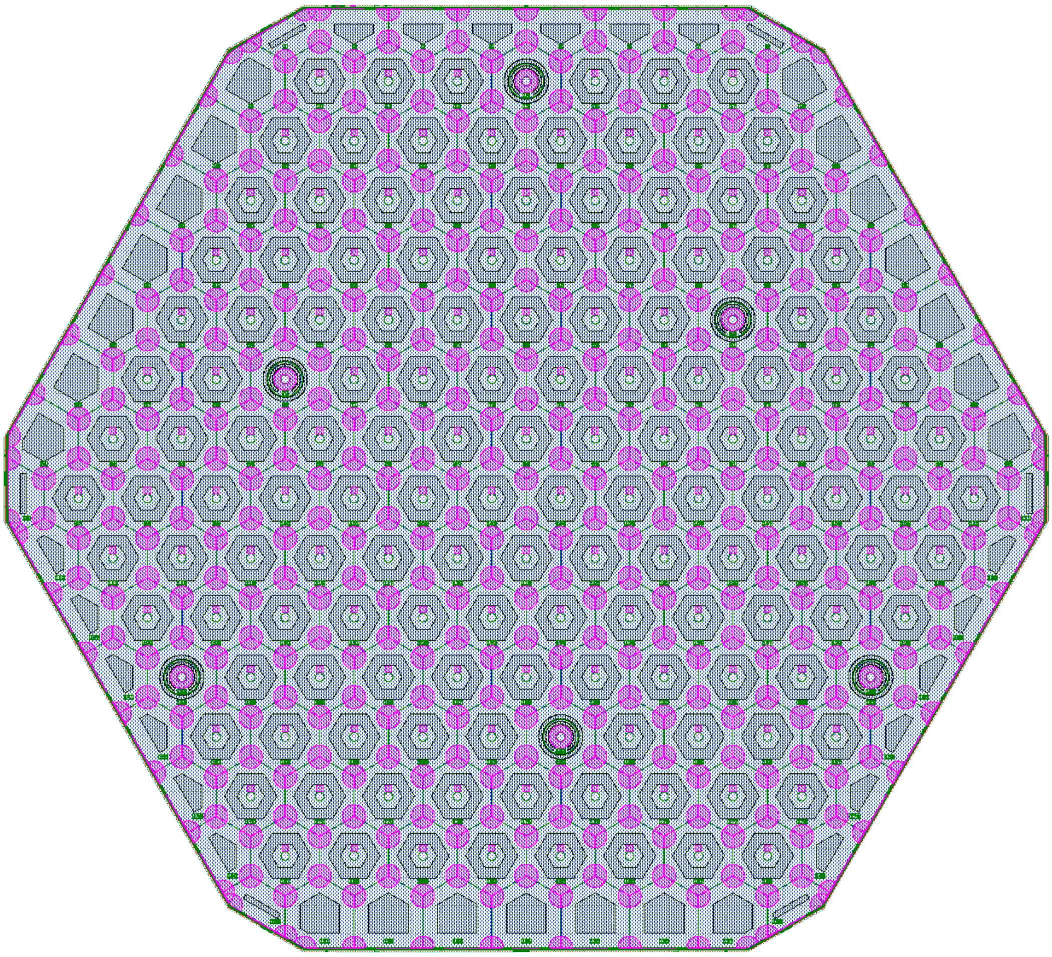

Figure 4.10: Layout of the prototype design for the 8-inch HGCal sensor. The sensor has 198 pads including 6 calibration cells.

cards needed. Another change in comparison to the old 8-inch design is that the contact pads at each corner of the hexagon have a larger radius of 2000 µm. It makes contacting the pads with a probe card easier. To ease laser signal measurements the metal hole in the centre of the pad is increased to a diameter of 1500 µm. Additionally, the height of the numbers in the labels is increased to 600 µm to improve readability with the naked eye.

The calibration cell, displayed in Figure 4.11b, is subdivided in a outer and inner part. The inner part is labelled with a number in this new design as well. Furthermore, the inner part is round and its metal layer has a diameter of 6076 µm. This size is chosen to get a defined

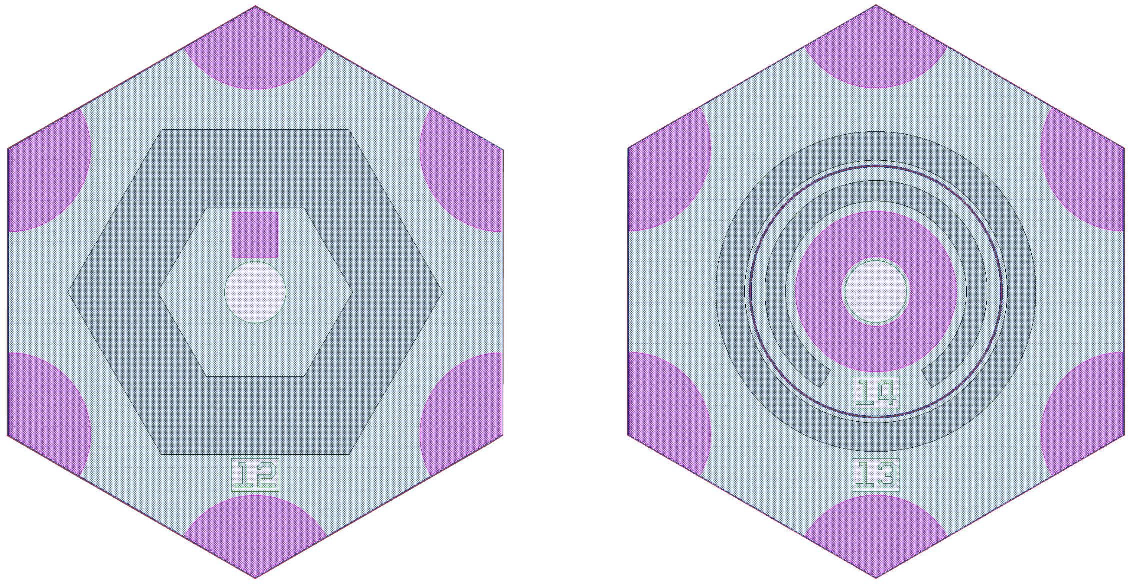

(a) (b)

Figure 4.11: A full cell in the optimised 8-inch prototype design is shown (a). The calibration cell with the small pad on the inside is displayed (b). In the middle of both pads is a 1500 µm diameter hole to enable signal measurements with a laser. The passivation openings in the shape of a circular sector with 120° central angle and a radius of 2000 µm are positioned at each corner of the hexagon.

cell capacity of 15 pF for 200 µm thick sensors.

The number and position of calibration cells is not random. It is chosen based on the number and position of the readout chips (HGCROC front-end readout ASICs) of the readout board (also called hexaboard) which is placed on top of the sensor in a module. Figure 4.12 shows an overlay of the readout chips with the metal routing to the sensor pads on top of the sensor design. In a module the signals from the sensor pads are directly digitized on board in the readout chips. It can be seen that three readout chips make use of the 120° symmetry of the design. In each symmetric third one calibration cell is positioned in front and one in the back of the chip. In this hexaboard overlay the routing to the calibration cell is not implemented, as it was used to define the calibration cell positions first.

The border cells in the design have five corners and two different types exist. One is 15 % smaller than the regular hexagonal cell the other is 15 % larger. Each side of the sensor hexagon is filled by either only larger or only smaller border hexagons. In the mousebite region special cells exist and separate the different border hexagons. It has to be noted, that additionally the width of the periphery and the sensor gap is cut away from the border cells. The sensor gap is the distance between the sensors when the modules are tiled in the calorimeter and has a value of 1000 µm. Hence, after tiling of the sensors, the cells form a uniform global hexagonal grid, which should help signal reconstruction. This is shown in Figure 4.13. The geometry of the special cells in the mousebite region is defined by the

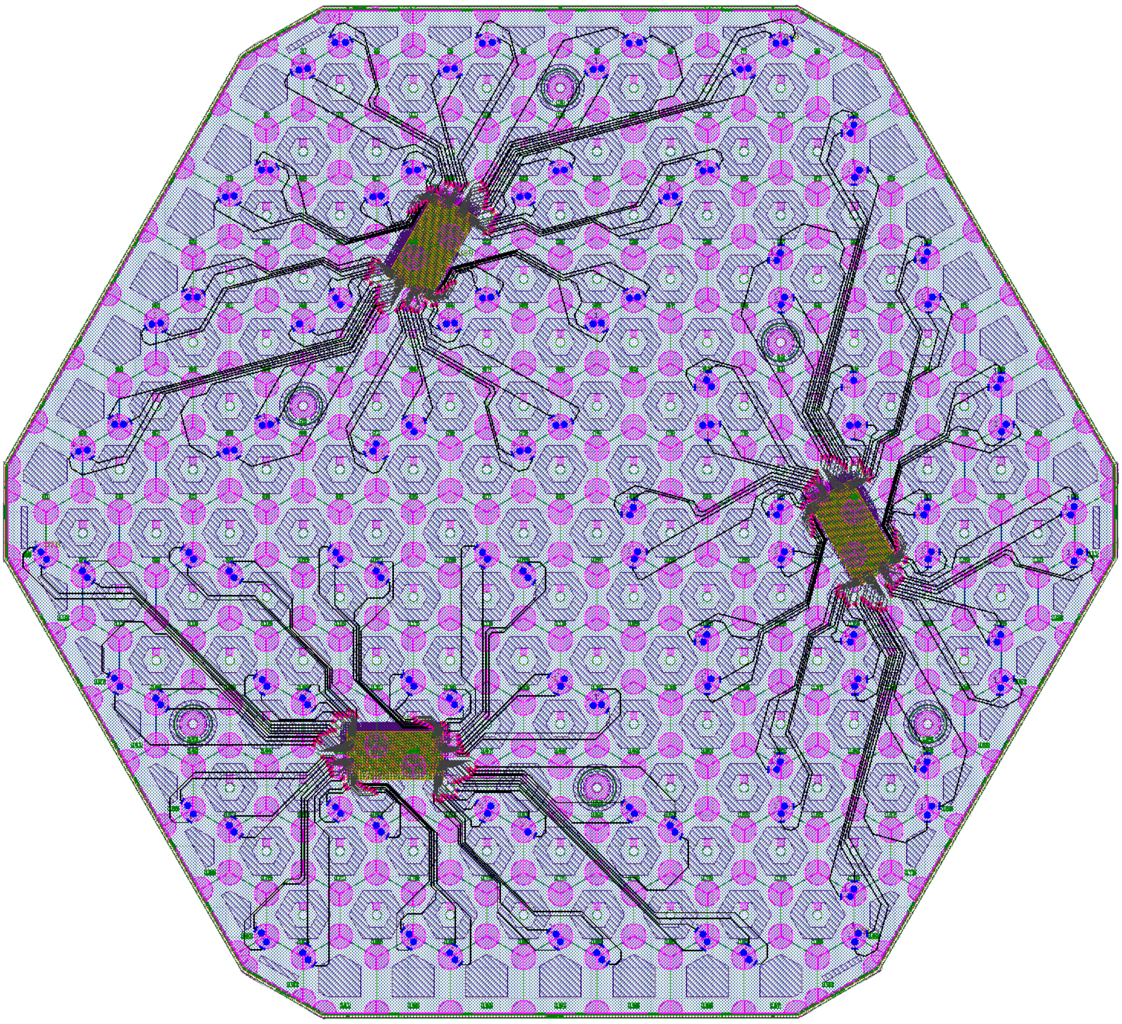

Figure 4.12: Display of the optimised 8-inch design with overlaid positions of the readout chips (HGCROC) and provisional metal routing (black lines) of the readout board (hexaboard). The position of the readout chips determine the position of the calibration cells. One is in front and one is behind the chip. Metal routing between the calibration cells and the readout chip is not included in this overlay, as this hexaboard design was chosen to determine the calibration pad position afterwards.

size of the truncated tips of the sensor. It is chosen in such way that, after tiling of the sensors, the distance between the outer edge of the edge ring and the centre of the three tiled sensors is 5000 µm. In Figure 4.13 this space is highlighted by a red circle having a radius of 5000 µm.

The p-stop geometry is similar to the old 8-inch design. Two variants are implemented, namely the p-stop common and the p-stop atoll. The thickness of the p-stop implantation is 6 µm in both cases. In the periphery, between the border pads and the inner guard ring, the same p-stop geometry is realised as between the sensor pads. Figure 4.14 displays the periphery of the optimised 8-inch design. The red lines denote the p-stop lines, in this case

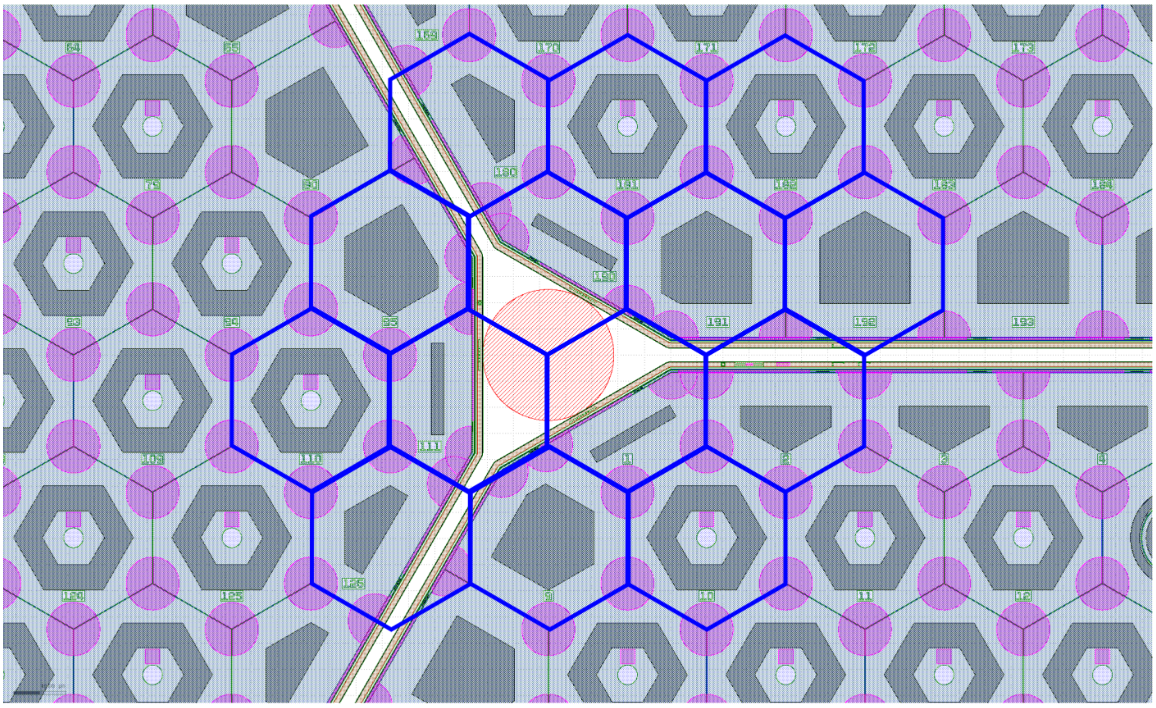

Figure 4.13: Tiling of sensors influence the design of the sensor itself. Three sensors with a distance of 1000 µm to each other are placed. The rows and columns of sensor pads are continued when going from one sensor to the next. A global uniform sensor pad grid should help with signal reconstruction.

p-stop atoll. The width of the whole periphery ranging from the edge of the implant of the sensor pad to the outer edge of the edge ring has a width of 853.5 µm in comparison to 967.5 µm of the previous 8-inch design. This can be traced back to the reduction of the width of the edge ring by about 100 µm. Unchanged to the previous design is the need for two guard rings. What changed is the detailed geometry of the guard rings according to the results of the breakdown simulations shown in Chapter 5. The essential biasing of the inner guard ring during sensor measurements can be performed on contact pads (passivation openings) with a width of 140 µm. This should be sufficient for wire bonding in the module or manual contacting with a needle under a microscope.

At the time of writing this thesis the optimised 8-inch design with 192 (or 198 with calibration cells) pads is being manufactured by different vendors. It is currently the base line design for the HGCal project and will most likely be used in the final realisation of the endcap. The 432 pads sensor version used for the 120 µm thick sensors will be designed and manufactured at a later time.

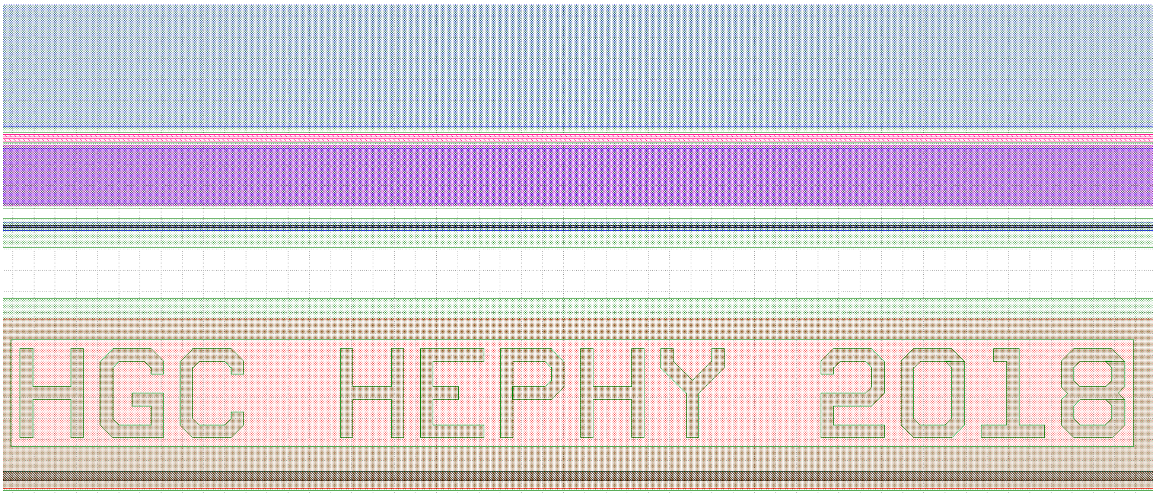

Figure 4.14: Enlarged view of the periphery of the optimised 8-inch prototype sensor. The label in the metal layer of the edge ring is visible as well. Location of the sensor pad, guard rings, and edge ring is indicated in Figure 4.2.

4.4 Test Structures

Figure 4.4 shows the design of the whole first 8-inch HGCal wafer demonstrator. The surrounding space next to the main sensor is used by teststructures or alignment marks. The teststructures are needed to characterise sensor properties without measuring the main sensor directly. Usually measuring test structures is faster and imposes less risk in comparison to the measurement of the main sensor. With dedicated test structures the extraction of specific parameters is often easier and more accurate. The production of the wafers happens in several lithography steps, which require the designed masks of each layer. These masks have to be aligned within a few micro metre precision in respect to each other. These alignment structures are implemented by the manufacturer and are not discussed further.

The most important test structures are diodes, because the pads of the HGCal sensor are diodes as well. In Figure 4.15 rectangular diodes of different size are shown. The three diodes have the same periphery with a width of 920 µm but a different pad implantation width of 1250 µm (4.15a), 2500 µm (4.15b) and 5000 µm (4.15c). The last diode shown in Figure 4.15c is often referred to *Diode-Large* throughout this thesis.

Diode test structures are used to perform voltage-current (IV), voltage-capacitance (CV) and charge collection efficiency (CCE) measurements. All measurements are in reverse biasing direction, as this is the way to operate the sensors. From the IV measurement on a test structure diode, the volume current can be calculated, which should be the same for all diodes spread across the wafer. Typical IV curves look like the one shown in Figure 2.3. This design of the standard test structure diodes exists on other CMS designs as well for comparison and has been chosen to be very robust with regard to high voltage. Having diodes with premature breakdown (before 1000 V) indicate process problems at the level of

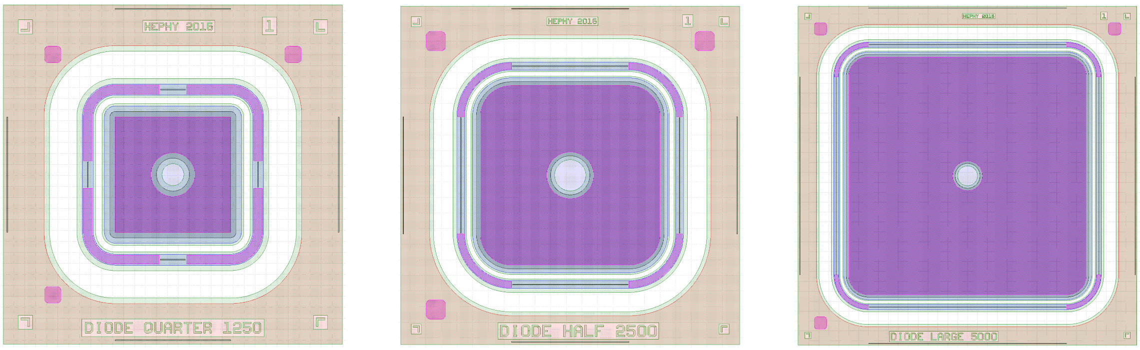

(a) (b) (c)

Figure 4.15: Layout of diode test structures of different sizes. Diode (a) has a pad implant width of 1250 µm. The structure in (b) has a width of 2500 µm. The largest rectangular diode shown here has a pad implant width of 5000 µm and will be referred to as *Diode-Large* throughout this work (c). In all three cases, the periphery containing a guard ring and an edge ring is 920 µm from the edge of the pad implant to the outer edge of the edge ring implant.

the manufacturer or simply mechanical damage like scratches. Irradiation studies are usually performed on diodes with this design. The increase of leakage current with irradiation can be determined on these small structures in the same way as for larger main sensors. Measuring larger irradiated sensors requires a more sophisticated measurement setup, as the whole sensor has to be cooled down equally across the whole surface to temperatures of typically −20 °C to reduce the leakage current.

The CV measurement performed on the diodes is used to determine the capacitance and the full depletion voltage V_{FD}. From the full depletion voltage the resistivity of the wafer material can be characterised by Equation 2.24. Figure 6.13 shows the result of an exemplary CV measurement on diodes of type *Diode-Large* of different thicknesses. One established way to determine the full depletion voltage is to take the intersection of two fit lines in the $1/C^2$ representation of the CV measurement. Determining and knowing the full depletion voltage in the irradiated case is of utmost importance, because the bias voltage for the HGCal sensor operation can, currently, only be increased to 800 V. If full depletion voltages are determined to be much higher than that in irradiation studies, the sensors will not be able to cope with the fluence level after 10 years of HL-LHC operation.

The last typical measurement method on diodes is the charge collection efficiency (CCE) measurement. A laser, or a radioactive source, or a particle beam can be used to induce a signal in the sensor. In unirradiated sensors the measured charge is very close to the induced charge. But for irradiated sensors the measured charge decreases more and more with fluence. Section 6.2.3 will highlight this measurement method in more detail.

Next to the rectangular diodes, round diodes are implemented. Using round diodes eliminates unwanted effects originating from the geometry, like higher electric field density in the corners of the rectangular diode. Simulating a complete round diode can also be accomplished in an efficient way by using only two dimensions and the rotational symmetry. Simulating the geometric effects in a rectangular diode would require an elaborate three dimensional simulation. Figure 4.16 shows three different types of round diodes. Figure 4.16a shows a round diode variant with a pad diameter of 2000 µm. The periphery dimensions of this diode are identical to the ones of the rectangular diodes. This type of test structure diode exists only on the first 8-inch wafer demonstrator version in four different versions, where the metal overhang of the pad and the p-stop is varied. Another round diode variant shown in 4.16b is only present in the optimised wafer prototype version. It is used together with 4.16c to investigate the influence of the periphery implemented in the main sensor. Both versions have a pad width of 4000 µm but only the latter sensor (4.16c) has both guard rings implemented. The goal is to check the periphery of the main sensor.

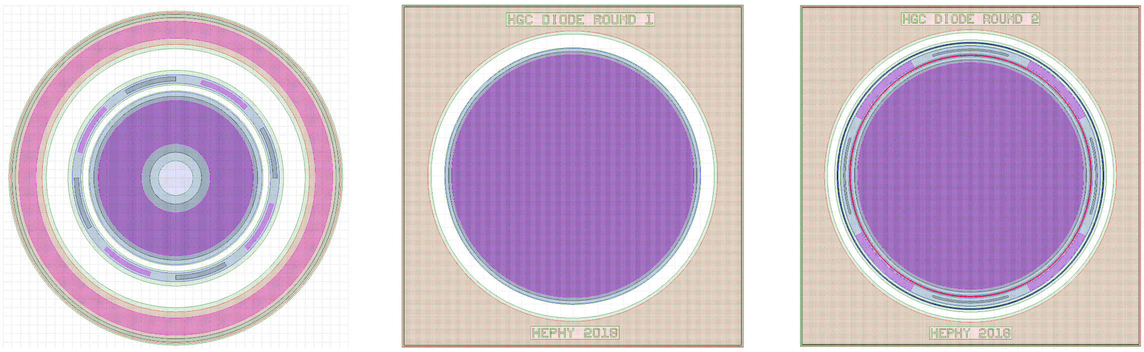

(a) **(b)** **(c)**

Figure 4.16: Layout of round diode test structures with different size and periphery. The diode in (a) shows a round diode with pad implant diameter of 2000 µm. The round diode in (b) shows a pad with diameter 4000 µm and no guard ring. This test structure is on the optimised 8-inch design wafer. In comparison, the structure in (c) has the same pad diameter but has the same periphery as the main sensor in the optimised design.

The next three test structures, shown in Figure 4.17 can be found on both 8-inch prototype designs. The first (shown in Figure 4.17a) is called a metal-oxide-semiconductor (MOS). It consists of a metal pad of width 2000 µm in the centre. In comparison to the diode the pad area does not have an implantation beneath the metal. The MOS with the design here are typically measured by applying a voltage ramp from about $-10\,\mathrm{V}$ to $10\,\mathrm{V}$ on the metal pad electrode and ground potential on the back. During this voltage sweep the capacitance is measured. From the course of this curve the flat-band voltage V_{fb} and the oxide capacitance C_{ox} can be extracted. The flat band voltage is the voltage, which can compensate the electric field generated by the fixed oxide charges [47]. The oxide capacitance is the capacitance of the MOS structure in accumulation. Accumlation is the condition, when majority carriers (holes in p-type) are accumulated below the oxide when applying voltages lower than flat band voltage (e.g. $-10\,\mathrm{V}$ for p-type bulk MOS). In this case, the thickness of the dielectric, which is seen in the capacitance measurement, is only the one of the oxide. Using this capacitance the thickness of the oxide can be determined with the parallel plate capacitance equation. The fixed oxide charges Q_{f} can be calculated with the measurement of the flatband voltage by Equation 4.1 [48]. The fixed oxide charge is an important parameter in the simulation of the periphery or the region between two sensor pads.

$$Q_f = C_{ox}(\phi_{ms} - V_{fb}) \tag{4.1}$$

$\phi_{\mathrm{ms}} = \phi_{\mathrm{m}} - \phi_{\mathrm{s}}$ is the metal-semiconductor work function difference. For metals, $q\phi_{\mathrm{m}}$ is in the order of 2 eV to 6 eV [21]. The semi-conductor work function ϕ_{s} is temperature and doping concentration dependent and given by Equation 4.2, where $\chi = 4.05$ is the electron affinity of silicon.

$$\phi_s = \chi - \frac{E_g}{2} - \frac{k_B T}{q} \ln\left(\frac{N_A}{n_i}\right) \tag{4.2}$$

The next test structure displayed in Figure 4.17b is a gate controlled diode (GCD). It is used to measure the surface current and surface recombination velocity, which is directly related to the interface trap density. The central pad area has a comb-shaped structure, where metal and pad implant strips alternate. This is basically a combination of a diode and a MOS structure. The origin of the measurement principle of a GCD and further information can be found in [49].

The last test structure, displayed in Figure 4.17 shows a test structure to probe interpad properties like the interpad capacitance or interpad resistance. Therefore, eight different versions of this test structure exist, which correspond to the eight different interpad regions in the demonstrator and prototype 8-inch design. Five different pad distances (21 µm, 40 µm, 50 µm, 60 µm, 80 µm) with p-stop common configuration and additional three pad distances (50 µm, 60 µm, 80 µm) with p-stop atoll configuration are implemented. All eight versions are used in the prototype 8-inch design wafer. In the demonstrator wafer only six versions exist without the 50 µm variants.

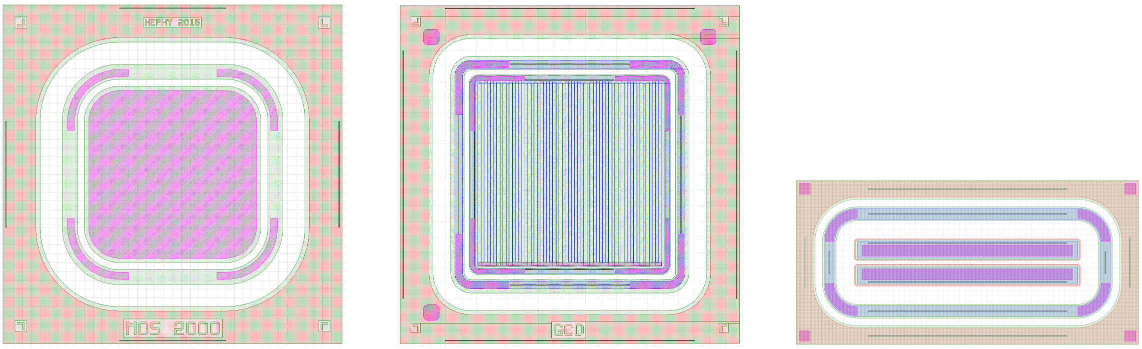

(a) (b) (c)

Figure 4.17: The structure in (a) is a metal-oxide-semiconductor (MOS) test structure. The main use is to measure the flatband voltage and hence the concentration of the fixed positive charges in the oxide. In the middle (b) is a gate controlled diode (GCD), which is used to measure, for example, the surface current. The test structure on the right (c) is used to test inter-pad properties of different geometries. This structure exists in 8 different versions to test all p-stop and pad distance variations of the 8-inch sensor of the demonstrator and prototype design.

4.5 Optimisation for Testing

All sensors produced in mass production have to be tested by either the manufacturer or the institutes of the HGCal collaboration, which are involved in sensor testing. Institutes will measure a small fraction of all sensors in full detail using a setup with a probe card able to contact all pads at the same time. The manufacturers can not use the same probe card setup but will have to depend on either single needle measurements or measurements with small probe cards, where only one pad and its surrounding neighbours are contacted. The difference in the biasing schemes will be a topic in Chapter 6. It will be shown that a 7-needle configuration, meaning the biasing scheme where the pad in question and its surrounding neighbours are biased to the same potential, is necessary.

The only choice for the manufacturer to accomplish the 7-needle configuration will be to use small probe cards together with a computer controlled coordinate table. For efficiency, to save time and cost, the least amount of probe cards to contact all cells should be used. Therefore, the author proposed a possible solution to the collaboration and implemented it in the optimised 8-inch design. Three different probe cards, which are shown in Figure 4.18 are needed. The first, shown in Figure 4.18a provides the positions for the probe card contact pins in the form of red circles for the full hexagonal pads and the calibration cells. With the implementation of the contact pad, shown in purple, close to the middle of the full hexagonal cell, the same probe card can be used for all cells except the border cells. The reason for the addition of the passivation opening is that the height level, where the tips of the contact needles touch the sensor should be the same.

The next probe card, shown in Figure 4.18b, is able to measure three out of the six sides of border pads. More specifically it is used to measure the type with the smaller border pads.

To measure all three sides with the same probe card the 120° symmetry of the design has to be used. This probe card can also be used to measure the pad in the mousebite region next to the small border pads. For this special pad an extra landing pad is implemented in the design outside the area of the main sensor. This area is not part of the active area of the wafer where the silicon sensors may be placed. The landing pad uses the same masks as the contact pads (passivation openings) of the main sensor pads to have the same height level during measuremnts. The landing pad is allowed to be placed in the inner part of the excluded zone because it does not have to be a working sensor with proper electrical characteristics of a diode. The difficulty in the design of this probe card is the fact that the inner guard ring needs to be contacted in addition to the border pads as well.

With the third probe card all the remaining pads of the main sensor can be measured. To measure the remaining three sides of the main sensor the 120° symmetry has to be used as well. Figure 4.18c shows the configuration for this probe card type. Additionally, it can be seen why no additional landing pad for this type is needed. The mousebite pad close to the larger border cell type has one truncated corner, which does not influence the design of the contact pins of the probe card.

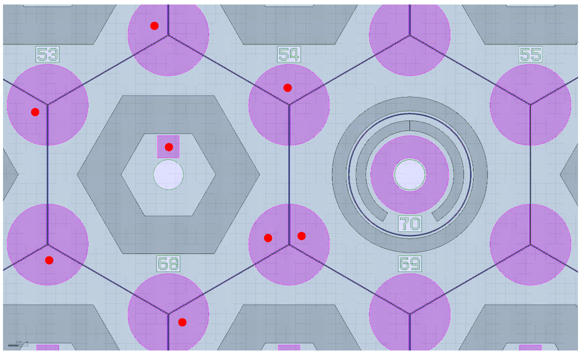

(a)

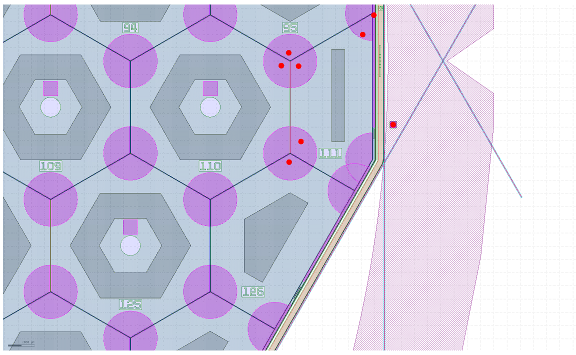

(b)

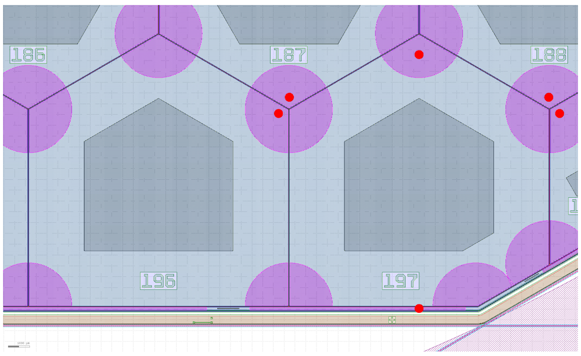

(c)

Figure 4.18: Red dots mark the positions for needles or pins for these small testing probe cards. The pin configuration for the full pads and the calibration pads is shown in (a). For the small border cells including the small mousebite cell, the probe card configuration is shown in (b). This probe card requires an additional pad on the outside of the sensor for each mousebite (6 in total). The third configuration shown in (c) shows the probe card for the large border cells including the large mousebite pad.

5

TCAD Simulations

5.1 Introduction to Synopsys TCAD

Simulations of sensor performance and properties were carried out with the commercial software package Synopsos TCAD [50]. The acronym stands for "Technology Computer-Aided Design". The software package allows the development and optimisation of semiconductor devices using computer simulations. This concept is widely used in the semiconductor industry. It proves advantageous where otherwise a more cost-intensive trial and error approach with various wafer runs would be necessary.

TCAD allows the simulation of semiconductor devices with a self-designed geometry in either 2D or 3D. Simulations are performed using the finite element method, where the Poisson and continuity equations are solved at various predefined points. For this purpose, the device structure is discretised in a mesh. The nodes of the mesh define the points where Poisson and continuity equations are solved. Figure 5.1 shows an example of the 2D representation of a sensor pad with metal overhang and p-stop implantation. For efficient usage of computational resources, the mesh is kept as coarse as reasonably possible and is specifically refined in areas of interest such as implants and interfaces.

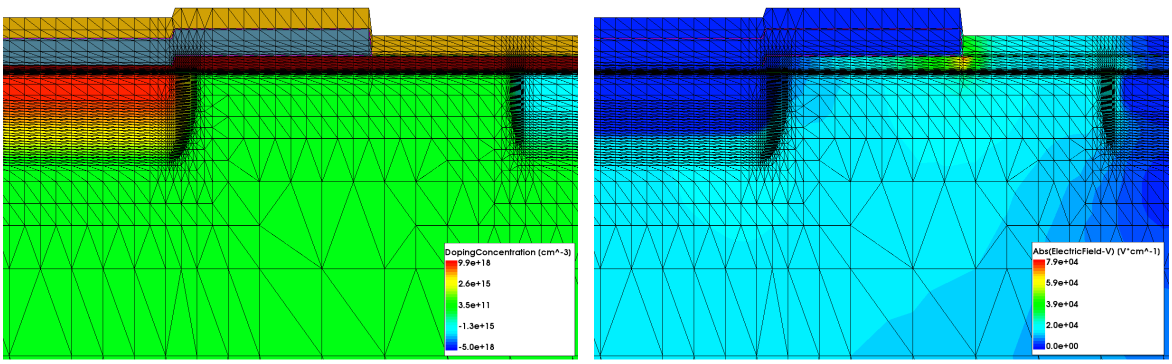

(a) **(b)**

Figure 5.1: Cut-out view of a 2D simulation of the region between pad and p-stop implantation of a HGCal sensor with superimposed mesh. (a) Distribution of the doping concentration. (b) Electric field distribution.

Synopsys TCAD has a framework with a graphical user interface called Sentaurus Workbench [51]. It provides easy access to the various tools used for different simulation tasks. The tool flow in Synopsys TCAD is illustrated in Figure 5.2 and described in the following sections. Individual experiments with different input parameters for the various simulation tools can be defined and grouped in the environment of Sentaurus Workbench. Each experiment is represented by a row in the graphical interface. Parameters are varied in each row. Rows and columns make up the simulation tree with all parameter combinations in its branches. Figure 5.3 shows a screenshot of the Sentaurus Workbench interface with an example simulation tree.

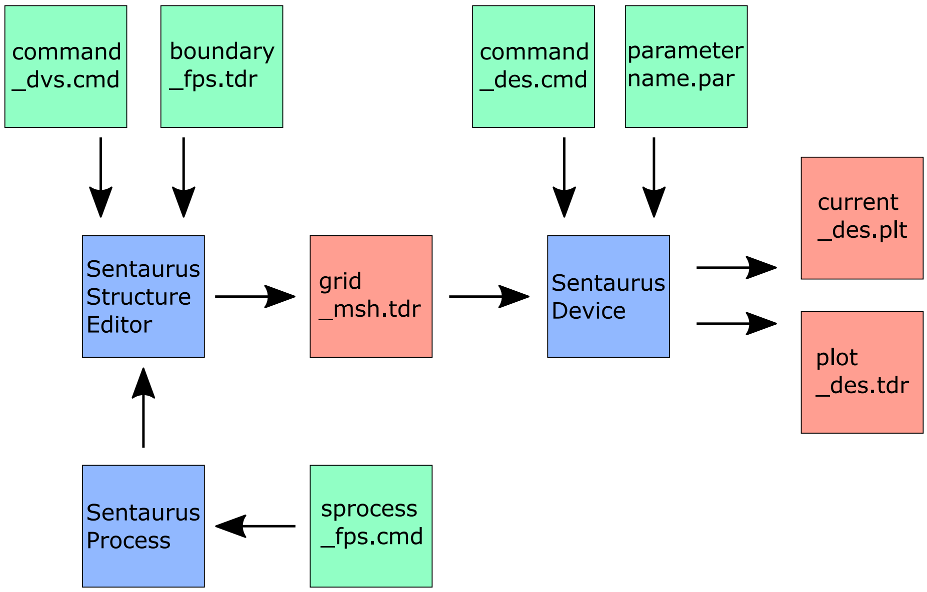

Figure 5.2: The tool flow in Synopsys TCAD. Green boxes mark the input files. Blue boxes are different tools used in the simulation process. The red boxes are the output files containing simulation results. Figure from [22].

5.1.1 Sentaurus Process

At the beginning of every simulation the geometry has to be defined. This is accomplished in Sentaurus Process [52] by issuing a sequence of commands that correspond to the individual process steps in a real sensor production. The commands are defined in the file sprocess_fps.cmd. Each lithographic process step, e.g. doping or etching, has to be defined in detail. For example, this requires knowledge of direction, dose, and energy of the ion beam needed for doping. Such simulations are essential for process development in the semiconductor industry for economic reasons.

After the process steps have been implemented the device is meshed. This can be done with the same tool. If desired to use the mesh engine of the Sentaurus Structure Editor the process simulation can be safed in a *.tdr file for further use.

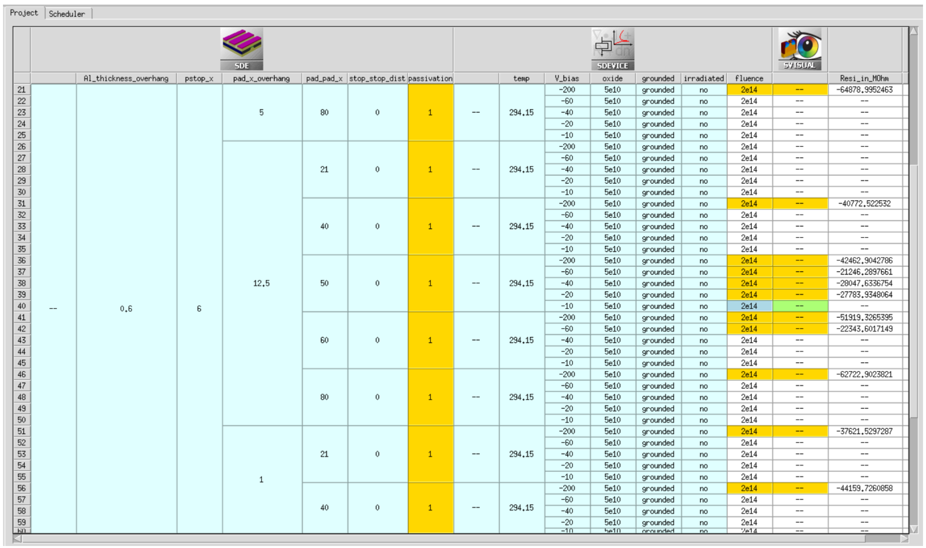

Figure 5.3: Screenshot of Sentaurus Workbench with a simulations tree of various experiments with different input parameters. Different colours mark the status of the simulation. Yellow nodes mark a successfully finished calculation, blue nodes show a simulation in progress, and green nodes mark pending computations, while preprocessed parameter inputs are coloured light-blue. Nodes without any computations are white.

5.1.2 Sentaurus Structure Editor

The Sentaurus Structure Editor [53] can also create 2D and 3D device structures. In contrast to the Sentaurus Process, it emulates the result of all process steps. This is done by defining a doping profile with a mathematical distribution, e.g. Gaussian function or error function. Alternatively, the measurement of the depth and concentration of a doping profile can be used as input as well. The definition of the doping and the size of various materials is defined in a script in the form of a *.cmd file. The location of so-called contacts has to be defined as well. A contact (as defined by [53]) is an interfacial region where subsequent TCAD tools, such as Sentaurus Device, apply electrical, thermal or other boundary conditions. They correspond to physical contacts in the real device. As input for the mesh engine used in the Sentaurus Structure Editor, the file boundary_fps.tdr is created by the Sentaurus Structure Editor, which saves the geometry. At last the structure is meshed. This includes the definition of the minimum and maximum size of the mesh elements and the definition of areas, where extra mesh refinement is necessary. The mesh is saved in the file *_msh.tdr.

With this tool the work load on the computer is lower and the process specific knowledge, e.g. how much energy or temperature budget is needed to reach a certain doping profile depth, is not required. Furthermore, the general goal in this thesis is not an optimisation of the process but an optimisation and development of a working sensor device. Hence, all simulations presented in this chapter use the Sentaurus Structure Editor and not Sentaurus Process.

5.1.3 Sentaurus Device

The next tool called Sentaurus Device [22] takes the previous file as input. At first, boundary conditions are associated with the contacts of the device. A contact can for example be set to a specific voltage, or to be ohmic, or to be floating. The latter means, that the contact is not biased and kept to a specific potential. Virtual electrical measurements can then be performed on the semiconductor device. The currents, voltages, and charges are numerically computed based on a set of physical device equations that describes the carrier distribution and conduction mechanisms. The virtual measurement and the physical models, which are used, are defined in a command file. Using unnecessary models increases the computation time and may increase the accuracy of the simulation only marginally. Using unfit models can even lead to convergence problems. In the simulation process a set of non-linear equations are solved with Newton's iteration method. If the convergence criteria are not fullfilled, the Newton iterations stop. One criterion is for example the relative error of the measured variables. In the case of a convergence problem the realtive error is increasing and not decreasing after each iteration step.
An even bigger source of convergence problems can usually be found in wrong meshing. For best efficiency, a mesh should be created with a minimum number of nodes, which are still sufficient to achieve the required level of accuracy. But it should be the densest in regions of the device where high current density, high electric fields, and high charge generation is expected. Therefore it is recommended to have a coarse mesh in the bulk and a refined one in the doped regions. Additional refinement in the region between two pads and below the Si/SiO2 interface should be considered as well.
Another input file for Sentaurus Device is the parameter file (*.par). In this file the parameters and coefficients of models describing various processes are saved. Not only can the parameters be changed in this file, but it is also possible to define new models.
Sentaurus Device can generate output files in the form of *.plt and *.tdr files. The former saves information about the charges, voltages, and currents passing through the contacts. For example, this information is required when simulating a standard IV curve. The latter file has information about the geometry, mesh and all calculated fields. These fields include, for example, the electrostatic potential, electric field or current densities.
Both file types can be visualised in Sentaurus Visual [54]. This tool can be used to generate and export plots directly in *.png format or export simulation data in *.csv format.

5.1.4 Physics Models

When all contacts of the device are biased to the same voltage it is in equilibrium and electron and hole densities can be described by a constant quasi-Fermi potential. Together with the solution of the Poisson equation, which is the electrostatic potential, the simplest possible device simulation can be performed. For the description of the electron and hole densities by the quasi-Fermi potentials either the Boltzmann statistics or Fermi-Dirac statistics can be used. For high carrier concentrations the Fermi statistics is physically more correct [22].

Numerous models describing the carrier transport in semiconductors exist. There is the drift-diffusion model, thermodynamic model, hydrodynamic model, and Monte Carlo model. The explanations of each of the models is taken from [22]. The drift-diffusion model is the default choice used in isothermal simulations, which are suitable for lower-power density devices with long active regions. The thermodynamic model accounts for self-heating and is suitable for devices with low thermal exchange, particularly, high-power devices with long active regions. The hydrodynamic model accounts for energy transport of the carriers and is suitable for devices with small active regions. The Monte Carlo model solves the Boltzmann equation for a full band structure.

A fundamental property of a semiconductor is its band structure. In Sentaurus Device different models are supported. They comprise the Bennett-Wilson, del Alamo, old Slotboom, Slotboom model, Jain-Roulston, and TableBGN model. In addition, bandgap narrowing can be switched on as well.

The models implemented in the following determine the mobility of the carriers. Different mobility contributions (μ_{x}) originating from a doping dependence, high field saturation, carrier carrier scattering, and mobility degradation at interfaces are combined by Mathiessen's rule:

$$\frac{1}{\mu} = \frac{1}{\mu_1} + \frac{1}{\mu_2} + ... \tag{5.1}$$

For each contribution several models can be used. All options can be found in [22].

Another essential part of the physics of the device are the generation and recombination models, that are responsible for the exchange of carriers between the conduction band and the valence band. They incorporate doping concentration-dependent, temperature-dependent, and electric field-dependent *Shockley-Read-Hall* (SRH) recombination. Additionally, Auger recombination, which is important at high carrier densities, can be included.

To be able to simulate the electrical breakdown of the device an avalanche model needs to be implemented. Supported models are the van Overstraeten - de Man, Okuto-Crowell, Lackner, University of Bologna Impact Ionization Model, and Hatakeyma Avalanche model [22]. Each model is optimised for use in different electric field and temperature ranges. In addition to each avalanche model, the driving force, which is the method used to compute the accelerating field of the charge carriers, can be chosen. The options consist of using the component of the electrostatic field in the direction of the current, the value of the gradient of the quasi-Fermi level, the carrier temperature in hydrodynamic simulations, and the electric field.

5.2 Comparison of Irradiation Models

5.2.1 Introduction and Parameters of different Irradiation Models

High energy radiation produces defects in the crystal lattice of silicon, as described in Section 2.4. In TCAD simulations, the macroscopic effect of the irradiation damage is parameterised by different models. All real existing defects and traps in the crystal cannot be implemented in the simulations. A multitude of real defects is typically condensed into two to five defects. In this section, four different irradiation models will be introduced and compared.

All simulations are performed on a geometry called *Simple Diode Geometry*. It features a 1 µm wide silicon bulk with a thickness of 200 µm or 300 µm. In the 2D simulation the depth of the device is defined as 1 µm as well. With the so-called area factor parameter this depth value can be scaled. This feature is used to simulate diodes with any area, but avoids the computational demand of large devices. The top side, the so called pad (or strip) implant, is doped with a doping concentration of 1×10^{19} cm^{-3} particles of opposing bulk polarity which is either a n-type or p-type implant. The implantation on the back has the same polarity as the bulk and a maximum doping concentration of 5×10^{18} cm^{-3}. The bulk resistivity is varied between 0.5 kΩ cm and 7 kΩ cm. This geometry is used because it requires only a few thousand mesh nodes, which allows to simulate many different parameters. Additionally, it solely reflects features of the bulk. If a periphery is added to the diode, it would increase the simulation time by one to two orders of magnitude and change the results only minimally.

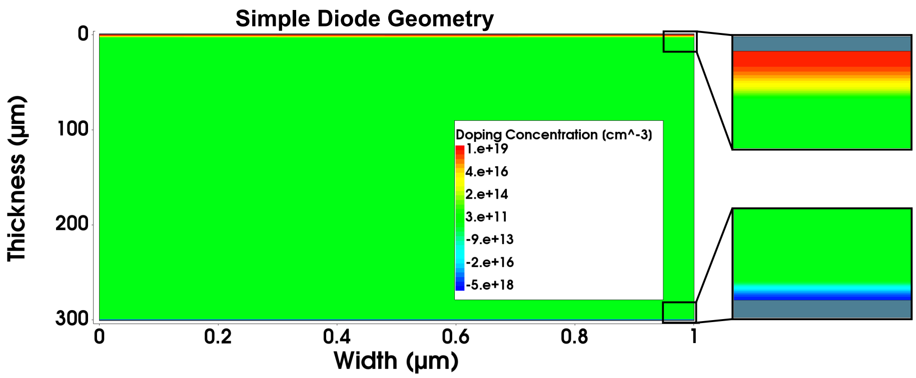

Figure 5.4: Depiction of the so called *Simple Diode Geometry*. It consists of a 1 µm wide silicon bulk. The pad implant has the opposite implantation polarity as the bulk and the implantation on the back.

The first model to be compared is the proton model by R. Eber [55]. It is a two trap model, which is based on trap levels based on works by Moll [31] and Eremin et al. [56]. Measurement and tuning of the parameters have been conducted at −20 °C, hence it is only reliable at this temperature. Additionally, it is only valid in the fluence range of 1×10^{14} n_{eq}/cm^2 to 1×10^{15} n_{eq}/cm^2. For thin sensors (< 300 µm) the error to reproduce the correct full depletion voltage is large. The model is most accurate for thick (e.g. 320 µm) n-type diodes. The proton model parameters are listed in Table 5.1.

Table 5.1: Model parameters for the R. Eber proton irradiation model [55]. They are used to simulate the proton damage in silicon in Synopsys TCAD. ϕ denotes the fluence.

Trap type	Energy (eV)	σ(e) (cm^2)	σ(h) (cm^2)	Concentration (cm^{-3})
Acceptor	$E_C - 0.525$	1.0×10^{-14}	1.0×10^{-14}	1.189 cm$^{-1} \times \phi + 6.454 \times 10^{13}$
Donor	$E_V + 0.48$	1.0×10^{-14}	1.0×10^{-14}	5.598 cm$^{-1} \times \phi - 3.949 \times 10^{14}$

For neutron irradiated sensors Eber proposed another irradiation model. The neutron model [55] uses two traps of the same energy level as the proton model. It is viable only at -20 °C and in the fluence range of $1 \times 10^{14}\,n_{eq}/cm^2$ to $1 \times 10^{15}\,n_{eq}/cm^2$. According to [55] the model should deliver accurate depletion voltages between $1 \times 10^{14}\,n_{eq}/cm^2$ to $5 \times 10^{14}\,n_{eq}/cm^2$ for n-type, p-type, thick and thin sensors. The model parameters are summarized in Table 5.2.

Table 5.2: Model parameters for the R. Eber neutron irradiation model [55]. They are used to simulate the neutron damage in silicon in Synopsys TCAD. F denotes the fluence.

Trap type	Energy (eV)	σ(e) (cm^2)	σ(h) (cm^2)	Concentration (cm^{-3})
Acceptor	$E_C - 0.525$	1.2×10^{-14}	1.0×10^{-14}	1.550 cm$^{-1} \times$ F
Donor	$E_V + 0.48$	1.2×10^{-14}	1.2×10^{-14}	1.395 cm$^{-1} \times$ F

The third model is called Perugia model [57]. It is applicable for p-type substrates up to a fluence of $7 \times 10^{15}\,n_{eq}/cm^2$. In the same work another set of parameters is introduced for the fluence range from $7 \times 10^{15}\,n_{eq}/cm^2$ to $2.2 \times 10^{16}\,n_{eq}/cm^2$. It is modelled after measurements on 300 µm thick proton irradiated p-type diodes. In comparison to the Eber models, the Perugia model uses three bulk traps. To simulate surface damage additional three interface traps between the silicon and silicon dioxide interface can be implemented. Since we are moslty interested in the bulk behaviour and the *Simple Diode Geometry* only represents the pure bulk, no interface traps are going to be used in the rest of the section. The parameters of all three traps are listed in Table 5.3.

Table 5.3: Model parameters for the Perugia irradiation model [55]. They are used to simulate irradiation damage in silicon in Synopsys TCAD. F denotes the fluence.

Trap type	Energy (eV)	σ(e) (cm^2)	σ(h) (cm^2)	Concentration (cm^{-3})
Acceptor	$E_C - 0.42$	1.0×10^{-15}	1.0×10^{-14}	1.613 cm$^{-1} \times$ F
Acceptor	$E_C - 0.46$	7.0×10^{-15}	7.0×10^{-14}	0.9 cm$^{-1} \times$ F
Donor	$E_V + 0.36$	3.23×10^{-13}	3.23×10^{-14}	0.9 cm$^{-1} \times$ F

The fourth irradiation model presented here is the Hamburg Penta Trap Model (HPTM) [58]. This model uses five traps. It was optimised for protons at 200 µm thick sensors. Equal to all previous models it is only valid at -20 °C. It should reproduce correct IV, CV and

CCE behaviour for protons in the fluence range $3.0 \times 10^{14}\,\mathrm{n_{eq}/cm^2}$ to $1.3 \times 10^{16}\,\mathrm{n_{eq}/cm^2}$. The missing temperature dependence is still being worked on by the authors of the model. In addition to the traps, this model requires changes to the physics model used so far. The default value in TCAD for the relative permittivity of silicon is 11.7 and is changed to 11.9 for this model. Additionally, the vanOverstraeten avalanche model is used with the gradient of the quasi-fermi level as driving force. For band gap narrowing the model of Slotboom is used. The Hurkx trap assisted tunneling model is used only for the trap at the energy level $\mathrm{E_C} - 0.545\,\mathrm{eV}$ with a changed tunnel mass of 0.25 $\mathrm{m_e}$ instead of the default value 0.5 $\mathrm{m_e}$. All five trap parameters are listed in Table 5.4.

Table 5.4: Model parameters for the Hamburg Penta Trap Model (HPTM) [58]. They are used to simulate proton irradiation damage in silicon in Synopsys TCAD. F denotes the fluence.

Trap type	Energy (eV)	σ(e) ($\mathrm{cm^2}$)	σ(h) ($\mathrm{cm^2}$)	Concentration ($\mathrm{cm^{-3}}$)
Donor	$\mathrm{E_C} - 0.1$	2.300×10^{-14}	2.920×10^{-16}	0.0497 $\mathrm{cm^{-1}} \times$ F
Acceptor	$\mathrm{E_C} - 0.458$	2.551×10^{-14}	1.511×10^{-13}	0.6447 $\mathrm{cm^{-1}} \times$ F
Acceptor	$\mathrm{E_C} - 0.545$	4.478×10^{-15}	6.709×10^{-15}	0.4335 $\mathrm{cm^{-1}} \times$ F
Donor	$\mathrm{E_V} + 0.48$	4.166×10^{-15}	1.965×10^{-16}	0.5978 $\mathrm{cm^{-1}} \times$ F
Donor	$\mathrm{E_V} + 0.36$	3.230×10^{-17}	2.036×10^{-14}	0.3780 $\mathrm{cm^{-1}} \times$ F

5.2.2 Comparison of Current-Voltage Behaviour

The first criterion for the comparison of the models is the ability to reproduce the correct leakage current for different fluences. Therefore, current-voltage (IV) curves are simulated with all four irradiation models and compared with the well-proven α-factor current calculation method described by Equation 2.33. The current calculated with this Equation is the current of sensors, after they reach the full depletion voltage [31].

The simulated p-type diode has the *Simple Diode Geometry* with a thickness of 200 µm and a resistivity 7 kΩ cm. To compare the simulated current with the expected current in the HGCal sensor pads and to ease the conversion of the current to a volume current ($\mathrm{A\,cm^{-3}}$), the area of the simulated diode is scaled to $1\,\mathrm{cm^2}$. The pads in the HGCal sensor have a pad (= cell) size in the order of $1\,\mathrm{cm^2}$ as well. Five different fluences ranging from $3 \times 10^{14}\,\mathrm{n_{eq}/cm^2}$ to $2.5 \times 10^{15}\,\mathrm{n_{eq}/cm^2}$ are chosen for the comparison.

Figure 5.5a shows IV curves simulated with the Eber proton model with full lines. Within the range of the irradiation model, where it is supposed to be valid, the simulated current after full depletion is about 38 % higher than the one calculated with the α-factor. The current originating from the α-factor calculation is shown as dashed line, since in some cases the sensors do not deplete at voltages lower than 1000 V. The IV curve at the largest investigated fluence exhibits a larger error in the current due to a runaway of the current after full depletion. The scaling of the acceptor and donor concentration in the model does not work after $1 \times 10^{15}\,\mathrm{n_{eq}/cm^2}$. The electric field at this fluence becomes so high that avalanche multiplication starts and increases the current.

In Figure 5.5b the IV curves simulated with the Eber neutron model are displayed. The range, in which the model is valid is the same as for the proton model. At the largest fluence at $2.5 \times 10^{15}\,\mathrm{n_{eq}/cm^2}$ the device is in full breakdown. At a fluence of $1 \times 10^{15}\,\mathrm{n_{eq}/cm^2}$ the increase of current is already starting. At lower fluences the simulated current is higher by about 38 % in comparison to the calculated one.

The third model to be compared is the Perugia model. The IV curves with this model are presented in Figure 5.5c. All tested fluences are within the valid range of the irradiation model, hence no abnormal breakdown happens. But all simulated currents are smaller by about a factor 4 in comparison to the expected ones. Additionally, after reaching full depletion voltage, the current at all fluences remains almost constant.

The last model indicates the simulated IV curves of the HPTM model. At all fluences a small rise in the leakage current can be observed. The increase in current is larger with larger fluence. With increasing fluence, the current at full depletion is between 25 % and 17 % smaller than the expected one. At $-800\,\mathrm{V}$ respectively $-900\,\mathrm{V}$ for the largest fluence, the simulated current matches the expected current from the α-factor calculation exactly.

The current increase with increasing fluence is summarized for all irradiation models in Figure 5.6.

All four models produce different results with regard to their ability to reproduce the current of irradiated diodes. For both Eber models the simulated current is 38 % too high, even when used within their intended fluence range. Out of the four tested models, the Perugia model reproduces the leakage current the least, as it is four times lower than expected. The best model to simulate the current is the HPTM, even though the currents at the full depletion voltage is between 25 % and 17 % smaller than the calculated one. At $-800\,\mathrm{V}$ and $-900\,\mathrm{V}$ respectively, the simulated current is identical with the calculated one by Equation 2.33.

5.2.3 Comparison of Capacitance-Voltage Behaviour

The next option to compare the irradiation models is by investigating the ability to reproduce the full depletion voltage of diodes. P-type diodes with a resistivity of $7\,\mathrm{k\Omega\,cm}$ are investigated at the thicknesses 200 µm and 300 µm for different fluences. In Figure 5.7 the capacitance is represented as the inverse squared to be able to better spot the full depletion voltage. This is important since irradiated sensors show a smeared out turning point. Smeared out means, the turning point is less abrupt and hence it is more difficult to allocate a concrete value of the full depletion voltage to the irradiated CV curve. In addition, for irradiated diodes temperature and frequency affect the CV behaviour [59].

Figure 5.7a shows the result of the CV simulation with the Eber proton model. For comparison, the unirradiated CV curve is also shown in red. According to the measurements from

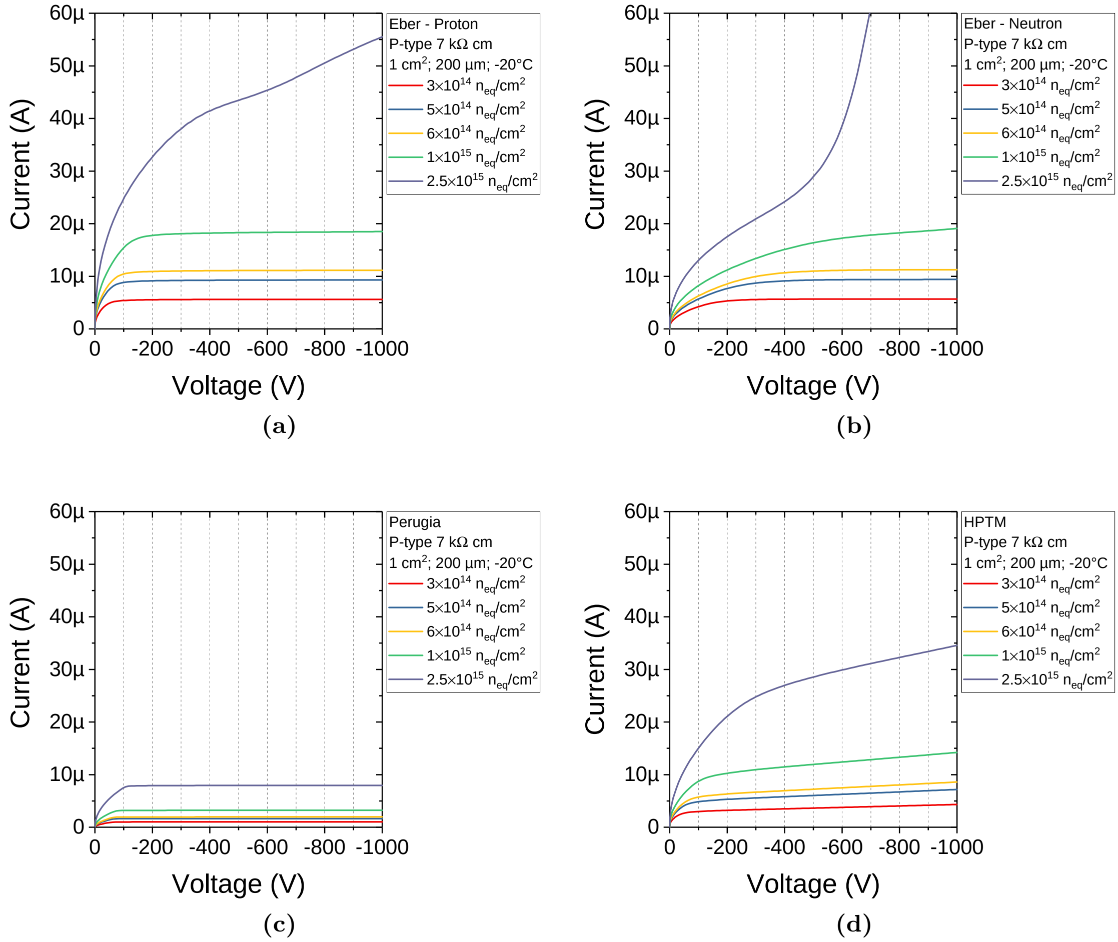

Figure 5.5: Four different irradiation models are compared. The ability to reproduce the current for different fluences is checked against the predicted current calculated by the α-factor. Figure (a) shows the Eber proton model and Figure (b) the Eber neutron model. Figure (c) shows the IV curves modelled with the Perugia model. The last Figure (d) shows the resulting currents from the HPTM model.

[55], on which the proton model is based, the full depletion voltage for p-type 200 µm thick diodes should be about 60 % higher. The largest fluence value, displayed in gray, is out of the range of the model and is therefore not representative.

In the Eber neutron model, displayed in Figure 5.7b, the full depletion voltages are in fairly good agreement with the measurements, shown in [55], which were used in the creation of the model. In general, all simulated CV curves show a much larger full depletion voltage in comparison to the Eber proton model.

The Perugia model, used in the simulation of the curves in Figure 5.7c, shows only little dependence on the fluence. Therefore, it is not a viable method to describe the capacitance behaviour.

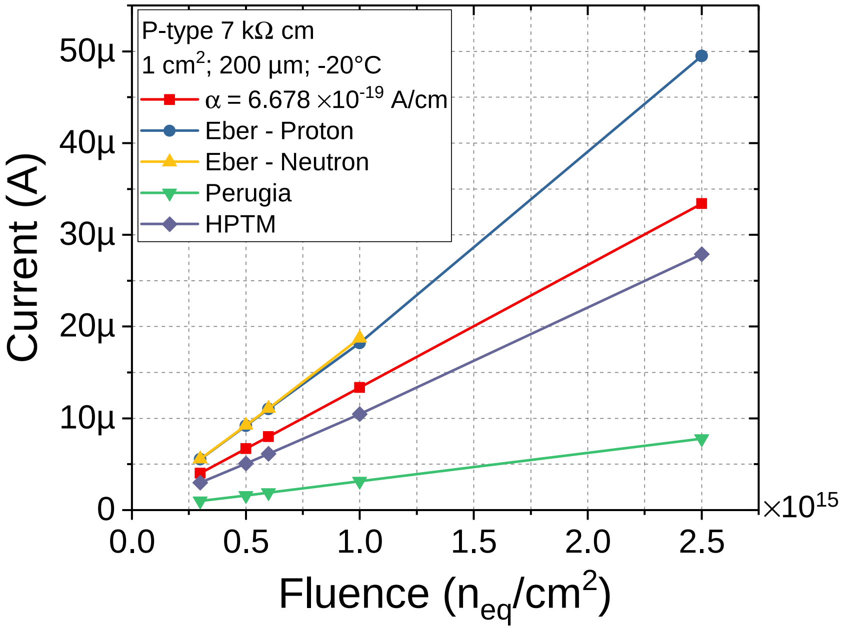

Figure 5.6: Current extracted at the full depletion voltage and plotted for different fluences and irradiation models.

Figure 5.7d represents the results from the HPTM model. On a first glance it can be seen, that the full depletion voltages for protons in this model are considerably smaller than the neutron damage simulated by the Eber neutron model. Additionally, simulated CV curves show a full depletion voltage, which is only about half of the one simulated with the Eber proton model. Even though it is smaller by a factor 2, the HPTM model has been tuned with measurements, which agreeded within 20 % with the simulations [58].

One of the reasons responsible for the differences in the measurements of the proton models is a fluence error of ±10 % to ±20 %, which is present in each irradiation. This error is due to uncertainties in the fluence calibration or possible missalignments of the test structure in the reactor or proton beam. Further discrepancies in the CV measurements of Eber and HPTM may be due to errors in the temperature measurement or using a different measurement frequency. Another bigger uncertainty factor is the method of the determination of the full depletion voltage itself. Using the typical method, fitting with two straight lines and taking the intersection point, has a large error for irradiated CV curves. This becomes clearer when looking at the shape of an irradiated CV curve, for example, the curve representing the fluence $1 \times 10^{15}\,\mathrm{n_{eq}/cm^2}$ in Figure 5.7a. The kink is not sharp anymore and starts at about −200 V and ends at about −600 V. Due to this, the fit algorithm to determine the full depletion voltage has a large error. Therefore, another method is chosen for the determination of the simulated full depeltion voltages for the simulations presented here.

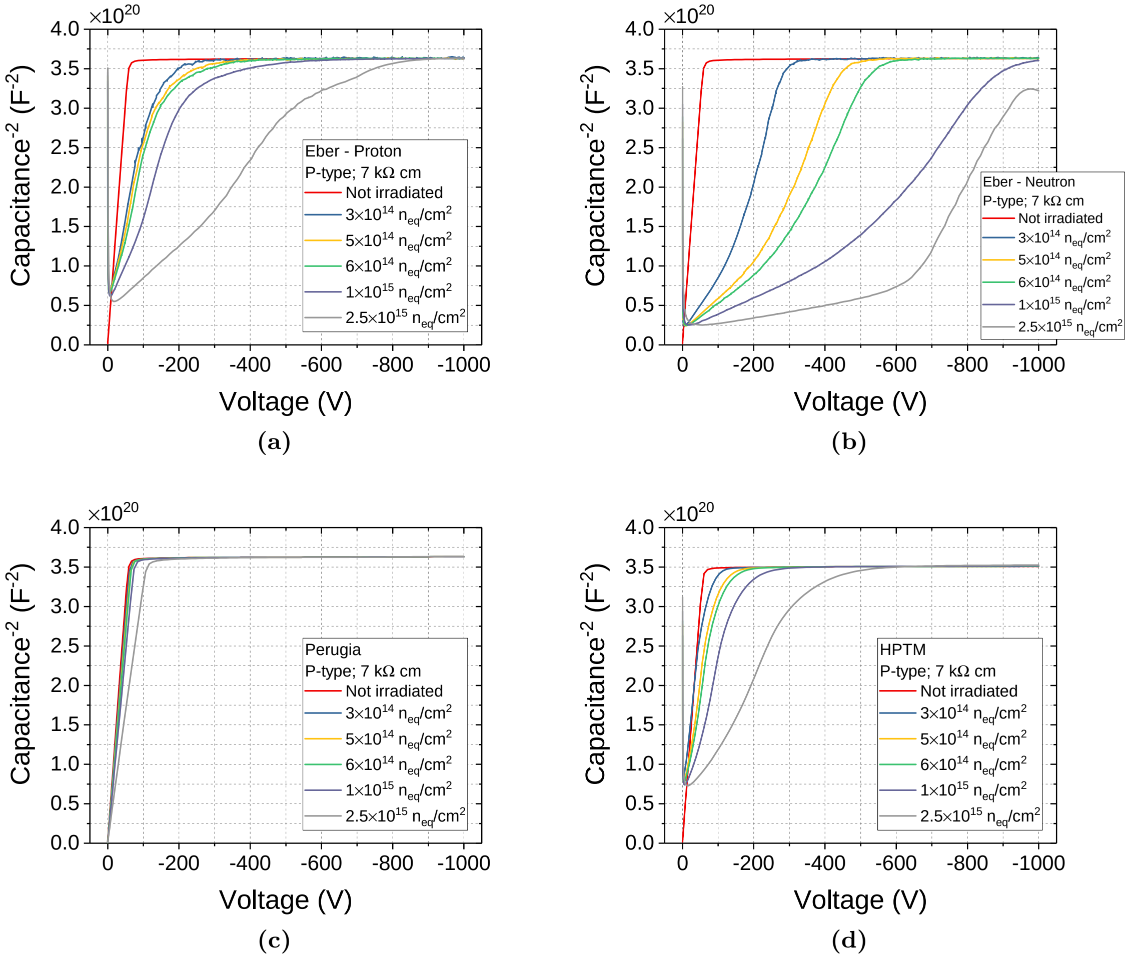

Figure 5.7: CV simulations at a frequency of 1 kHz were performed. 200 µm thick diodes were used and the result for different irradiation models and different fluences are shown. The full depletion voltage caused by neutron damage is considerably higher in comparison to proton damage, when comparing both Eber models. In the Perugia model the full depletion voltage is barely affected by higher fluence. The HPTM model produces lower full depletion voltages than the Eber proton model.

According to theory a p-type diode of thickness 200 µm and resistivity of 7 kΩ cm has a full depletion voltage of 60.26 V. Using the method to fit the CV curve with two straight lines on the simulated unirradiated CV curve, reproduces this value. The full depletion voltage in the CV curve corresponds to a $1/C^2$ value which is about 97 % of the maximum value at −1000 V. Since the determination of the full depletion voltage is not reliable with the two lines fit method, the full depletion voltage for the irradiated curves is defined as the voltage, where 97 % of the $1/C^2$ value is reached. The values plotted in Figure 5.9 are determined by this method.

Figure 5.9a shows a summary of the extracted full depletion voltages for different fluences and irradiation models for 200 µm thick diodes. Neutron irradiation leads to much higher full depletion voltages in comparison to proton damage. When comparing the Eber proton model with the HPTM, it can be seen that for low fluences, the full depletion voltage of the former model is 2.0 times the one of the latter. The ratio decreases for higher fluences and is 1.84 at a fluence of $1 \times 10^{15}\,\mathrm{n_{eq}/cm^2}$. The full depletion voltages originating from the Perugia model are in general much lower than the rest and show only little increase with fluence. The model is not able to reproduce proper full depletion voltages.

The difference in proton and neutron damage can be explained in the following way. In n-type devices, donor removal happens with hadron irradiation. One of the main processes is that an electrically active phosphorus atom enters a radiation induced vacancy and forms an electrically inactive VP-defect [55], which lowers the donor concentration in the bulk. Together with acceptor creation the material undergoes type inversion from n-type to p-type. With further irradiation the device becomes more “p-type” and the full depletion voltage rises again. This effect is more pronounced for protons in comparison to neutrons. High energy protons produce a mixture of point-like and cluster defects, whereas neutrons produce mostly cluster defects. They contribute differently to the effective space charge, which leads to the different full depletion development. For p-type devices and low fluences, acceptor removal is the dominating process. For p-type sensors no space charge sign inversion takes place. More details on donor or acceptor removal can be found in [60].

Figure 5.8 shows the CV curves for different irradiation models for 300 µm thick diodes at the fluence of $5 \times 10^{14}\,\mathrm{n_{eq}/cm^2}$. The full depletion voltage simulated with the Eber neutron model is above $-1000\,\mathrm{V}$, whereas for protons it is considerably lower. This behaviour is similar to the 200 µm thick diodes. Another thing to note is the lower maximal $1/C^2$ value of the HPTM in comparison to the Eber proton or Perugia model. This is related to the different relative permittivity of silicon used for this model, namely 11.7 instead of 11.9.

The extracted full depletion voltages are shown in Figure 5.9b. The values are produced by the same method as for the 200 µm version. 97 % of the maximal $1/C^2$ of the unirradiated 300 µm thick curve are taken for reference, which defines the point of full depletion. The full depletion voltages simulated with the Eber proton model are 1.97 ± 0.04 times the ones from the HPTM model. In general the full depletion values from the 300 µm thick diodes are on average 2.16 ± 0.05 times higher than the full depletion voltages of the 200 µm thick diodes.

5.2.4 Comparison of Voltage-Charge Collection Efficiency Behaviour

The third and last criterion, which is used to describe sensors and compare irradiation models is the simulation of the charge collection efficiency. For this task a diode with the *Simple Diode Geometry* and an unirradiated resistivity of $7\,\mathrm{k\Omega\,cm}$ is used. The simulations are all performed at $-20\,^{\circ}\mathrm{C}$. In the simulation a MIP is induced and charge is deposited homogenously along the track trough the detector. The arising current signal is integrated

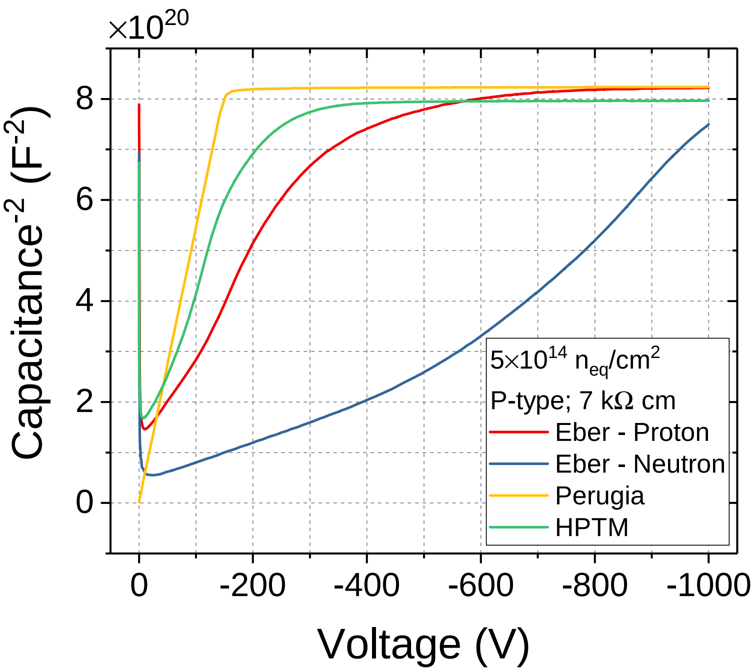

Figure 5.8: The figure shows the CV simulation of 300 µm thick diodes at the fluence of $5 \times 10^{14}\,\mathrm{n_{eq}/cm^2}$. Four different irradiation models are compared. The maximal $1/C^2$ value of the HPTM model is lower than for the other models due to a different relative permittivity value of silicon (11.7 instead of 11.9). Only the neutron model results in a full depletion voltage above $-1000\,\mathrm{V}$.

over time and the resulting charge is compared to the charge of the signal of the unirradiated diode.

Figure 5.10a shows the CCE for different irradiation models at a fluence of $2.5 \times 10^{15}\,\mathrm{n_{eq}/cm^2}$ corresponding to the expected maximum at HL-LHC for 200 µm thick sensors. At this fluence regime both models by Eber are not suitable. The neutron model would indicate a CCE above 1 at $-1000\,\mathrm{V}$. This means that at such a high fluence the scaling of the donor and acceptor traps is wrong. In this case it leads to higher electric fields, where effects like charge multiplication can happen. The effect of charge amplification due to higher fluence irradiation has been observed before by different groups [61] [62] [63]. Even though the effect exists the Eber neutron model should not be trusted at this fluence, since the (too) high field leads to early break down of the leakage current (see Figure 5.5b). If the device is already in break down and amplificates charges, the signal charges may get amplificated as well. The HPTM and Perugia model show similar CCEs within a 5 % margin. This is surprising, because even though the Perugia model fails to reproduce a proper IV and CV behaviour it is still able to predict similar CCE as the HPTM model. The Eber proton model is showing 20 % to 15 % lower CCE values in comparison to the HPTM model. But it should be noted that the model is out of its intended usable range and should not be used for the prediction of the CCE of sensors in this condition. Out of the four models used here the HPTM model is the most reliable in this fluence region. For the HL-LHC operation

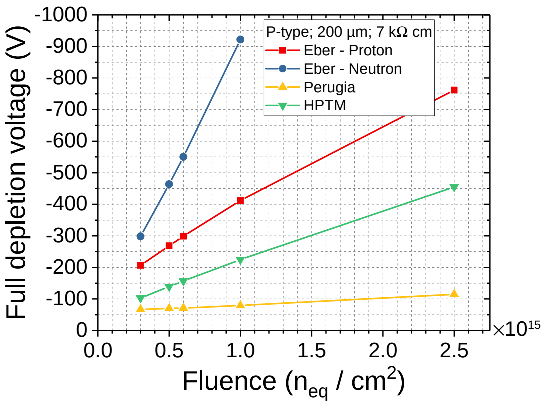

(a)

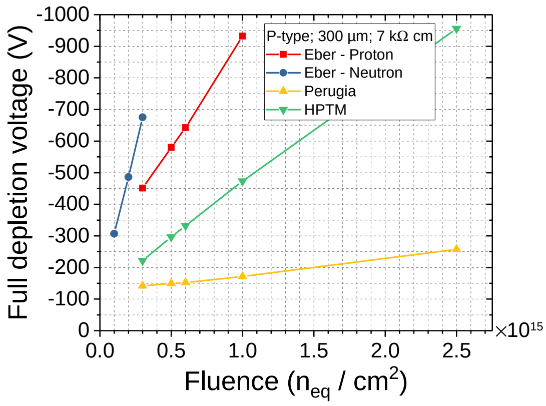

(b)

Figure 5.9: Both figures show the full depletion voltage for different fluences. The full depletion voltages are extracted from simulated CV curves with all four different irradiation models on 200 µm (a) and 300 µm (b) thick diodes. The increase of the full depletion voltage is increasing linearly with fluence. For p-type diodes no type inversion happens with irradiation. The full depletion voltage of the neutron model is increasing faster than all proton models. In Figure (a) the Eber proton model results in almost twice as high full depletion voltages in comparison to the HPTM model. In Figure (b), for 300 µm thick diodes, the full depletion voltage is about twice as high.

of the 200 µm thick sensors it predicts a CCE of about 68 % at −800 V. For −1000 V bias voltage it would increase the CCE to a value of about 69 %. Hence it is not mandatory to operate the sensor at this bias voltage.

Figure 5.10b displays the CCE measurement for 300 µm thick diodes at the corresponding HL-LHC fluence of $5 \times 10^{14}\,\mathrm{n_{eq}/cm^2}$. In this fluence range all models are supposed to work. Comparing the HPTM, the Perugia and the Eber proton model, it can be seen that the margin between the lowest (Eber proton) and the highest (HPTM) predicted CCE values are the same as for the high fluence case shown in Figure 5.10a. The Eber neutron model is also in its intended range and predicts CCE values at −1000 V comparable to the proton models. The lower CCE in comparison to the proton models at lower voltages is expected due to the higher full depletion voltage of the neutron irradiated device. Even though the full depletion voltage differs by roughly a factor of 2 between the Eber neutron model and the proton models, the CCE value is 37 % smaller than the HPTM model and 19 % smaller than the Eber proton model. In this simulation, even in the worst case the CCE is above 70 % for a bias voltage of −800 V. At −1000 V only the neutron model suggests an improvement of up to 10 % in CCE, whereas the proton models show only negligible improvement.

For completeness five different fluences are simulated for all four different simulation models. Figure 5.11 shows the results for 200 µm thin diodes and Figure 5.12 for 300 µm thick ones. True for all cases is the fact, that the CCE decreases with increasing fluence. For the thinner diodes, the gain in CCE with bias voltage is only very small within the intended

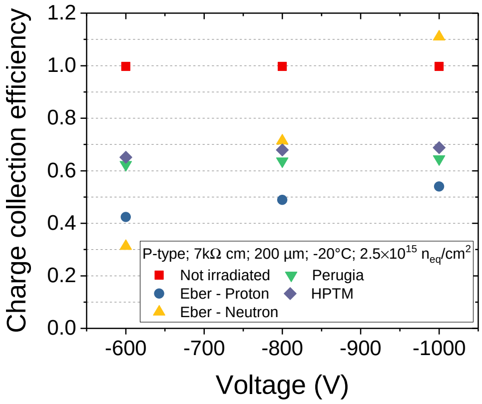

(a)

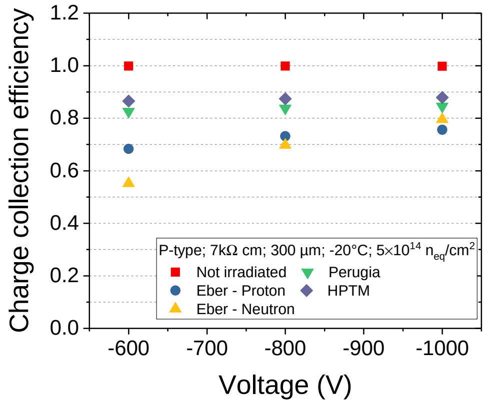

(b)

Figure 5.10: The figure shows the simulated charge collection efficiencies (CCE) for different bias voltages and irradiation models. Figure (a) describes a 200 µm thick diode at the expected HL-LHC fluence of $2.5 \times 10^{15}\,\mathrm{n_{eq}/cm^2}$ for this sensor type. Figure (b) shows the same measurement for 300 µm thick diodes at a fluence $1 \times 10^{14}\,\mathrm{n_{eq}/cm^2}$.

fluence range of each model. The only exception is the Eber neutron model at a fluence of $1 \times 10^{15}\,\mathrm{n_{eq}/cm^2}$. In this context very small means that the CCE value is increasing by less than 5 % of the absolute CCE value. In comparison for thick diodes, the gain in CCE with bias voltage is only very small for the HPTM and Perugia model and the Eber proton model at the lowest fluence. For the largest simulated fluence here this is only true for the Perugia model. Since the Eber models show higher full depletion voltages it is clear that the CCE has to decrease more with lower bias voltage. For the neutron model this effect is even more pronounced. When comparing the HPTM and Perugial model for thin and thick diodes, one can see that for each fluence the difference in the absolute CCE value is less than 5 %. For both thicknesses, the Eber proton model's absolute CCE value is about 5 % to 25 % larger in comparison to the other models, with the lower discrepancy being at the lower fluences and increasing deviation with higher fluences.

In the Eber neutron model, the difference between the 200 µm and 300 µm thick diode is the largest. In the thin diode simulation only for fluences up to $6 \times 10^{14}\,\mathrm{n_{eq}/cm^2}$, the absolute CCE value is within 5 % of all other models. Higher fluences diverge stronger. For the thick diode, only the lowest fluence of $3 \times 10^{14}\,\mathrm{n_{eq}/cm^2}$ is within a 10 % absolute CCE value margin.

The CCE simulations also show why the thick sensors are only used in a lower fluence environment in comparison to thinner sensors. The CCE is getting lower with increasing sensor thickness at the same fluence.

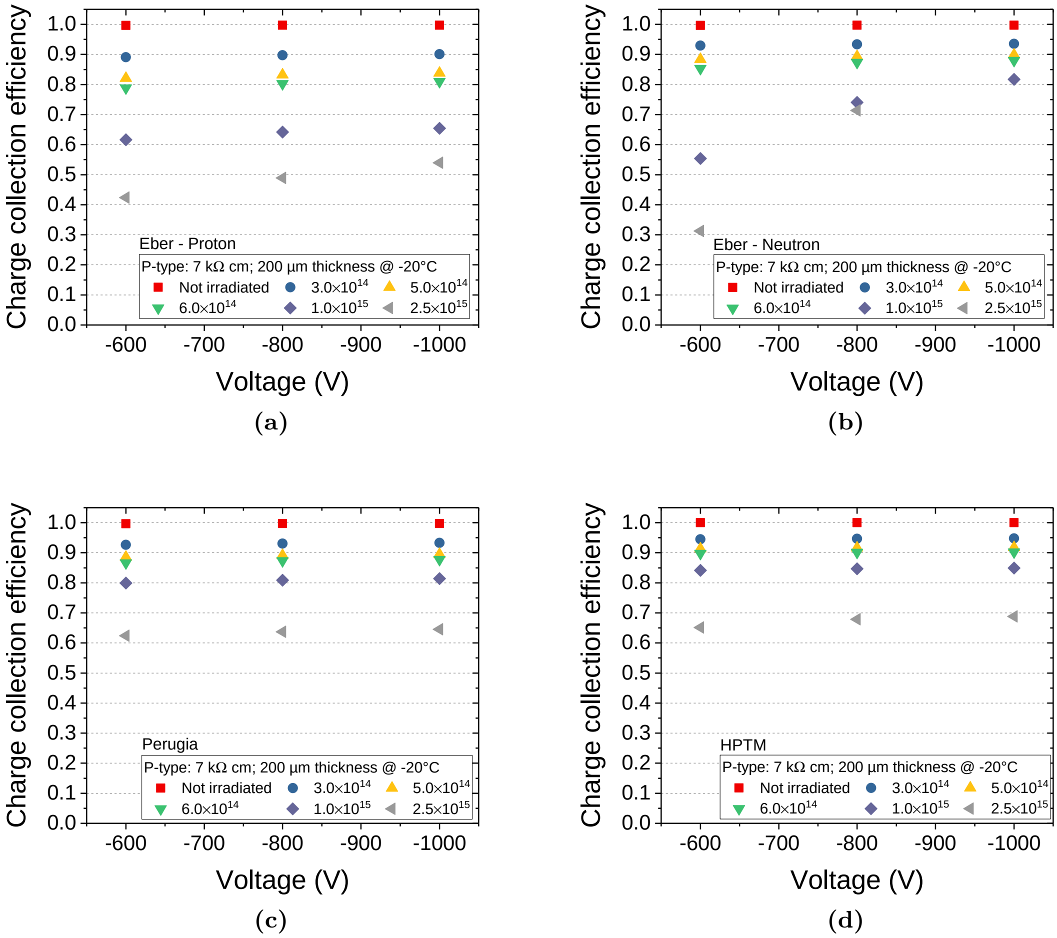

Figure 5.11: CCE simulations of 200 µm thick diodes for different irradiation models and different fluences and different bias voltages. With higher fluence the CCE reduces. Within the applicable range of each model the CCE value increases only slowly between -600 V and -1000 V. The only exception being the Eber neutron model at a fluence of $1 \times 10^{15}\ \mathrm{n_{eq}/cm^2}$.

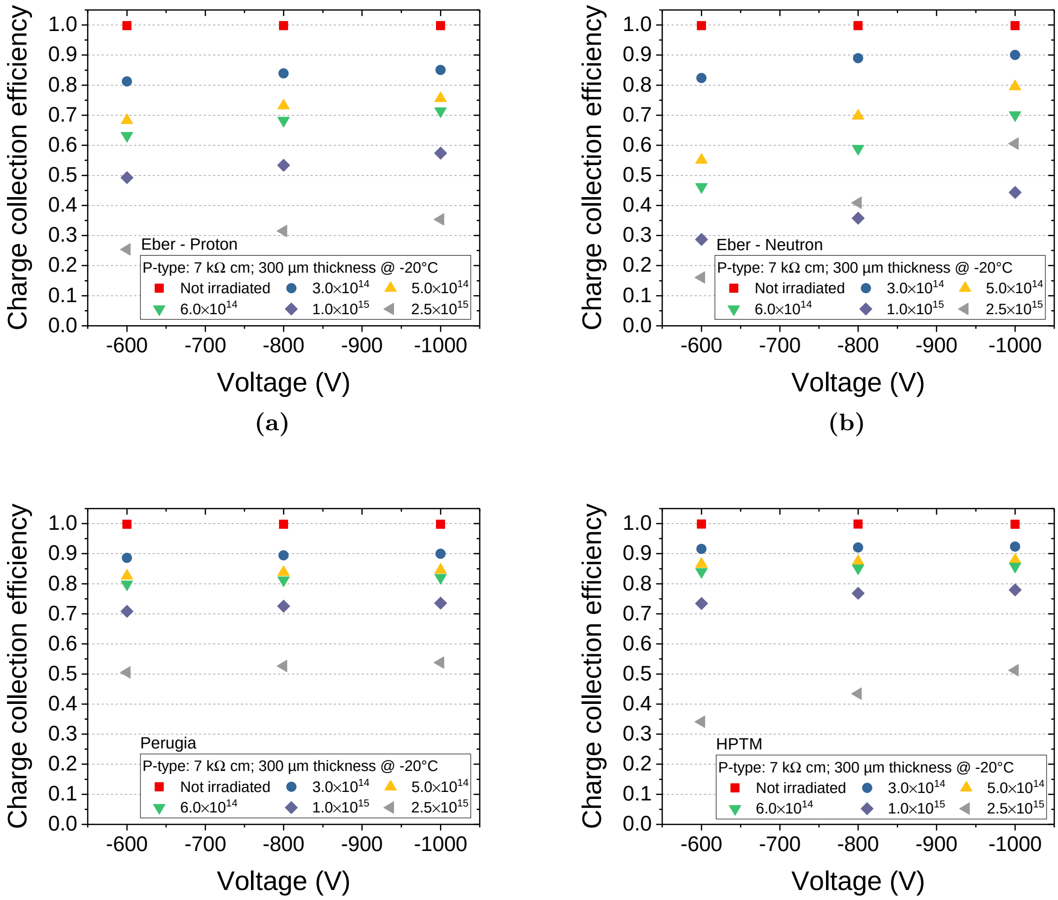

(a) (b) (c) (d)

Figure 5.12: CCE simulations of 300 µm thick diodes for different irradiation models and different fluences and different bias voltages. For the Eber neutron model higher bias voltage is most beneficial with regard to increasing the CCE in comparison to all other proton models. Up to a fluence of $1 \times 10^{15}\,\mathrm{n_{eq}/cm^2}$ the HPTM and Perugia model are within a 5 % CCE value interval. The Eber proton model CCE drops faster with fluence than the other two proton models. Only at the lowest fluence of $3 \times 10^{14}\,\mathrm{n_{eq}/cm^2}$, all models produce similar results within a 10 % of CCE value margin.

5.3 Comparison of N-Type and P-Type Diodes

As mentioned in Chapter 3, it is not decided yet whether the 300 µm thick HGCal sensors should be n-type or p-type because of economic reasons. To be able to come to a conclusion, the current-voltage (IV), capacitance-voltage (CV), and charge collection efficiency (CCE) of diodes is simulated. Both diode types in the unirradiated and the irradiated case are considered. For this task a so-called *Simple Diode Geometry*, which is shown in Figure 5.4, is used in the simulations.

5.3.1 Unirradiated

In this section unirradiated diodes are investigated. All simulations are performed at a temperature of 20 °C. The following physics models are used in Sentaurus Device for all simulations.

- Fermi-Dirac statistics
- Hydrodynamic carrier transport model
- Band structure model (Slotboom)
- Band to band tunneling (Hurkx)
- Mobility models with doping dependence (Masetti), high field saturation (Canali), carrier-carrier scattering (Conwell-Weisskopf), interface degradation (Enormal)
- SRH recombination model with doping dependence, temperature dependence, electric field dependence
- Auger recombination
- Avalanche model (van Overstraeten)

IV Simulation

To test the predicted current of the TCAD simulations, a current-voltage characteristic of a real diode of type *Diode-Large* is compared to simulation. A description of the measurement setup is given in Chapter 6. The diode is measured with a single needle without contacting the guard ring. The measurement data is compared to simulated IV curves at 295 K, where the *Simple Diode Geometry* is used and the area is scaled to the area of the pad of a diode of type *Diode-Large*. Taking into account the rounded corners of the pad, the implant area is about 24.86 mm^2. For the simulation of the IV curve, the resistivity

9 kΩ cm is used. The full depletion voltage (143 V) and hence this resistivity value was determined by a CV measurement shown in section 5.3.1. To match the simulated current with the measured current, the SRH recombination lifetime parameters $\tau_{\mathrm{max,e^-}}$ and $\tau_{\mathrm{max,h^+}}$ for electrons and holes are adjusted. The result can be seen in Figure 5.13. The black dots represent the IV measurement at room temperature with the surrounding red region being the corresponding temperature error of 1 °C. The blue line is produced with the default TCAD parameter values for $\tau_{\mathrm{max,e^-}} = 1.0\times10^{-5}$ and $\tau_{\mathrm{max,h^+}} = 3.0\times10^{-6}$. With the transition from the blue to the green coloured simulated curves, both lifetime parameters are increased. It can be observed that with increasing electron and hole recombination lifetime parameter, the current decreases.
The SRH recombination takes place through material impurities or defects in the semiconductor crystal that introduce some intermediate energy levels in the bandgap [64, 65]. These levels act as recombination centres or traps. Depending on the purity of the crystal the number of these defects changes. Higher purity means less recombination centres and hence higher recombination lifetimes. This corresponds to smaller generation and recombination rates which imply less dark current.
When comparing the measured and simulated curves in Figure 5.13 it can be seen, that for $\tau_{\mathrm{max,e^-}} = 2.5\times10^{-4}$ and $\tau_{\mathrm{max,h^+}} = 2.5\times10^{-4}$ the curves match within the ±1 °C error margin. Nevertheless, above full depletion the measured current increases faster with increasing voltage than the simulated current. This can be traced back to the different geometry used in the simulation. In the real diode the depletion region will not only spread from the pad implant at the top (p-type diodes are used here) to the back, but also spread laterally with increasing bias voltage. With an increasing active diode area the leakage current increases as well. In the case of the *Simple Diode Geometry* this effect cannot happen, because the full width of the geometry is depleted equally.

With a single needle IV-measurement the active diode area is not exactly constricted. The effective diode area is larger than the pad implant area. But in the simulation here, the current in the active volume is tuned to the pad area with the adaption of the lifetime parameter. A measurement showing the effect will be shown in Chapter 6.

Using the previously found lifetime parameters, a new simulation to estimate the leakage current in the unirradiated bulk for different materials is performed. The resulting IV curves of the simulation are shown in Figure 5.14. Figure 5.14a features a p-type diode with three different bulk resistivities, which are 1 kΩ cm, 3 kΩ cm and 7 kΩ cm. In the simulation the diodes have a thickness of 300 µm. As known from theory, different bulk resistivity leads to different full depletion voltages. The full depletion voltage is typically determined by capacitance-voltage (CV) measurements. But since the *Simple Diode Geometry* is used and no irradiation damage is simulated, there is no disruptive factor and the simulated IV curves show the full depletion voltage in the kink. Even though the full depletion voltage is different the leakage current in the bulk after full depletion is the same. At −1000 V the current is 86.5 nA. Figure 5.14b shows the same simulation setup but with a n-type bulk. Here four different resistivities ranging from 0.5 kΩ cm, 1 kΩ cm , 3 kΩ cm and 7 kΩ cm are tested. For this bulk polarity the leakage current is again the same after the sensor reached full depletion. The reason for the increase of current for voltages higher than full depletion is due to the SRH field enhancement. Field enhancement reduces the SRH recombination lifetimes in regions of strong electric fields [22]. With decreasing SRH recombination lifetime

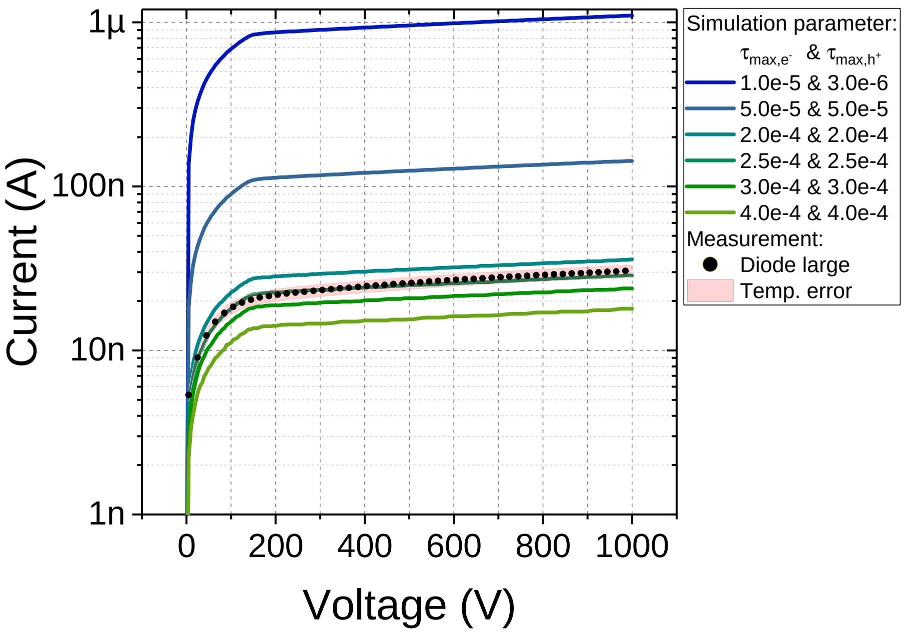

Figure 5.13: The simulation parameters τ_{max,e^-} and τ_{max,h^+} are adjusted in order to match the simulated IV curve with the measured IV curve. The resulting parameters, $\tau_{max,e^-} = 2.5\times10^{-4}$ and $\tau_{max,h^+} = 2.5\times10^{-4}$, can henceforth be used to represent diodes of the same bulk material.

the current increases, as can also be seen in Figure 5.13. If the field enhancement model is not implemented in the TCAD simulation the current of the diode would remain constant after full depletion.

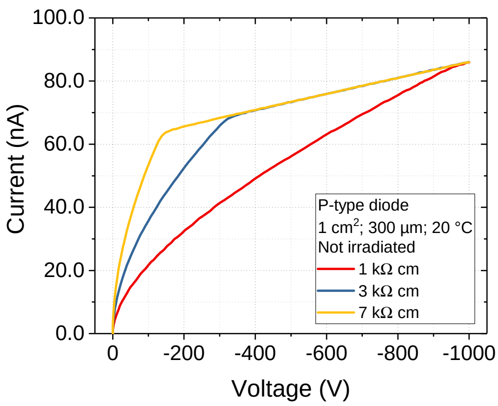

(a)

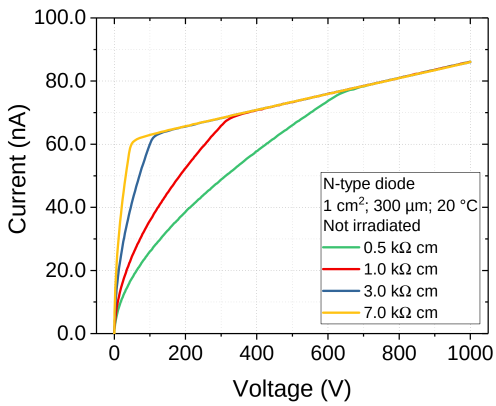

(b)

Figure 5.14: The figure shows IV curves of an unirradiated p-type (a) and n-type (b) diode at 20°C for different resistivities.

CV Simulation

Another standard measurement technique to characterise diodes are CV measurements. With increasing reverse bias voltage the depletion region increases in the diode. The depletion region starts spreading at the p-n junction and proliferates to the back of the diode. The back is reached at the full depletion voltage. With increasing depletion region the measured capacitance decreases until full depletion and then remains constant. This corresponds with the parallel plate condensator equation, where the capacitance decreases with increasing thickness of the dielectric medium. To highlight the point of full depletion in the CV measurement to a greater extent, the squared inverse of the capacitance is plotted against the voltage instead of the capacitance. Figure 5.15 shows such a CV measurement of a diode of type *Diode Large* and compares it with simulated CV curves. One measurement is performed with a single needle contacting only the pad of the 350 µm thick diode (black curve). The second measurement measures the capacitance of the pad, while the guard ring is grounded (red curve). The simulated curves are depicted as solid lines.
In the simulation the *Simple Diode Geometry* is used and therefore has no periphery as the real diode has. The effective area of the real diode is not perfectly constrained and known due to the periphery. To gauge the effective area of the diode in a capacitance measurement, different areas, which correspond with certain sections of the periphery of the measured diode, are assumed and simulated. The solid blue line corresponds with an effective area, which is the size of the pad implant of the diode of type *Diode Large*. As the inverse squared capacitance value is about 44 % larger than the measurement value without a grounded guard ring, the simulated effective capacitance is accordingly smaller. The three other simulated curves assume effective areas from the centre up to the inner guard ring implant, to the outer guard ring, and the outer guard ring metal. The measurement without a grounded guard ring can be best described by the last assumption, where the effective area of the diode expands up to the outer guard ring metal. The measurement with a grounded guard ring corresponds with the simulation, which assumes an effective area up to the inner guard ring. The capacitance contribution coming from the periphery and the pad is important to know when determining the doping profile with CV measurements [66]. The authors also showed that in order to differentiate the edge and pad capacitance, measurements of diodes with different sizes but the same periphery are needed for the calculation.
The error bands in Figure 5.15 are the measurement errors originating from a sensor thickness variation of ± 10 µm. Within this black and red band the measured and simulated points mostly coincide.

For the development of the 300 µm thick HGCal sensors, it is important to choose the right bulk material. Therefore, and to test the simulation against theory, a study concerning the bulk full depletion voltage for some possible configurations was conducted. Figure 5.16 shows CV curves of unirradiated p-type and n-type diodes. The *Simple Diode Geometry* is used. For both bulk polarities different resistivities are chosen. They are 1 kΩ cm, 3 kΩ cm, and 7 kΩ cm. For n-type an additional resistivity of 0.5 kΩ cm is simulated. The extracted full depletion voltages of the curves are identical to the predictions of Equation 2.24. The full depletion voltages are summarized in Table 5.5.

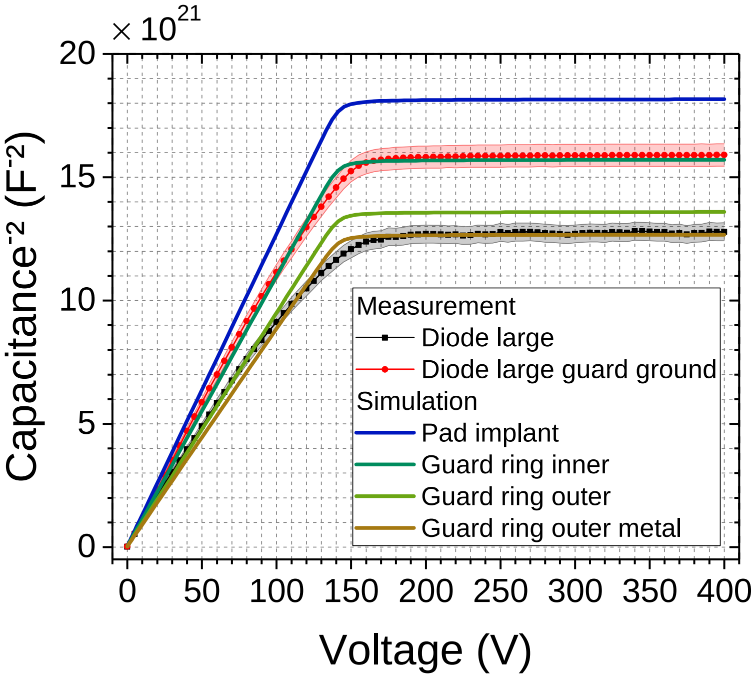

Figure 5.15: A CV simulation with different areas is compared with a diode of type *Diode Large*. The effective area of such a diode extends up to the end of the guard ring outer metal, when measured with a single needle, according to TCAD simulations. With a grounded guard ring the effective area extends up to the guard ring implant.

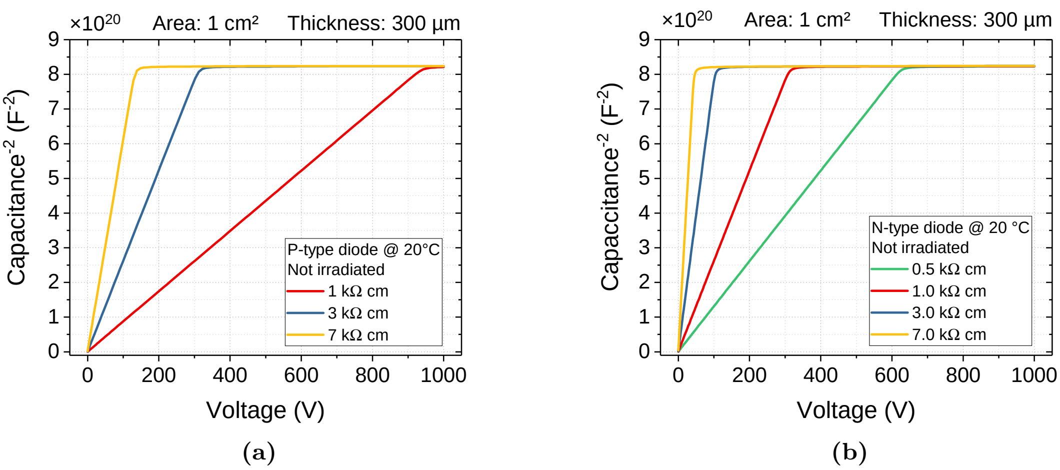

Figure 5.16: The figure shows simulated CV curves of an unirradiated p-type (a) and n-type (b) diode at 20°C for different resistivities. A diode area of $1\,\mathrm{cm}^2$ with a thickness of $300\,\mu\mathrm{m}$ is simulated.

Table 5.5: Simulated full depletion voltages of unirradiated p-type and n-type diodes for different resistivities. The diode thickness is 300 µm. The simulated values are the same as the values calculated with Equation 2.24.

Resistivity	Sim:	p-type: V_{FD}	n-type: V_{FD}	Calc:	p-type: V_{FD}	n-type: V_{FD}
0.5 kΩ cm		-	632 V		1898 V	633 V
1.0 kΩ cm		949 V	316 V		949 V	316 V
3.0 kΩ cm		316 V	105 V		316 V	105 V
7.0 kΩ cm		135 V	45 V		136 V	45 V

5.3.2 Irradiated

In the previous section the basic simulations about IV and CV measurements of unirradiated diodes are shown. In this section a study of the irradiated bulk by means of IV and CV simulations is performed. Additionally, charge collection efficiency (CCE) simulations are shown. The neutron irradiation model of R. Eber [55] is used throughout this section, since mostly neutrons are expected to be responsible for the radiation damage in HGCal sensors [8]. The parameters are listed in Table 5.2, where F represents the fluence. A more detailed description of the model is given in 5.2. The neutron model is a two-trap model, where the donor and acceptor defect concentration scales with fluence. To perform studies regarding the material type for the 300 µm thick HGCal sensors, this model is the ideal tool. The model is only useable at the fluence range expected at the position of HGCal sensors with this thickness.

Current-Voltage

The first characterisation method for irradiated sensors is an IV measurement. In Figure 5.17 the current for different fluences and for both bulk polarities are shown. The temperature in the simulation is $-20\,°\mathrm{C}$. For the p-type diode a resistivity of 7 kΩ cm and for the n-type diode a resistivity of 1 kΩ cm is shown. These values are chosen from the list of values used in 5.3.1. Out of these resistivity values they translate to the smallest full depletion voltage for their respective bulk polarity type and hence are of most interest. The first thing to note is that the current increases with increasing fluence from $1 \times 10^{14}\,\mathrm{n_{eq}/cm^2}$ to $1 \times 10^{15}\,\mathrm{n_{eq}/cm^2}$. At a fluence of $5 \times 10^{14}\,\mathrm{n_{eq}/cm^2}$ the current is about 14 µA at 1000 V. At voltages above full depletion, the current at a specific fluence is the same for both polarities. The current increase after full depletion for different fluences is described by Equation 2.33.

In Figure 5.18 the current for different resistivities is plotted at a fluence of $5 \times 10^{14}\,\mathrm{n_{eq}/cm^2}$ for both polarities. For p-type the different IV current values are due to the different full depletion voltages of the diodes with different resistivity. At all of the three chosen resistivities of the diodes, they are not fully depleted at 1000 V and hence the current is not in saturation. N-type diodes, with the resistivities simulated here, can be fully depleted at this fluence. Therefore all simulated IV curves saturate.

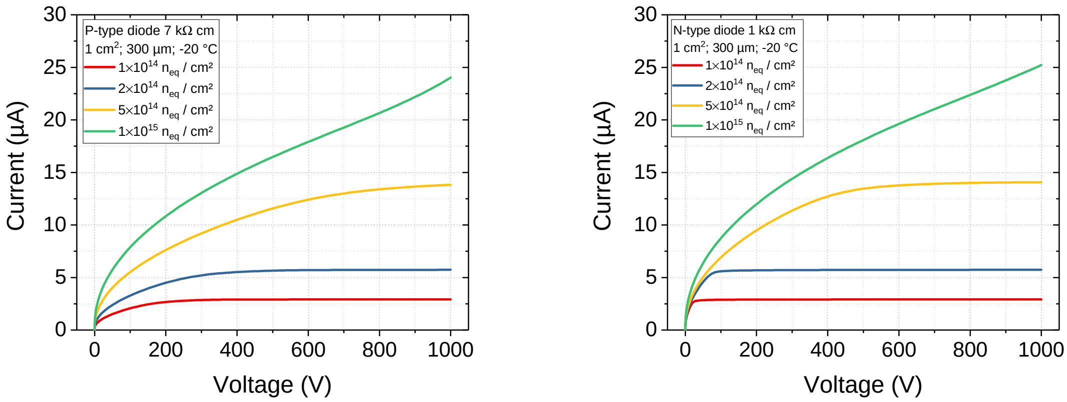

(a) (b)

Figure 5.17: The figure shows simulated IV curves of an irradiated p-type (a) and n-type (b) diode at -20°C for different fluences.

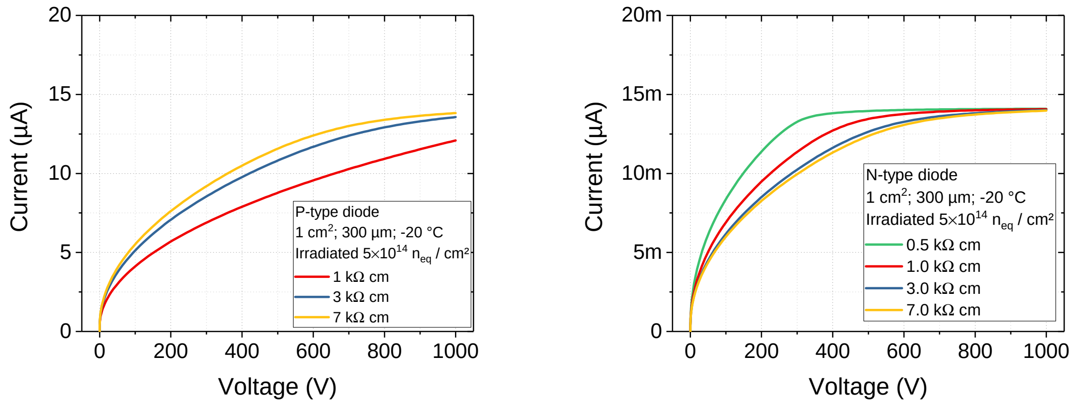

(a) (b)

Figure 5.18: The figure shows simulated IV curves of an irradiated p-type (a) and n-type (b) diode at -20°C for different resistivities.

Capacitance-Voltage

The second standard measurement to characterise irradiated diodes is a CV measurement. Figure 5.19 shows simulated $1/C^2$ curves for $1\,\mathrm{cm}^2$ diodes with a thickness of 300 µm at different fluences. The temperature is -20°C. As mentioned in the previous section the full depletion voltage increases with increasing fluence ranging from 1×10^{14} $\mathrm{n}_{eq}/\mathrm{cm}^2$ to 1×10^{15} $\mathrm{n}_{eq}/\mathrm{cm}^2$. This holds true for both polarities, because the n-type diode with a resistivity of $1\,\mathrm{k\Omega}\,\mathrm{cm}$ is already type inverted at this fluence. Type inverted means that the original n-type bulk changed its polarity due to the increase of the acceptor concentration due to irradiation.

The p-type diode with an initial resistivity of 7 kΩ cm and a thickness of 300 µm is fully depleted at a fluence of 1×10^{14} n_{eq}/cm^2 and 2×10^{14} n_{eq}/cm^2. For the fluences 5×10^{14} n_{eq}/cm^2 and 1×10^{15} n_{eq}/cm^2 the diode cannot be fully depleted at 1000 V. For the n-type diode only the largest before mentioned fluence cannot be full depleted anymore. The simulated fully depletion voltages V_{FD} are summarized in Table 5.6.

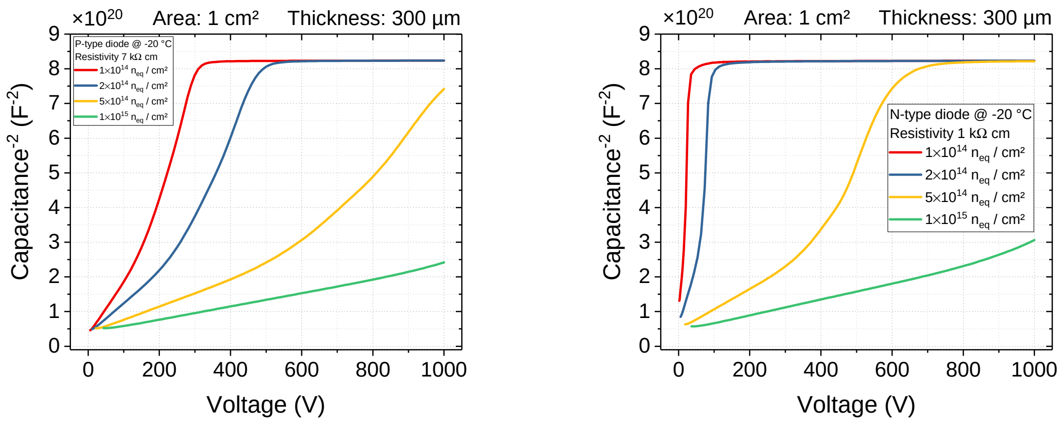

(a) (b)

Figure 5.19: The figure shows simulated CV curves of an irradiated p-type (a) and n-type (b) diode at -20°C for different fluences.

Table 5.6: Simulated full depletion voltages V_{FD} for neutron irradiated diodes of p-type and n-type.

Fluence	V_{FD}: P-type	V_{FD}: N-type
1×10^{14} n_{eq}/cm^2	≈ 300 V	≈ 50 V
2×10^{14} n_{eq}/cm^2	≈ 500 V	≈ 100 V
5×10^{14} n_{eq}/cm^2	> 1000 V	≈ 700 V
1×10^{15} n_{eq}/cm^2	> 1000 V	> 1000 V

Figure 5.20 shows CV curves at a neutron fluence 5×10^{14} n_{eq}/cm^2 for different resistivities, ranging from 1 kΩ cm to 49 kΩ cm. With higher resistivity the full depletion voltage is lower. Only diodes at the highest two simulated resistivities can be fully depleted at a bias voltage lower than 1000 V. N-type diodes at resistivities ranging from 0.5 kΩ cm to 7 kΩ cm have full depletion voltages lower than 1000 V. The full depletion behaviour regarding the resistivity is reversed in comparison to p-type. For smaller resistivities the bulk is depleted earlier.

P-type diodes with a thickness of 300 µm cannot be fully depleted at a bias voltage lower than 800 V, when being neutron irradiated at a fluence 5×10^{14} n_{eq}/cm^2. To find the conditions when p-type can be used in the HGCal at this fluence, the full depletion voltage is simulated for different thicknesses and resistivities. The result is summarized in Table 5.7. For a desired full depletion voltage lower than 800 V, the diode thickness should be 250 µm or smaller, insensible to the resistivity. The resistivity should be larger than 7 kΩ cm, even though 3 kΩ cm is sufficient for 200 µm and 225 µm thick diodes. With larger resistivity the

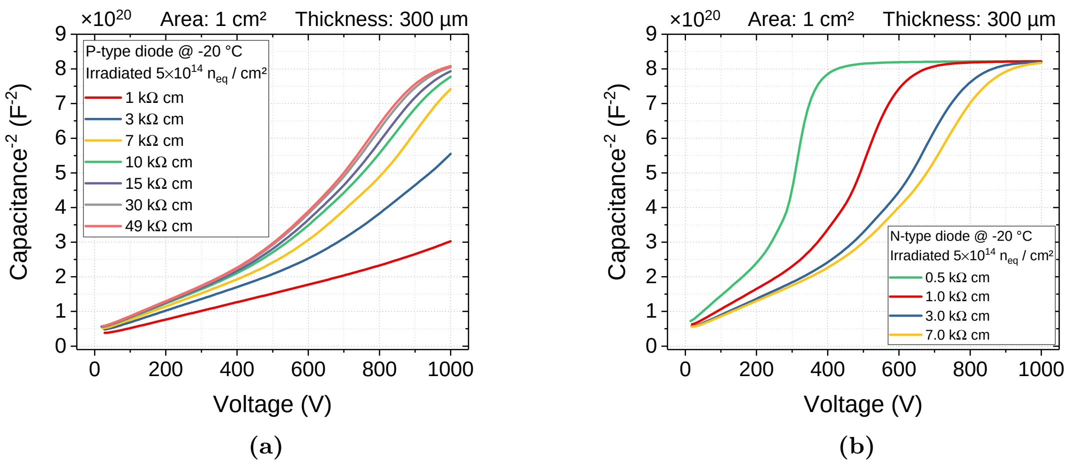

Figure 5.20: The figure shows simulated CV curves of an irradiated p-type (a) and n-type (b) diode at -20°C for different resistivities.

decrease in V_{FD} gets smaller. Higher resistivity p-type bulk is more cost intensive. Therefore, it is recommended to reduce the sensor thickness and not increase the resistivity to very high values to reach full depletion voltages below 800 V.

Table 5.7: Simulated full depletion voltages V_{FD} for neutron irradiated p-type diodes at a fluence of $5 \times 10^{14}\ n_{eq}/cm^2$. The thickness and resistivity are varied.

V_{FD} (V)	200 µm	225 µm	250 µm	275 µm	300 µm
1 kΩ cm	813	-	-	-	-
3 kΩ cm	541	690	859	-	-
7 kΩ cm	463	592	738	902	-
10 kΩ cm	447	571	712	869	-
15 kΩ cm	433	554	691	844	-
30 kΩ cm	420	537	669	818	979
49 kΩ cm	415	530	661	808	967

Charge Collection Efficiency

In this section charge collection efficiency (CCE) studies are performed on diodes with the *Simple Diode Geometry*. To generate a MIP signal in the sensor a heavy ion depositing a constant amount of energy per length in the detector is used in the simulation. A single MIP produces in the present simulation 22000 electrons in the 300 µm thick diode, which corresponds to a charge of about 3.5 fC. Figure 5.21 shows the signal of the deposited charge of 10 MIPs for different bias voltages. The signal is induced at a time t = 1 ns and sampled every 100 ps. Since no external electronics is taken into account but purely the silicon bulk, the signal curves shows a steep rise followed by a sharp peak. One can compare the figure with Figure 2.7, where the signal contribution of electrons and holes is simulated using the software Weightfield2. In Figure 5.21a an unirradiated p-type diode with a resistivity of 7 kΩ cm is shown. The signal simulated in TCAD shows the two characteristic straight lines originating from the electrons and holes. The effect is more pronounced after full depletion of the sensor. For bias voltages smaller than the full depletion voltage $V_{fd} \approx 150\,V$ the signal does not reach zero after 20 ns. With increasing bias voltage up to 1000 V the signal decays faster, down to within a time of about 6 ns after signal induction. Figure 5.21b shows a 10 MIP signal for different bias voltages in the same diode, which additionally has been irradiated by neutrons with a fluence of $5 \times 10^{14}\,n_{eq}/cm^2$. The irradiation damage is simulated with the neutron model from R. Eber. In comparison to the unirradiated case, the height of the peak is lower. This is due to trapping of charge carriers caused by the irradiation damage. With increasing bias voltage the signal shape remains very similar but increases in value in a more evenly way than the unirradiated case. The decay time increases until full depletion, which cannot be reached here. The full depletion voltage of the 300 µm thick diode is 1079 V. The curves, representing the voltage values 700 V to 1000 V, exhibit a slightly different decay behaviour, because the diode is slowly reaching full depletion and the decay time becomes faster similar to the unirradiated case. After 16 ns the signal reaches zero for a bias voltage of 1000 V.

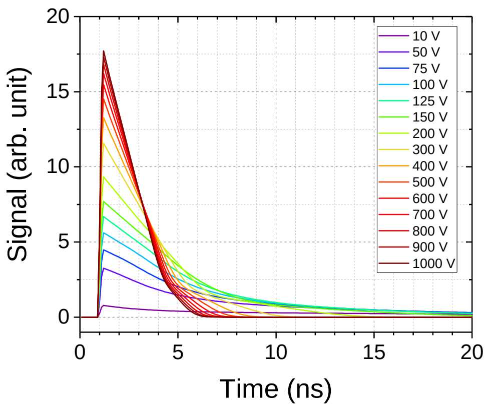

(a)

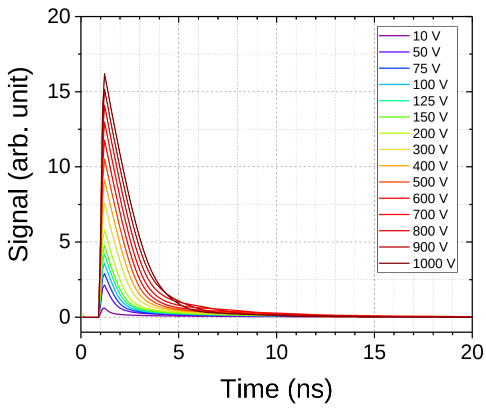

(b)

Figure 5.21: The figure shows a signal of 10 MIPs for different bias voltages in an unirradiated (a) and irradiated (b) diode. For the neutron irradiation a fluence of 5×10^{14} n_{eq}/cm^2 is chosen together with the neutron model by R. Eber.

To calculate the charge collection efficiency from the signal curves as shown in Figure 5.21, the charge has to be integrated. Here, it is integrated from time t=0 ns to t=30 ns. Even though for some bias voltages not 100 % of the signal charge are collected, it is a good compromise between computation time and precision. To estimate the value of lost charge, the signal curve between the interval t=25 ns to t=30 ns is fitted by a straight line and extrapolated to find the intersection with the time-axis at zero signal. The area of the extrapolated triangle is the lost charge. In the worst case for the unirradiated diode, at 10 V bias voltage, only 81.38 % of the total charge are collected. But at voltages above full depletion up to 99.79 % are collected. For the irradiated diode with this irradiation model already 99.69 % of the charge are within the integration interval at the worst case at 10 V bias voltage. Therefore, the end time of the integration interval with a value of 30 ns is reasonable.

Figure 5.22 shows the summarized charge collection efficiency for different bias voltages, bulk polarities, and resistivities in the unirradiated and irradiated case. In Figure 5.22a the 300 µm thick p-type diode is displayed for the resistivities 3 kΩ cm and 7 kΩ cm, which is in the typical range for the p-type HGCal sensors. For the two curves describing the unirradiated case, the CCE simulation delivers exactly the full depletion voltage, which would usually be determined by CV measurements. See Figure 5.16 for comparison. In the neutron irradiated case the simulation shows a maximum CCE between 75 % and 80 %, while having a slightly curved, almost linear increase in CCE with bias voltage. Having a higher resistivity is advantageous for p-type sensors, as the full depletion voltage will be lower and hence a higher charge collection efficiency. For n-type, displayed in Figure 5.22b, a smaller resistivity is desired to minimize the full depletion voltage. The unirradiated resistivity values are chosen in such a way, that the full depletion voltage for p-type and n-type are the same. Nevertheless, in this simulation the maximum CCE for n-type at 1000 V is about 83 %. The same CCE values as for p-type could be achieved by a bias voltage of about 700 V. This difference is either due to the inaccuracy of the irradiation model describing the full depletion models of p-type and n-type diodes, or due to n-type being more irradiation hard.

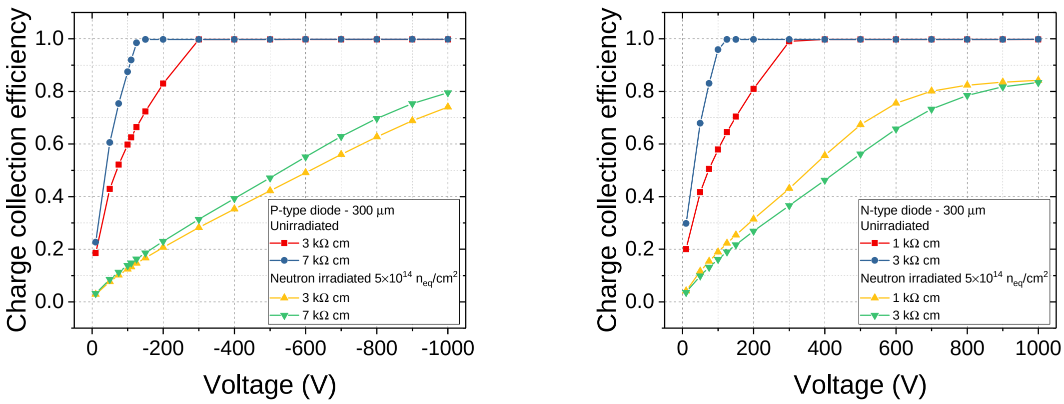

(a) **(b)**

Figure 5.22: The figure shows the simulated charge collection efficiency (CCE) for different bias voltages for p-type (a) and n-type (b). Irradiated n-type diodes require only about 700 V to produce the same CCE as p-type diodes according to the neutron irradiation model of R. Eber.

To check the irradiation models, measurements were performed and compared with the simulations of the Eber models. A detailed description of the measurement setup can be found in Section 6.2.3. Due to the unavailability of a proper method to control the temperature in the laser setup the measurements have been performed at room temperature. This is problematic, since all available irradiation models are tuned and viable for a temperature of −20 °C and the charge collection efficiency is temperature dependent. Figure 5.23a shows the CCE for different bias voltages for 200 µm thick p-type diodes for a neutron fluence of

$1 \times 10^{14}\,\mathrm{n_{eq}/cm^2}$ (red) and $9 \times 10^{14}\,\mathrm{n_{eq}/cm^2}$ (blue). The dark red and blue curve with the box and circle symbols denote the measurement of the real diodes at room temperature. Simulations with the Eber neutron irradiation model at $-20\,°\mathrm{C}$ are shown with the dashed lines. At the lower of the two fluences at 1000 V the simulation predicts a CCE of 98 %, while the measurement results in a CCE of 87 %. For the higher fluence at 1000 V the simulation predicts a CCE of 83 % and the measurement a value of 62 %. To correct for the different temperature a new set of trap parameters has been found, which is listed in 5.8. It is based on the neutron model by Eber, but has changed values for the electron and hole capture cross sections. The difficulty in building new irradiation models is the fact that when changing parameters, which, for example, represent the CCE better, do not deteriorate the ability to describe the IV or CV behaviour. Which parameters to adapt to implement a different temperature is already proposed by [55], but was not performed there for room temperature. With the new set of parameters the simulation at room temperature, shown as full line without marks, results in CCE values at 1000 V of 95 % and 64 % for a fluence of $1 \times 10^{14}\,\mathrm{n_{eq}/cm^2}$ and $9 \times 10^{14}\,\mathrm{n_{eq}/cm^2}$. For the smaller fluence only a small improvement could be achieved, but for the higher one the improvement is large, as the relative error is only about 3.2 % between measurement and simulation.

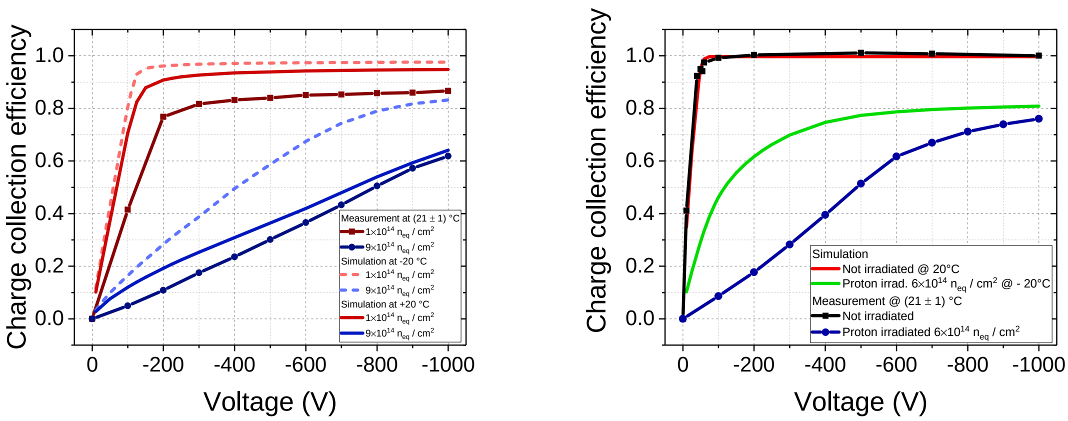

(a) **(b)**

Figure 5.23: The figure shows the simulated and measured charge collection efficiencies (CCE) for different bias voltages. The result of neutron irradiation is shown in (a) and the result of proton irradiation in (b). To simulate the CCE at room temperature the Eber neutron model needs to be adjusted.

Table 5.8: Model parameters for the new neutron irradiation model useable at 20°C. It is a two trap model based on the Eber model with parameters shown in Table 5.2. F denotes the fluence.

Parameter	Donor	Acceptor
Energy (eV)	E_V + 0.48	E_C - 0.525
Concentration ($\mathrm{cm^{-3}}$)	1.395 $\mathrm{cm^{-1}} \times$ F	1.55 $\mathrm{cm^{-1}} \times$ F
σ(e) ($\mathrm{cm^2}$)	1.1×10^{-14}	2.4×10^{-14}
σ(h) ($\mathrm{cm^2}$)	2.4×10^{-14}	1.1×10^{-14}

Figure 5.23b shows a CCE measurement of 200 µm thick p-type diodes, which have been irradiated with protons at a fluence of $6 \times 10^{14}\,\mathrm{n_{eq}/cm^2}$. For comparison the unirradiated diode at room temperature is shown as well, which exhibits a very good agreement between measurement and simulation. The measurement of the proton irradiated diode and the simulation differ strongly at lower voltages. But the difference grows smaller with increasing bias voltage. Parts of this can be traced back to the inaccuracy of the Eber proton model to deliver proper full depletion voltages for sensors having a thickness of 200 µm. The error in full depletion means, that the measured full depletion is about 60 % higher than the simulated one, with measurements taken from [55]. Despite the wrong behaviour at lower voltages, the CCE at 1000 V is 78 % in the measurement and 81 % in the simulation. The damage in the bulk introduced by protons and modelled with the proton model seems to be less temperature dependant at higher voltages than the neutron damage. The full difference at lower voltages cannot be explained by the inaccurate simulated full depletion of the proton model. The remaining difference has to originate from the temperature difference. For proton irradiated devices, the CCE is higher at lower temperatures. This effect is also confirmed by measurements from [58].

5.4 Inter Pad Region

In this section various simulations regarding the *Inter Pad Region* are performed. This region describes the area between two pads of the HGCal sensor. The simulations are performed in two dimensions due to two reasons. First, because the edges of the metal or pad implant of two sensor cells are parallel to each other. Hence the two dimensional simulation can easily be scaled to the full pad length in the simulation. Second, this is also due to the limited computational resources, as conducting three dimensional simulations of two or more pads is not possible. The geometry of the *Inter Pad Region* is shown in Figure 5.24. All simulations in this section are simulated at room temperature and with a bulk doping concentration of $1 \times 10^{19}\,\mathrm{cm^{-3}}$. This corresponds to a full depletion voltage of $\approx$ 58 V for 200 µm thick p-type (7.3 kΩ cm) and n-type (2.433 kΩ cm) sensors.
For the design of the sensor layout it is important to understand and optimise different characteristics like the breakdown stability, inter pad resistance and inter pad capacitance. These issues are addressed in the following sections.

5.4.1 Breakdown Simulation

An essential quality of the HGCal sensor is high voltage stability. The sensors have to be designed in a way to withstand bias voltages up to 1000 V. This is due to the intention to fully deplete the sensor to get the maximum charge collection efficiency. With higher irradiation damage higher bias voltage is required to reach that goal. To achieve this goal, geometry variations are performed to find the optimal design of the *Inter Pad Region* with regards to the breakdown stability. In the simulation the breakdown voltage is defined as the voltage where the ionization integrals equal 1. This means that the avalanche condition is reached, which means that the electric field is strong enough to produce extra electron-

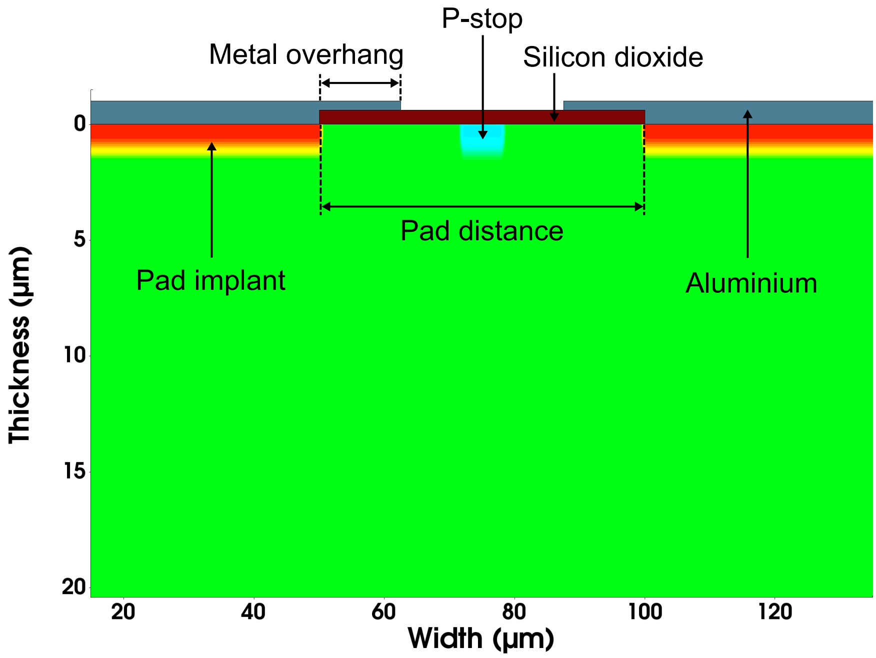

Figure 5.24: The figure shows the cross section of the geometry between two pads used for 2D simulations. It is called *Inter Pad Region*. The outer edge of the implants of the pads have a distance to each other, which is simply referred to as "pad distance".

hole pairs. The ionization integrals use ionization coefficients for electrons and holes and the integration is along the electric field lines through the depletion zone. They are calculated after the entire system of carrier transport equations is solved in a postprocessing mode. This method is more precise than the regular approximate breakdown analysis, which solves only the ionization integrals, but is also fast and has fewer convergence issues than other methods.

Figure 5.25a shows the electric field at $-1000\,\mathrm{V}$ of the *Inter Pad Region* geometry. Both pads are grounded and the back is biased to $-1000\,\mathrm{V}$. Each pad has aluminium on top of the implant. The metal additionally extends on top of the silicon dioxide. The amount of extension of the metal is called metal overhang and is $10\,\mathrm{\mu m}$ in this figure. It can be seen that the highest electric field region is directly beneath the edge of the metal overhang in the silicon dioxide and the silicon bulk. The reason for the metal overhang is that the highest electric field is shifted into the dioxide. Since the silicon dioxide has a much higher dielectric strength in comparison to the silicon bulk, it increases the breakdown voltage of the whole device. The second highest peak in the silicon bulk is near the corner of the pad implants. Another high field region is next to the p-stop implant. The electric field in the p-stop is zero and in general it increases when going towards the pads. In Figure 5.25b two p-stops with a distance of $10\,\mathrm{\mu m}$ are implemented instead of a single one. The rest of the parameters is the same as in Figure 5.25a. Between the two p-stops the electric field is zero. In comparison to the case with a single p-stop, the distance between the edge of the p-stop and the high field beneath the metal edge is smaller. Hence the electric field gets more condensed in this region. This leads in general to higher electric fields in the two p-stop (p-stop atoll) geometry in comparison to the single p-stop (p-stop common) geometry and hence to earlier breakdowns.

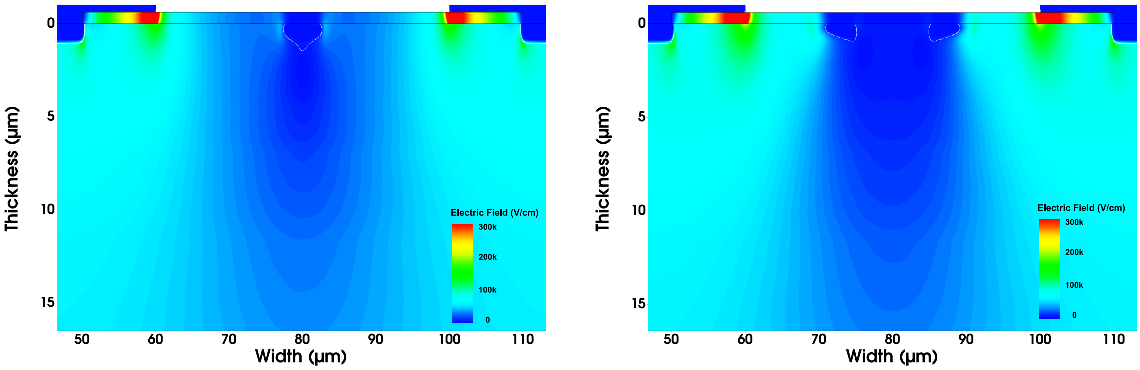

(a) **(b)**

Figure 5.25: Electric field distribution at −1000 V of the *Inter Pad Region* geometry with 10 µm metal overhang and 60 µm pad distance (a). The same but with two p-stop implants is shown in (b). In the silicon bulk the highest field peaks are located beneath the metal edge. Next to the corner of the pad implant is the second highest peak. The metal overhang shifts the region with the highest electric field in the silicon dioxide. Since this material has a higher breakdown voltage in comparison to silicon the whole device is more robust against high voltage.

The results of the breakdown simulations with the p-stop common *Inter Pad Region* geometry is shown in Figure 5.26a. Increasing pad distance leads to a decrease of the breakdown voltage. An additional variation of the metal overhang shows, that with increasing metal overhang the breakdown voltage increases as well. Both behaviours can be explained in the following way. If the metal overhang decreases, the distance between the high electric field beneath the metal edge and the one near the pad implant gets closer. When this happens the local electric field near the pad implant gets higher from both contributions and hence leads to earlier breakdowns. The increasing high voltage stability with lower pad distances is explained by the higher homogeneity of the electrostatic potential between the two pads, and hence the lower electric fields between the pad and the p-stop. Higher homogeneity means, that the potential at the p-stop region is closer to the potential of the pads. Even though the distance between the metal edge and the p-stop edge is larger, the higher potential difference leads to higher electric fields near the pad in the case of larger pad distances.

Figure 5.26b shows a cut line of the electric field 50 µm below the Si/SiO_2 interface. The geometry is the *Inter Pad Region* with a pad distance of 40 µm. Different metal overhang values are simulated. As previously explained, the electric field peak is located beneath the edge of the metal overhang. With increasing metal overhang the position of the highest electric field peak moves in accordance with the metal edge and simultaneously decreases in maximum value.

Figure 5.27 shows the results from simulations using the two p-stop geometry. It is similar to the geometry shown in *Inter Pad Region*, but with two p-stops, which have a distance to

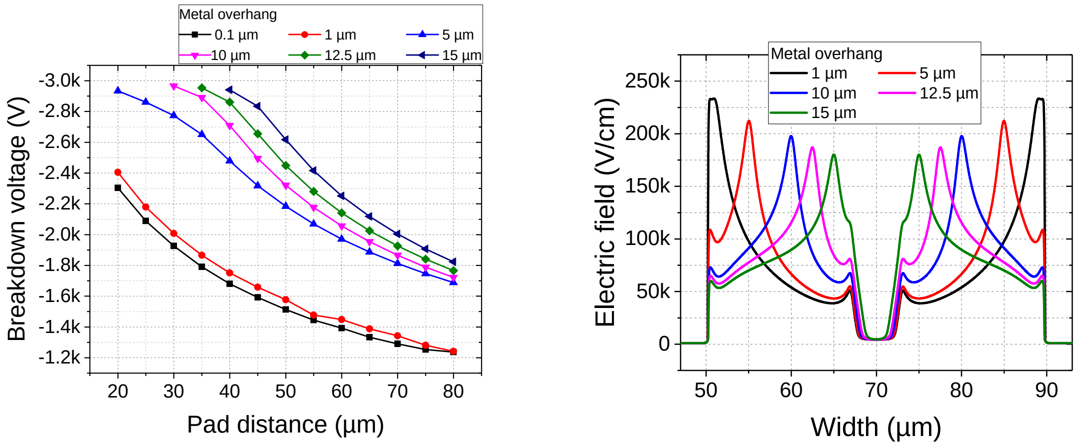

(a) **(b)**

Figure 5.26: Breakdown simulation with the *Inter Pad Region* geometry. In Figure (a) the pad distance and the metal overhang are varied. Increasing pad distance lowers the breakdown voltage. Increasing metal overhang increases the breakdown voltage. In Figure (b) the cut line of the electric field 50 nm below the Si/SiO_2 interface is shown. The pad distance is 40 µm and the position of the maximal peaks, located beneath the metal edge, moves in accordance with the metal overhang. Larger metal overhang decreases the value of the electric field peaks.

each other called "p-stop distance". In the breakdown simulation the pad distance, p-stop distance and metal overhang parameter are varied. All of them influence the breakdown behaviour. The first plot, Figure 5.27a, shows the result of the p-stop distance and pad distance variation at a fixed metal overhang of 10 µm. With higher p-stop distance the breakdown voltage decreases. The same effect can be seen in Figure 5.27b. With the increase of the p-stop distance, the distance between the outer edge of the metal overhang and the p-stop implant gets smaller. Consequently, the area with high electric field under the edge of the metal overhang gets closer to the p-stop implant. The breakdown voltage will decrease in this case. If the metal overhang is decreased, the electric field peaks beneath the metal edge and near the pad implant get closer. This leads to premature breakdown, which is shown in 5.27b, where the pad distance is fixed to 60 V. It can also be seen that between 1 µm and 5 µm metal overhang the breakdown voltage increases a lot more than for all other simulated metal overhang values. From the simulations presented here, one can conclude that a minimum metal overhang of 5 µm is the most efficient solution regarding both high-voltage stability and space consumption.

In Figure 5.27c the p-stop distance is fixated to 10 µm and the metal overhang and pad distance are varied. The metal overhang variation is performed in finer steps in comparison to the one in Figure 5.27b and it can be seen that the most efficient solution is actually 4 µm. With increasing metal overhang the breakdown voltages increase and reache a plateau until it starts to drop again. The decrease starts when the metal overhang is so large and the pad distance so small that the electric field maximum below the metal edge gets too close to the p-stop. Getting too close means, that the degrading effect of the field peak beneath the metal edge reaching the p-stop outweighs the beneficial effect of the increasing metal overhang.

In Figure 5.27a, 5.27b and 5.27c is a black circle. It highlights the only common parameter set, which consists of 10 µm metal overhang and 10 µm p-stop distance and 60 µm pad distance. This set has no further meaning besides making the comparison of the results from one figure to the other easier.

Figure 5.27d shows a cutline of an electric field simulation 50 nm below the Si/SiO_2 interface. In this simulation the p-stop distance is varied and each distribution is centred around a width of 80 µm for better visibility. The metal overhang is fixed to 10 µm. It can be observed that with increasing p-stop distance the electric field peak beneath the metal edge is increasing. Additionally, the smaller peak at the edge of the p-stop implant is increasing as well.

Complementary to the p-type simulation, n-type has been investigated as well. Figure 5.28a shows the electric field at 1000 V for the n-type version of the *Inter Pad Region* geometry. This means that the bulk polarity is n-type and that there is no p-stop. Furthermore a metal overhang of 10 µm and a pad distance of 60 µm is chosen. The electric field distribution is very similar to the single p-stop case. It shows the main electric field peak beneath the edge of the metal overhang. In addition, the second highest field region is again close to the corner of the pad implant in the bulk. Even though there is no p-stop, the electric field in the middle is close to zero.

A more detailed view of the electrical field distribution below the Si/SiO_2 interface is shown in Figure 5.28b. Several different pad distances are simulated and compared at 1000 V, while the metal overhang is fixed to 12.5 µm. All cutlines are centred around the width of 90 µm. The decrease of the electric field peaks with decreasing pad distance can be seen immediately. The highest peaks are again located beneath the edge of the metal overhang. In the centre of the two pads is the region with the lowest electric field.

The result of the breakdown simulation for n-type is summarized in Figure 5.29. Both geometry defining parameters, the metal overhang and the pad distance, are varied. The result is the same as the single p-stop case. With increasing pad distance the breakdown voltage decreases. The increase of the metal overhang leads to an increase of the breakdown voltage as well.

When comparing the behaviour of p-type and n-type, it can be seen that for the same geometric dimensions the single p-stop variant has the highest breakdown voltages. It has up to 20 % higher breakdown voltages in comparison to the n-type version. The two p-stop version has the worst performance regarding the high voltage stability. It is about 15 % worse than the n-type version, at the smalles simulated p-stop distance. The difference is larger for larger p-stop distances.

From the previous simulations it is clear that the optimum breakdown voltage has to be finely balanced with respect to the pad distance, metal overhang, and p-stop distance. In general the breakdown stability is the best, when the pad distance is as small as possible.

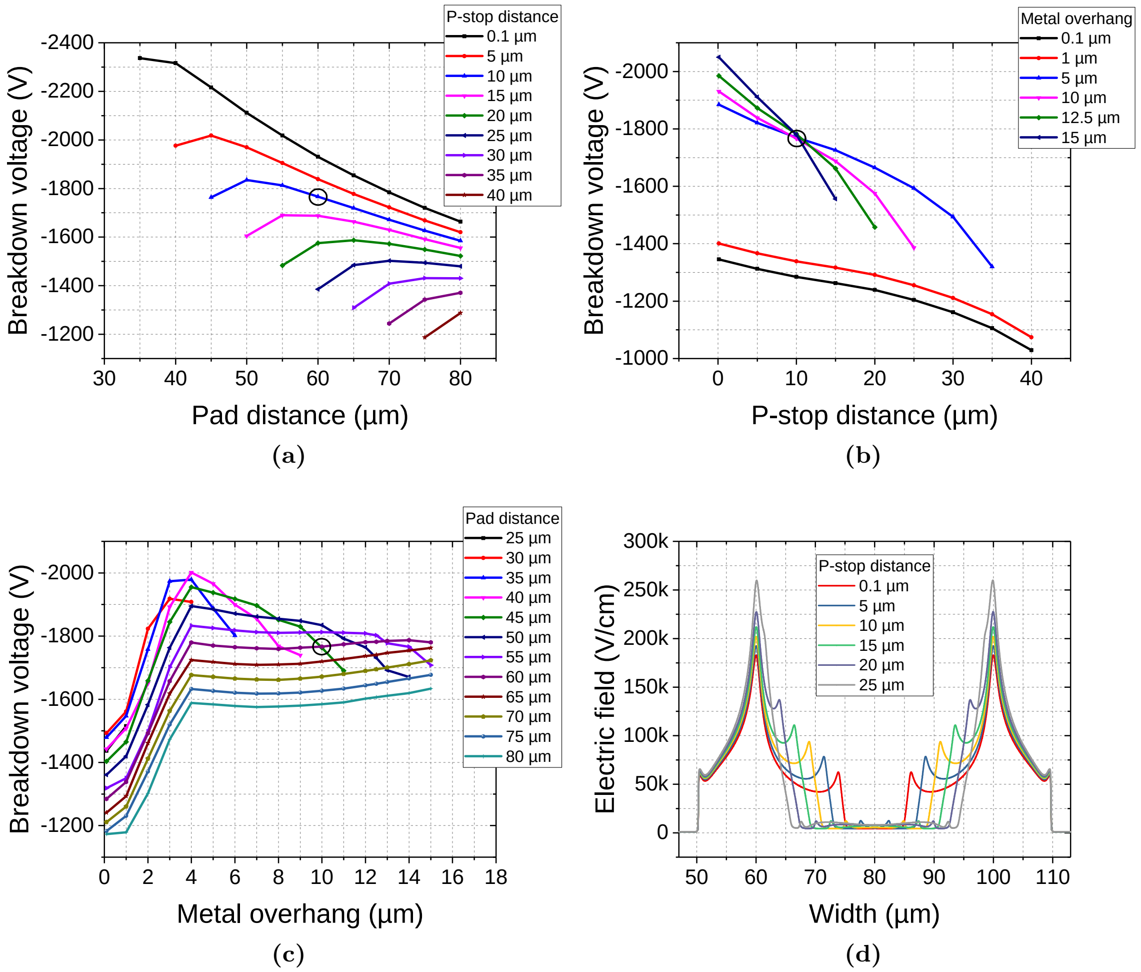

Figure 5.27: Simulated breakdown voltages for different pad distances, metal overhangs, and p-stop distances. The geometry used is like the *Inter Pad Region* but with two p-stop implants instead of one. In Figure (a) the metal overhang is fixed to 10 µm, while the other two parameters are varied. Figure (b) has the pad distance fixed to 60 µm and Figure (c) has the distance between the two p-stops fixed to 10 µm. Highlighted with a black circle is the only point, which overlaps in all three figures. Lower pad distance and lower p-stop distance lead to higher breakdown voltages. Higher metal overhang leads to higher breakdown voltages, as long as the pad distance is large enough and the p-stop distance is small. Figure (d) displays the electric field cut line 50 nm below the Si/SiO_2 interface.

The exception is, when the pad distance is so small that the metal edge is too close to the p-stop implant. In this case the behaviour gets worse. Furthermore, the breakdown voltage improves with higher metal overhang, as the electric field peaks beneath the metal edge and near the pad implant get separated further. Without exception it can be said, that the performance with regard to the breakdown stability improves with smaller p-stop distances. In this regard, optimally one uses only a single p-stop.

When using this simulation in the design of the sensors, it should be taken into account, that the production of real sensors has to obey some design rules given by the manufacturer.

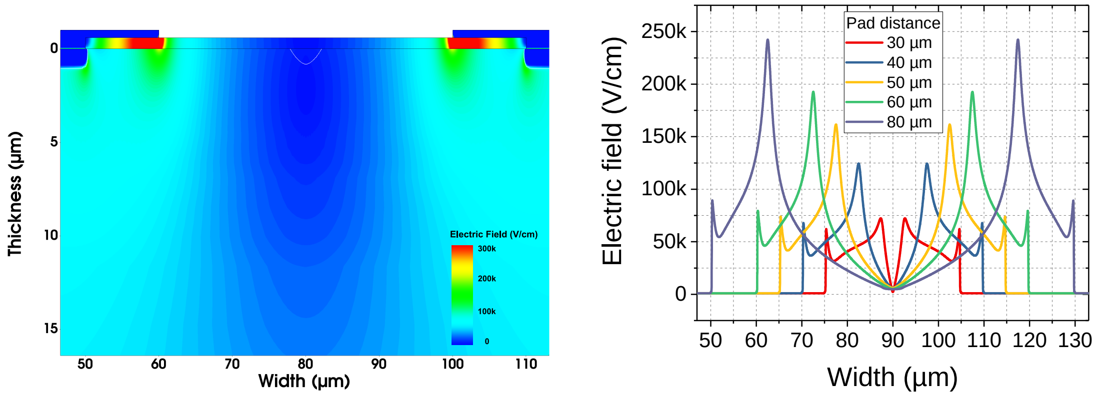

(a) (b)

Figure 5.28: The electric field distribution at 1000 V of the *Inter Pad Region* of a n-type device is shown. It has no p-stop and has 10 µm metal overhang and 60 µm pad distance (a). The highest field peaks are beneath the edge of the metal overhang. Equivalent to the p-type case is the location of the second highest electric field region in the silicon bulk, which is near the corner of the pad implant. Figure (b) shows the electric field cut lines 50 nm beneath the Si/SiO_2 interface for different pad distances at 1000 V. Decreasing the pad distance decreases the highest electric field peaks.

Design rules, for example, dictate minimum distances between certain mask layers or minimum structure size. Also effects like mask alignment errors have to be taken into account. Therefore, each geometric parameter has to be chosen in such a way that the design is robust even with an error of a few micro meter on each parameter. That is why, for example, the choice of using 5 µm metal overhang and a pad distance of 20 µm is bad, even though it resulted in one of the highest breakdown voltages in the single p-stop simulation. With metal over-edging or mask misalignment the effective metal overhang can be reduced to zero and the breakdown voltage reduces significantly. For the prototype HGCal sensor 50 µm pad distance with a metal overhang of 12.5 µm is used. This is a robust solution, which allows to use the two p-stop variant with a p-stop distance of 4 µm. Even though the breakdown voltage is clearly higher for the unirradiated single p-stop case, the use of two p-stops might have an advantage when the sensor is irradiated.

5.4.2 Inter Pad Resistance

Another important property of the interpad region is the inter pad resistance. It should be as high as possible in the unirradiated case, as it will significantly decrease after the sensor is being irradiated. In case of the HGCal sensor geometry, the inter pad resistance is the resistance between a full pad and all its six neighbours. In the simulations here a full pad with the area 1 cm^2 is used. This corresponds to a circumference of 37 215 µm. The simulation of the interpad resistance is performed by biasing the sensor up to at least full depletion first. Afterwards a low voltage ramp is conducted between the full pad and its neighbours. Here the sensors are biased with ± 200 V and the low voltage ramp is up to 2 V.

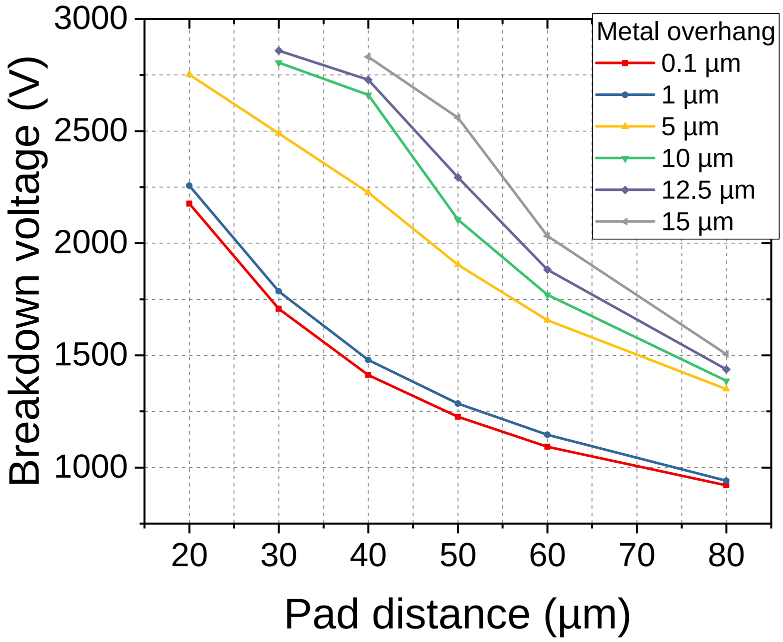

Figure 5.29: Breakdown simulation of the n-type version of the *Inter Pad Region* geometry. The pad distance and the metal overhang are varied. With increasing pad distance the breakdown voltage decreases and with increasing metal overhang the breakdown voltage increases. The behaviour is the same as for p-type.

The simulation is performed in 2D with a geometry similar to the *Inter Pad Region*. To get simulation results comparable with real measurements, the geometry has to be implemented as realistically as possible. Therefore, the width of the oxide is adjusted, the chamfer of the aluminium pads and the passivation layer are included for this simulation. The doping profile and concentration of the p-stop implant is according to a SRP (spreading resistance profile) measurement of a wafer of the first 8-inch HGCal demonstrator run. IV and CV measurements have been performed on a diode of the same wafer to extract the volume current and full depletion voltage. With a full depletion voltage of 53.9 V a bulk doping concentration of $1.78 \times 10^{12}\,\mathrm{cm}^{-3}$ can be calculated for the 200 µm thick diode with the use of Equations 2.5 and 2.24. With the knowledge from Figure 5.15, that the effective area of the diode is up to the outer edge of the guard ring, and the IV measurement of the real diode, the recombination liftetime $\tau_{\mathrm{e,h}}$ for electrons and holes can be adjusted. It is done in the same fashion as shown in Figure 5.13 and results in a value of $\tau_{\mathrm{e,h}} = 1.1 \times 10^{-4}\,\mathrm{s}$. The simulated current between the pads is fitted with a straight line fit. With the inverse slope of the fit the resistance is known.

The inter pad resistance is simulated for p-type with p-stop common and p-stop atoll geometry and for n-type. Figure 5.30a shows the results of the p-stop common geometry simulation. The first thing to note is that with increasing pad distance the inter pad resistance rises as well. This effect holds true even for different metal overhangs. Increasing the metal overhang leads to a decrease of the inter pad resistance. With larger metal overhang the electric field between the pads becomes smaller. This means a smaller potential barrier, which is located in the middle of the pads, needs to be overcome. Hence, the inter pad resistance is lower.

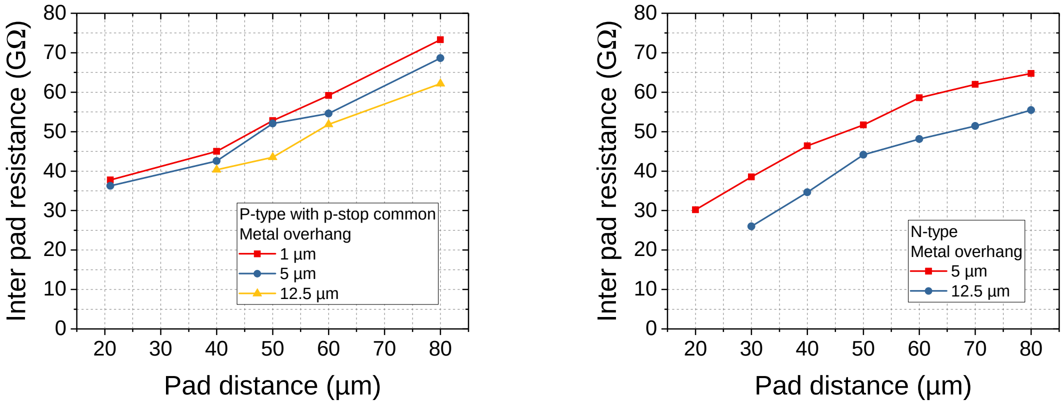

(a) **(b)**

Figure 5.30: Figure (a) shows the results of the interpad resistance simulation for p-stop common geometry. Increasing the pad distance increases the resistance. Increasing the metal overhang decreases the inter pad resistance. Figure (b) shows the same type of simulation but for n-type bulk without p-stop. The pad distance and metal overhang variation behaviour is the same as for p-type.

This phenomenon is the same when increasing the bias voltage of the sensor. With higher bias voltage, the inter pad resistance increases. This is shown in Figure 5.31. In the simulation the same p-stop common geometry is used as in Figure 5.30a. The inter pad resistance at a pad distance of 60 µm and a metal overhang of 12.5 µm is determined to be 51.92 GΩ at a bias voltage of −200 V. For a bias voltage of −60 V the result is 22.34 GΩ. The ratio of the resistance values is 2.32. In Figure 5.31 the cut lines of the electric field in x direction 100 nm below the silicon and silicon dioxide interface are shown. Theses lines are integrated and plotted in the same diagramme. The integral in x direction results in the potential the charges encounter between the pads. It can be seen, that in the middle of the pads, at the position of the p-stop the potential maximum is located. Comparing these maximal potential values for different bias voltages (−60 V and −200 V), it can be seen, that the higher bias voltage resulted in a 2.34 times higher potential maximum. In the inter pad resistance simulation a small voltage difference of 2 V is applied between the two pads. With higher bias voltage the potential barrier in the middle of the pads is higher by the same factor as the simulated inter pad resistance calculated from the inverse slope of the IV curve between the pads. The small difference can be attributed to a small error coming from the mesh of the simulation and the fact, that the cut line position is at one point only. This ratio of the integrated electric fields varies for other positions of the cut lines in the order of 1 %. The positions 50 nm, 200 nm and 700 nm beneath the surface were tested.

Figure 5.30b shows the inter pad resistance simulation results for n-type bulk. The increase with the pad distance and the decrease with increasing metal overhang is the same

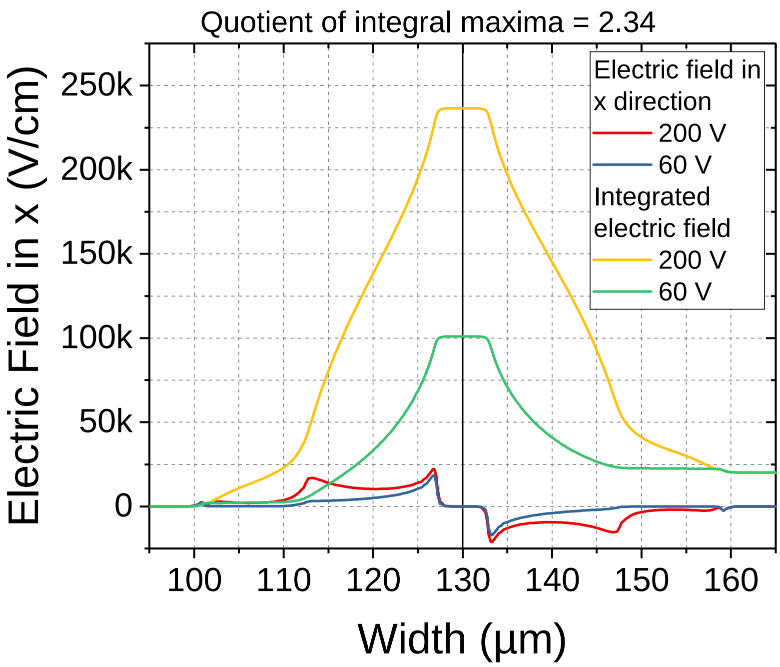

Figure 5.31: Cut lines of the electric fields for two different bias voltages in the inter pad resistance simulation shown in Figure 5.30a. Additionally, the electric field in x direction is integrated to calculate the potential, which is seen by the charge carriers between the pads. Higher simulated inter pad resistance values scale in the same way as the higher potential peaks due to different electric fields due to higher bias voltage.

as for p-type. At a first glance it might look like the overall resistance is about 10 % smaller than for p-type. After fitting with straight lines, the fit parameters listed in Table 5.9 are obtained. From them it can be seen that the difference between the p-type and n-type simulations are within the simulation uncertainty. No distinct difference between n-type and p-type can be observed. Furthermore, the gain in resistance with increasing pad distance is on average $(0.57 \pm 0.05)\,\mathrm{G\Omega\,\mu m^{-1}}$ for all geometries tested in Figure 5.30.

Table 5.9: Fit parameters for a linear fit for the graphs in Figure 5.30.

Type	Metal overhang (µm)	Intersection with y-axis (GΩ)	Slope ($\mathrm{G\Omega\,\mu m^{-1}}$)
P-type	5	22.96 ± 2.79	0.55 ± 0.05
P-type	12.5	16.86 ± 3.01	0.57 ± 0.05
N-type	5	21.25 ± 2.40	0.58 ± 0.04
N-type	12.5	11.62 ± 3.85	0.58 ± 0.07

In Figure 5.32a the results of the simulation of the p-type geometry with two p-stops is shown. The p-stop distance has a fixed value of 4 µm. In the same way as the two previous geometry variations, a larger metal overhang leads to a lower inter pad resistance. With increasing pad distance the inter pad resistance increases as well. The expected gain in inter pad resistance due to a second p-stop implantation is compensated by the deteriorating effect of the p-stop distance, which can not be too small due to design rules of the manufacturers. The effect of the p-stop distance variation is shown in Figure 5.32b. With increasing p-stop distance the inter pad resistance decreases significantly. In the 8-inch HGCal demonstrator design a p-stop distance of 34 µm is used in the 80 µm pad distance quadrant. According to the simulation the inter pad resistance for this geometry can be improved by factor six, when decreasing the p-stop distance to 4 µm.

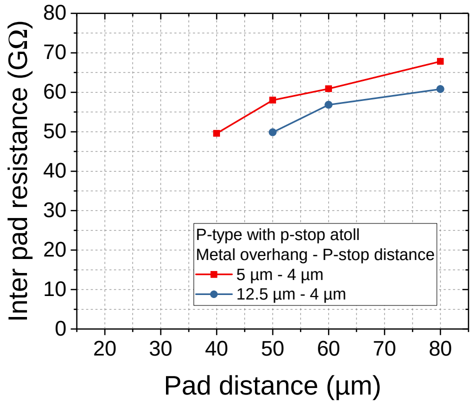

(a)

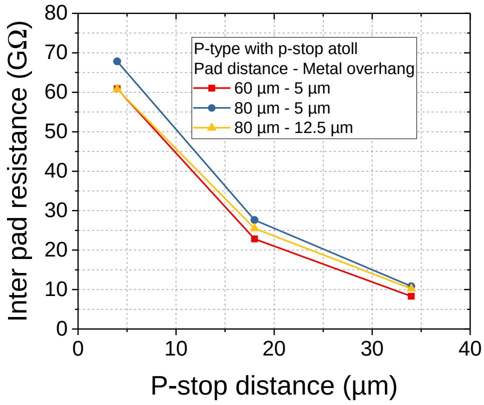

(b)

Figure 5.32: Figure (a) shows the results of the interpad resistance simulation for p-stop atoll geometry with a fixed p-stop distance of 4 µm. With increasing pad distance, the inter pad resistance increases as well. Increasing the metal overhang lowers the inter pad resistance. Figure (b) shows the results of the p-stop distance variation. With increasing p-stop distance the inter pad resistance decreases.

5.4.3 Inter Pad Capacitance

The total capacitance of a sensor pad consists of two components. One is the substrate capacitance, which mostly depends on the area of the pad and can be approximated with the parallel plate capacitor equation. The second component is the inter pad capacitance. This component can not be estimated with the parallel plate equation, since the effective thickness of the pads, which corresponds to the area in the equation, is not trivially known. Simulating the inter pad capacitance in TCAD is much more accurate, as it uses the correct geometry and solves the whole SPICE network between all contact electrodes.

The capacitance simulation here is performed at room temperature and at a frequency of 1 kHz. The dielectric constant of silicon used in the TCAD simulation is 11.7. An upgraded version of the *Inter Pad Region* geometry is used, similar to the one in 5.4.2. The bias voltage in the simulation is −200 V applied to the contact on the back. With a bulk resistivity of 7 kΩ cm and p-type polarity, the sensor is fully depleted. P-stop common and p-stop atoll geometry are simulated, but since the results are basically identical only the p-stop common results are presented here. Both pad contacts, each having a width of 200 µm are kept to ground. The capacitance between these two pads is plotted in Figure 5.33. It can be seen that the inter pad capacity decreases with pad distance. The curvature of the curves remain the same for different thicknesses. But for a higher metal overhang the descent is steeper. With higher sensor thickness the inter pad capacitance increases. The offset between two curves of different thickness is constant. Between 300 µm and 200 µm there is, on average, a difference of (0.483 ± 0.009) pF. And between 200 µm and 120 µm there is, on average, a difference of (0.621 ± 0.031) pF. The effective area for the inter pad capacitance does not only consist of the metal and implant of the pad but also of parts of the silicon bulk.

For comparison, the capacitance values of the full cells are shown in Figure 5.33b. This is the second component or the substrate capacitance. The figure shows simulated values for the three thicknesses of HGCal sensors and for three different areas. For example, for the 200 µm thick sensors with a pad distance of 50 µm and full pad area, this component is about 20 times larger than the inter pad capacitance. Additionally, this figure highlights the 65 pF value with a black line. This value marks the maximum cell capacitance. This value is defined, to limit the electronic noise to be less than 2500 electrons during the whole operation to allow MIP visibility [8]. It also shows the necessity to use thinner pads (about $0.5\,\mathrm{cm}^2$) for the thinner sensors. Using normal full pad size with areas about $1\,\mathrm{cm}^2$ would result in cell capacitances beyond 90 pF.

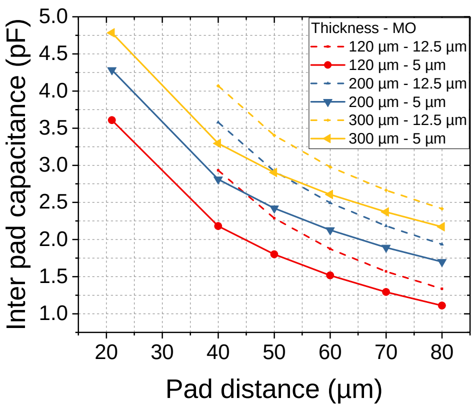

(a)

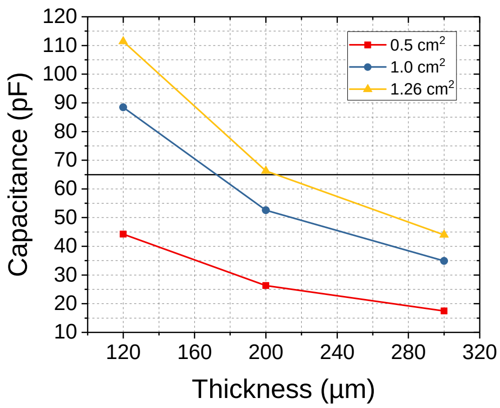

(b)

Figure 5.33: Result of inter pad capacitance simulation (a). With increasing pad distance the inter pad capacitance decreases. For thicker sensors the inter pad capacitance increases as well. In Figure (b) the capacitance of the full cell for different areas and sensor thicknesses is shown.

The area of a full cell in the prototype 8-inch HGCal design is almost $1.26\,\mathrm{cm}^2$. The bulk capacitance is very close to 65 pF for the 200 µm thick sensor. Together with the simulated inter pad capacitance, the total pad capacitance would be 5 % higher than the maximum value. This should be considered in future iterations when finalizing the design of the cell size or the readout electronics.

5.5 Sensor Periphery Optimization

For the construction of a high voltage stable sensor the design of the periphery is crucial. The periphery consists of two main components. The first is the edge ring, which is a ring of high doping concentration similar to that of the pad implant, but with the same polarity as the bulk doping. Above the implant is a metal layer like the one on top of the sensor pad. The reason for the edge ring is to bring the high voltage potential of the back to the front. Each sensor has to be cut out of the wafer. When dicing (cutting) the sensors on the wafer a multitude of crystal defects or micro cracks will be created at the edge of the sensor. If a high potential difference is applied at this cutting edge the leakage current and high electric fields will deteriorate the performance of the sensor significantly. To avoid the effects of the unavoidable defects, the area surrounding the sensor has to be an edge ring. The second important component of the periphery is called guard ring. It is located between the biased sensor pads and the edge ring. The function of the guard ring is to smooth out the electric field between the high potential on the edge ring and the ground potential of the biased pads. To accomplish the former, the guard ring is floating, meaning it is not contacted to any power supply and hence on undefined potential.

Figure 5.34 shows an image of the cross-section of the periphery. The parameters used to describe the geometry of the periphery are indicated as well. This geometry is used in the 2D TCAD simulation. On the left in red colour is the implantation of the edge ring. In the middle and right part of the figure the implantation of the guard ring and the biased part is shown in green. The design of the 8-inch HGCal sensors foresees two guard rings. One is floating and fullfills the purpose described above, while the other one is biased. It is biased to avoid a capacitative coupling of the signal of a border pad to its neighbours via a floating guard ring. The geometry between the biased guard ring and the biased sensor pads are described in the same way as the inter pad region in 5.4.1. Therefore the periphery here only includes the area between the biased guard ring and the edge ring.

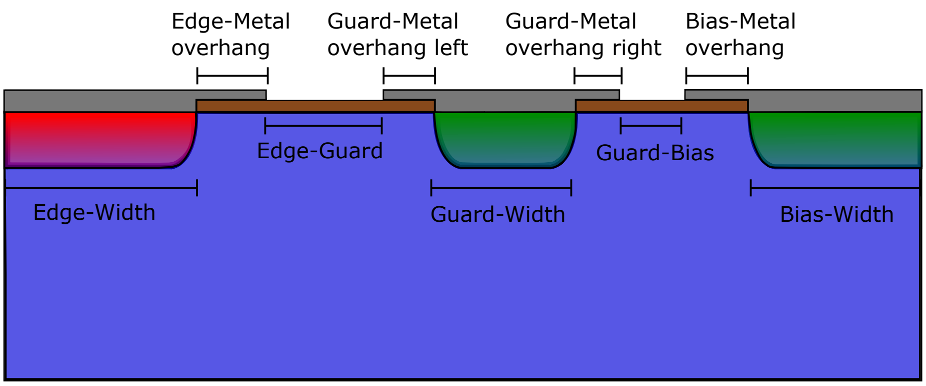

Figure 5.34: Image of the periphery of the HGCal sensor. All important parameters for the geometry variation simulation are presented.

The parameters used in the first 8-inch demonstrator HGCal sensor are used as the starting point of the optimisation. They are listed in Table 5.10. Due to the huge amount of combination possibilities, when varying 9 different parameters, lots of work had to be put into the meshing of the device in the simulation. On one hand the mesh should be as small as possible to reduce the computation time, on the other hand the accuracy should not suffer. Furthermore, due to the floating contact in the simulation, convergence issues arised with many different meshes. The final mesh had about 55000 elementes. Aggravating the simulation is the fact, that most parameters have an influence on each other.

Table 5.10: Parameters for the periphery of the first 8-inch demonstrator HGCal sensor. These parameters are the starting parameters for the optimisation. The abbreviation MO means metal overhang.

Edge-Width	Edge-MO	Edge-Guard	Guard-MO left	Guard-Width	Guard-MO right	Guard-Bias	Bias-MO	Bias-Width
502 µm	50 µm	119.5 µm	32.5 µm	18 µm	12.5 µm	17 µm	22.5 µm	131.5 µm

To get a first impression only three parameters are varied at the same time. In Figure 5.35 IV curves are shown, where the Guard-Metal overhang right, Guard-Bias, and Bias-Metal overhang are varied. The variation of the three parameters resulted in about 200 IV curves, which are coloured green in the figure. Three curves are highlighted. The red one shows the baseline geometry parameters, whereas the orange one shows the best geometry and the blue one the optimised set of parameters. First of all it can be seen that the simulated breakdown starts already below −1000 V. In comparison to the simulated inter pad breakdown voltages in Section 5.4.1, these values are up to factor 3 smaller. Therefore, it can be said for sure that the weak point of the sensor design with regard to the high voltage stability is the periphery. The curve coloured in orange showed the highest breakdown voltage in the variation of the three parameters. This set incorporates a metal overhang of 5 µm. To create a robust design, which takes into account process inaccuracies like metal over-edge or mask misalignment, the 5 µm solution should not be used. Consequently, the optimised parameter set has a value of 10 µm for parameters Guard-MO right and Bias-MO. The Guard-Bias parameter becomes 24.5 µm.

A more detailed investigation of the single parameter Guard-Bias can be found in Figure 5.36a. Figure 5.36b shows the same data set but is more focused on the breakdown region. Increasing this parameter until a value of 24.5 µm improves the breakdown voltage. After this value the performance degrades.

The next parameter varied is the so-called Edge-Guard parameter. Figure 5.37a shows the IV curves for parameter values ranging from 20 µm to 200 µm. For the two lowest values the periphery performance drops considerably. Figure 5.37b shows the same data but more zoomed into the breakdown region. The curve with the highest breakdown has the Edge-Guard parameter value 119.5 µm. With increasing Edge-Guard parameter the breakdown voltage increases up to this point and starts to drop again afterwards. It can also be seen that this value is rather robust, as a change of this parameter by ±10 µm changes the performance only marginally.

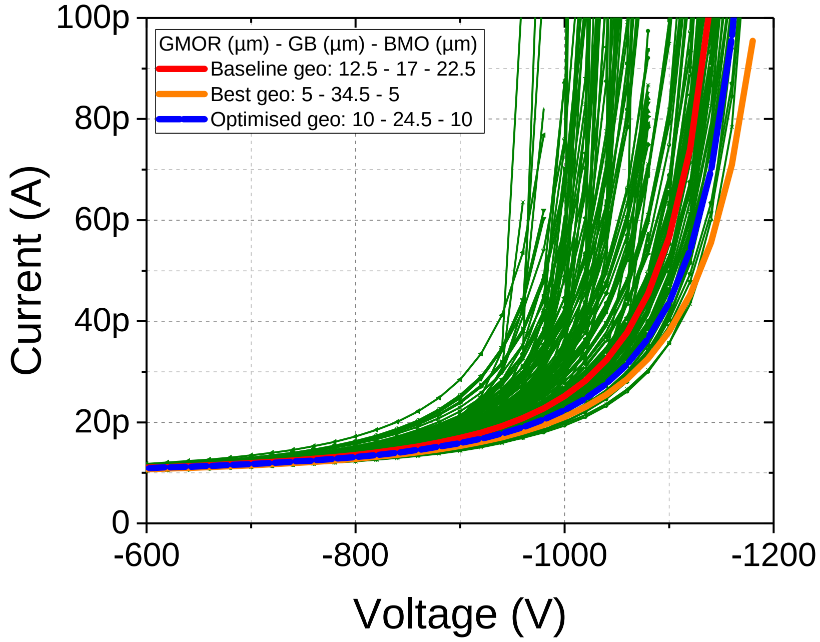

Figure 5.35: Many IV curves from different geometry parameter combinations are shown. The parameters Guard-MO right, Guard-Bias and Bias-MO are varied. The IV curves originating from the baseline, best, and optimised geometry are highlighted.

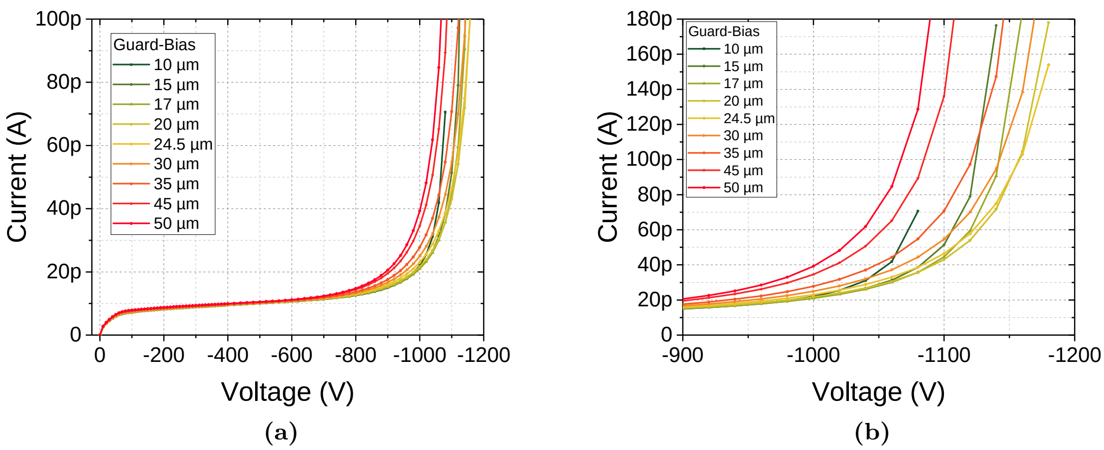

Figure 5.36: Figure (a) shows IV curves, where the parameter Guard-Bias is varied. Figure (b) shows the same data set but with more focus on the breakdown region. It can be seen that the breakdown voltage is highest at a value of 24.5 µm and decreases for smaller and larger parameter values.

The last single parameter, which is varied here is the Guard MO-left parameter. The simulated IV curves are displayed in full in Figure 5.38a and with higher focus in the

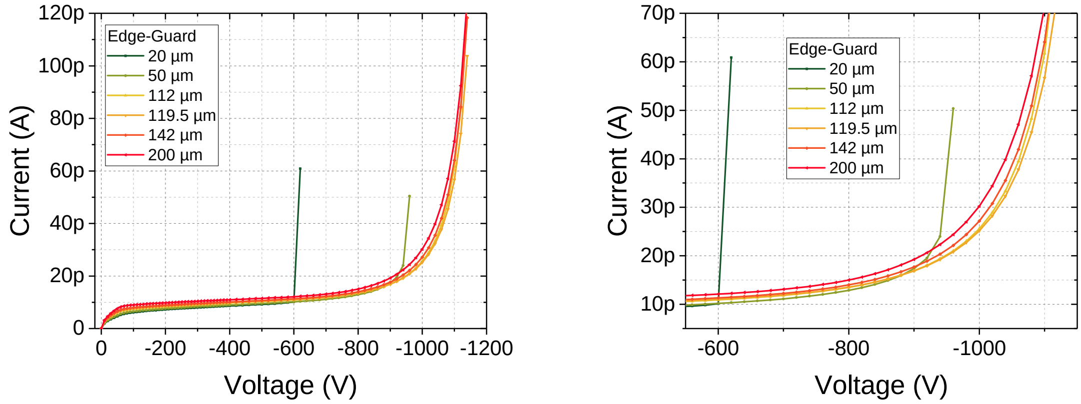

(a) (b)

Figure 5.37: Figure (a) shows simulated IV curves for different values of the Edge-Guard parameter. Figure (b) displays the same set of data, but shows an enlarged view of the breakdown region. It can be seen that the breakdown voltage increases up to an Edge-Guard value of 119.5 µm and drops afterwards. Hence the baseline value ist already the best and most robust choice.

region of interest in 5.38b. The optimal value with the highest breakdown voltage is at 40 µm. For both smaller and larger values the performance degrades. The optimal value is a robust solution as well. Changing the value by ±10 µm changes the breakdown voltage only slightly.

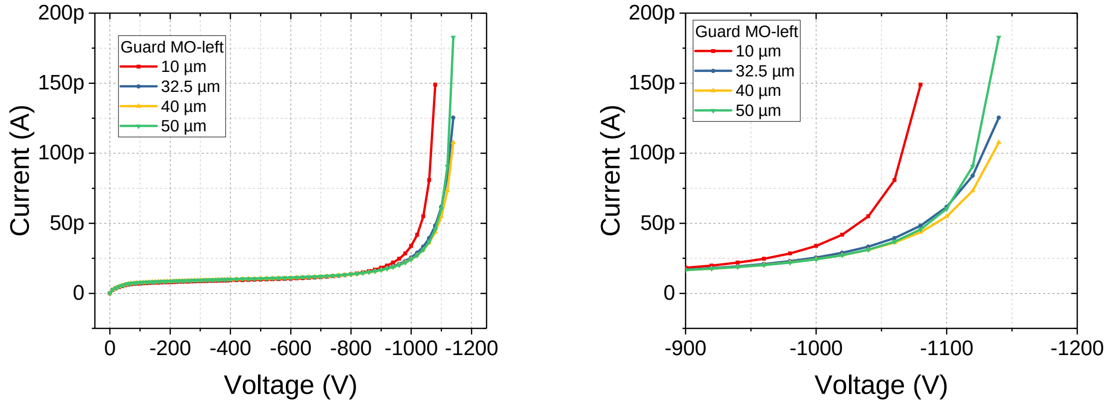

(a) (b)

Figure 5.38: Figure (a) displays IV curves with different Guard-MO left parameters. Figure (b) shows the same data with more focus on the breakdown region. It can be seen that the parameter value 40 µm is the best solution and is also robust.

The breakdown values so far are rather low, partially even below −1000 V. For a more realistic simulation the passivation layer, which is on every real sensor, can be added. Figure 5.39a shows the distribution of the electric field when the passivation is added at

$-1000\,\mathrm{V}$ bias voltage. As expected, the highest electric field peaks are below the edges of the metal overhang. In Figure 5.39b a cut line 50 nm below the Si/SiO_2 interface is shown. The electric field distribution of the optimised and baseline geometry are compared. It can be seen that the optimised geometry has the position of the peak beneath the bias-metal edge shifted and at 3.8 % lower.

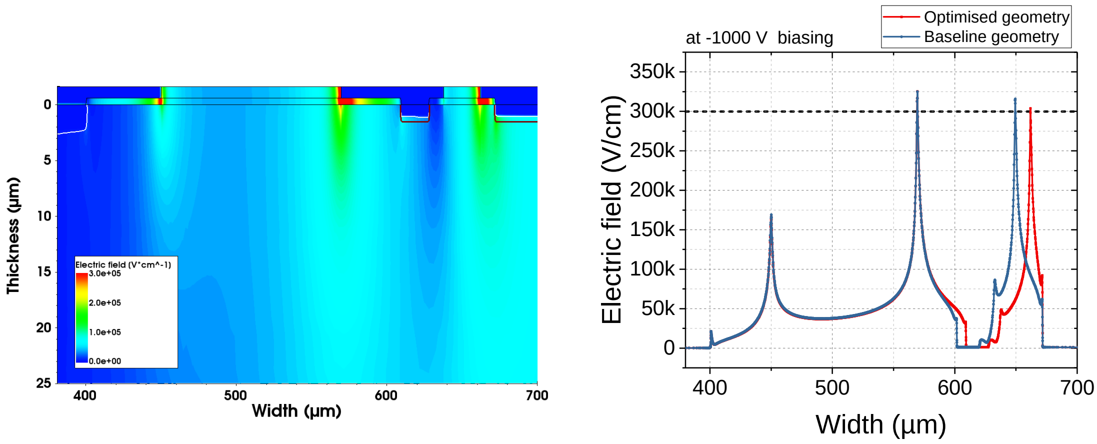

(a) **(b)**

Figure 5.39: Figure (a) shows the electric field distribution of the periphery with the addition of the passivation layer. The bias voltage is $-1000\,\mathrm{V}$. The breakdown voltage in the simulation is higher when the passivation is implemented. The electric field spreads in the passivation and reduces the maximum electric field seen in the silicon bulk. Figure (b) shows the electric field values at a cut line 50 nm below the Si/SiO_2 interface for the optimised and baseline geometry. The optimised geometry shows lower electric field peaks.

Besides the passivation, a different interface oxide charge can be present in a real sensor. So far a value of $5 \times 10^{10}\,\mathrm{cm}^{-2}$ is used, which is a typical value for Infineon sensors. It can be seen in Figure 5.40a that the breakdown voltage changes with a different interface oxide charge. Additionally, IV curves for the optimised and baseline geometry are shown. With increasing interface oxide charge the breakdown voltage increases. The optimised geometry is always better than the baseline geometry. Figure 5.40b shows IV curves only for an interface oxide charge value of $5 \times 10^{10}\,\mathrm{cm}^{-2}$ with passivation. The difference between the optimised geometry and the baseline geometry is 50 V. This corresponds to a 3.8 % lower breakdown voltage of the baseline geometry. It is equivalent to the behaviour shown in Figure 5.39b. The lower electric field in the new geometry directly translats into a higher breakdown voltage.

The sensors of other another vendor such as HPK typically have a higher oxide charge in the range of $1 \times 10^{11}\,\mathrm{cm}^{-2}$. This means that this sensors would have a higher breakdown voltage by about 160 V according to this simulation shown in Figure 5.40a.

Comparing the simulations without passivation, as shown in Figure 5.35, with the ones with passivation, as shown in Figure 5.40a, an increase in breakdown voltage between 100 V and 200 V can be determined.

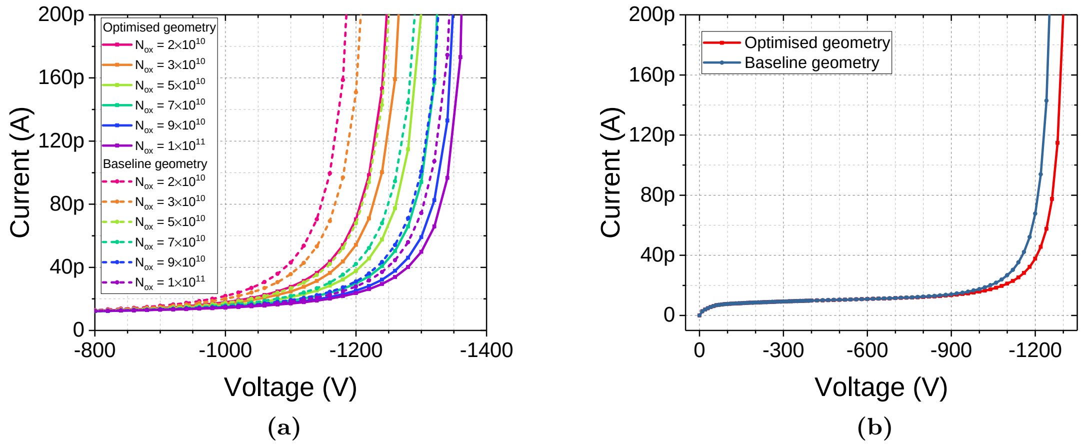

Figure 5.40: Comparison of the current-voltage behaviour for the optimised and baseline geometry. (a) Simulated IV curves for different interface oxide charges. (b) Geometry comparison for $N_{OX} = 5 \times 10^{10}\,\mathrm{cm}^{-2}$.

The final set of parameters that makes up the optimised geometry is summarized in Table 5.11. The parameters Guard-MO left, Guard-MO right, Guard-Bias, and Bias-MO are changed to optimise the breakdown behaviour. An increase of breakdown voltage of 50 V is achieved with the new parameter set. The parameter Edge-Width is reduced down to 400 µm as well. This does not influence the breakdown behaviour but the sole purpose is to reduce the active area lost due to the periphery. The periphery parameters used as baseline in the first 8-inch prototype sensor are already partly optimised. Nevertheless, the geometry of the periphery could not only be validated but also improved to have about 4 % or 50 V higher breakdown.

Table 5.11: Parameters for the periphery of the 8-inch HGCal prototype sensor. These parameters are the result of the optimisation. The abbreviation MO means metal overhang.

Edge-Width	Edge-MO	Edge-Guard	Guard-MO left	Guard-Width	Guard-MO right	Guard-Bias	Bias-MO	Bias-Width
400 µm	50 µm	119.5 µm	40 µm	18 µm	10 µm	24.5 µm	10 µm	131.5 µm

6

Measurements of Silicon Sensors

This chapter is about the measurement of test structures and HGCal sensors. Test structure measurements include current, capacitance, and charge collection measurements. Sensor measurements include current, capacitance, inter pad capacitance, inter pad resistance, and inter pad punchthrough measurements. Additionally, three different types of current measurement methods are compared. They comprise the single-needle measurement, 7-needle measurement, and probe card measurement. These measurements are performed on HGCal prototypes of 6-inch sensors from Hamamatsu and on the first 8-inch HGCal demonstrator sensors from Infineon Technologies Austria AG. At the time of writing this thesis, the sensors with the 8-inch prototype design were not yet delivered by the vendor and hence could not be investigated.

At first, four different measurement setups will be introduced. These sections will be followed by measurements of test structures that are needed for the extraction of relevant parameters needed in TCAD simulations. Measurements of 6-inch sensors will be used to describe all measurement methods in detail. In the end of the chapter, two 8-inch HGCal demonstrator sensors from Infineon will be compared.

6.1 Measurement Setup

6.1.1 Probe Needle Positioner Setup

The first setup used in the sensor measurements is the probe needle positioner setup. It is a highly flexible setup as it can be used for all measurements except the IV measurements with the probe card. Figure 6.1a shows an overview of the setup. On top of the dark box is a metal construction housing several devices needed for electrical measurements. They include two source measure units (SMUs), namely Keithley 237A and Keithley 2657A. Additionally, an Agilent E4980A LCR meter is present. The dark box can be humidity controlled with dry air and two defined set points. In the measurements performed with this setup, the humidity is always between 25 % and 35 %. The temperature cannot be controlled in the box. The temperature in the box is the ambient temperature of the temperature-controlled clean room of $(22 \pm 1)\,°\mathrm{C}$. The dark box consists of metal plates to shield against noise and make the setup light-tight. In the box is a baseplate with a motorised and computer controlled xyz-table. Fixed to the moveable table is an isolated metal plate, the so-called chuck. It has holes to fixate sensors on the chuck with the use of vacuum. Additionally, the chuck is biased with high voltage, allowing to apply the voltage to the back of the sensors. Above the chuck is a Nikon stereo microscope, which is needed to contact the sensor pads with probe needles.

In Figure 6.1b, an enlarged view of the chuck with an 8-inch HGCal sensor and 7 probe needle positioners is visible. Next to the chuck is a metal platform for the positioners. They are fixated to the platform with magnets embedded into their base. The platform and the position of the needles is fixed. Only the table with the sensor moves during automatic measurements.

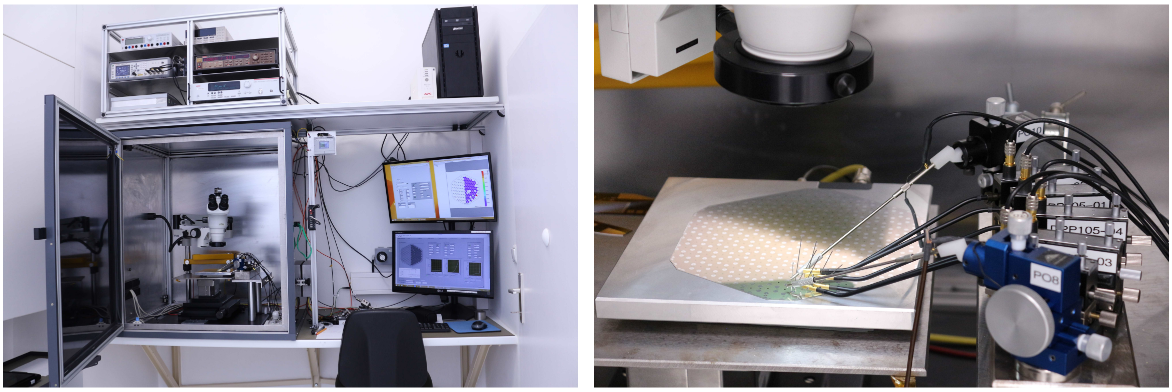

(a) **(b)**

Figure 6.1: (a) Overview of the probe needle positioner setup. On top of the dark box various instruments like an SMU or LCR meter are shown. In the dark box, a metal chuck is located on top of an xyz-table. (b) Enlarged view of the chuck with an 8-inch HGCal demonstrator sensor on top. The microscope in the top part of the picture is needed to manually contact the sensor pads with the probe needle positioners.

6.1.2 Probe Card Setup

A probe card allows fast automated checks of the electrical sensor properties. During series production, almost 27000 wafers need to be tested before they are implemented in the HGCal endcap. The manufacturers of the sensors and several institutes of the HGCal group of the CMS collaboration share the responsibility to test all of them. While the manufacturers focus on testing every sensor to verify whether it is within the specifications of the sensor order, the institutes measure a part of the sensors in more detail. Even though only a fraction of all sensors have to be measured by a single institute, it is mandatory that the measurement is efficient, no sensors are destroyed during measurement, and the measurement is fast so that all sensors can be measured in a reasonable amount of time. Therefore, the goal for each sensor characterising institute is to have a working probe card setup.

Figure 6.2 shows the status of the self-made probe card setup at HEPHY. It features an aluminium frame with a steel platen on top, which holds the probe card. In the centre of the construction, below the probe card, the isolated metal chuck is located. When a sensor is measured, it is placed on the chuck. The chuck has several holes, which enable the application of vacuum to fixate the sensor. When the setup construction at HEPHY is finished, the chuck will be able to control the temperature to enable measurements on irradiated sensors. The chuck is placed on top of a xyz-table. Holes in the probe card and switching card on top allow the finding of alignment marks on the sensor when the probe card is mounted on top. A Nikon stereo microscope is used to perform the manual alignment. To speed up the alignment procedure, additional marks (e.g. with kapton tape or grooves) can be implemented on the chuck to prealign the sensor by eye when putting it on the chuck. For simplification of the placement or removal of a sensor on the chuck, the platen with the probe card is mounted on two rails. At the time of the sensor measurements, a dark box, like the one shown in 6.1a, was not available. Because of this, a light-tight blanket, as seen in Figure 6.2a, had to be used. Figure 6.2b shows the setup without the blanket.

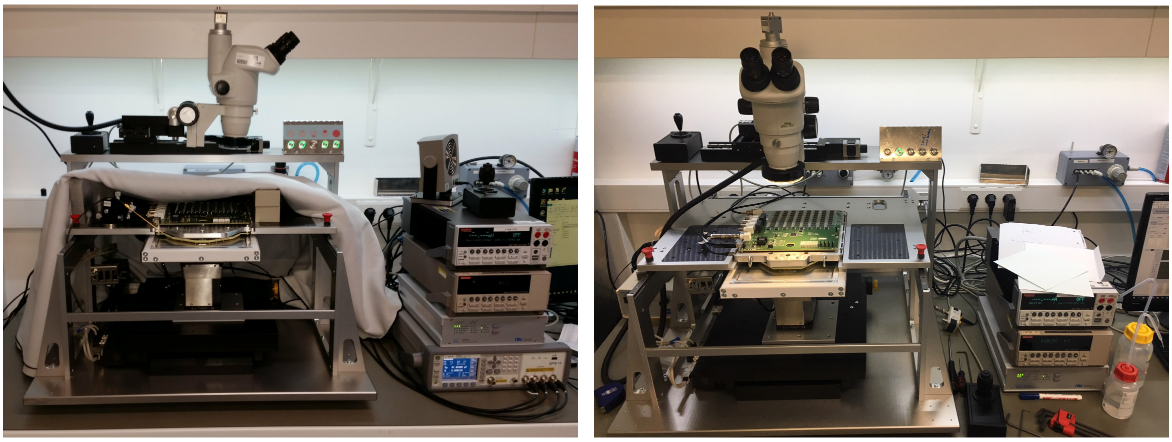

(a) **(b)**

Figure 6.2: (a) HEPHY probe card setup for automated sensor measurements. A light-tight blanket is put on top of the custom made metal platen that holds the probe card. (b) Setup without blanket. The probe card position is fixed. For positioning of the sensor, the metal chuck can be moved with an xyz-table. The microscope and a sufficiently large hole in the probe card (and switching card) are used for the alignment.

The probe card and switching card sandwich a steel plate to prevent sagging. Both were designed and manufactured at CERN. Figure 6.3 displays a CAD view of the assembly of the connected cards. The advantage of the two-card system is to be able to test sensors with different geometry, by changing only the probe card. The probe card has spring loaded pins, the so-called pogo pins, which contact each pad. For different sensor types, the pogo pin position and the metal routing change, but the positions of the connectors between the two cards remain the same. Because of this, the switching card can be used for every HGCal sensor type.

The schematic circuit diagramme of the two-card system is shown in Figure 6.4. The switching card is a 512-channel multiplexer with an on-board microprocessor. It controls the components of the board and provides the user interface. The switching can be done manually or remotely via a computer. Each channel is connected with a pogo pin of the probe card through a 10 kΩ series resistor for high-voltage protection. The channels that are not measured are grounded to confine the spread of the depletion region to a single pad. For biasing of the sensor, a Keithley 2410 SMU is used. It is directly connected with the switching card, which applies the bias voltage to the chuck and hence the back of the sensor. For current and capacitance measurements, an additional ampere meter and LCR meter need to be connected to the switching card. Since both measurements cannot be conducted at the same time, the card is able to switch between the two measurement types. For the current measurements a Keithley 6514 electrometer is used.

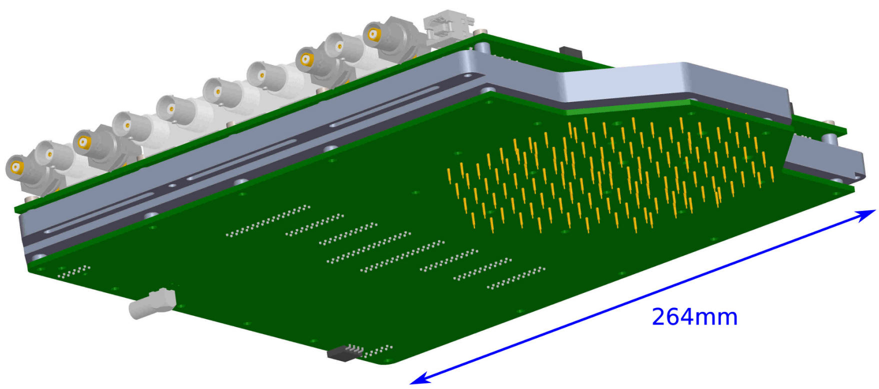

Figure 6.3: A 3D CAD drawing of the probe card and switching matrix [8].

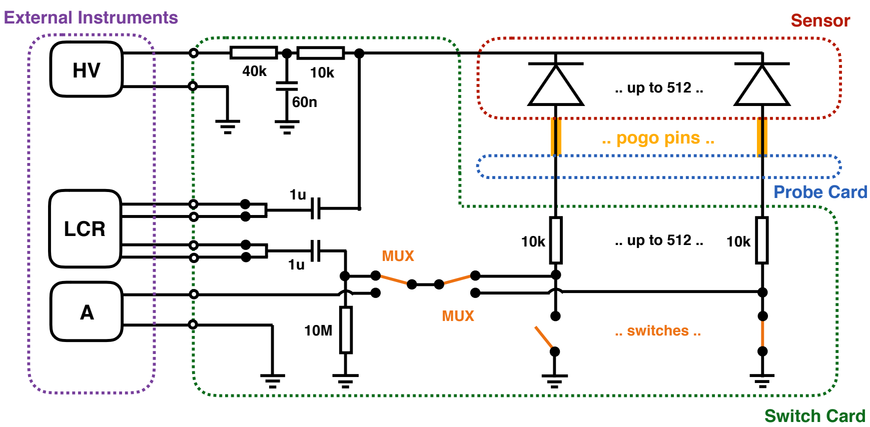

Figure 6.4: Schematics of the probe card setup. Each pad of the silicon sensor is contacted by a spring loaded pin of the probe card, which is placed directly on top of the sensor. On top of the probe card is the 512-channel multiplexer switching card, which has connections needed for high voltage biasing, capacitance, and current measurements. Figure taken from [8].

6.1.3 Test Structure Setup

A photograph of the setup used for test structure measurements is shown in Figure 6.5. It features a dark box with humidity control. The chuck can be temperature controlled and is surrounded by a plastic glove box. To help contact test structures with probe needles, an Olympus microscope is used. The platform for positioners is next to the chuck. Both cannot be moved automatically. A rack with measurement instruments is located next to the dark box. The most important instrument for electrical measurements is a Keithley 237 SMU. For capacitance measurements, an Agilent E4980A LCR meter is used. The measurements were controlled by a custom made LabVIEW [67] software.

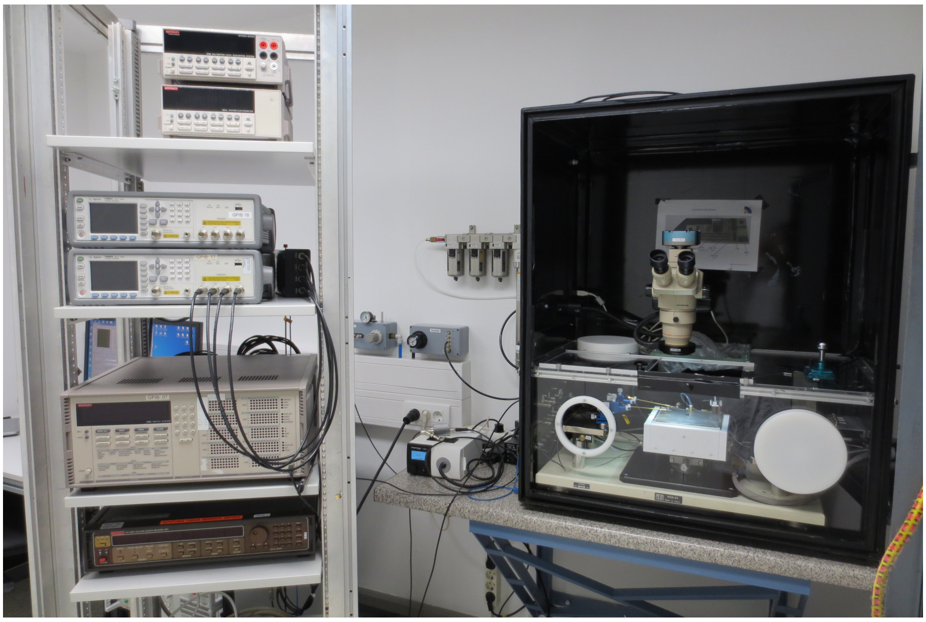

Figure 6.5: Picture of the measurement setup used for IV and CV measurements.

6.1.4 Laser Setup

The third setup used in the measurements is a laser setup. An overview of the setup can be seen in Figure 6.6a. A coordinate table, moveable in both directions parallel to the floor, is placed in a dark box. The dark box is humidity controlled but not temperature controlled. On top of the table in the dark box, self-built modules like the one shown in 6.6b can be placed. The module has a copper housing. In the module a diode is connected with wire bonds to a SMA connector. Through a hole on top of the copper housing laser pulses can induce a signal in the diode. Above the module a Pilas gain-switched diode laser module PiL106X is placed on a vertically movable stage. The pulsed infrared laser has a wave length of 1060 nm and a pulse width smaller than 60 ps. The maximum pulse repetition rate is 120 MHz, and the average power is 1 mW. Outside of the dark box, several instruments needed for transient current technique (TCT) measurements are placed. The schematics of the laser setup are shown in Figure 6.7. The signal in the diode gets transmitted to a Cividec

C2-TCT amplifier with an analog bandwidth of 2 GHz and 40 dB gain. The amplifier has a bias-tee included. The necessary 12 V for operation are provided by a HAMEG power supply, and the bias voltage for the diode is delivered by a Keithley 2410 source meter instrument. The amplified signal is displayed with the Tektronix MSO4104 mixed signal oscilloscope with a bandwidth of 1 GHz. The oscilloscope gets trigger signals from the Pilas laser control box.

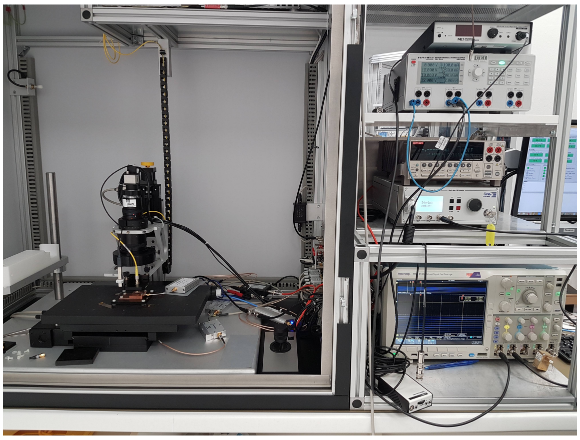

(a)

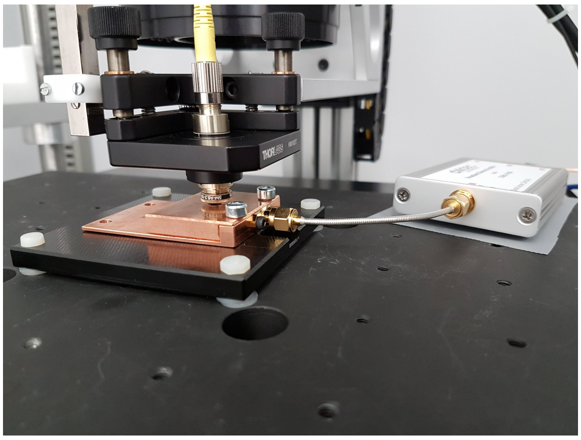

(b)

Figure 6.6: (a) HEPHY laser setup. (b) Closeup of the module with the diode inside.

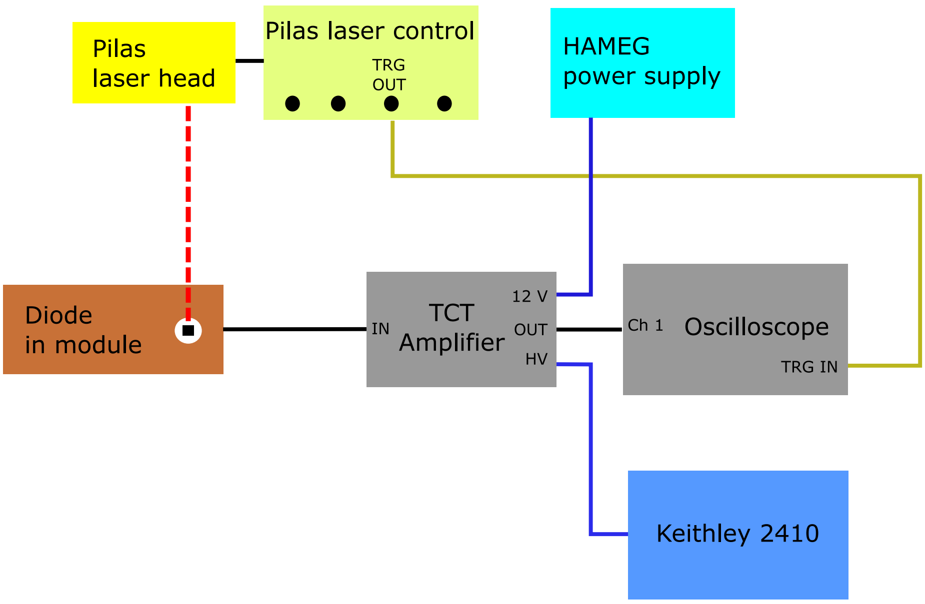

Figure 6.7: Diagramme of the schematics of the laser setup.

6.2 Test Structures

6.2.1 Current Measurements

Scratch Tests

Firstly, scratch tests were performed on an Infineon diode of type *Diode-Large*. To investigate the effect of mechanical damage on the diode current, defined scratches were inflicted. After each scratch, a current-voltage (IV) measurement was performed. The setup used for this task is a modification of the probe needle setup described in 6.1.1. A photograph of the setup can be seen in Figure 6.8a. The locations of the probe needle positioners and the sensor are switched in comparison to the regular setup. The probe needle positioner is fixated with magnets on the automatic coordinate table. The diode is fixated with the help of vacuum to a Gel-Pak [68], which is the black plastic square in the centre of Figure 6.8a. The Gel-Pak is placed on top of a precision weighing scale. By adjusting the probe needle position vertically, the weight and hence the weight force applied with the probe needle on the diode can be tuned. The scratch is inflicted by moving the coordinate table by a defined length. The force and length of each scratch are summarized in Table 6.1. Figure 6.8b shows two scratches on the back of the diode. Each scratch is consecutively numbered, ranging from the numbers 1 to 8. The first three scratches were inflicted on the front of the diode and the following five on the back. The probe needles are made out of tungsten and have a 1.2 µm tip radius.

(a)

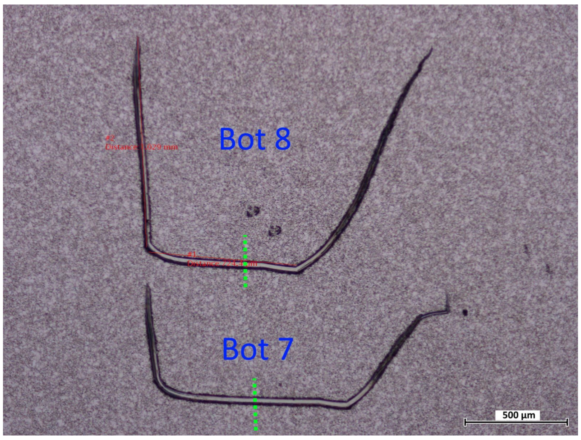

(b)

Figure 6.8: Setup used to produce defined scratches on the diode (a). Two scratches on the back metallisation of the diode (b). Scratch “Bot 8” destroyed the diode.

The test diode has a thickness of 200 µm and a full depletion voltage of about 55 V. Before applying the sratches, no breakdown was observed up to −1000 V. The IV measurements were performed after each defined scratch. The curves are plotted in Figure 6.9. For the first 7 curves, no change in the performance was observed. After applying a weight of 40 g with the needle on the sensor, the performance of the diode deteriorated (black curve). After the application of the scratch, the diode starts to break down at a bias voltage of −100 V. For bias voltages larger than −300 V the current decreases again. The observed increase in current can be attributed to the damage inflicted on the crystal lattice by the focussed application of force on the back of the sensor. This leads to the creation of defects and electric field maxima near the back. Since the base material of the test structure is p-type silicon, the depletion region spreads from the pad implant to the back of the diode. Because of this, the defects show impact only slightly after full depletion.

With atomic force microscopy (AFM) measurements conducted at the "Universitäre Service-Einrichtung für Transmissions-Elektronenmikroskopie" (USTEM) of the University of Technology Vienna, the average depth of the scratches could be determined to be (3.08 ± 0.07) µm. The AFM measurement method is described in detail in [69]. The profile measurements were performed in the middle of the scratch, indicated by the green dotted line in Figure 6.8b. The maximum depth of the scratches at this position was not influenced by the applied weight. Since the back metallization has a thickness of about 3 µm, a probe needle tip will immediately penetrate the metal and scratch at the silicon bulk. Regular contacting on the front of the diode with a probe needle usually applies about 5 g weight. Since the depth of the scratch that destroyed the diode is not deeper in comparison to the other scratches, the damage manifested only in micro cracks in the silicon crystal below the silicon surface, which cannot be measured by the AFM method. It can be concluded that contacting of the diode for electrical measurements as it is conducted for the measurements presented in this thesis will not damage the silicon sensor.

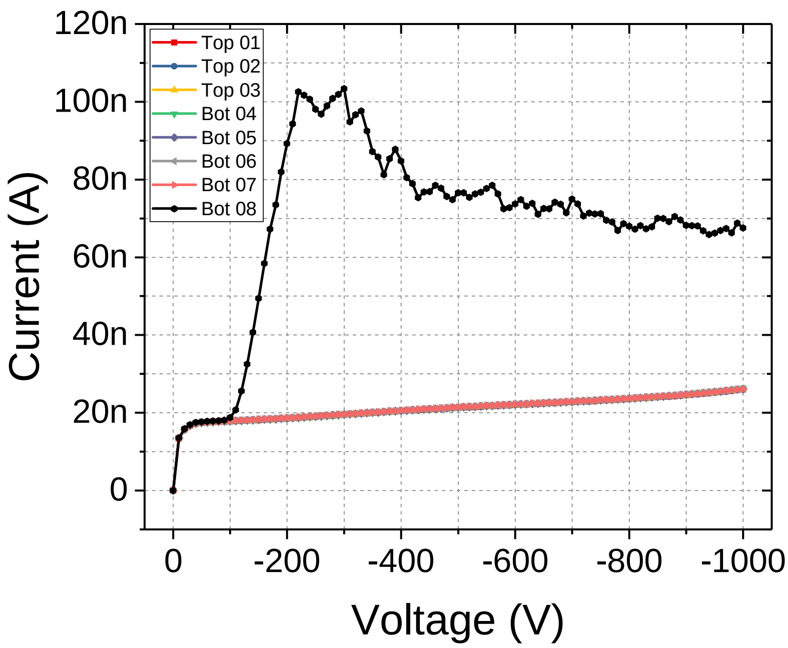

Figure 6.9: IV curves measured on a single diode with a thickness of 200 µm after inflicting scratches with increasing force to the front (Top 01 - Top 03) and back (Bot 04 - Bot 08).

Table 6.1: List of scratch length and applied weight for the individual scratches inflicted on the test diode.

Position	No.	Weight (g)	Length (µm)
Top	1	6	200
Top	2	11	200
Top	3	18	500
Bot	4	5	500
Bot	5	10	500
Bot	6	16	1500
Bot	7	31	1500
Bot	8	40	1500

Diode

The current-voltage (IV) characteristics of test structure diodes of the demonstrator HGCal batch were measured in the test structure setup described in 6.1.3. In the measurement, high-voltage is applied to the back of the diode and ground potential on the front. The measurements were performed at room temperature ((22 ± 1) °C). 8 different wafers with different thicknesses were measured. IV curves of two diodes of type *Diode-Large* of each wafer, located at the same wafer positions, are compared. All IV curves are plotted in Figure 6.10. Diodes labelled with the number 1 are indicated with a full line. Diodes with the label number 2 are plotted with symbols only. Different colours symbolise different sensor thicknesses. The 140 µm thick diodes are black and grey. Different tones of red represent 200 µm thick wafers. The shades of green denote 300 µm thickness. 350 µm sensor thickness is indicated by different tones of blue.

It can be seen that half of the diodes have breakdown voltages above -800 V and show no irregular IV behaviour. Six out of eight diodes with label number 2 show abnormal increase of the leakage current at about -200 V. All diodes at this position with a sensor thickness of 300 µm and 350 µm show this behaviour. The current increase does not originate from a typical avalanche breakdown in the device, but rather from a defect at the back of the diodes. Since the same defect appears on all wafers at the same position, it can be concluded that it is either due to an irregularity in the silicon ingot or a systematic processing problem at the back. Localized defects on the wafer, which, for example, increase the leakage current, reduce the yield of silicon chip production in the industry. For the HGCal sensors, which cover almost the whole wafer, this means that single pads in the wafer can produce high leakage current. It is important that, in case of bad cells the additional leakage current does not influence the measurements on the rest of the sensor.

Another current measurement was performed on a diode of the same type (18-Diode_1) to evaluate the active area of the measured diodes. In Figure 6.11a, IV curves of the diode are shown, where in one case the guard ring is not contacted and put to pad potential ($\equiv$ floating). In the second case the guard ring is kept on pad potential. The former case is depicted as a red line and the latter as a blue line. In both cases, ground potential is applied

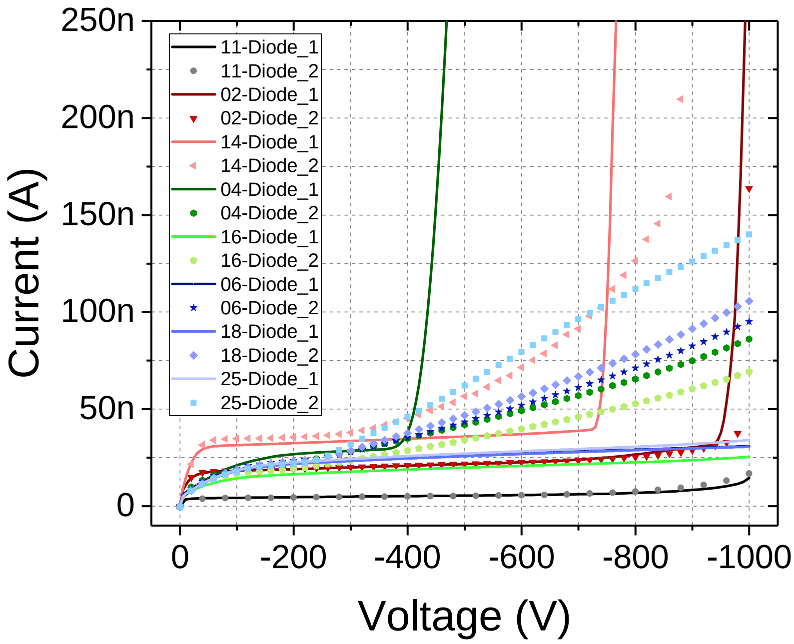

Figure 6.10: IV curves of diodes of type *Diode-Large*. Four different diode thicknesses at the same two test structure positions are tested. 140 µm thick diodes are coloured black, 200 µm diodes red, 300 µm diodes green, and 350 µm thick diodes blue.

to the back of the sensor and high-voltage on the pad. The HV guard connection of the Keithley 237 SMU was used to apply pad potential to the guard ring. This way the current flowing through the guard ring was not measured by the SMU sense contact. Therefore, the effective area for the measured current can be constrained to the pad area. The ratio of both currents is shown in Figure 6.11b. Between full depletion voltage and a bias voltage of 200 V, the ratio is approximately constant at a value of 1.672. This means that, in case of floating guard ring, the diode volume producing the leakage current is 1.672 times larger than the pad area. Assuming uniform extension of the depletion region across the full diode thickness, the effective diode area is larger by the aforementioned factor. This corresponds to an extension of the pad area in each lateral direction by 772 µm. The thus deduced effective area extends roughly up to the middle of the edge ring.

At higher voltages, the current ratio decreases, which indicates a decreasing periphery contribution to the total current. The slope of the current after full depletion in case of the floating guard ring is $(21.75 \pm 0.01)\,\mathrm{pA\,V^{-1}}$. In case of a biased guard ring, the slope of the IV curve after full depletion is $(16.73 \pm 0.09)\,\mathrm{pA\,V^{-1}}$. Both slopes were determined by linear fits. The current originating from the periphery area increases at a faster pace than the pad current. This indicates that after full depletion the periphery volume continues to increase with increasing voltage.

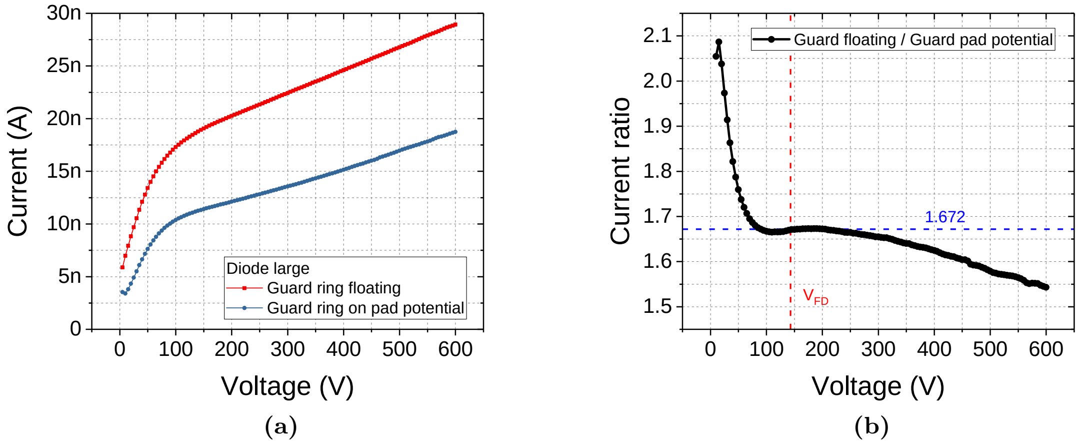

Figure 6.11: IV measurement of the same diode with a guard ring floating and a guard ring on pad potential (a). The ratio of both currents shows the spread of the effective diode area with increasing voltage due to the lateral extension of the depletion zone (b).

6.2.2 Capacitance Measurement

Diode

Capacitance measurements on test structure diodes were performed to determine the resistivity of the silicon bulk. The measurements were performed with the test structure probe station described in 6.1.3. High voltage is applied to the back of the diode and low voltage is applied on the pad with a single needle. The detailed circuitry is shown in Figure 6.12.

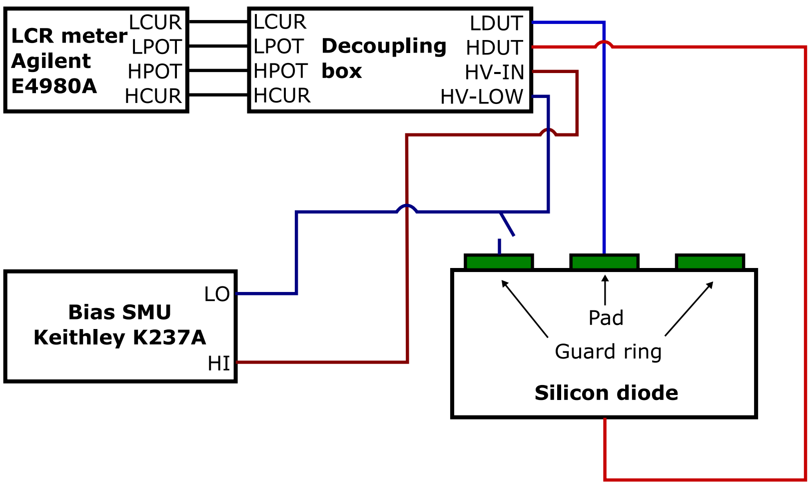

Figure 6.12: Schematic circuitry used in capacitance measurements of diodes. For measurements with a grounded guard ring, the switch connecting the ground potential of the SMU with the diode guard ring can be closed.

The results of the CV measurement are displayed in Figure 6.13. Different sensor thicknesses are indicated by different colour tones. The 140 µm thick diodes are depicted in black and grey. Different tones of red represent 200 µm thick wafers. The shades of green denote 300 µm thickness. 350 µm sensor thickness is indicated by different tones of the colour blue.

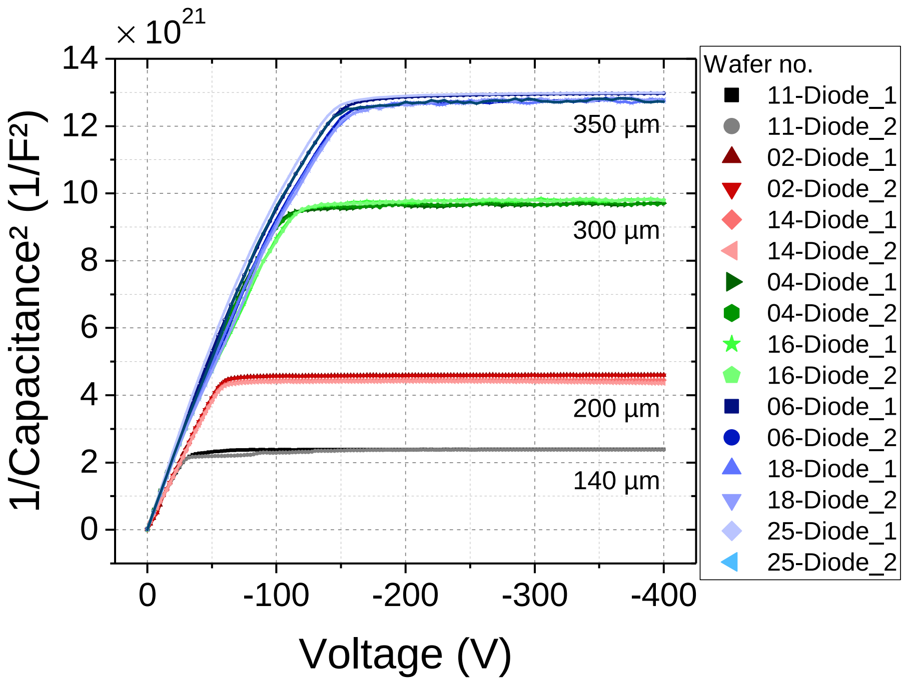

Figure 6.13: Capacitance measurement on test structures of type *Diode-Large*. Diodes from wafers with different thickness were measured.

The full depletion voltages V_{FD} are extracted by fitting two linear functions to the curves and taking the intersection point. They are summarized in Table 6.2. Additionally, the resistivity is calculated from the full depletion voltage using Equation 2.24. On average, the resistivity of the 350 µm thick diodes is $(9257 \pm 271)\,\Omega\,\text{cm}$. The 300 µm thick diodes have a resistivity of $(9056 \pm 391)\,\Omega\,\text{cm}$. Sensors from both wafer thicknesses most likely originate from the same silicon ingot. The resistivity of diodes with a thickness of 200 µm was determined to be $(7294 \pm 127)\,\Omega\,\text{cm}$. Both diodes measured on the 140 µm thick wafer have the same full depletion voltage. Therefore, no statistical error can be stated for their average resistivity of $6479\,\Omega\,\text{cm}$.

Metal Oxide Semiconductor

Capacitance measurements were performed on metal oxide semiconductor (MOS) test structures to determine the interface oxide charge concentration N_{OX}, which is an important parameter for TCAD simulations. In the measurement, high voltage was applied on the back and ground potential on the metal pad. The capacitance measurement resulted in the

Table 6.2: Full depletion voltage and resistivity of the measured diodes of type *Diode-Large*.

Wafer no.	V_{FD} (V)	Resistivity (Ω cm)
11-Diode_1	31.9	6479
11-Diode_2	31.9	6479
02-Diode_1	57.0	7400
02-Diode_2	57.4	7349
14-Diode_1	57.4	7349
14-Diode_2	59.6	7077
04-Diode_1	100	9491
04-Diode_2	101	9397
16-Diode_1	110	8628
16-Diode_2	109	8707
06-Diode_1	138	9361
06-Diode_2	140	9227
18-Diode_1	141	9162
18-Diode_2	145	8909
25-Diode_1	132	9786
25-Diode_2	142	9097

curves displayed in Figure 6.14. The flatband voltage V_{FB} is determined by the intersection point of two linear fits to the capacitance-voltage characteristic. The black dashed lines indicate the position of the fitting lines.

The calculated flatband voltage and the calculated interface oxide charge density are summarized in Table 6.3. For the calculation of the interface charge density, Equations 4.1 and 4.2 were used. From the capacitance of the MOS structure in accumulation the thickness of the oxide can be calculated with the parallel plate capacitor equation. Averaging of the three samples results in $N_{OX} = (7.00 \pm 0.25) \times 10^{10}\,\mathrm{cm}^{-2}$ and an average oxide thickness of (666.7 ± 2.3) nm.

Table 6.3: Parameters determined from capacitance measurements on MOS structures.

Wafer no.	V_{FB} (V)	N_{OX} (1/cm^2)	Oxide thickness (nm)
04-MOS	1.38	6.74×10^{10}	668
06-MOS	1.54	7.25×10^{10}	668
18-MOS	1.44	7.01×10^{10}	664

6.2.3 Charge Collection Efficiency Measurement

In this section the signal induced in diodes by a pulsed infrared laser in diodes is investigated. The diodes have a hole in the centre of the top metal layer so that the laser pulse can enter the bulk. The laser setup as described in 6.1.4 is used for this task. The test structure diodes have *Diode-Large* geometry and feature a thickness of 200 µm. The same signal is induced in each diode by keeping the laser head at a constant distance to the module for all

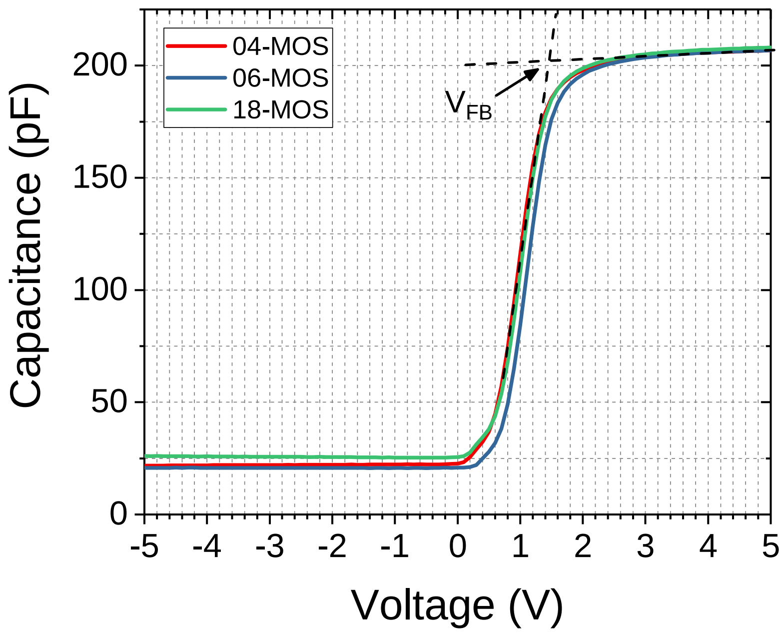

Figure 6.14: Capacitance measurement on metal oxide semiconductor (MOS) test structures. MOS structures with a quadratic metal pad, which has a side length of 2000 µm, are tested.

measurements. The laser intensity remains constant for all measurements. When exchanging the module, the horizontal position of the automatic table has to be adjusted to position the laser peak in the centre of the diode opening again.

Figure 6.15a shows a MIP-like signal induced by an infrared laser with a wavelength of 1060 nm. The diode is unirradiated and the signal is recorded for different bias voltages. The signal curve is sampled at a frequency of 5 GHz using a 1 GHz bandwidth oscilloscop. The average of 512 signals is calculated to reduce the effect of electronic noise. Despite having the diode shielded entirely with copper, the noise could be reduced by applying ground potential to the automatic coordinate table and the dark boxl. For voltages below full depletion, the total charge generated by the laser depends on the extension of the depletion zone into the silicon bulk. Maximum charge is reached at full depletion (about 45 V for the diode here). After reaching full depletion voltage, the signal peak height increases and the decay time decreases with increasing bias voltage. Higher bias voltage leads to stronger electric fields and higher drift velocities. At a bias voltage of 100 V, the contribution of the electrons and holes to the signal can easily be seen. The signal shape is very similar to the one shown in Figure 2.7b, which shows a signal pulse simulated with the software Weightfield2. Electrons have a higher mobility in comparison to holes, and hence the signal decays in a shorter time.

The signal of a diode irradiated with protons at a fluence of $6.07 \times 10^{14}\ \mathrm{n_{eq}/cm^2}$ is displayed in Figure 6.15b. The diode has the same thickness and resistivity as the one used for the measurements depicted in Figure 6.15a. Because a cold chuck was not available for the laser system, the measurements were performed at room temperature. Before the measurement, the diode was annealed about 400 days at −20 °C, 30 min at 22 °C, and 10 min at 60 °C. This corresponds to a total annealing time of 13.77 min at 60 °C. The signal measurement takes about 30 min, which corresponds to an additional annealing step of 0.23 min at 60 °C. With increasing bias voltage, the signal peak height increases. In comparison to the unirradiated diode, the maximum peak height is smaller because of the trapping of charge carriers. From this measurement a full depletion voltage V_{FD} between 500 V and 600 V can be deduced. At a bias voltage of 600 V, the signal decays faster than at 500 V, which marks the point of full depletion.

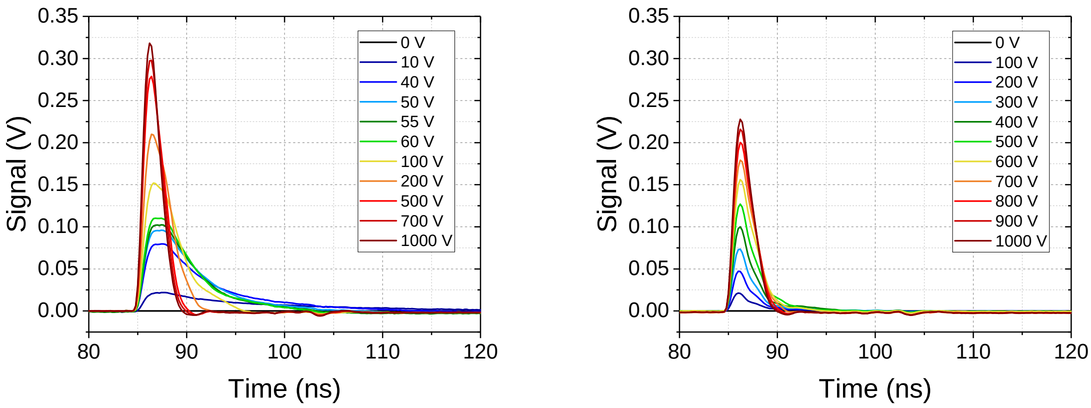

(a) **(b)**

Figure 6.15: MIP-like signal induced by a 1060 nm laser in an unirradiated diode (a) and a diode irradiated with protons at a fluence of 6.07×10^{14} n_{eq}/cm^2 (b).

Signal measurements were performed on neutron irradiated samples as well. They were exposed to the same annealing steps as the proton-irradiated sample. Figure 6.16a shows signal curves for different bias voltages for a neutron irradiated diode at a fluence of 1×10^{14} n_{eq}/cm^2. Using the same method as before, a full depletion voltage between 200 V and 300 V is determined. The diode irradiated at a fluence of 9×10^{14} n_{eq}/cm^2 shown in Figure 6.16b has a full depletion voltage between 900 V and 1000 V. The maximum peak height is lower for higher fluences due to trapping of charge carriers.

The currents of the measured signal curves are integrated over time to determine the total amount of collected charge. It should be noted that the signal in Figures 6.15 and 6.16 is given in volts. This corresponds to the measured value in the oscilloscope, which can be converted to current by dividing it by 50 Ω. The collected charge value is compared for the irradiated diodes and the unirradiated diodes. Since the induced charge is the same for all diodes, the charge collection efficiency (CCE) can be calculated, albeit the initially induced charge is not known. It is important to compare only unirradiated and irradiated diodes with the same thickness and resistivity, otherwise the collected charge values cannot be compared. The result of such a CCE measurement is shown in Figure 6.17. The collected charge of the unirradiated diode at a bias voltage of 1000 V is used to define the maximum efficiency of 100 % or “1”. The CCE value at a bias voltage of 500 V

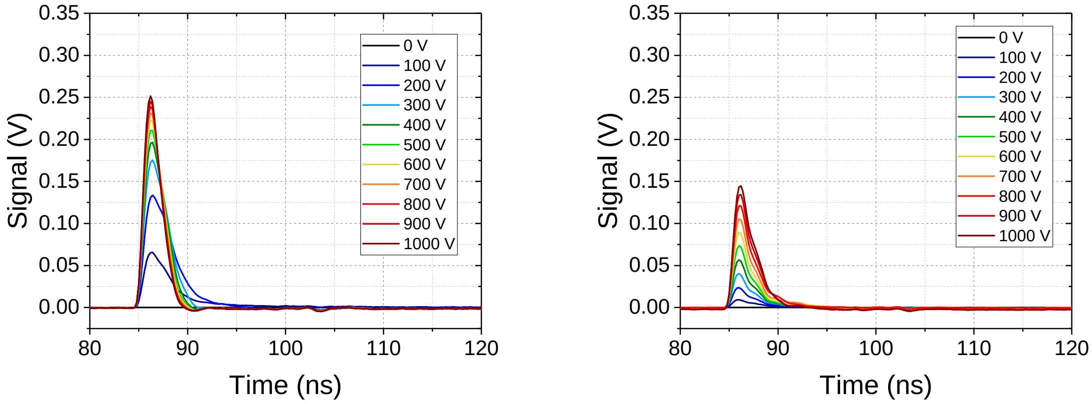

(a) (b)

Figure 6.16: MIP signal induced by a 1060 nm laser in a diode irradiated with neutrons at a fluence of 1×10^{14} n_{eq}/cm^2 (a) and at a fluence of 9×10^{14} n_{eq}/cm^2 (b).

is about 1.01, which solely originates from measurement errors and uncertainties in the definition of the borders used for the integration of the current. To avoid an undershoot of the signal, the integration borders were defined in such a way that only positive signals were integrated.

With increasing fluence, the CCE value decreases. With increasing bias voltage, the CCE value increases. Typically, CCE measurements are performed at $-20\,°C$ to avoid annealing of the device and to keep the temperature at a defined value. The trapping of charges is temperature dependent. At lower temperatures, higher CCE values can be expected. This effect is described by Equation 2.38, where it is evident that the trapping rate increases with increasing temperature.

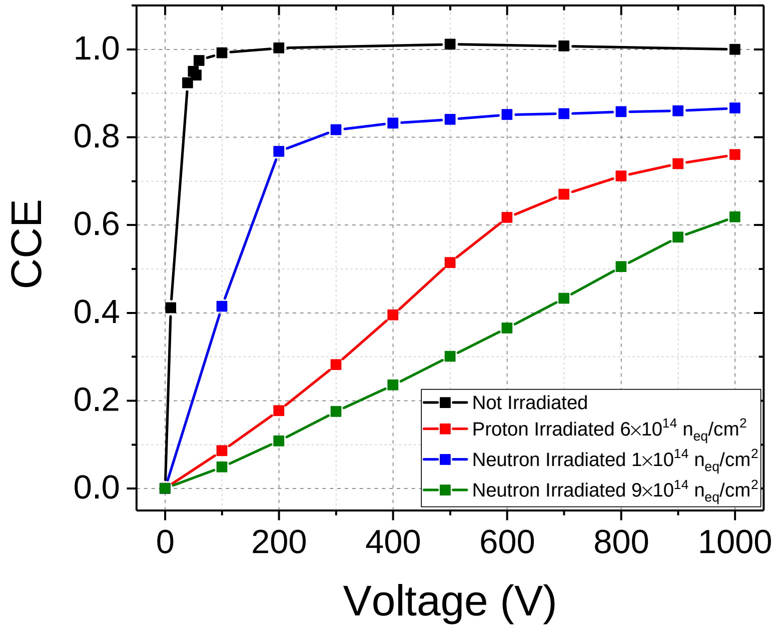

Figure 6.17: Charge collection efficiency measurement at room temperature for diodes of type *Diode-Large* at different fluences.

6.3 6-Inch Prototypes

At the time of writing this work, Hamamatsu Photonics have produced 166 HGCal 6-inch wafers featuring the geometry shown in Figure 4.3. The wafers show excellent quality and are used in the following to introduce the different measurement types used throughout the thesis.

6.3.1 IV Measurement

The first measurement type is the current measurement with 7 needles. The probe needle positioner setup shown in Section 6.1.1 is used with the circuitry shown in Figure 6.18. High voltage is applied to the back of the silicon sensor with a Keithley K237A SMU. The central pad is connected to the HI connection of a second SMU, which is a Keithley K2657A. For the current measurement, the central pad is kept at 0 V. All neighbour pads are shorted and connected to the LO connection of both SMUs, which are connected to ground potential. This configuration ensures, that the measured central pad is biased in the same way as in a probe card measurement.

Figure 6.19 shows a current measurement with 7 needles at −300 V bias voltage of the 6-inch sensor HPK_3010 from Hamamatsu. The sensor is processed on p-type base material with

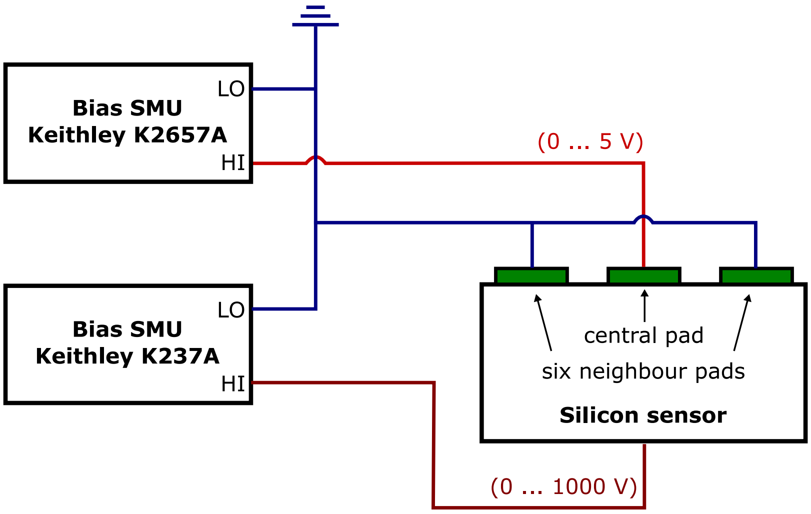

Figure 6.18: Circuit diagramme of the 7-needle measurement . It is needed for measurements of a single pad with all of its neighbours kept at the same potential. Inter pad measurements, like the inter pad resistance or punchthrough voltage, can be conducted using the same circuitry by ramping up the central pad to voltages higher than 0 V.

common p-stop and has a thickness of 320 µm. The top left quadrant features a pad distance of 62 µm, while the top right one has a value of 82 µm. The bottom left distance is 22 µm and the bottom right one 42 µm. The current is measured at room temperature with the probe needle setup described in 6.1.1. The current of the pads is displayed according to the geometry of the hexagonal sensor and sensor pads. This way it is easier to associate sensor characteristics to the location on the real sensor. Two halves with different pad current can be identified. The left half of the sensor shows about 30 % higher pad current than the right half. This is due to high current in two hotspots of the sensor. Excluding the border pads, 91 pads are measured, which have on average a current of (1.15 ± 0.26) nA (median is 1.15 nA). The minimum pad current is 0.73 nA and the maximum 2.04 nA. The total current of all measured pads is 104.87 nA. To estimate the current of the whole sensor, the border cells have to be taken into account. Using the average pad current for extrapolation, the total sensor current measured with the 7-needle method is 139.37 nA. A dependence of the current on inter cell geometry cannot be detected.

The hexagonal plot in Figure 6.19 shows the current only at a fixed voltage of −300 V. The whole current development is represented in regular IV curves. For the sensor HPK_3010, an overlay of all IV curves is shown in Figure 6.20a. The current of the central pad measured with the 7-needle method is shown. Within the first −200 V bias voltage, the range where the sensor is not yet fully depleted, the current is very low and almost constant compared to the currents after full depletion. The median of the current of all pads and measured voltages in this range is 0.30 nA. At these voltages, the characteristic does not look like a typical IV curve. One explanation for this behaviour could be that the bulk material has very little defects and thus a low leakage current. When the full depletion region spreads from the pad towards the back of the sensor, only this very low current is measured. Only when the depletion zone reaches the back of the sensor, defects at the back of the sensor would cause

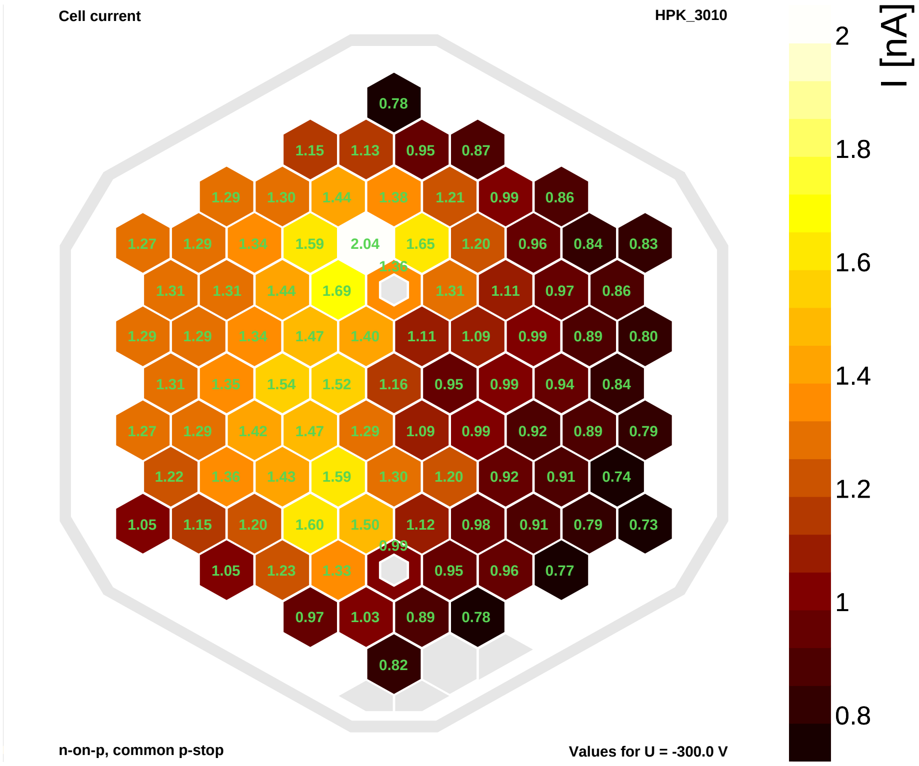

Figure 6.19: Current distribution of the 6-inch sensor HPK_3010 from Hamamatsu at a bias voltage of −300 V. The current of the pads is measured with the 7-needle method. Pad currents range from 0.73 nA to 2.04 nA. Pads in the left half show higher currents than those in the right half.

the observed rapid increase of the leakage current.

With the 7-needle method the current through the neighbour pads is measured at the same time as well. In Figure 6.20b, the current of all neighbour pads is plotted for each measured central pad. The measured current of the neighbours corresponds to the current of the sensor excluding the central pad of the 7-needle configuration. This current would be measured in the central pad, if only a single needle would be used for the measurement. Without the biasing of the neighbour cells, the lateral spread of the depletion zone is not confined. In this plot, the current of the neighbour cells is about 100 times larger than the current of the central pad current for all bias voltages. However, the increase of current after full depletion is slower in comparison to the central pad current.

The current of the neighbour cells at a bias voltage of −500 V is plotted for each cell in Figure 6.21. The average value of the neighbour pad current is (102.6 ± 29.0) nA and the median is 109.1 nA. The minimum value is 43.3 nA and the maximum 146.2 nA. The sum of the current of all measured pads is 9336.6 nA. Taking into account the borderpads, the total sensor current is 12 414.6 nA. Dividing this value by the sum of the current through the central pads at −500 V, a factor of about 60 is obtained. This clearly shows, that if the

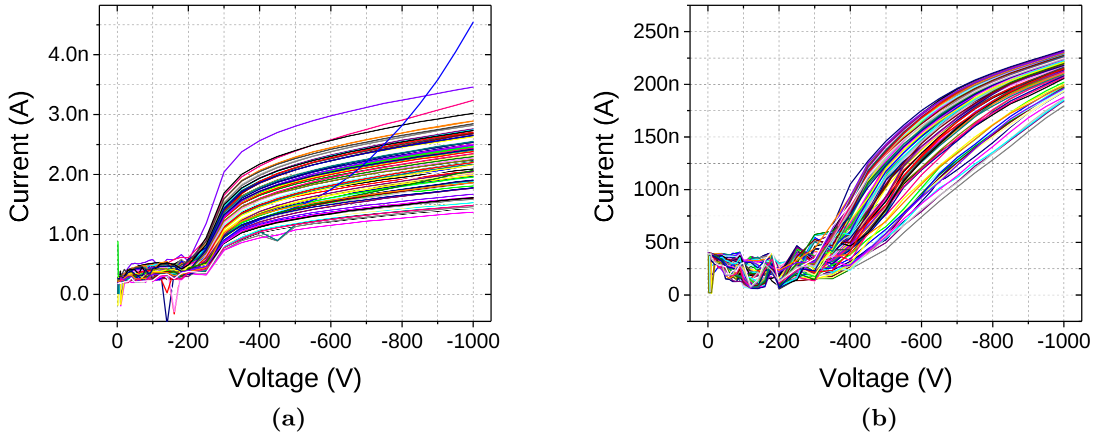

Figure 6.20: Summary of IV curves of all pads for the sensor HPK_3010. The current through the central pad measured with the 7-needle method is shown in (a). The current of the six neighbour cells in the same measurement is plotted in (b).

surrounding pads were not kept the same potential as the central pad, the current of the surrounding floating pads, which is 60 times higher at −500 V, would be measured at the central pad.

The additional current introduced by the floating neighbour pads can be attributed to the lateral spread of the depletion region. This depends on the inter cell geometry. In Figure 6.21 four quadrants with different current can be identified. Quadrants with lower pad distance show a higher neighbour current in comparison to quadrants with higher pad distance. With increasing pad distance, the punchthrough voltage required for the lateral spread of the full depletion zone from one pad to the neighbour pad and the inter pad resistance increase. Thus the current increases slower in quadrants with high pad distance.

6.3.2 Inter Pad Resistance Measurement

The inter pad resistance is measured on the 6-inch sensor HPK_3010, which is the same sensor as in Section 6.3.1. The setup used is the probe needle setup with the schematic circuitry of the 7-needle method as shown in Figure 6.18. The difference to the 7-needle pad current measurement is a voltage ramp from 0 V to 5 V applied on the central pad with the SMU K2657A. The neighbour pads are kept on ground potential. Thus, current flows between the central and neighbour pads. The inverse slope of the linear current increase corresponds to the resistance between the pads.

The result of the inter pad resistance measurement for each pad at a bias voltage of −300 V is plotted according to the sensor pad distribution in Figure 6.22a. The measured resistance ranges from 41.14 GΩ to 265.04 GΩ. Comparing this figure with Figure 6.19, it can be

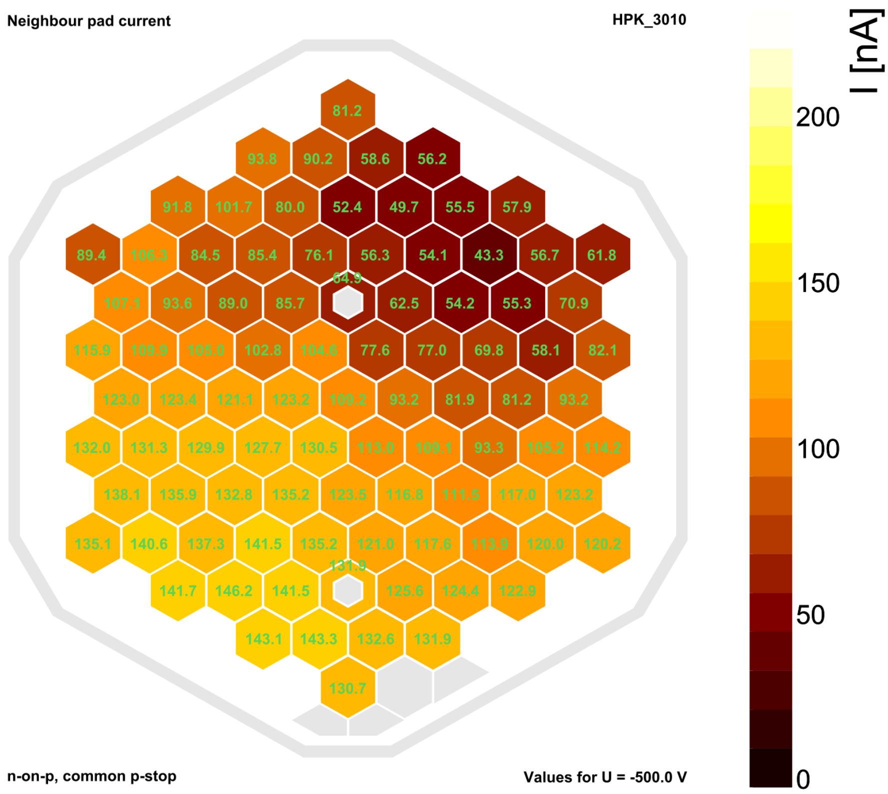

Figure 6.21: Current distribution of the 6-inch sensor HPK_3010 from Hamamatsu at a bias voltage of −500 V. The current of the pads is measured by the 7-needle method, but the current of the six neighbouring pads is plotted and not the one of the central pad. The total current of the neighbouring pads range from 43.3 nA to 146.2 nA. Four quadrants can be distinguished.

seen that the region with higher pad current corresponds to the region with lower inter pad resistance. Pads with higher leakage current will show higher current in the inter pad resistance measurement, which, according to Ohm's law, results in lower inter pad resistance. This is in agreement with the simulations of the inter pad resistance (Section 5.4.2), where the bulk current, defined by the charge carrier lifetime τ, influences the inter pad resistance in the same way. In addition to the effect of lower inter pad resistance with higher leakage current, the effect of quadrants with different pad distances can be indentified in the distribution of the inter pad resistance. The top quadrant on the right half of the sensor with a pad distance of 82 µm, for example, shows resistance values ranging from about 200 GΩ to 260 GΩ. In the bottom quadrant (pad distance 42 µm) the resistance values range from about 127.08 GΩ to 206.34 GΩ. On average, the resistance values are higher in the top right quadrant. The values in the left sensor half are distorted because of the previously mentioned higher pad currents. Nevertheless, on average in the top left quadrant (pad distance 62 µm), a higher inter pad resistance than in the bottom left quadrant (pad distance 22 µm) can be observed.

The result of the inter pad resistance measurement for bias voltages ranging from −50 V to $-1000\,\mathrm{V}$, is plotted in maximum voltage steps of $100\,\mathrm{V}$ in Figure 6.22b. It is evident that the inter pad resistance depends on the bias voltage. According to the simulations (Section 5.4.2), the resistance increases with bias voltage. In the measurement, below $-200\,\mathrm{V}$, the resistance values range from $750\,\mathrm{G\Omega}$ to $1.5\,\mathrm{T\Omega}$ and drops to a minimum at $-300\,\mathrm{V}$. Only after full depletion, the resistance rises with bias voltage as expected from simulations. The explanation for this behaviour is most likely related to the same phenomenon responsible for the low leakage current before full depletion observed in Section 6.3.1. The abrupt change in pad leakage current by a factor of 5 after reaching full depletion corresponds to the drop in resistance by a factor of 5. It should be noted that for measurements of resistances in the order of $1\,\mathrm{T\Omega}$ the measurement error is in the order of a few $100\,\mathrm{G\Omega}$.

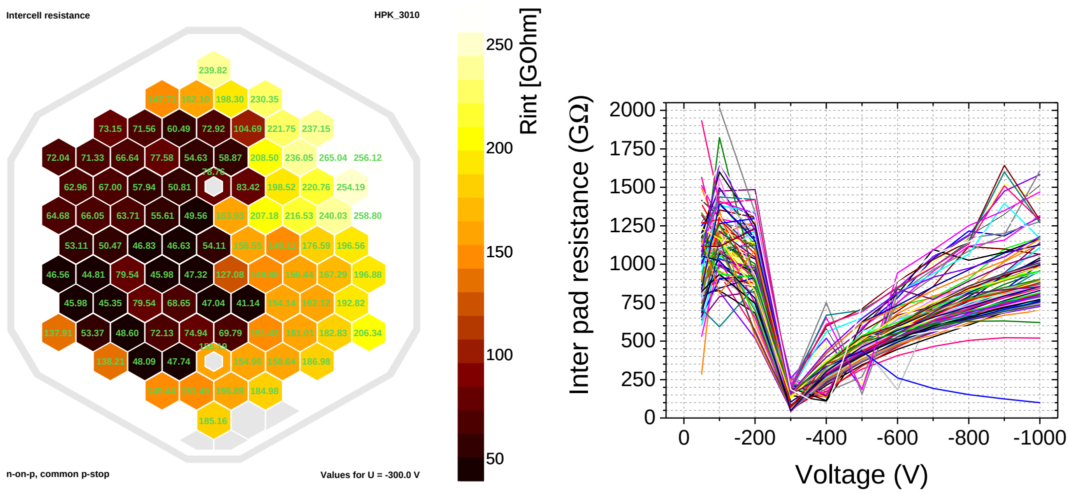

(a) (b)

Figure 6.22: Result of inter pad resistance measurement. (a) Distribution of the inter pad resistance values at $-300\,\mathrm{V}$. (b) Inter pad resistance of all pads for different bias voltages ranging from $-50\,\mathrm{V}$ to $-1000\,\mathrm{V}$. This sensor shows very high resistance values at low bias voltages. After full depletion, the inter pad resistance increases with bias voltage.

6.3.3 Punchthrough Measurement

With the 7-needle measurement scheme shown in Figure 6.18 not only the current and inter pad resistance, but also the inter pad punchthrough voltage can be measured. The measurement setup is the same as for the inter pad resistance measurement detailled in Section 6.3.2. A voltage ramp is applied on the central pad until breakdown of the inter pad current curve. The rise in current with voltage applied between the pads is linear and shows a sharp breakdown. The linear rise of current is fitted with a robust straight line fit (LabVIEW Bisquare fit), and the punchthrough voltage is defined as the highest voltage at which the current value is still compatible with the fit. The result at a bias voltage of $-300\,\mathrm{V}$ is plotted according to the pad positions in Figure 6.22a. The measured punchthrough voltage ranges from $20\,\mathrm{V}$ to $95\,\mathrm{V}$. Four quadrants can clearly be distinguished, where smaller pad distances correspond to lower punchthrough voltages and larger pad distances to larger punchthrough voltages. On average, the punchthrough voltages in the single quadrants excluding the borderpads are (36.7 ± 5.0) V, (46.5 ± 9.4) V, (67.4 ± 13.9) V, and (88.1 ± 4.9) V for the pad distances 22 µm, 42 µm, 62 µm, and 82 µm, respectively. Except for the smallest pad distance, the punchthrough voltages increase by about 20 V for 20 µm larger pad distances. The deviation at the smallest pad distance arises because of the different metal overhang configuration and, consequently, a different electric field in the inter pad region.

In Figure 6.23b the punchthrough voltage for different bias voltages is plotted. For pads without any defects and for bias voltages above full depletion, the punchthrough voltage rises linearly. The slope is steeper for pads with larger pad distances. The mechanism responsible for the increase of the punchthrough voltage with bias voltage is the increased potential barrier between the pads, which needs to be overcome.

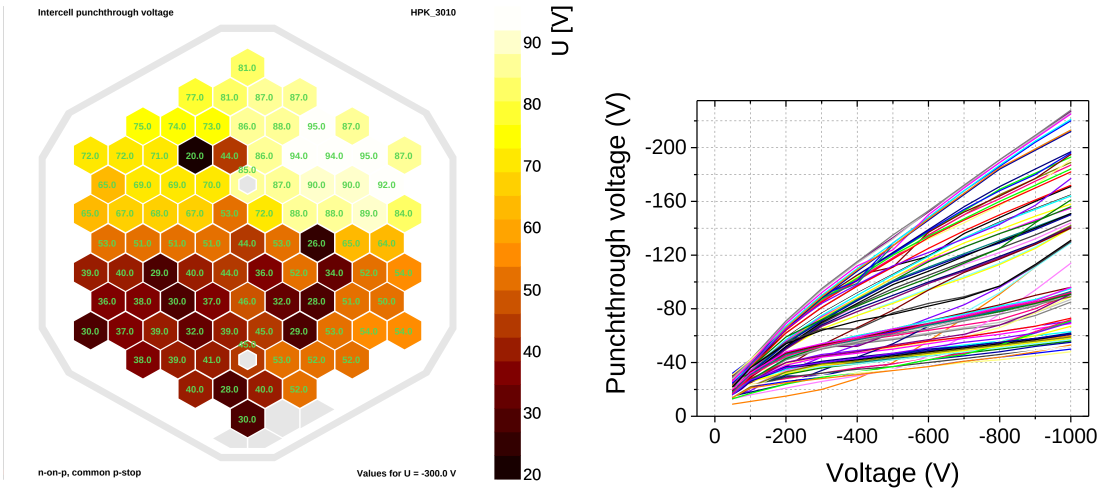

(a) (b)

Figure 6.23: Inter pad punchthrough measurement with the 7-needle method. The punchthrough voltage according to the pad position is plotted at a bias voltage of -300 V in (a). An overlay of all pads for all bias voltages is shown in (b). The punchthrough voltage increases with bias voltage and pad distance.

6.3.4 CV Measurement

For the capacitance measurement of the pads, the sensor HPK_1103 is used. It is a n-type sensor with 300 µm thickness and 134 pads. It features the same pad geometry as the HPK_3010 investigated in the previous sections. The schematic circuitry of the pad capacitance measurement is shown in Figure 6.24. As LCR meter an Agilent E4980A is used, which is connected to a decoupling box, which protects the LCR metre from high voltage. The LCR metre measurement frequency is 10 kHz. A Keithley bias SMU K237A is used to bias the sensor. The six neighbour pads are kept on low potential to confine the lateral spread of the full depletion zone. If this is not done, the effective area of the pad is undefined.

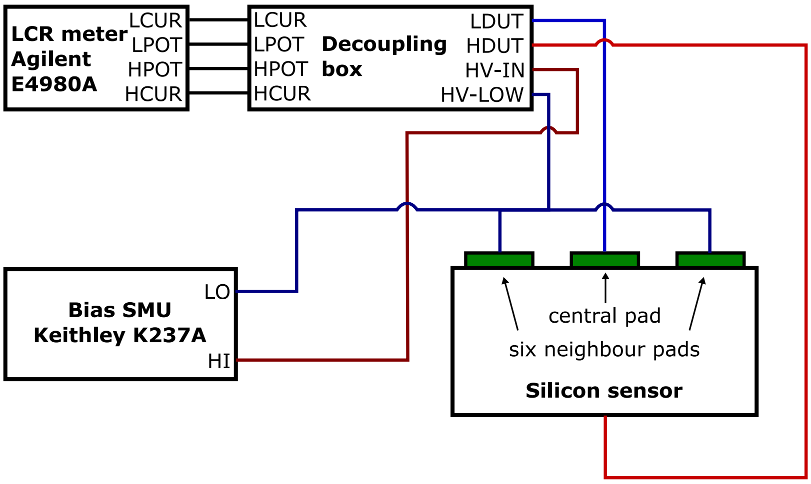

Figure 6.24: Circuitry to measure the pad capacitance. For the protection of the LCR meter from high voltage, a decoupling box is used. The HI and LO connection of the SMU are connected to the input connections of the decoupling box. The neighbour pads are connected to the LO connection of the SMU to put them on the same potential as the central pad to confine the lateral spread of the depletion zone. Back and central pad are connected to the HDUT and LDUT connections of the decoupling box.

The result of the measurement at a bias voltage of 250 V is shown in Figure 6.25a. The average capacitance of both calibration cells is 34.51 pF. The other full cells display an average capacitance of (38.82 ± 0.06) pF. A single cell shows a cell capacitance 1.3 % higher than the average. No influence of the quadrants with different pad distances can be seen. In Figure 6.25b the distribution of the full depletion voltage of the pads is plotted. The full depletion voltage is determined from the intersection point of two straight line fits to the $1/\mathrm{C}^2$ versus voltage characteristic. The full depletion voltage decreases radially from the centre from 213.0 V to 193.4 V. However, the capacitance does not show any radial behaviour, which indicates a constant active thickness across the sensor. Using Equation 2.24, the radial decrease of the depletion voltage can be attributed to a radial increase of the wafer resistivity.

6.3.5 Inter Pad Capacitance Measurement

The measurement of the inter pad capacitance uses the circuitry shown in Figure 6.26. The high potential of the SMU is connected to the sensor back directly. The low potential of the SMU is connected to the central pad and the neighbour pads. Both LO connections are separated by a 2 MΩ resistor to shield the SMU from the AC current of the LCR meter. The measurement frequency of 90 kHz and the resistance value are chosen such that the cutoff frequency of the resulting lowpass is much lower than the measurement frequency.

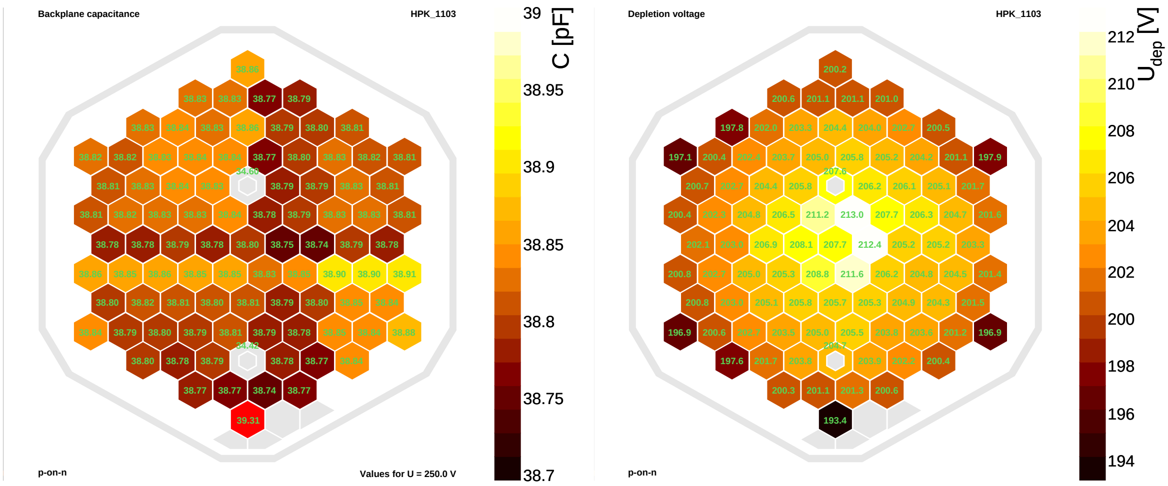

(a) **(b)**

Figure 6.25: Capacitance measurement of the central pad with 7 needles (a). Average pad capacitance of 38.82(6) pF is measured. (b) The full depletion voltage distribution shows a radial decrease that can be attributed to a radial increase of the wafer resistivity.

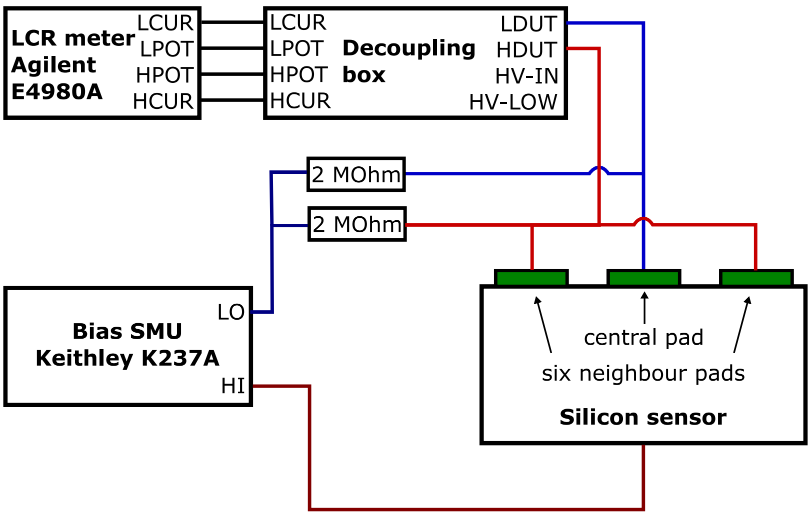

Figure 6.26: Circuitry used for inter pad capacitance measurements. It uses one SMU, which biases the sensor back with high potential and applies ground to the front. The HDUT connection of the decoupling box is connected to the neighbour pads, while the LDUT connection is connected to the central pad.

The results of the inter pad capacitance measurement are shown in Figure 6.27. The sensor is biased to 250 V (about 20 % above full depletion). Excluding the border pads, the pads at the borders of the quadrants, and the calibration cells from calculations, the measurement of the quadrant with pad distance 22 µm results in an average inter pad capacitance value of (15.87 ± 0.01) pF. The average capacitance values of the other quadrants with pad distances 42 µm, 62 µm, and 82 µm are (15.04 ± 0.02) pF, (14.03 ± 0.01) pF, and (13.44 ± 0.04) pF, respectively. With increasing pad distance the inter pad capacitance decreases. Plotting the capacitance values against the pad distance and fitting the curve with a straight line yields a slope of $(-0.0416 \pm 0.0029)\,\mathrm{pF\,\mu m^{-1}}$. For every 10 µm pad distance the inter pad capacitance decreases by about 0.42 pF. This value is in good agreement to the one extracted from the simulations shown in Section 5.4.3, Figure 5.33. The measured sensor has a thickness of 300 µm and a metal overhang of 12.5 µm for the 42 µm, 62 µm, and 82 µm quadrants and a metal overhang of 5 µm for the 22 µm quadrant.

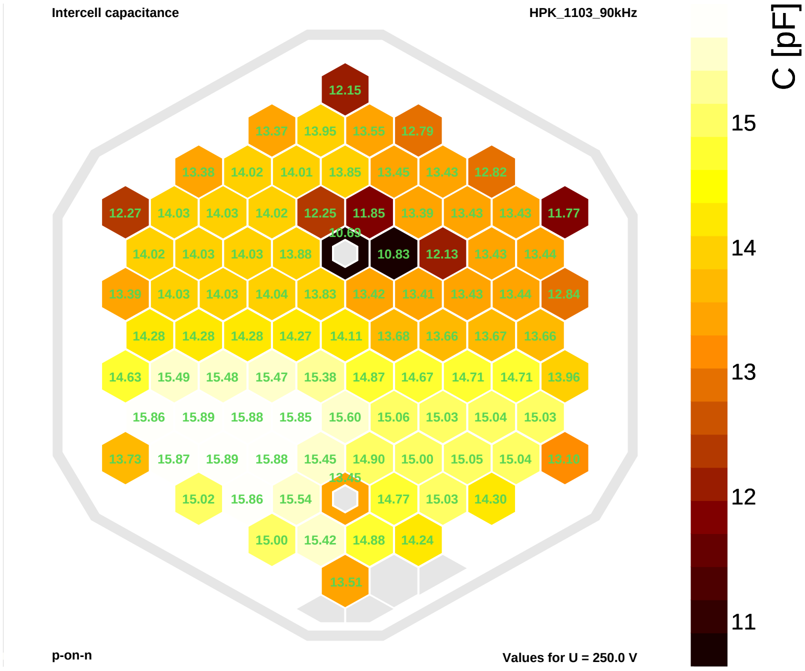

Figure 6.27: Inter pad capacitance measurement of the sensor HPK_1103 at a bias voltage of 250 V and a measurement frequency of 90 kHz. The effect of the four quadrants with different pad distances is clearly visible. The inter pad capacitance shows an offset that can be attributed to the fact that no short correction was performed prior to the measurement.

In general, the measured inter pad capacitance values are too high when compared to simulations. The difference to the simulation of about 11 pF is due to the fact that no short correction was performed before the capacitance measurement to correct for stray series capacitances introduced through the circuitry.

6.4 Demonstrator on 8-Inch Wafers

In this section, two 8-inch Infineon sensors are compared. Both have a thickness of 350 µm and differ only in the p-stop geometry. Infineon sensor No. 18 features p-stop common geometry in the quadrants with 60 µm and 80 µm pad distance. Whereas Infineon sensor

No. 25 features p-stop atoll geometry in both quadrants. In the two remaining quadrants, both sensors feature p-stop common geometry, because p-stop atoll geometry cannot be implemented in the given space.

6.4.1 IV Measurement

7-Needle

The first measurement performed on both sensors is a voltage current measurement using the 7-needle method. The schematics of the circuitry are shown in Figure 6.18. For the measurement, the probe needle setup as described in Section 6.1.1 is used. The current was measured at room temperature (22 °C). The resulting currents at −200 V bias voltage are shown in Figure 6.28a and Figure 6.28b for sensor No. 18 and No. 25. All pads, excluding the border pads and the inner calibration cells, were measured. This results in 181 measured pads per sensor.

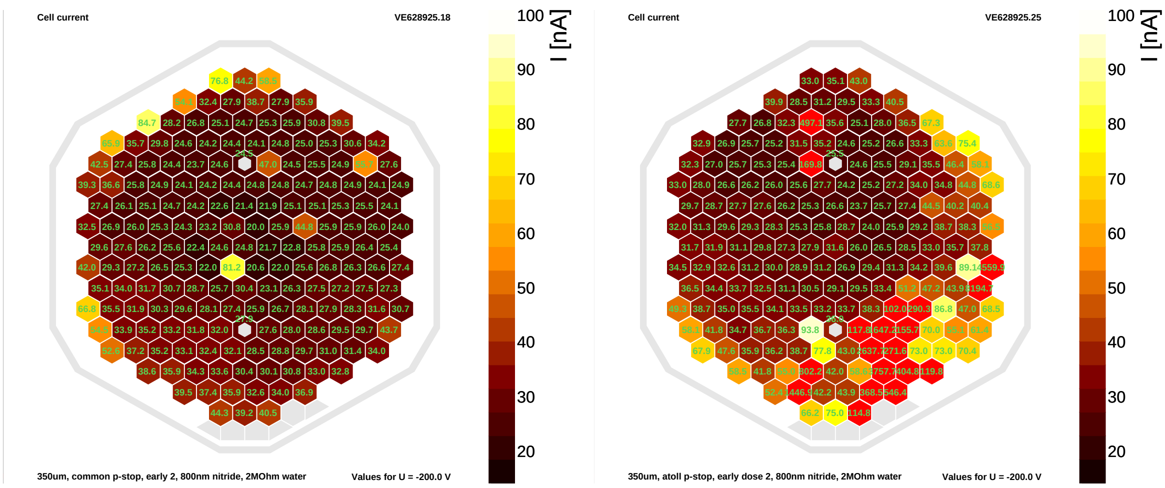

(a) (b)

Figure 6.28: Current measurement with the 7-needle method. The 8-inch Infineon sensor No. 18 (a) and No. 25 (b) are shown.

In Figure 6.28a, individual pads showing twice and three times the current of a regular cell can be observed. These pads have either started to break down already at the given voltage, or have multiples of the individual pad current due to a very low inter pad resistance, as will be shown in Figure 6.30a. No difference in the current can be observed between the quadrants with pad distance 21 µm and 40 µm. Additionally, the quadrant on the bottom left (80 µm pad distance) shows a general pad current, higher than the average by about 10 %. The current increase is higher on the outside of the wafer than near the centre. The quadrant on the bottom right (60 µm pad distance) shows an average current between the currents of the bottom left quadrant (80 µm pad distance) and the quadrants on the top (21 µm and 40 µm pad distance).

It can be observed in Figure 6.28b that pads on the right edges of the sensor have about twice the current than a regular pad. Additionally, in the bottom right quadrant (60 µm pad distance) a cluster of pads in breakdown can be observed. One pad, for example, has a leakage current of about 8 µA at a bias voltage of −200 V. Omitting the pads on the outside and the defect pads, the current measured in the bottom left quadrant is on average higher by about 20 % than the current measured in the top left quadrant. Additionally, the current measured in the bottom left quadrant of sensor No. 25 is higher by about 10 % than the average current of the same quadrant in sensor No. 18.

The detailed statistics of the current of each wafer can be found in Table 6.4. For sensor No. 18 no pad is already in full breakdown at −200 V. Sensor No. 25 however, shows a defective pad with a leakage current about one hundred times larger than the regular pad current. Such a pad can be considered to be in full breakdown.

Table 6.4: Summary of the current statistics of sensor No. 18 and No. 25. The current was measured with the 7-needle method.

Name	Average	Std. dev.	Minimum	Maximum	Median
No. 18	31.0 nA	10.2 nA	20.0 nA	84.7 nA	27.6 nA
No. 25	178.8 nA	782.0 nA	23.7 nA	8194.7 nA	34.1 nA

Probe Card

In the following, current measurements with the probe card setup described in Section 6.1.2 are presented. During the measurements, the probe card and the switching card and the sensors were shielded beneath the light-tight blanket. Because of heat development by the electronics of the switching card, the measurement temperature was (27 ± 1) °C. Referring to Equation 2.35 the leakage current at this temperature is about 54 % larger than at 22 °C.

In Figure 6.29a the probe card measurement of sensor No. 18 is shown. All 237 pads of the sensor are measured. The measured current is larger compared to the measurement with the 7-needle method. Firstly higher temperature, originating from the difference in the measurement setup, contributes to the larger current. Secondly, stray light that enters the setup through irregularities in the covering blanket causes the observed current increase. From the measurements it can be seen that on the right third of the sensor the current is higher by about 50 %. This increase indicates imperfections in the light shielding of the setup. On top of the two previously mentioned effects, a radial increase of current can be seen. The current on the outside is higher by 50 % to 100 %, similar to the values observed in the current measurement with the 7-needle method. Omitting the border cells, which show early breakdowns and higher leakage current, the average current in the bottom left quadrant is larger by about 10 % than the current in the top left quadrant.

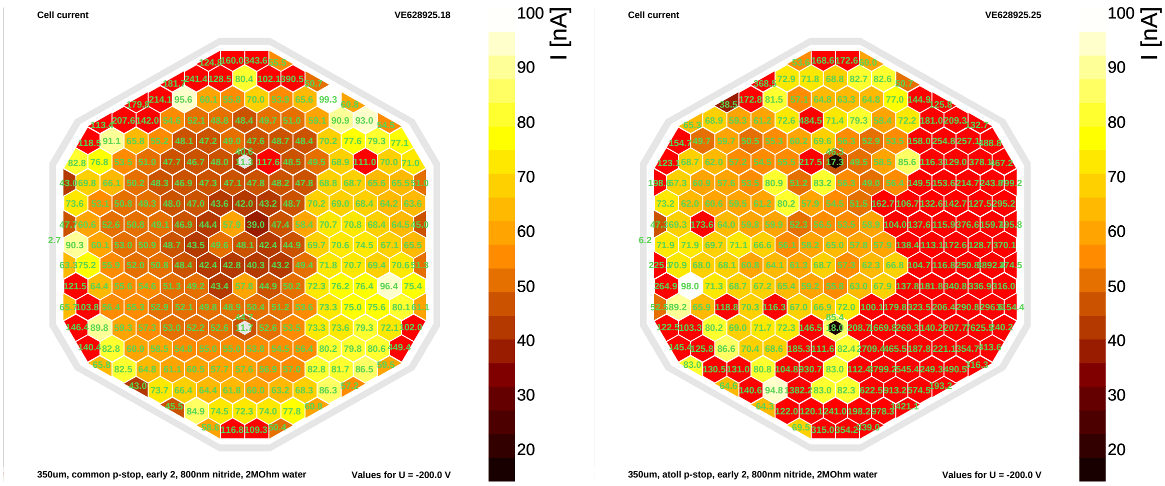

(a) (b)

Figure 6.29: Current measurement with a probe card contacting all pads at the same time. The 8-inch Infineon sensors, No. 18 (a) and No. 25 (b) are shown.

In Figure 6.29b the probe card current measurement of sensor No. 25 at a bias voltage of $-200\,\mathrm{V}$ can be seen. The higher measurement temperature and the additional current contribution due to light incident on the right third of the sensor leads to an increase of the current for this sensor as well. Both effects in addition to the effect of cells that already have increased leakage current, for example, due to breakdown, lead to pad currents higher than $100\,\mathrm{nA}$. Pads with currents higher than $100\,\mathrm{nA}$ are highlighted in red in the figure. Omitting pads with a current above $100\,\mathrm{nA}$, a radial increase of the current can be seen, albeit largely overshadowed by the aforementioned temperature and light effects.

Table 6.5 shows a summary of the statistics of all pad currents for both sensors.

Table 6.5: Summary of the current statistics of sensors No. 18 and No. 25. The current was measured with the probe card method.

Name	Average	Std. dev.	Minimum	Maximum	Median
No. 18	71.5 nA	47.2 nA	11.3 nA	449.4 nA	59.5 nA
No. 25	251.1 nA	673.2.0 nA	17.3 nA	7625.5 nA	83.0 nA

The main advantage of the probe card measurement is that the measurement is about four times faster than the 7-needle method. Another advantage is that all pads have to be contacted with a signle pin to fully measure the sensor. In the 7-needle measurement each pad has to be contacted seven times. This reduces the risk of scratching due to miss-aligned probe needles in automatic measurements. The differing measurement results of the probe card and the 7-needle method originate from the incomplete probe card setup. When construction is finished, the setup will include a dark box similar to that of the probe needle setup and temperature control to prevent the two main sources of increased current.

6.4.2 Inter Pad Resistance Measurement

As another parameter to determine the quality of the sensors the inter pad resistance was investigated. It was measured with the 7-needle method using the probe needle setup described in Section 6.1.1. The resistance between the central pad and all six neighbours is measured.

The result of the measurement for sensor No. 18 is shown in Figure 6.30a. The measurement of pads with higher leakage current results in lower inter pad resistance. Border pads and the pads of the quadrant in the bottom left show leakage current higher than the average value in the 7-needle measurement. These pads also show lower inter pad resistance. Omitting these pads, the average inter pad resistance in the top right quadrant (21 µm pad distance) is 55 GΩ and 60 GΩ in the top left quadrant (40 µm pad distance). With increasing pad distance, the inter pad resistance should increase as well. This behaviour cannot be seen in the bottom quadrants because the influence of the increased leakage current is larger than the influence of the increased pad distance.

In Figure 6.30b, the results of the measurements on sensor No. 25 are displayed. Cells that do not show increased leakage current, and hence show no reduced inter pad resistance, have a resistance value between 50 GΩ and 60 GΩ in the top quadrants. Due to the numerous defective cells in the bottom quadrants, no comparison between these quadrants can be made.

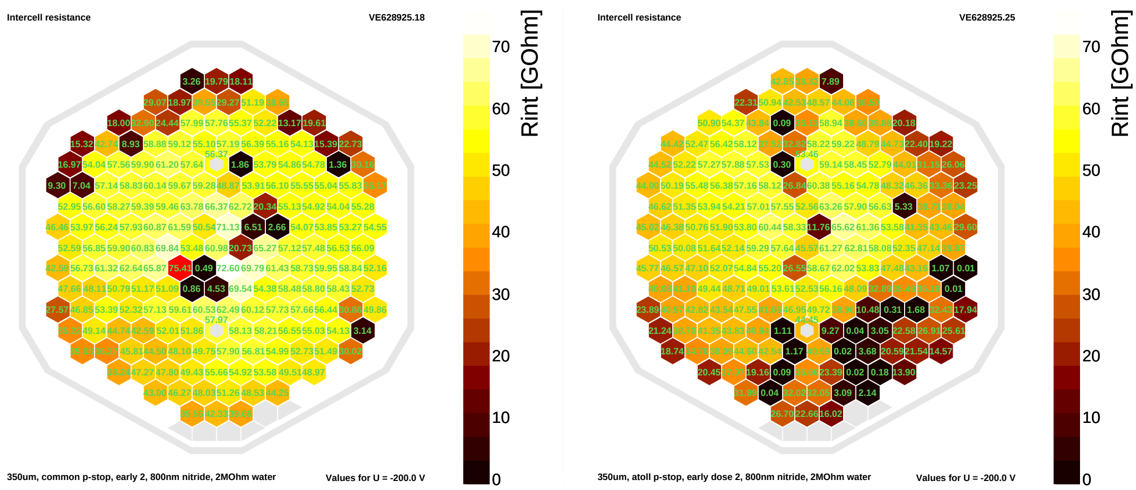

(a) (b)

Figure 6.30: Interpad resistance measurement with 7-needles. The 8-inch Infineon sensors No. 18 (a) and No. 25 (b) are shown.

An advantage of the inter pad resistance measurement method is that it is very susceptible to any kind of defects. If the pad current is too high or the inter pad region is damaged, this will be ascertained by the measurement. With inter pad resistance measurement alone, however, the origin of these problems cannot be determined exactly. Additionally, for higher resistance values (above $100\,\mathrm{G\Omega}$) the measurement error of the current becomes not negligible.

6.4.3 Punchthrough Measurement

For measurements of the punchthrough voltage, the probe needle setup described in Section 6.1.1 is used. The measurement method to determine the punchthrough voltage is described in Section 6.3.3.

The results of the measurements of sensor No. 18 are shown in Figure 6.31a. A distinction into four quadrants can be observed. Table 6.6 lists the average punchthrough through voltage for each quadrant. With increasing pad distance, the punchthrough voltage increases. In the bottom left quadrant ($80\,\mathrm{\mu m}$ pad distance), the punchthrough voltage is on average the lowest of all quadrants. The lowest value can be attributed to an area of pads with roughly two times lower punchthrough voltages that exists within the quadrant. The area corresponds to the area with lower inter pad resistance shown in the previous section. A linear fit of the average punchthrough voltages for the three smallest pad distances results in a slope of $(0.378 \pm 0.013)\,\mathrm{V\,\mu m^{-1}}$. The slope equals the punchthrough voltage increase per micro meter pad distance.

Figure 6.31b shows the results of the measurements on sensor No. 25. The average punchthrough voltages of each quadrant are summarized in Table 6.6. To determine the increase of the punchthrough voltage per micro meter, a linear fit was applied to the punchthrough voltages of all four quadrants with different pad distances. The resulting value is $(0.605 \pm 0.084)\,\mathrm{V\,\mu m^{-1}}$. The statistical fluctuation of the punchthrough voltage for different pad distances is visualised for both sensors in Figure 6.32.

The measurement of the punchthrough voltage gives more information about the pure inter pad isolation than the inter pad resistance measurement, since it is not influenced by the leakage current of the pads. To determine the nature of observed defects, current, inter pad resistance measurement, and inter pad punchthrough voltage have to be taken into account. If the punchthrough voltage shows no abnormalities, but the inter pad resistance does, it can be concluded that the irregular leakage current influences the inter pad resistance measurement. If the punchthrough voltage and the interpad resistance show irregularities on the same pads, an isolation issue exists.

6.4.4 CV Measurement

The capacitance measurement was performed at a an LCR metre measurement frequency of $50\,\mathrm{kHz}$. The probe needle setup described in Section 6.1.1 is used. The schematics of the

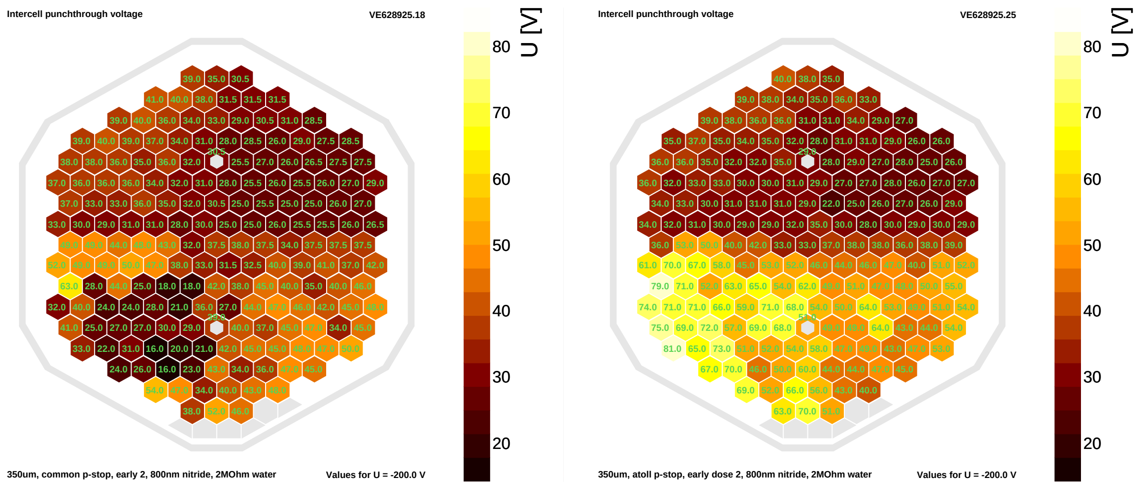

(a) (b)

Figure 6.31: Interpad punchthrough voltage measurement with 7-needles. The 8-inch Infineon sensors No. 18 (a) and No. 25 (b) are shown.

Table 6.6: Summary of the statistics of the punchthrough voltage measurements of sensors No. 18 and No. 25.

Name	Pad distance	Average	Std. dev.	Median
No. 18	21 µm	27.3 V	2.0 V	26.8 V
No. 18	40 µm	34.9 V	3.4 V	35.5 V
No. 18	60 µm	42.0 V	5.4 V	43.0 V
No. 18	80 µm	33.8 V	11.7 V	32.0 V
No. 25	21 µm	29.0 V	3.3 V	28.5 V
No. 25	40 µm	33.6 V	2.9 V	33.5 V
No. 25	60 µm	49.5 V	6.0 V	49.0 V
No. 25	80 µm	63.4 V	9.0 V	65.5 V

circuitry are displayed in Figure 6.24. During the measurement, the neighbouring pads are kept on the same potential as the measured central pad and the capacitance between the central pad and the back of the sensor is measured.

In Figure 6.33a the capacitance is shown at a bias voltage of $-200\,\mathrm{V}$ for sensor No. 18. No specific capacitance distribution pattern could be identified. Excluding the calibration cells, an average capacitance of $(29.800 \pm 0.067)\,\mathrm{pF}$ was measured. Assuming a sensor thickness of 350 µm and a pad area of $0.99\,\mathrm{cm}^2$, the capacitance calculated using the parallel plate capacitor formula is 29.803 pF. Thus, it can be concluded that the sensor thickness remains reasonably constant at 350 µm across the whole sensor area.

The result of the capacitance measurement on sensor No. 25 is shown in Figure 6.33b. In the bottom left quadrant, a group of 7 pads with a slightly larger capacitance than the rest of the pads can be identified. The capacitance increase of about 4 % results from a

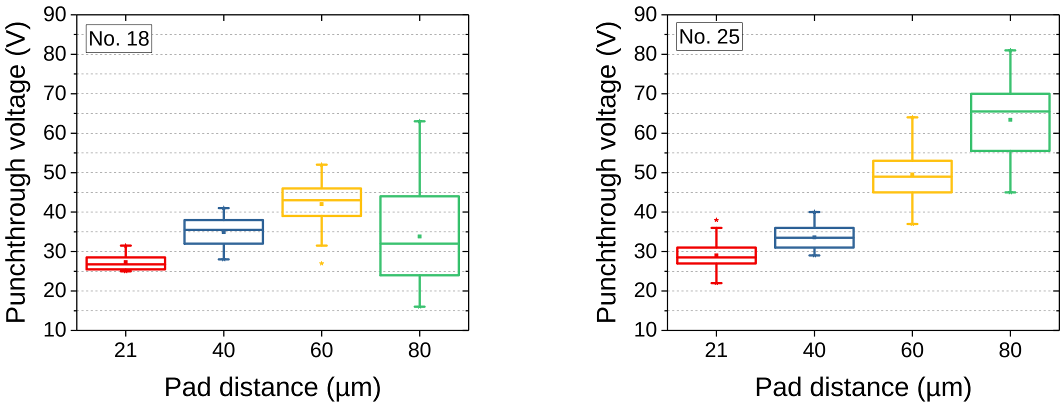

(a) (b)

Figure 6.32: Dependence of the punchthrough voltage on pad distance. (a) Wafer No. 18. (b) Wafer No. 25.

bad probe needle connection on at least one of the neighbour pads. If a neighbour pad is on undefined potential, an additional capacitance contribution is measured on the central pad. Additionally, five pads exist where the central probe needle did not have sufficient contact with the pad and hence a non-sensible value of $-43.79\,\mathrm{pF}$ is read out for these cells. This value corresponds to the correction for stray parallel capacitances introduced by the circuitry. Omitting the cells with non-sensible measurement results and the calibration cells, an average capacitance of $(29.844 \pm 0.271)\,\mathrm{pF}$ is measured.

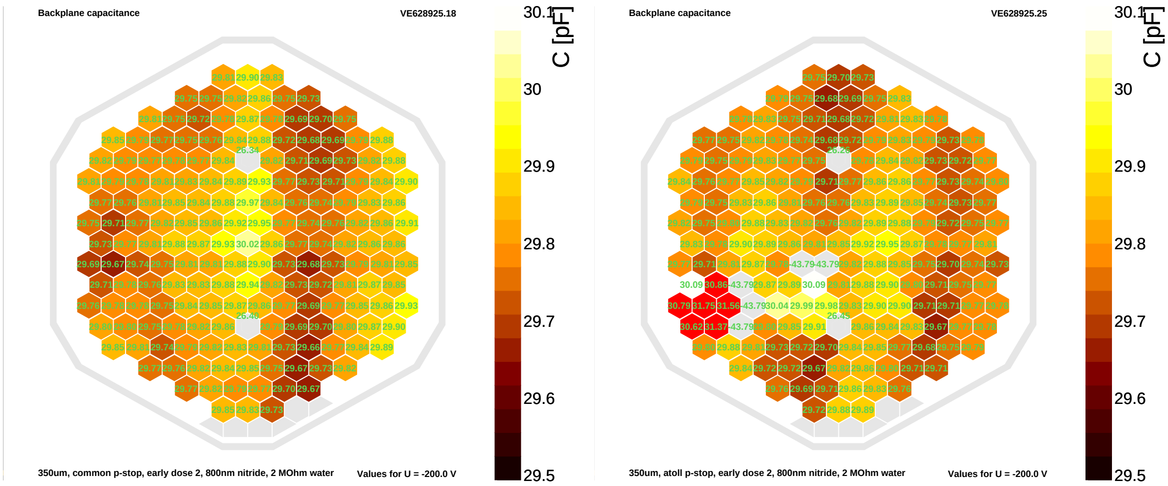

(a) (b)

Figure 6.33: Pad capacitance measurement with 7-needles. The 8-inch Infineon sensors No. 18 (a) and No. 25 (b) are shown.

The full depletion voltage is determined from the capacitance measurement. The result for sensor No. 18 is plotted in Figure 6.34a. A radial distribution of the full depletion voltage can be observed. The full depletion voltage is about 10 V higher in the centre than on the outer edge of the sensor. On average, the full depletion voltage is 150 V. The small radial variation is attributed to a radial resistivity variation, since a thickness variation can be excluded by the capacitance measurement. The relation between the resistivity and the full depletion voltage is given in Equation 2.24.

The full depletion voltages for sensor No. 25 are plotted in Figure 6.34b. The pad full depletion voltage ranges from 150 V to 160 V. The values in the bottom left quadrant are not representative due to wrong fitting originating from a contact loss between the probe needles and the pads. The extracted values in the bottom right quadrant are lower than the average value for the rest of the quadrants. This behaviour can be traced back to the bad IV behaviour observed in the 7-needle current measurement, since pads in breakdown usually do not show the CV behaviour of a regular diode.

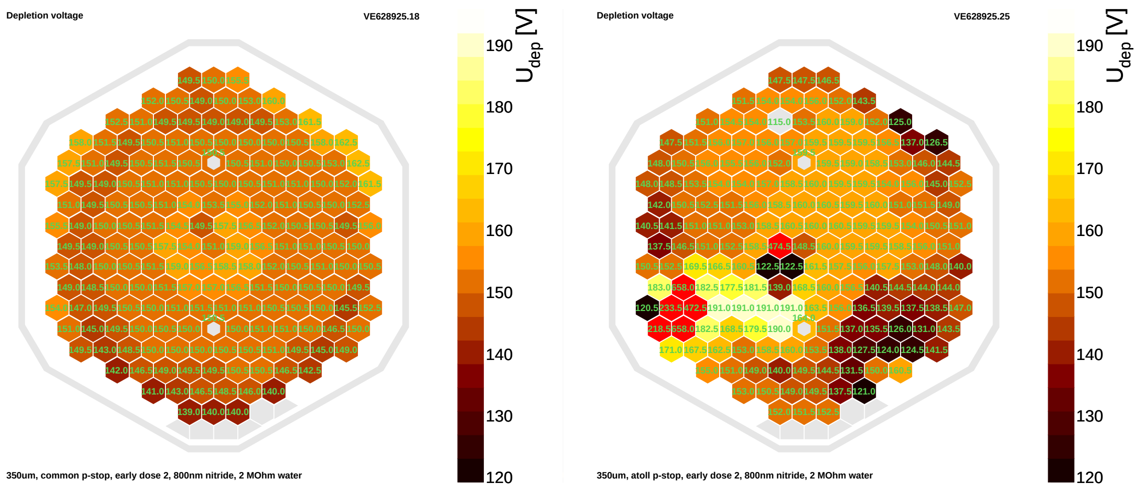

(a) (b)

Figure 6.34: Distribution of the determined full depletion voltage. The 8-inch Infineon sensors No. 18 (a) and No. 25 (b) are shown.

6.4.5 Inter Pad Capacitance Measurement

Inter pad capacitance measurements were performed at an LCR metre measurement frequency of 600 kHz using the probe needle setup described in Section 6.1.1. The schematic circuitry of the measurement is shown in Figure 6.26. Due to missing correction for stray series capacitances introduced by the circuitry, all measured capacitances have a constant offset.

The result of the measurement of sensor No. 18 at a bias voltage of −200 V is shown in Figure 6.35a. A clear distinction of four quadrants with different pad distance can be seen. With increasing pad distance, the inter pad capacitance decreases. Omitting all border cells, the average inter pad capacitance value for each quadrant is determined. This value is plotted against the pad distance and fitted with a linear function. The slope of the fit corresponds to the decrease of the inter pad capacitance with increasing pad distance. A value of $(-0.0457 \pm 0.0033)\,\mathrm{pF\,\mu m^{-1}}$ is determined. This means that for a 10 µm larger pad distance the inter pad capacitance decreases by about 0.46 pF.

Figure 6.35b shows the result of the inter pad capacitance measurement for sensor No. 25. Four quadrants can be distinguished. The sensor pads were not contacted anew between the pad capacitance and the inter pad capacitance measurements. Because of this, the same area in the bottom left quadrant as observed during the pad capacitance measurement presented in Section 6.4.4 suffers from non-representative capacitance values caused by probe needle contact problems. Omitting these cells and the border pads, the decrease of the inter pad capacitance with increasing pad distance can be determined in the same way as for sensor No. 18. The value for sensor No. 25 is $(-0.0458 \pm 0.0031)\,\mathrm{pF\,\mu m^{-1}}$. Increasing the pad distance by 10 µm leads to a decrease of the inter pad capacitance value by about (0.46 ± 0.03) pF. The change of inter pad capacitance with changing pad distance is for nearly identical both wafers.

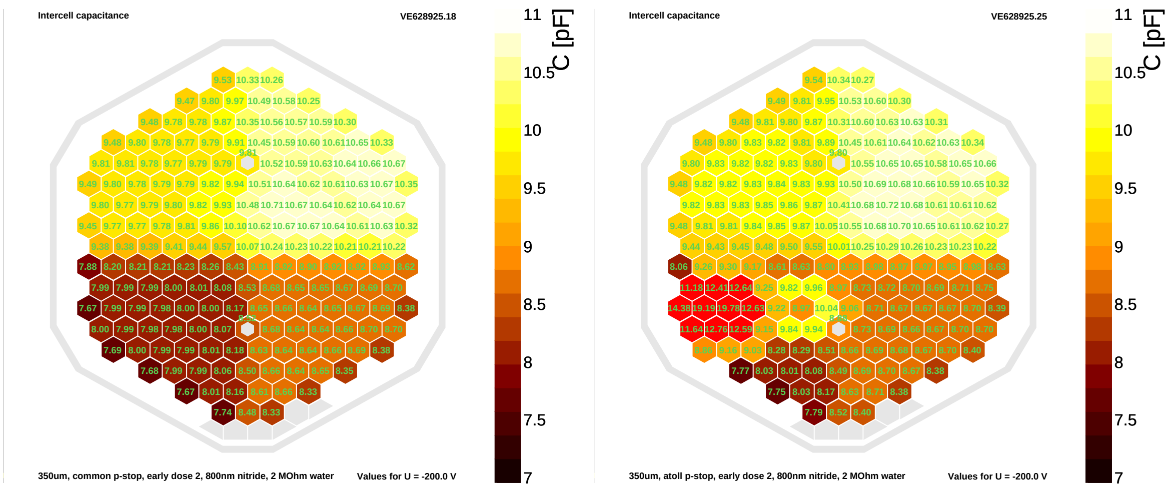

(a) **(b)**

Figure 6.35: Interpad capacitance measurement with 7-needles. The 8-inch Infineon sensors No. 18 (a) and No. 25 (b) are shown.

A TCAD simulation of the inter pad capacitance with a sensor thickness of 350 µm predicts the capacitance values listed in Table 6.7. The simulation was performed at a bias voltage of -200 V. A linear fit to the simulated inter pad capacitance versus pad distance characteristic yields a slope of $(-0.0415 \pm 0.0034)\,\mathrm{pF\,\mu m^{-1}}$. Increasing the simulated pad distance by 10 µm leads to a decrease of the simulated inter pad capacitance by about (0.42 ± 0.03) pF. The simulation and the measurement coincide within their respective errors.

Table 6.7: Simulated interpad capacitance values for the geometry of the 8-inch HGCal demonstrator sensors with a thickness of 350 µm. The TCAD simulation was performed at a bias voltage of −200 V.

Pad distance	Metal overhang	Inter pad capacitance
21 µm	5 µm	4.942 pF
40 µm	12.5 µm	4.231 pF
60 µm	12.5 µm	3.144 pF
80 µm	12.5 µm	2.582 pF

7 Conclusion

This thesis presents the development of 8-inch silicon sensors for the *High Granularity Calorimeter* (HGCal) of the CMS experiment for HL-LHC operation.

It starts with an overview of the present CMS experiment at the LHC and motivates the upgrade to the high luminosity operation. Special focus is given to the endcap calorimeter of CMS. The current electromagnetic calorimeter consists of lead tungstate scintillating crystals. The current hadronic calorimeter uses plastic scintillator tiles, which are read out by silicon photomultipliers. Scintillator technology will not be able to cope with the maximum expected fluences of the HL-LHC era. Radiation damage in the scintillator reduces the light output, which is the main reason for the replacement of the present calorimeter endcap with the new *High Granularity Calorimeter*.

A detailed description of the features and requirements is presented. These include the need for radiation tolerance up to a fluence of about $1 \times 10^{16}\,\mathrm{n_{eq}/cm^2}$, fine lateral and transversal granularity, and timing capability. The detector technology that can meet these demands, makes use of silicon. Using silicon sensors in a calorimeter of the size of the HGCal is unprecedented. The design and structure of the new endcap calorimeter is shown. Depending on the expected fluence levels in the endcap, the sensors have a different thickness. This is due to the degradation of the charge collection efficiency with radiation damage in silicon. In total about $600\,\mathrm{m^2}$ of silicon sensors are needed. This corresponds to almost 27000 8-inch wafers. In the initial technical proposal of the HGCal project, 6-inch silicon sensors were foreseen. At that point in time, 6-inch technology was the standard for the sensor production for experiments in high energy physics.

The first main part of the author's work is the complete design of the first 8-inch HGCal demonstrator sensor. In general, the concept of the design was based on the knowledge from previous 6-inch prototypes. The design was created using script programming. The polygons that make up each lithography mask had to be defined with sub-micro metre precision. Different masks are needed for the lithography steps in the silicon sensor production. The design included not only the main sensor but also various test structures and alignment marks, which are essential for the wafer production. The main sensor is designed as a hexagon with truncated tips, resulting in a dodecagonal shape. Its area is as large as possible utilizing the optimum available wafer area. This feature is needed not only for module construction but also to use the space on the round wafer efficienctly. Test structures are implemented on the otherwise empty parts of the wafer around the main sensor. The mask design was used by Infineon Technologies Austria AG to produce the 8-inch

HGCal demonstrator sensors. These sensors proved the feasibility of the 8-inch sensors to the HGCal community.

Two 8-inch sensors that only differed in the p-stop mask were compared in detail in the thesis. IV measurements with the 7-needle method and a probe card, inter pad resistance measurements, inter pad punchthrough voltage measurements, pad capacitance measurements, and inter pad capacitance measurements were performed. The thesis explains all measurement methods in detail. All measurement types were proven to yield feasible results. Furthermore, it was shown that the inter pad resistance measurement alone is not enough to decide whether a sensor pad is badly isolated from its neighbours. To disentangle abnormal resistivity values from the effect of pads with high leakage current, the inter pad punchthrough voltage measurement is required. The capacitance measurements were reproduced with TCAD simulations.

The first 8-inch HGCal demonstrator design acted as a proof of principle for the feasibility of producing the calorimeter sensors on 8-inch wafers. In the next step the author optimised the first sensor design with Synopsys TCAD. Extensive periphery simulations were performed. The optimisation process started from the geometry of the demonstrator design and culminated in a new set of parameters, which increased the simulated breakdown voltage by about 50 V. Additionally, the inter pad geometry was simulated and optimised. It was found that increasing pad distance leads to decreasing breakdown voltage when both neighbouring pads are biased to the same potential. To get realistic simulation results, test structure measurements were performed to extract necessary parameters for the simulation. The current of diodes, the resistivity, and the interface oxide charge concentration are extracted. Charge collection efficiency (CCE) measurements were performed as well.

The knowledge gained throughout this work was used by the author to programme the prototype design of the 8-inch HGCal sensors with 192 pads. This design is used by all vendors that produce 8-inch HGCal sensors. Sensors with this design will be implemented in the *High Granularity Calorimeter* of CMS for the *CMS Phase II upgrade*.

For silicon sensors in a high radiation environment like a calorimeter, the description and understanding of irradiation damage is important to choose the right sensor specifications. Therefore, four different irradiation models are compared in the thesis using Synopsys TCAD. The HPTM model reproduces the current predicted by theory best. The simulated full depletion voltage is larger by about a factor of two in the Eber proton model in comparison to the HPTM model. All models confirmed that the CCE gets smaller for thicker sensors. The simulated CCE values for a fully depleted sensor are slightly lower in the Eber proton and neutron model in comparison to the other two models. The Eber models show a faster degradation of the CCE values with fluence. The only model able to describe neutron damage is the neutron model by Eber.

It has not yet been decided by the HGCal collaboration if the 300 µm thick HGCal sensors will be p-type or n-type. Therefore, diodes of the same thickness are compared with TCAD simulations at the fluence levels expected in the experiment. Neutron damage is simulated using the Eber neutron model. The decisive factor is the full depletion voltage. N-type diodes with a resistivity of 1 kΩ cm fully deplete at bias voltages smaller than 800 V. P-type diodes with a resistivity of 7 kΩ cm fully deplete at bias voltages smaller than 800 V only when decreasing the sensor thickness to about 250 µm. N-type sensors may be cheaper than p-type sensors, but when using p-type sensors the dual polarity requirement of the readout chip would not be needed, which is economically advantageous.

Acknowledgements

I would like to express my gratitude to all the people who supported me during the last three years of my work at HEPHY. Without their support and advice this work would not have been possible.

First of all, I would like to thank my doctoral supervisor Manfred Krammer who gave me the opportunity to work at this highly interesting topic and supported me throughout the years. Equal thanks should go to my second supervisor Thomas Bergauer, who helped me and gave me valuable advice on many occasions.

Additionally, I would like to thank Marko Dragicevic, who supported me in the creation of the wafer design. He was always a valuable contact person to discuss about CMS related topics. I would also like to express my gratitude towards Johannes Hacker, the project leader at Infineon. Many issues and details of the design had to be discussed with him during the creation process of the 8-inch HGCal demonstrator sensor.

Special thanks is also owed to my colleagues, Axel König, Johannes Großmann, Dominic Blöch, and Viktoria Hinger. All of them became very good friends over the years. A problem of any nature could always be discussed with them. Their support was a huge help in the creation of the work.

I would like to express my gratitude towards Manfred Valentan as well. His contribution in the sensor measurements helped me a lot and saved me lots of time.

I also want to thank my parents, brothers, sisters, and my uncle who all showed interest in my work and supported me throughout the years. Special thank goes to my beloved girlfriend Viktoria, who always supported and encouraged me.

The research leading to these results has received funding from the European Commission under the Horizon-2020 Research Infrastructures project “AIDA-2020”, grant agreement no. 654168.

Bibliography

[1] *60 year CERN anniversary*, URL https://cern60.web.cern.ch/en/exhibitions/cern. pages 1

[2] *LHC Guide* (2017), URL https://cds.cern.ch/record/2255762. pages 2

[3] Herr, W. and Muratori, B., *Concept of luminosity*, URL http://cds.cern.ch/record/941318. pages 2

[4] *CMS Public Lumi Results*, URL https://twiki.cern.ch/twiki/bin/view/CMSPublic/LumiPublicResults. pages 2

[5] *HiLumi Project Schedule*, URL https://project-hl-lhc-industry.web.cern.ch/content/project-schedule. pages 3

[6] Contardo, D. et al., *Technical Proposal for the Phase-II Upgrade of the CMS Detector*, Tech. Rep. CERN-LHCC-2015-010. LHCC-P-008. CMS-TDR-15-02, Geneva (2015), URL https://cds.cern.ch/record/2020886, upgrade Project Leader Deputies: Lucia Silvestris (INFN-Bari), Jeremy Mans (University of Minnesota) Additional contacts: Lucia.Silvestris@cern.ch, Jeremy.Mans@cern.ch. pages 4, 5, 10, 11, 40, 41

[7] CMS Collaboration, *Observation of a new boson at a mass of 125 GeV with the CMS experiment at the LHC*, Physics Letters B, 716(1) (2012) 30–61, ISSN 0370-2693, URL http://www.sciencedirect.com/science/article/pii/S0370269312008581. pages 5

[8] CMS Collaboration, *The Phase-2 Upgrade of the CMS Endcap Calorimeter*, Tech. Rep. CERN-LHCC-2017-023. CMS-TDR-019, CERN, Geneva (2017), URL https://cds.cern.ch/record/2293646, technical Design Report of the endcap calorimeter for the Phase-2 upgrade of the CMS experiment, in view of the HL-LHC run. pages 5, 40, 41, 43, 44, 46, 47, 48, 49, 51, 96, 114, 124

[9] Aaboud, M. et al., *Search for Higgs bosons produced via vector-boson fusion and decaying into bottom quark pairs in* $\sqrt{s} = 13$ TeV *pp collisions with the ATLAS detector*, Tech. Rep. arXiv:1807.08639, CERN, Geneva (2018), URL http://cds.cern.ch/record/2632158, * Temporary entry *. pages 5

[10] Barney, D., *CMS Detector Slice* (2016), URL https://cds.cern.ch/record/2120661, cMS Collection. pages 7

[11] Saha, A., *Phase 1 upgrade of the CMS pixel detector*, Journal of Instrumentation, 12(02) (2017) C02033, URL http://stacks.iop.org/1748-0221/12/i=02/a=C02033. pages 8

[12] Beddall, A. and Beddall, A., *Measurement of the Dalitz-decay branching ratio of the π^0*, Eur. Phys. J. C, 54(CERN-ALEPH-ARCH-DATA-2009-003. 3) (2009) 365–370. 6 p, URL `http://cds.cern.ch/record/1156138`. pages 8

[13] CMS Collaboration, *Energy calibration and resolution of the CMS electromagnetic calorimeter in pp collisions at sqrt(s) = 7 TeV*, Journal of Instrumentation, 8(09) (2013) P09009, URL `http://stacks.iop.org/1748-0221/8/i=09/a=P09009`. pages 8

[14] Cooper, S. I., *Phase I Upgrade of the CMS Hadron Calorimeter*, Nuclear and Particle Physics Proceedings, 273-275 (2016) 1002 – 1007, ISSN 2405-6014, URL `http://www.sciencedirect.com/science/article/pii/S240560141500646X`, 37th International Conference on High Energy Physics (ICHEP). pages 9

[15] CMS Collaboration, *Performance of the CMS hadron calorimeter with cosmic ray muons and LHC beam data*, Journal of Instrumentation, 5(03) (2010) T03012, URL `http://stacks.iop.org/1748-0221/5/i=03/a=T03012`. pages 9

[16] Abbrescia, M., *The upgrade of the CMS muon system*, PoS, EPS-HEP2013 (2013) 485. pages 10

[17] Bayatyan, G. L. et al., *CMS TriDAS project: Technical Design Report, Volume 1: The Trigger Systems*, Technical Design Report CMS, URL `https://cds.cern.ch/record/706847`. pages 10

[18] Cornat, R., *Design of a Si-W electromagnetic calorimeter for the International Linear Collider and study of crosstalk in silicon sensors*, *2008 IEEE Nuclear Science Symposium Conference Record*, pp. 2701–2708 (2008), ISSN 1082-3654. pages 11, 43

[19] Adloff, C. et al., *Response of the CALICE Si-W electromagnetic calorimeter physics prototype to electrons*, Nuclear Instruments and Methods in Physics Research Section A: Accelerators, Spectrometers, Detectors and Associated Equipment, 608(3) (2009) 372 – 383, ISSN 0168-9002, URL `http://www.sciencedirect.com/science/article/pii/S0168900209014673`. pages 11

[20] Sze, S., *Semiconductor devices, physics and technology*, Wiley (1985). pages 13, 14, 20

[21] Sze, S. and Ng, K., *Physics of Semiconductor Devices*, Wiley (2006). pages 15, 20, 68

[22] Synopsys, *Sentaurus Device User Guide* (2016). pages 18, 74, 76, 77, 92

[23] Patrignani, C. et al., *Review of Particle Physics*, Chinese Physics C, 40 (2016 and 2017 update) 100001, URL `http://pdg.lbl.gov/2017/reviews/contents_sports.html`. pages 22, 23, 24, 25, 26

[24] Alig, R. C., Bloom, S. and Struck, C. W., *Scattering by ionization and phonon emission in semiconductors*, Phys. Rev. B, 22 (1980) 5565–5582, URL `https://link.aps.org/doi/10.1103/PhysRevB.22.5565`. pages 24

[25] Shockley, W., *Currents to Conductors Induced by a Moving Point Charge*, Journal of Applied Physics, 9 (1938) 635–636. pages 27

[26] Ramo, S., *Currents Induced by Electron Motion*, Proceedings of the IRE, 27(9) (1939) 584–585, ISSN 0096-8390. pages 27

[27] Cenna, F. et al., *Weightfield2: A fast simulator for silicon and diamond solid state detector*, Nuclear Instruments and Methods in Physics Research Section A: Accelerators, Spectrometers, Detectors and Associated Equipment, 796 (2015) 149 – 153, ISSN 0168-9002, URL `http://www.sciencedirect.com/science/article/pii/S0168900215004842`, proceedings of the 10th International Conference on Radiation Effects on Semiconductor Materials Detectors and Devices. pages 27, 28

[28] Hartmann, F., *Evolution of Silicon Sensor Technology in Particle Physics* (2017), ISBN 978-3-319-64434-9. pages 28, 29, 34, 58

[29] Huhtinen, M., *Simulation of non-ionising energy loss and defect formation in silicon*, Nuclear Instruments and Methods in Physics Research Section A: Accelerators, Spectrometers, Detectors and Associated Equipment, 491(1) (2002) 194 – 215, ISSN 0168-9002, URL `http://www.sciencedirect.com/science/article/pii/S0168900202012275`. pages 31

[30] Moll, M., *Displacement Damage in Silicon Detectors for High Energy Physics*, IEEE Transactions on Nuclear Science, pp. 1–1, ISSN 0018-9499. pages 30, 32, 33, 34, 35

[31] Moll, M., *Radiation damage in silicon particle detectors: Microscopic defects and macroscopic properties*, Ph.D. thesis, Hamburg University (1999). pages 30, 33, 78, 80

[32] Srour, J. R. and Palko, J. W., *Displacement Damage Effects in Irradiated Semiconductor Devices*, IEEE Transactions on Nuclear Science, 60(3) (2013) 1740–1766, ISSN 0018-9499. pages 31

[33] Moll, M., Fretwurst, E. and Lindström, G., *Leakage current of hadron irradiated silicon detectors – material dependence*, Nuclear Instruments and Methods in Physics Research Section A: Accelerators, Spectrometers, Detectors and Associated Equipment, 426(1) (1999) 87 – 93, ISSN 0168-9002, URL `http://www.sciencedirect.com/science/article/pii/S0168900298014752`. pages 31

[34] Kramberger, G., *Signal development in irradiated silicon detectors*, Ph.D. thesis, Stefan Inst., Ljubljana (2001), URL `http://inspirehep.net/record/1088069/files/CERN-THESIS-2001-038.pdf`. pages 35

[35] Rossi, B. B., *High Energy Particles*, Prentice-Hall (1952). pages 38

[36] Kolanoski, H. and Wermes, N., *Teilchendetektoren*, Springer (2016), ISBN 9783662453490, 9783662453506. pages 38

[37] Sirunyan, A. et al., *Particle-flow reconstruction and global event description with the CMS detector*, Journal of Instrumentation, 12(10) (2017) P10003, URL `http://stacks.iop.org/1748-0221/12/i=10/a=P10003`. pages 42

[38] Apresyan, A., *Investigation of fast timing capabilities of silicon sensors for the CMS high granularity calorimeter at HL-LHC*, *2016 IEEE Nuclear Science Symposium, Medical Imaging Conference and Room-Temperature Semiconductor Detector Workshop (NSS/MIC/RTSD)*, pp. 1–8 (2016). pages 42

[39] Currás, E. et al., *Radiation hardness and precision timing study of silicon detectors for the CMS High Granularity Calorimeter (HGC)*, Nuclear Instruments and Methods in Physics Research Section A: Accelerators, Spectrometers, Detectors and Associated Equipment, 845 (2017) 60 – 63, ISSN 0168-9002, URL `http://www.sciencedirect.com/science/article/pii/S0168900216303679`, proceedings of the Vienna Conference on Instrumentation 2016. pages 42, 45

[40] CMS Collaboration, *The Phase-2 Upgrade of the CMS Tracker*, Tech. Rep. CERN-LHCC-2017-009. CMS-TDR-014, CERN, Geneva (2017), URL `https://cds.cern.ch/record/2272264`. pages 51

[41] Cornat, R. and the CALICE collaboration, *Semiconductor sensors for the CALICE SiW EMC and study of the cross-talk between guard rings and pixels in the CALICE SiW prototype*, Journal of Physics: Conference Series, 160(1) (2009) 012067, URL `http://stacks.iop.org/1742-6596/160/i=1/a=012067`. pages 52

[42] *KLayout - High Performance Layout Viewer And Editor*, URL `http://www.klayout.de`. pages 52

[43] Bergauer, T. et al., *First thin AC-coupled silicon strip sensors on 8-inch wafers*, Nuclear Instruments and Methods in Physics Research, Section A: Accelerators, Spectrometers, Detectors and Associated Equipment, 830(Supplement C) (2016) 473–479, ISSN 01689002. pages 55

[44] König, A., *Planar Silicon Strip Sensors for the CMS Phase-2 Upgrade*, Thesis, TU Wien (2018), URL `http://katalog.ub.tuwien.ac.at/AC14526557`. pages 55

[45] Klein, N. and Gafni, H., *The maximum dielectric strength of thin silicon oxide films*, IEEE Transactions on Electron Devices, ED-13(2) (1966) 281–289, ISSN 0018-9383. pages 58

[46] Printz, M., *Analysis of n-in-p type silicon detectors for high radiation environment with fast analogue and binary readout systems*, Ph.D. thesis, Karlsruher Institut für Technologie (KIT) (2016), URL `https://ekp-invenio.physik.uni-karlsruhe.de/record/48797`, karlsruher Institut für Technologie (KIT), Diss., 2016. pages 59

[47] Hinger, V. et al., *Process quality control for large-scale silicon sensor productions*, Nuclear Instruments and Methods in Physics Research Section A: Accelerators, Spectrometers, Detectors and Associated Equipment, ISSN 0168-9002, URL http://www.sciencedirect.com/science/article/pii/S0168900218309276. pages 67

[48] Schroder, D. K., *Semiconductor Material and Device Characterization*, John Wiley & Sons, Inc. (2005), ISBN 9780471749097, URL http://dx.doi.org/10.1002/0471749095. pages 67

[49] Grove, A. S. and Fitzgerald, D. J., *Surface effects on p-n junctions: Characteristics of surface space-charge regions under non-equilibrium conditions*, Solid State Electronics, 9(8) (1966) 783–806, ISSN 00381101. pages 68

[50] *Synopsys TCAD*, URL https://www.synopsys.com/. pages 73

[51] Synopsys, *Sentaurus Workbench User Guide* (2016). pages 74

[52] Synopsys, *Sentaurus Process User Guide* (2016). pages 74

[53] Synopsys, *Sentaurus Structure Editor User Guide* (2016). pages 75

[54] Synopsys, *Sentaurus Visual User Guide* (2016). pages 76

[55] Eber, R., *Untersuchung neuartiger Sensorkonzepte und Entwicklung eines effektiven Modells der Strahlenschädigung für die Simulation hochbestrahlter Silizium-Teilchendetektoren*, Ph.D. thesis, Karlsruher Institut für Technologie (KIT) (2013). pages 78, 79, 82, 85, 96, 102, 103

[56] Eremin, V., Verbitskaya, E. and Li, Z., *The origin of double peak electric field distribution in heavily irradiated silicon detectors*, Nuclear Instruments and Methods in Physics Research Section A: Accelerators, Spectrometers, Detectors and Associated Equipment, 476(3) (2002) 556 – 564, ISSN 0168-9002, URL http://www.sciencedirect.com/science/article/pii/S0168900201016424, proc. of the 3rd Int. Conf. on Radiation Effects on Semiconductor Materials, Detectors and Devices. pages 78

[57] Moscatelli, F. et al., *Measurements and TCAD simulations of bulk and surface radiation damage effects in silicon detectors*, *2015 IEEE Nuclear Science Symposium and Medical Imaging Conference (NSS/MIC)*, pp. 1–6 (2015). pages 79

[58] Schwandt, J. et al., *A new model for the TCAD simulation of the silicon damage by high fluence proton irradiation* (2018), URL https://indico.cern.ch/event/719814/contributions/3022491/attachments/1661107/2661343/js_RD50_Hamburg_20180604.pdf, talk at 32^{nd} RD50 Workshop. pages 79, 80, 83, 103

[59] Borchi, E. et al., *Temperature and frequency dependence of the capacitance of heavily irradiated silicon diodes*, Solid-State Electronics, 42(11) (1998) 2093 –

2096, ISSN 0038-1101, URL http://www.sciencedirect.com/science/article/pii/S0038110198001865. pages 81

[60] Wunstorf, R. et al., *Investigations of donor and acceptor removal and long term annealing in silicon with different boron/phosphorus ratios*, Nuclear Instruments and Methods in Physics Research Section A: Accelerators, Spectrometers, Detectors and Associated Equipment, 377(2) (1996) 228 – 233, ISSN 0168-9002, URL http://www.sciencedirect.com/science/article/pii/0168900296002173, proceedings of the Seventh European Symposium on Semiconductor. pages 85

[61] Mandić, I. et al., *Observation of full charge collection efficiency in heavily irradiated n+p strip detectors irradiated up to $3\times10^{15} n_{eq}/cm^2$*, Nuclear Instruments and Methods in Physics Research Section A: Accelerators, Spectrometers, Detectors and Associated Equipment, 612(3) (2010) 474 – 477, ISSN 0168-9002, URL http://www.sciencedirect.com/science/article/pii/S0168900209015721, proceedings of the 7th International Conference on Radiation Effects on Semiconductor materials, Detectors and Devices. pages 86

[62] Lange, J. et al., *Charge collection studies of proton-irradiated n- and p-type epitaxial silicon detectors*, Nuclear Instruments and Methods in Physics Research Section A: Accelerators, Spectrometers, Detectors and Associated Equipment, 624(2) (2010) 405 – 409, ISSN 0168-9002, URL http://www.sciencedirect.com/science/article/pii/S0168900210007990, new Developments in Radiation Detectors. pages 86

[63] Casse, G. et al., *Enhanced efficiency of segmented silicon detectors of different thicknesses after proton irradiations up to $1\times10^{16} n_{eq}/cm^2$*, Nuclear Instruments and Methods in Physics Research Section A: Accelerators, Spectrometers, Detectors and Associated Equipment, 624(2) (2010) 401 – 404, ISSN 0168-9002, URL http://www.sciencedirect.com/science/article/pii/S0168900210003906, new Developments in Radiation Detectors. pages 86

[64] Hall, R. N., *Electron-Hole Recombination in Germanium*, Phys. Rev., 87 (1952) 387–387, URL https://link.aps.org/doi/10.1103/PhysRev.87.387. pages 92

[65] Shockley, W. and Read, W. T., *Statistics of the Recombinations of Holes and Electrons*, Phys. Rev., 87 (1952) 835–842, URL https://link.aps.org/doi/10.1103/PhysRev.87.835. pages 92

[66] Fretwurst, E. et al., *The influence of edge effects on the determination of the doping profile of silicon pad diodes*, Nuclear Instruments and Methods in Physics Research, Section A: Accelerators, Spectrometers, Detectors and Associated Equipment, 867(April) (2017) 231–236, ISSN 01689002, URL http://dx.doi.org/10.1016/j.nima.2017.04.020. pages 94

[67] *LabVIEW*, URL http://www.ni.com/de-at/shop/labview/labview-details.html. pages 125

[68] *Gel-Pak*, URL `https://www.gelpak.com/`. pages 127

[69] Binnig, G., Quate, C. F. and Gerber, C., *Atomic Force Microscope*, Phys. Rev. Lett., 56 (1986) 930–933, URL `https://link.aps.org/doi/10.1103/PhysRevLett.56.930`. pages 128